First Light for the Next Generation of Compton and Pair Telescopes

Andreas Christian Zoglauer

Technische Universität München

Max-Planck-Institut für extraterrestrische Physik
Garching bei München

First Light for the Next Generation of Compton and Pair Telescopes

Andreas Christian Zoglauer

Vollständiger Abdruck der von der Fakultät für Physik der Technischen Universität München zur Erlangung des akademischen Grades eines

Doktors der Naturwissenschaften

genehmigten Dissertation.

Vorsitzender:		Univ.-Prof. Dr. Andrzej Jerzy Buras
Prüfer der Dissertation:	1.	apl. Prof. Dr. Volker Schönfelder
	2.	Univ.-Prof. Dr. Franz von Feilitzsch

Die Dissertation wurde am 17.11.2005 bei der Technischen Universität München eingereicht und durch die Fakultät für Physik am 8.12.2005 angenommen.

Zusammenfassung

Gamma-Astronomie im MeV-Bereich von einigen hundert keV bis zu einigen zehn MeV liefert einzigartige Informationen über das Universum: Die verhältnismäßig geringe Wechselwirkungswahrscheinlichkeit von Gammastrahlen ermöglicht es Quellen zu studieren, deren Strahlung bei niedrigeren Energien vom umgebenden Material stark absorbiert wird. Linien aus Kernzerfällen liefern Informationen über Ursprung und Verteilung einzelner Isotope im Kosmos. Ein Instrument, das effizient sowohl Compton- als auch Paarereignisse — die beiden dominanten Wechselwirkungsprozesse — aufzeichnet, könnte bedeutend empfindlichere Beobachtungen in diesem Energiebereich ermöglichen.

Die Entwicklung einer möglichen zukünftigen Mission für "**M**edium **E**nergy **G**amma-ray **A**stronomy" wurde am Max-Planck-Institut für extraterrestrische Physik in Garching unter dem Namen MEGA vorangetrieben. MEGA besteht aus einem Spurdetektor und einem Kalorimeter und soll mindestens den Energiebereich von 0,4 MeV bis 50 MeV abdecken. Der Spurdetektor besteht aus einem Stapel doppelseitiger Silizium-Streifendetektoren, in denen die Compton-Streuung oder Paarerzeugung stattfindet. Er misst die Richtung und die Energie der Elektronen und Positronen. Ein Kalorimeter aus CsI(Tl) Kristallen umgibt den Spurdetektor. Es soll alle Sekundärteilchen komplett absorbieren und aufzeichnen.

Die Kenntnis der Streurichtung der Compton Elektronen ermöglicht es, den Ursprung eines Ereignisses auf ein kleines Segment des klassischen Kegels aller möglichen Einfallsrichtungen einzuschränken. Um diese Information auszunutzen, mußten völlig neue Methoden für die komplette Datenanalysekette entwickelt werden — von Messungen oder Simulationen über die Ereignisrekonstruktion bis hin zur Bildrekonstruktion.

Die Datenanalyse für ein kombiniertes Compton- und Paarteleskop beinhaltet zwei große Herausforderungen. Eine davon ist die korrekte Rekonstruktion jedes einfallenden Photons aus den gemessenen Energie- und Positionsinformationen. Ein realer Detektor hat immer Fehler und Eigenheiten, die zu suboptimalen Meßdaten führen. Um die von einem realen Detektor gemessenen Ereignisse erfolgreich rekonstruieren zu können, ist ein detailliertes Verständnis der Wechselwirkungsprozesse im Instrument eine Grundvoraussetzung. Ausgehend von idealen Compton- und Paar-Wechselwirkungen werden die Auswirkung von Molière-Streuung auf die gemessenen Elektronenspuren diskutiert, sowie die Folgen von fehlenden oder ungenügenden Energie- oder Richtungsmessungen als auch von Dopplerverbreiterung erläutert. Insbesondere im Falle der komplexen Rekonstruktion von Compton-Ereignisreihenfolgen führt eine detaillierte Beschreibung eines an die Wechselwirkungsphysik angepassten, mehrdimensionalen Ereignisdatenraums zu optimierten Ereignisauswahl-Kriterien und einer Diskussion ihrer Anwendbarkeit auf verschiedene Ereignistypen. Es wurden zwei fundamental unterschiedliche Methoden für die Ereignisrekonstruktion entwickelt: Die eine basiert auf Korrelationen zur Rekonstruktion der Elektronenspur und einem χ^2-Ansatz zur Bestimmung der korrekten Compton-Sequenz, die andere auf Bayes-Statistik und einer mehrdimensionalen Detektor-Antwortfunktion. Die Leistungsfähigkeit beider Algorithmen wird diskutiert. Simulationen eines MEGA-Satelliteninstruments zeigen, daß der Bayes-Ansatz im Mittel zu einer um einen Faktor 1,5 besseren Sensitivität führt.

Die zweite Herausforderung ist die Rekonstruktion von Bildern aus den Ereignissen. Ein Algorithmus basierend auf der List-Mode Maximum-Likelihood Expectation-Maximization Methode wurde für die MEGA-Bildanalyse weiterentwickelt. Dieser Ansatz ermöglicht es problemlos die verschiedenen Ereignistypen (Compton-Ereignisse mit und ohne Elektronenspur sowie Paarereignisse) in ein Bild zusammenzufassen. Die hierfür entwickelten Abbildungs-Antwortfunktionen berücksichtigen die meisten Aspekte des Verhaltens dieses komplexen Detektors.

Der MEGA Prototyp, der grob ein Zwölftel des Volumens eines denkbaren Satelliteninstruments besitzt, wurde sowohl mit radioaktiven Laborquellen als auch an der High Intensity Gamma Source an der Duke University kalibriert. Messungen mit monoenergetischen, 100% linear

polarisierten Photonen im Energiebereich von 710 keV bis 49 MeV ($\Delta E/E < 2\%$) ermöglichen die Bestimmung der Spektral-, Abbildungs- und Polarisationseigenschaften des Prototypen.

Im MEGA Prototypen werden Gammaquanten, vor allem mit höheren Energien, oft nicht vollständig absorbiert. Gründe für eine unvollständige Erfassung der gesamten Wechselwirkungskette sind Verluste in passiven Strukturmaterialien, Instabilitäten der Elektronik sowie die unvollständige Abdeckung der unteren Hälfte des Spurdetektors. Außerdem führen die moderate Energieauflösung vor allem des Kalorimeters und die vorgenannten Instabilitäten gemeinsam zu einer signifikanten Verbreiterung des Photopeaks. Deshalb ergeben die Beschleunigermessungen mit dem Prototypen einzig bei 710 keV einen Photopeak (41 keV 1σ-Breite).

Trotz der sehr moderaten Energieauflösung konnte die Winkelauflösung des Prototypen bestimmt werden. Für Comptonereignisse ohne Elektronenspur wird die Winkelauflösung von $\sim 7^\circ$ bei 710 keV zu $\sim 4^\circ$ bei 2 MeV stetig besser. Gleiches gilt für Comptonereignisse mit Elektronenspur ($\sim 9^\circ$ bei 2 MeV, $\sim 3^\circ$ bei 8 MeV) und Paarereignisse (12° bei 12 MeV, $4{,}5^\circ$ bei 49 MeV). Punktquellen von 710 keV bis 49 MeV mit Einfallswinkeln zwischen 0° und 80° werden problemlos auf die korrekte Position rekonstruiert — selbst wenn nur $\sim$100 komplett absorbierte Ereignisse gemessen wurden. Außerdem konnte gezeigt werden, dass der Prototyp — zusammen mit den Ereignisrekonstruktions- und Bildrekonstruktionsalgorithmen — mehrere Quellen differenzieren und ausgedehnte Quellen korrekt abbilden kann.

Da die azimuthale Compton-Streurichtung gemäß dem differentiellen Klein-Nishina Wirkungsquerschnitt von der Polarisation des einfallenden Photons abhängt, ist jedes Comptonteleskop automatisch auch ein Polarimeter. Bei 710 keV, wo die gemessene Polarisationsmodulation wesentlich von den Detektoreigenschaften beeinflußt wird, konnte eine Modulation von 17% mit dem MEGA-Prototypen nachgewiesen werden. Wie erwartet fällt für 100% polarisierte Strahlung mit steigender Photonenenergie die Modulation auf 13% bei 2 MeV und auf 6% bei 5 MeV.

Die Eigenschaften eines möglichen Satelliteninstruments (hier basierend auf der Pre-Phase A Studie für MEGA) wurden auf der Basis ausführlicher Simulationen vorhergesagt. Diese umfassen Simulationen von Kontinuums- und Linienquellen sowie von allen Hintergrundkomponenten, die in einer äquatorialen Umlaufbahn in 525 km Höhe erwartet werden. Für das Satelliteninstrument aus der pre-Phase A Studie ist eine Winkelauflösung von $\sim 4^\circ$ bei 511 keV für Comptonereignisse ohne Spur und $\sim 3^\circ$ bei 1809 keV für Comptonereignisse mit Spur zu erwarten; beide konvergieren für höhere Energien gegen die durch die Detektor-Positionsauflösung gegebene Grenze von $\sim 1^\circ$. Die gesamte effektive Fläche im Photopeak für alle Compton-Ereignisse ohne weitere Ereignisauswahl beträgt $\sim 120\,\mathrm{cm}^2$ bei 511 keV, $\sim 50\,\mathrm{cm}^2$ bei 1809 keV und $\sim 2\,\mathrm{cm}^2$ bei 6130 keV. Für Paarereignisse beträgt die effektive Fläche vor jeglicher Ereignisauswahl $\sim 35\,\mathrm{cm}^2$ bei 10 MeV und $\sim 60\,\mathrm{cm}^2$ bei 50 MeV. Nach Anwendung optimierter Ereignisauswahlkriterien wird nach fünf Jahren Himmelsdurchmusterung eine Kontinuumssensitivität von $\sim 1 \cdot 10^{-5}\,\mathrm{MeV/cm^2/s}$ um 1 MeV und $\sim 5 \cdot 10^{-5}\,\mathrm{MeV/cm^2/s}$ um 50 MeV erzielt. Nach derselben Missionsdauer wird eine Liniensensitivität von $\sim 4.3 \cdot 10^{-6}\,\gamma/\mathrm{cm^2/s}$ bei 511 keV und $\sim 1.7 \cdot 10^{-6}\,\gamma/\mathrm{cm^2/s}$ bei 1809 keV für jeden beliebigen Punkt am Himmel erreicht. Für eine Crab-ähnliche Quelle kann nach fünf Jahren Himmelsdurchmusterung eine lineare Polarisation von 0.5% nachgewiesen werden.

Einige Modifikationen des Satelliten-Instrumentkonzepts der pre-Phase A Studie, wie z.B. mehr Silizium im Spurdetektor oder eine Verbesserung der Energieauflösung der Kalorimeter über die bereits angenommene hinaus, könnten dieses kombinierte Compton- und Paarteleskop weiter verbessern. MEGA könnte unerreicht sensitive Messungen im Kontinuum und in einzelnen Linien liefern und überdies als erstes sensitives Compton-Polarimeter Neuland beschreiten und so die MeV-Gammaastronomie einen großen Schritt voranbringen.

Abstract

Gamma-ray astronomy in the MeV regime, from a few hundred keV to several tens of MeV, can provide unique information about the universe: The high penetration power of the gamma rays enables studies of highly obscured sources, and nuclear lines carry information about origin and distribution of individual isotopes in the cosmos. A leap in observational capabilities in this energy regime could be achieved by an instrument able to efficiently record events resulting from both dominating interaction mechanisms, Compton scattering and pair creation.

One potential future mission for **M**edium **E**nergy **G**amma-ray **A**stronomy is MEGA, which has been pursued at the Max-Planck-Institut für extraterrestrische Physik in Garching. MEGA is intended to operate from 0.4 to at least 50 MeV and consists of a tracker and a calorimeter. The tracker is a stack of double-sided Silicon-strip detectors in which the Compton scattering or pair creation takes place. It measures the direction and energy of the electrons and positrons. A calorimeter consisting of CsI(Tl) crystals surrounds the tracker. It is intended to fully absorb and measure all secondary particles.

The knowledge of the direction of the Compton recoil electron enables the reconstruction of the individual events not only to a Compton cone, but to a small segment of this cone. As consequence, a new set of data analysis tools had to be developed, covering the complete chain from measurements or simulations via event reconstruction to high-level data analysis such as image reconstruction.

One of two major challenges of analyzing data from a combined Compton and pair telescope is the reconstruction of the parameters of each original photon from the measured data, which consist only of several energy and position measurements. In order to properly reconstruct events recorded by a real-life detector, which always has some flaws resulting in less-than-perfect measurement data, the interaction processes in the instrument must be extremely well understood. Along with picture-perfect Compton and pair interactions, the effects of Molière scattering on electron tracks are discussed as well as the effects of incomplete energy or direction measurements and Doppler broadening on Compton event reconstruction. For the complex task of Compton sequence reconstruction in particular, the detailed description of a dedicated multi-dimensional event data space naturally leads to a discussion of possible event quality selection criteria and their applicability to different event types. Two independent event reconstruction algorithms have been developed, one based on correlations for tracking the path of the electron and on a χ^2 approach for reconstructing the sequence of Compton interactions, the other based on Bayesian statistics and multi-dimensional detector response functions. The performance of both is evaluated. Simulations of a MEGA satellite instrument show that the Bayesian approach achieves on average a factor of 1.5 better overall sensitivity.

The second challenge is the reconstruction of sky images from the event data. A list-mode maximum-likelihood expectation-maximization approach has been chosen, and an enhanced algorithm has been developed for imaging with MEGA. This approach naturally allows to incorporate all different event types (not tracked and tracked Compton events as well as pair events) into one image. Detailed imaging response descriptions have been developed which cover most aspects of the complex behavior of the detector.

The MEGA prototype, which encompasses one twelfth of the volume of the satellite version under study, has been calibrated with laboratory radioactive sources and at the High Intensity Gamma Source of the Free Electron Laser facility at Duke University. Exposures to monoenergetic (range 710 keV to 49 MeV, $\Delta E/E < 2\%$), 100% linearly polarized pencil beams allow the derivation of the spectral, imaging and polarization properties of this prototype instrument.

Especially high-energy gamma rays are not always completely absorbed in the MEGA prototype. Reasons for the incomplete measurement are the large amount of passive materials, electronics instabilities, and significant gaps in the prototype calorimeter. Moreover, the mod-

est energy resolution primarily of the calorimeter modules and instabilities in the detector system lead to a significantly broadened photo peak. As a result, the prototype beam measurements did not yield a significant photo peak except at 710 keV, where an energy resolution of ∼41 keV (1σ) was achieved.

Despite the modest spectral resolution, meaningful information about the angular resolution can be retrieved. For not tracked events, the angular resolution improves from ∼7° at 710 keV to ∼4° at 2 MeV, for tracked events from ∼9° at 2 MeV to ∼3° at 8 MeV and for pair events from 12° at 12 MeV to 4.5° at 49 MeV. Point sources from 710 keV up to 49 MeV as well as from 0° to 80° incidence can be easily reconstructed at the correct positions with the developed imaging algorithms from every one of the Duke measurements — even if only ∼100 fully absorbed events were recorded. In addition, it could be shown that the prototype — in conjunction with the event reconstruction and imaging algorithms — can correctly disentangle multiple sources and faithfully image extended sources.

Since the azimuthal direction of Compton scattering according to the differential Klein-Nishina cross-section depends on the incident photon's polarization, any Compton telescope is intrinsically sensitive to polarization. At 710 keV, where the retrieved polarization modulation is most influenced by detector limitations, a polarization modulation of 17% could be detected with the MEGA prototype. The expected modulation for 100% linearly polarized gamma rays decreases with higher photon energy; modulations of 13% at 2 MeV and 6% at 5 MeV were obtained.

The expected performance of one possible satellite instrument, based on the MEGA pre-phase A study, has been derived from extensive simulations of continuum and gamma-ray line point sources as well as all background components expected for an equatorial low-earth (525 km) orbit. This simulation approach is validated by the good agreement achieved between the MEGA prototype calibration measurements and corresponding Geant simulations. The satellite instrument of the pre-Phase A study is expected to achieve an angular resolution of ∼4° for not tracked events at 511 keV and ∼3° for tracked events at 1809 keV, both converging towards the detector position resolution limit at ∼1° for higher energies. The total photo-peak effective area for all Compton events before background cuts is ∼120 cm^2 at 511 keV, ∼50 cm^2 at 1809 keV, and ∼2 cm^2 at 6130 keV. For pair events without any event restrictions the effective area is ∼35 cm^2 at 10 MeV and ∼60 cm^2 at 50 MeV. Applying optimized event selections results in an average continuum sensitivity after 5 years all-sky survey of $\sim 1 \cdot 10^{-5}\,\mathrm{MeV/cm^2/s}$ at around 1 MeV and $\sim 5 \cdot 10^{-5}\,\mathrm{MeV/cm^2/s}$ at around 50 MeV. In the same 5-year period, a narrow line sensitivity of $\sim 4.3 \cdot 10^{-6}\,\gamma/\mathrm{cm^2/s}$ at 511 keV and $\sim 1.7 \cdot 10^{-6}\,\gamma/\mathrm{cm^2/s}$ at 1809 keV would be achieved for any arbitrary point on the sky. For a Crab-like source, a 0.5% linear polarization can be detected after 5 years all-sky survey.

Some changes to the pre-Phase A satellite instrument design, such as simply increasing the total amount of Silicon or finding a way to further improve the energy resolution in the calorimeters, could improve the performance of this tracking Compton and pair telescope even further, enabling MEGA to provide a significant leap in continuum and narrow-line sensitivity as well as polarimetry for medium-energy gamma-ray astronomy.

Contents

Part I

Measuring extraterrestrial gamma rays

Chapter 1

On the road to a new mission in Medium-Energy Gamma-ray Astronomy

The universe in the medium-energy gamma-ray regime, from a few hundred keV up to several tens of MeV, is characterized by the most violent explosions as well as the most powerful and dynamic sources. The high penetration power of those gamma-rays allows a unique view into the inner engines of those objects, which are hidden at lower energies, and the nuclear lines generated by deexitation of newly generated nuclei allow to unveil the secrets of the origin of the elements.

Several instruments have successfully started to explore this energy regime, including GRE on SMM (*Forrest et al.*, 1980), TGRS on WIND (*Owens et al.*, 1991), and notably the instruments aboard the Compton Gamma-Ray Observatory (CGRO, 1991-2000), especially COMPTEL (*Schönfelder et al.*, 1993) in the energy band from 0.7 to 30 MeV and EGRET (*Kanbach et al.*, 1988) above 50 MeV. Currently, the spectrometer SPI aboard INTEGRAL (*Winkler et al.*, 2003) and RHESSI (*Lin et al.*, 2002), which both were launched in 2002 and measure photons up to a several MeV, are exploring this energy regime. This work is dedicated to a potential future mission in this energy regime, the tracking Compton and pair telescope MEGA (Medium Energy Gamma-ray Astronomy).

In recent years two important concepts have been promoted to establish a new mission in medium-energy gamma-ray astronomy to follow CGRO and INTEGRAL. The first concept is a next-generation Compton telescope. One of the candidates, realizable on short time scales, is MEGA. A larger, more sensitive approach is the Advanced Compton Telescope (ACT), also known as NACT, the Nuclear Astrophysics Compton Telescope (*Boggs et al.*, 2005), which however is up to two decades in the future. The other concept is based on Laue Lenses to focus gamma rays. A small version, which could be implemented in the near future, is MAX (*von Ballmoos et al.*, 2004), the more futuristic version is the Gamma-Ray Imager (*Knödelseder*, 2005).

Although the two concepts apply different techniques and have slightly different energy bands as well as significantly different fields-of-view, they share several key science objectives. Some of the most pressing questions in medium-energy gamma-ray astronomy are summarized below, followed by a discussion of the different detection and imaging methods available to perform such observations. Finally the reasoning for choosing an electron-tracking Compton and pair telescope, MEGA, for the given task is presented.

1.1 Medium-Energy Gamma-ray Astronomy

1.1.1 Cosmic accelerators

Due to their high penetrating power, gamma rays can carry information from the inner regions of cosmic accelerators like black holes, pulsars, or the still largely mysterious gamma-ray bursts. Especially helpful to constrain emission geometries and source magnetic field configurations would be sensitive measurements of the polarization of those photons, for which current and previous instruments have only extremely limited capability.

Black holes are believed to be at the heart of active galactic nuclei (AGN). These black holes are surrounded by an accretion disk and at least radio-loud AGN such as blazars exhibit relativistic jets in which gamma rays are generated, probably via inverse Comptonization. However, just how these jets are generated, what their links to the accretion disk are, and how they are collimated is still a matter of debate (*de Gouveia dal Pino*, 2005). Other open questions are related to the composition of the jets which could be made up of protons and relativistic electrons (hadronic model), or alternatively of relativistic electron-positron pairs (leptonic model) (*Massaglia*, 2003). Since some blazars have both a spectral break and their luminosity maximum in the MeV range, sensitive medium-energy gamma-ray observations could yield new insights in the mechanisms behind AGN. Blazars show fast time variability down to timescales of less than an hour in the TeV regime. A scanning gamma-ray mission with a large field-of-view is ideally suited to observe transients since it could easily monitor the variablity of many such objects. Microquasars are the small-scale, galactic counterpart to AGN. Their black holes only have a few solar masses, and their accretion disks are fueled by a companion star. The same mechanisms as in AGN seem to be at work, and thus the same questions wait to be answered.

Pulsars are rotating neutron stars with extreme magnetic fields. The latter make them ideal accelerators of charged particles. These charged particles in turn are responsible for the emission of radiation, including continuum gamma radiation in the MeV regime. However, up to now the exact photon production mechanisms as well as the production sites in the magnetosphere (polar cap, outer gap, or two-pole caustic model) remain unclear. The polarization of the emitted photons is inherently linked to the particle creation and emission region. Sensitive measurements of this polarization could help to distinguish between various models of the emission in pulsar magnetospheres (*Dyks et al.*, 2004).

Although some clues about the origins and mechanisms behind **gamma-ray bursts** (GRBs) have been obtained in recent years, a lot of mysteries remain. While a connection between long-duration GRBs and supernovae has now been established (*Stanek et al.*, 2003), short-duration GRBs remain a mystery. Some of the short-duration GRBs might originate from mergers of e.g. two neutron stars (*Hjorth et al.*, 2005), and a small fraction of the short duration bursts could originate from soft gamma-ray repeaters (*Hurley et al.*, 2005). The inner GRB engine in most cases remains uncertain. According to the fireball model, gamma-rays are produced in the initial phase of the burst by internal shocks and thus are produced rather close to the inner engine of the burst. Therefore they are likely carrying information which cannot be obtained from the optical afterglow of the burst, which is generated in later stages in external shocks. Measuring the gamma-ray polarization would greatly help to constrain the inner engines of GRBs. In particular, polarization measurements would help determine whether or not strong, organized electromagnetic fields are present. Up to now there has been only one possible detection of polarization in a gamma-ray burst (*Coburn and Boggs*, 2003) by RHESSI (*Lin et al.*, 2002), which is however not generally accepted (*Wigger et al.*, 2004).

1.1.2 Nucleosynthesis

When hydrostatic or explosive burning in stars results in the generation of "metals" (elements heavier than Helium), radioactive nuclei are produced along with stable elements. The decay of newly synthesized radioactive nuclei is accompanied by subsequent deexitation through emission of gamma rays of characteristic energy. From the distribution of such photons of a given line energy on the sky one can draw conclusions about that isotopes' producers and thus the origin of the elements that the universe is made of.

Novae, supernovae and late-stage massive stars are the most prominent production sites of detectable radioactivity. Those objects expel radioactive "metals" on small enough time scales so that the decay happens outside the star itself, in an environment of low enough density that the resulting gamma ray can reach us.

One of the most challenging questions in gamma-ray astronomy is related to **type Ia supernovae**. When a white dwarf in a tight binary system accretes enough mass from its companion to exceed the Chandrasekhar mass limit, thermonuclear burning in the core sets in and detonates the white dwarf. Supernova Ia explosions are considered to be standard candles due to their uniform progenitors and consequently are used for distance determinations. Lately, they have even been used in cosmology, leading to the conclusion that the expansion of the universe is accelerating (*Riess et al.*, 1998). However, the picture of supernovae Ia as standard candles is not perfect, and several competing models of their explosion mechanism exist (e.g. *Leibundgut*, 2000): Does the explosion happen only when the white dwarf exceeds the Chandrasekhar limit, or possibly in some cases while it is still a sub-Chandrasekhar white dwarf? Is the speed of the burning front subsonic (deflagration model) or supersonic (detonation model) or a mixture of the two? Since supernovae Ia are rare, a telescope needs an excellent sensitivity ($\sim$100 better than COMPTEL) to be able to — within the time frame of a mission — distinguish for tens of supernovae between competing models via the production rates and ejection velocities of the individual radioactive isotopes (*Milne et al.*, 2002). Two supernovae Ia were observed with CGRO: SN1991T (distance $\sim$13 Mpc), which resulted in a marginal detection by COMPTEL (*Morris et al.*, 1995), and SN1998bu (distance $\sim$9 Mpc), for which only upper limits where derived (*Georgii et al.*, 2002). A telescope with a significantly improved sensitivity over COMPTEL to the broadened 847 keV line of the ^{56}Co decay ($T_{1/2}$ = 77 d) is needed to untangle the explosion mechanisms which drive type Ia supernovae.

Generally, any detection of a close supernova, irrelevant of the type, by a gamma-ray telescope more sensitive than its predecessors will greatly enhance the knowledge about supernovae and help to constrain the explosion models via the production rate of different elements during the explosion.

A not-yet detected source of gamma rays are expected to be **novae**. Through Roche lobe overflow, a white dwarf can accumulate an outside layer from its main sequence companion in a binary system until hydrogen ignition conditions are reached in this layer. This will lead to a thermonuclear runaway burning, the nova. During this hydrogen burning phase, short-lived β^+-unstable elements such as ^{13}N ($T_{1/2}$ = 10 m) and ^{18}F ($T_{1/2}$ = 110 m) are produced and result in a prompt flash of 511 keV photons as well as a positronium continuum below this line, which can be detected even before the nova is visible in the optical. The detection of such a flash would yield constrains on the generation rates of these two radioactive elements, the duration of the emission, and the transport of those elements in the expanding nova envelope (*Hernanz*, 2004). Other candidates for gamma-ray line emission from novae are 1275 keV from ^{22}Na ($T_{1/2}$ = 2.6 a) and 478 keV from ^{7}Be ($T_{1/2}$ = 53 d), which can still be detected long after the actual nova and would allow constraints on the composition of the progenitor and the production rate of those elements.

The decay chain of ^{44}Ti ($T_{1/2}$ = 63 a) with its characteristic 1.157 MeV line is a unique

tracer of young **supernova remnants**. Up to now one source, Cas A (*Iyudin et al.*, 1994), has been detected definitely and another, Vela Junior, marginally by COMPTEL (*Schönfelder et al.*, 2000). The latter has not been detected yet by INTEGRAL (*Renaud et al.*, 2005). Since gamma rays have only a small extinction in our galaxy, a sensitive survey for point sources of ^{44}Ti-decay lines should reveal hidden SN remnants and thus stringently constrain the supernovae rate in our galaxy as well as the supernova yields of ^{44}Ti.

^{26}Al ($T_{1/2} = 7.2\ 10^5$ a) is produced in the cores of massive stars. **Wolf-Rayet stars** are very massive stars ($m > 30\ M_\odot$) in a late evolutionary phase which is characterized by heavy mass loss. After their original hydrogen-rich envelope has been removed by stellar winds, or sufficient rotation led to diffusion of ^{26}Al into the outer envelopes of the star (e.g. *Palacios et al.*, 2005), ^{26}Al is ejected and its decay can be detected by the characteristic 1.809 MeV line. Up to now no ^{26}Al from an individual Wolf-Rayet star has been detected. For the closest, γ^2 Velorum, only upper limits have been determined by COMPTEL (*Oberlack et al.*, 2000a) and SPI (*Mowlavi et al.*, 2004). An ^{26}Al measurement of γ^2 Velorum would allow to constrain the ^{26}Al outflow from and production rate in those stars and thus help to determine the total contribution of Wolf-Rayet stars to the overall detected ^{26}Al.

^{60}Fe ($T_{1/2} = 1.5\ 10^6$ a), whose decay results in 1.173 and 1.333 MeV gamma rays, should be produced mainly in massive stars before as well as during their death in a core-collapse supernova, but not be expelled in Wolf-Rayet stars (*Palacios et al.*, 2005). Since ^{60}Fe is mainly ejected by core-collapse supernovae and some by supernovae Ia, but ^{26}Al is ejected by supernovae, massive stars especially in Asymptotic Giant Branch and Wolf-Rayet phases, and novae, the ratio of ^{60}Fe to ^{26}Al should yield constraints to the overall amount of ^{26}Al which is produced in massive stars (e.g. *Prantzos*, 2004), and all-sky ^{60}Fe maps will trace core collapse supernovae. Up to now only the overall line emission of ^{60}Fe and thus the ratio ^{60}Fe/^{26}Al in our galaxy has been measured by RHESSI (*Smith*, 2004) and INTEGRAL (*Harris et al.*, 2005), but current instrumentation is not nearly sensitive enough to resolve individual supernovae in the ^{60}Fe line.

Most ^{26}Al is believed to originate in massive stars and core-collapse supernovae. Its half-life of $T_{1/2} = 7.2\ 10^5$ years is long enough for ^{26}Al to accumulate in the interstellar medium around regions with massive stars. Due to the relatively short lifetime of massive stars on the main sequence, late-stage massive stars and core-collapse supernovae are indicators for regions with ongoing **star formation**. Mapping the universe in ^{26}Al with significantly improved sensitivity and/or angular resolution compared to COMPTEL and INTEGRAL will reveal those regions in much more detail.

Generally, all large scale structures are best imaged if the telescope has a wide field-of-view and is operated in scanning instead of pointing mode to obtain a smooth, 4π exposure.

1.1.3 Capture, annihilation and deexcitation

When a neutron is captured on hydrogen a characteristic **2.223 MeV** gamma ray is produced. Due to the short mean life time of neutrons (918 s), this capture has to happen close to where the neutrons are produced mainly via nuclear interactions. Besides solar flares, compact objects such as accreting neutron stars and black holes are the most likely sources of such radiation. From the width of the line and a potential redshift the production site close to the compact object can be deduced: for example gravitational redshift would indicate a production close to a neutron star atmosphere (*Bildsten et al.*, 1993), a strongly broadened line would indicate that the neutron capture happened in the hot plasma of the accretion disk, and a narrow line would indicate that the capture happened in the outer regions of the accretion flow or in the atmosphere of the companion star (e.g. *Agaronian and Sunyaev*, 1984). Up to now, only one extra-solar 2.2 MeV line source has been claimed by COMPTEL, but no optical counterpart has been identified (*McConnell et al.*, 1997).

Observations with SPI on INTEGRAL have revealed that a significant amount of the **511 keV** annihilation radiation of positrons is consistent with emission from or near the galactic bulge (*Knödelseder et al.*, 2005). While the observed weak emission from the galactic disk can be explained entirely by radioactive beta decay from ^{26}Al and eventually ^{44}Ti, the origin of the positrons responsible for the galactic bulge emission remains uncertain. Candidates range from Type Ia supernovae, novae, or low-mass X-ray binaries to light dark matter annihilation (*Diehl et al.*, 2005; *Knödelseder et al.*, 2005; *Boehm et al.*, 2004). Detecting positron emission from any one of the above point source candidates would shed light on the mystery. To achieve this, an excellent angular resolution and sensitivity surpassing that of INTEGRAL/SPI would be required.

After energetic particles, with energies in the tens of MeV/nucleon, inelastically scatter off and excite matter, deexcitation results in characteristic **nuclear interaction lines**. The strongest gamma-ray lines that are unique signatures of nuclear excitations (as opposed to also being produced in radioactive decays) are those of ^{12}C* (4.44 MeV) and ^{16}O* (6.13 MeV) (*Ramaty et al.*, 1979). The strength of the lines should allow inference of the molecular composition of the ambient matter, of the low energy particles themselves, and potentially of their sources. Up to now nuclear excitation lines have only been conclusively detected from the sun.

1.1.4 Other sources of interest

Nuclei can not only be excited by decay or energetic particle interaction, but also by gamma rays. The best-studied case is the Giant Dipole Resonance (GDR), in which the protons and neutrons collectively oscillate around their common center of gravity until the oscillation stops by either emitting gamma rays or neutrons. The necessary photon energy depends on the radius of the nucleus. For light elements it is between 20 and 30 MeV. Besides the GDR, other resonance features in the total absorption cross-section of photons on nuclei exist, such as the pygmy dipole resonance ($\sim$7 MeV). **Absorption** features in the spectra of distant gamma-ray sources like AGN that can be attributed to these resonances have recently been found by *Iyudin et al.* (2005). The absorption lines allow to constrain the column density and eventually the composition of the medium by analyzing the peak position, the width and the strength of the absorption features.

Another source of interest is the origin of the **extragalactic and galactic gamma-ray background**. While at lower gamma-ray energies ($<$ 100 keV) the extragalactic background is expected to mainly originate from Seyfert galaxies (e.g. *Watanabe and Hartmann*, 2001), at higher energies ($>$ 10 MeV) the main contribution to this background is expected to be from blazars (*Stecker and Salamon*, 2001). The largest part of the galactic gamma-ray background at lower energies ($<$ 100 keV) seems also to be resolved into point sources (*Lebrun et al.*, 2004). At higher energies ($>$ 10 MeV) most of the galactic background can be explained via interaction of cosmic rays with the interstellar medium, which creates gamma rays through the generation and the decay of π^0, bremsstrahlung and inverse Compton scattering (e.g. *Strong et al.*, 2005). Between $\sim$0.1 and $\sim$10 MeV the situation is less clear. It still has to be determined how far the low and high energy sources reach into this regime and how large the contribution of e.g. supernovae Ia is to the background (e.g. *Strigari et al.*, 2005, expects roughly 10%) or if there are completely different mechanisms at work, e.g. like a dark matter annihilation contribution to the cosmic gamma-ray background (*Ahn and Komatsu*, 2005). Thus one of the main tasks of a future medium energy gamma-ray telescope is to resolve as much as possible of the diffuse galactic and extragalactic background into point sources and to measure the remaining diffuse emission with far higher accuracy.

Besides the main motivations for improved observations in medium-energy gamma-ray astronomy outlined above, there is of course the unexpected, which awaits its discovery with a

future mission which significantly surpasses the sensitivity of COMPTEL and INTEGRAL!

1.2 Instrumentation for medium-energy gamma-ray astronomy

The energy band from a few hundred keV up to several tens of MeV, in which initially Compton scattering is the dominating interaction mechanism followed by the onset of pair creation (see cross-sections in Figure 1.1), is one of the hardest to explore. The atmosphere is almost opaque to MeV photons and therefore high-altitude balloon or satellite missions are needed for its exploration. It is ironic that two properties of the MeV regime that make observations at these energies particularly rewarding — the high penetration power and the information carried in nuclear lines — also make this regime particularly challenging for observers. Around 2 MeV, depending on the material, the interaction probability reaches a minimum and a significant amount of material ($\sim$40 g/cm^2) is needed to stop a sufficient portion of the gamma rays in the active detector material. But up to a few MeV the most demanding challenge is the high internal instrumental background induced by the time-variable space radiation environment. This generally leads to very low signal-to-background ratios. Thus the single most important feature of any future mission in medium-energy gamma-ray astronomy is improved background prevention and rejection. This can be achieved by the applied gamma-ray measurement process itself as well as by detector design and sophisticated data analysis techniques.

The following sections describe the different detector concepts which can be used for gamma-ray imaging in this energy band. Most of the presented detectors are surrounded by an anti-coincidence shield to reject parts of the cosmic and atmospheric background radiation. Such shields are either made of thin plastic to reject charged particles only or of significantly heavier material (CsI, BGO) to reject also photon components. They will not be discussed further in this chapter.

1.2.1 Spatial and temporal modulation

One way of determining the origin of gamma rays is by obscuring parts of the field-of-view of the detector, either permanently or in a well-defined temporal manner. From the detected modulated signal and the knowledge of the obscuration scheme, the original distribution of the photons can be recovered by means of deconvolution.

The simplest system is a collimator. Only those photons can reach the detector which are not blocked by the collimator. One recent example is the Hard X-ray detector (HXD) aboard Astro-

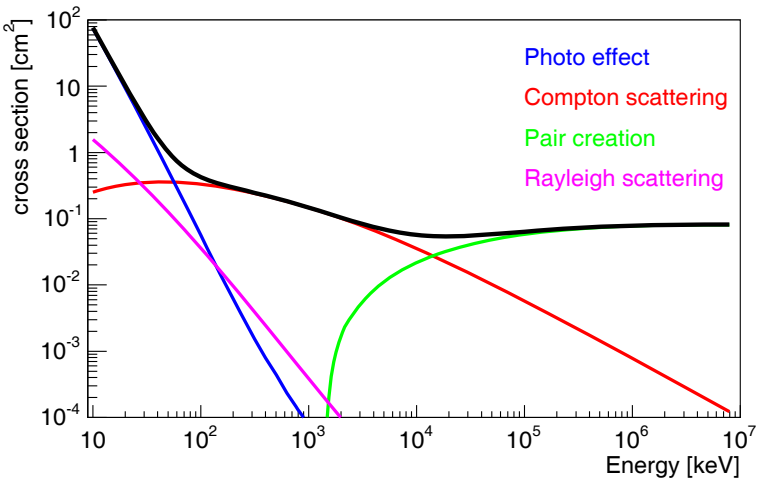

Figure 1.1: Cross-section for photon interactions in Silicon in the MeV range. The four dominating interaction mechanisms are photo effect, Compton scattering, pair creation and Rayleigh scattering.

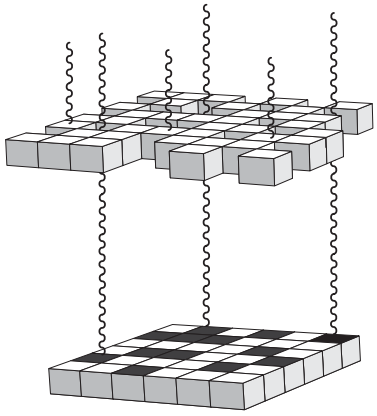

Figure 1.2: The basic design of a coded mask telescope as used on INTEGRAL and on SWIFT: The gamma rays have to pass through a mask. From the resulting shadowgram on the detector, the origin of the photons can be reconstructed.

E2/Suzaku (*Inoue et al.*, 2003). However this simple system has one large drawback: it provides only a small field-of-view and the background determination requires off-source pointings which reduce the observation time.

The next step is a coded mask system. Different sources on the sky cast different shadows of the mask onto a spatially resolving detector system (see Figure 1.2). From the measured shadowgrams and the knowledge of the mask, the original distribution of the photons can be deconvolved (*Caroli et al.*, 1987). Currently three coded masks instruments (SPI, IBIS and JEM-X) operate aboard INTEGRAL (*Winkler et al.*, 2003), from which two, the imager IBIS and the spectrometer SPI, extend into the MeV range. Coded masks are also used for the burst alert telescope (BAT) aboard SWIFT (*Gehrels et al.*, 2004) and planned for the EXIST hard X-ray telescope (*Grindlay et al.*, 2003).

Another approach is to rotate two collimators above a monolithic detector and derive the information of the origin of the photons through Fourier analysis of the temporally encoded information (*Hurford et al.*, 2002). This approach is used by the solar spectroscopic imager RHESSI (*Lin et al.*, 2002).

Coded masks and rotation modulation collimators have several limiting factors: First, it is not possible to derive a unique origin for one single photon, but one needs enough events to produce a complete shadowgram or enough events to generate the complete temporal information. Second, once the event is registered in the detector it is not possible to further analyze it and potentially identify it as background as long as only simple detectors are used. Thus generally the background level is high in this approach. Third, those systems are best suited for point sources and small emission regions; it is more difficult to image large scale structures. Finally, multiplexing approaches are better suited for lower energies, because they need a decent amount of photons to deconvolve the image and at higher energies require rather thick masks to block the photons.

Nevertheless, since those systems allow for a high angular resolution and utilize relatively simple detector concepts, they are currently wide-spread in gamma-ray astronomy.

1.2.2 Single event detector systems

A completely different way of reconstructing the origin of photons becomes feasible at energies above a few hundred keV with the onset of Compton scattering and pair creation. Recording energies and directions of the secondary/scattered particles allow to retrieve origin, energy and sometimes polarization of the original photon.

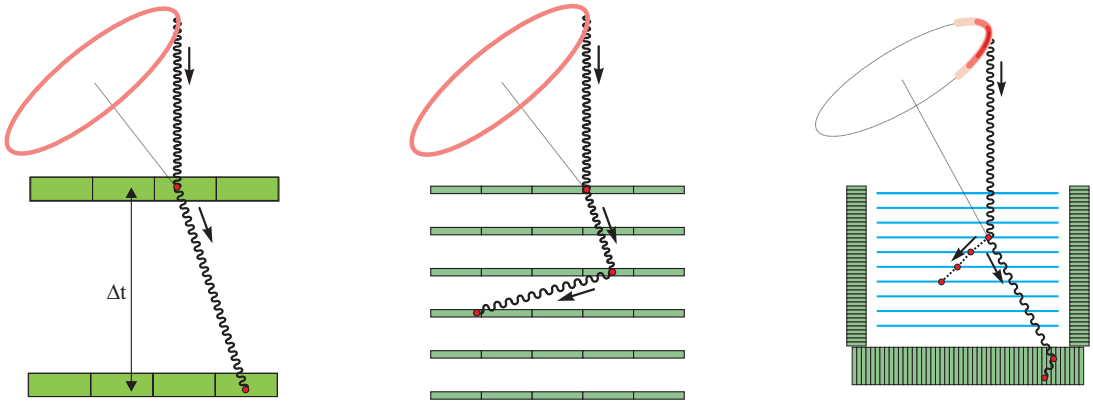

Figure 1.3: Comparison of the different Compton telescopes: The left figure shows the classical COMPTEL type instrument. It comprises two detector planes. The first one is the scatterer (D1) and the second is the absorber (D2). The planes have a large distance in order to measure the time-of-flight of the scattered gamma-ray. The central picture shows a Compton telescope consisting of several thick layers in which the photon undergoes multiple Compton scatterings. The redundant scatter information allows to determine the direction of motion of the photon. The figure on the right shows an electron tracking Compton telescope like MEGA. The tracker consists of several layers, thin enough to track the recoil electron. The scattered photon is stopped in a second detector which encloses the tracker. The track of the electron determines the direction of motion of the photon. The illustrations are not to scale.

1.2.2.1 Compton Telescopes

Compton scattering is the dominant interaction process between ∼200 keV and ∼10 MeV (depending on the scatter material). If one measures the position of the initial Compton interaction, energy and direction of the recoil electron as well as direction and energy of the scattered gamma-ray, then the origin of the photon can be identified. The final accuracy depends on several factors, which are extensively discussed in Section 2.2.

The key objective for a Compton telescope is to determine the direction of motion of the scattered gamma-ray. For this problem three solutions exist which distinguish the three basic types of Compton telescopes (see Figure 1.3).

In COMPTEL (Figure 1.3 left) the two detector systems, a low Z scatterer, where the initial Compton interaction takes place, and a high Z absorber, where the scattered gamma ray is stopped, are well separated so that the time-of-flight of the scattered photon between the two detectors can be measured. Thus top-to-bottom events can be distinguished from bottom-to-top events. With COMPTEL it was not possible to measure the direction of the recoil electron, so an ambiguity in the reconstruction of the origin of original photon emerged: the origin could only be reconstructed to a cone. This ambiguity has to be resolved by measuring several photons from the source and by image reconstruction (details see Chapter 5).

Several of the instrument concepts currently under consideration for an Advanced Compton Telescope (ACT) (*Boggs et al.*, 2005) will detect more than one Compton interaction per photon (Figure 1.3 center). From the resulting redundant information the ordering of the interactions can be retrieved. A detailed discussion of this approach is given in Chapter 4. Representatives of this group of Compton telescopes are NCT (*Boggs et al.*, 2004), LXeGRIT (*Aprile et al.*, 2000) or the thick Silicon concept described by (*Kurfess et al.*, 2004).

In contrast to COMPTEL and most ACT concepts, a third group of detectors is capable of measuring the direction of the recoil electron (Figure 1.3 right). This enables the determination of the direction of motion of the scattered photon and allows to resolve the origin of the photon much more accurately: the Compton cone is reduced to a segment of the cone, whose length depends on the measurement accuracy of the recoil electron. The main representatives of this

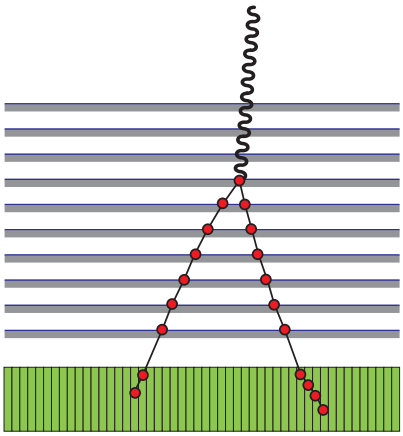

Figure 1.4: Basic design of a pair telescope: it comprises two detector systems, a tracker/converter in which the direction of the electron and positron are measured and a calorimeter which measures the energy of the particles.

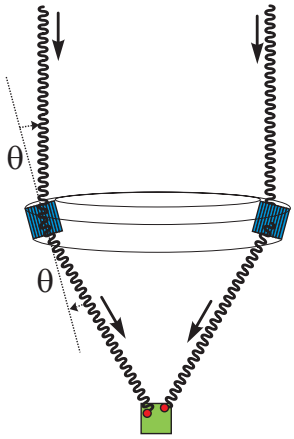

Figure 1.5: Basic design of a crystal diffraction lens: Gamma rays are Laue-diffracted in a lens and focused on a small detector

group are MEGA, which will be discussed in this work, and TIGRE (*Bhattacharya et al.*, 2004).

Compton telescopes have the advantage that only a few photons are needed to recover the position of sources, depending on background conditions and quality of the events. They are also inherently sensitive to polarization, especially if the detector allows to measure photons under large Compton scatter angles and at low energies (details see 2.2.3). Furthermore they can easily have a very large field-of-view.

However for all those advantages a price must be paid: The original photon is measured via several individual measurements at different interaction positions. Each of these introduces measurement errors which are propagated into the recovery of the origin and energy of the photon. Moreover, modern versions of Compton telescopes are extremely complex with hundreds of thousands of channels, which all need to provide excellent energy and position information. In addition, the complexity of the measurement process requires non-trivial techniques to find the direction of motion of the photons (see Chapter 4) and the origin of the photons (see Chapter 5). Finally, a fundamental limit for the angular resolution of Compton telescopes exists, since the initial (pre-scattering) momentum of the target electron cannot be determined (see Section 2.2.6).

1.2.2.2 Pair-Tracking Telescopes

Compared to Compton scattering, pair production enables a significantly more straight-forward determination of the origin of the photon. In its basic design a pair telescope consists of two detectors: A converter and an absorber (compare Figure 1.4).

The converter consists of layers of high-Z conversion foils combined with position sensitive detectors to determine the tracks of the generated electron and positron. While semiconductors are used in modern-day pair telescopes like GLAST (*Gehrels and other*, 1999) and AGILE (*Tavani et al.*, 2003), in previous pair telescopes like EGRET (*Kanbach et al.*, 1988) a spark chamber was used for this task. The energy measurement happens in the bottom absorber, the calorimeter. From the directions and energies of electron and positron the origin of the incoming photon can easily be determined (for more details see Section 2.3). Even if the photon-induced shower is not contained in the detector, an analysis of the morphology of the tracks allows to roughly determine the energy of the initial photon.

Pair telescopes are a simple and efficient approach to determining the origin of gamma rays above ∼10 MeV. However, the use of conversion foils, which are necessary to obtain high

efficiencies, limits the angular resolution and energy measurement at low energies. Thus to give reasonable performance in the medium-energy gamma-ray regime a pair telescope should not contain such foils.

1.2.3 Focusing gamma-rays

The latest development for detecting gamma-rays in medium-energy gamma-ray astronomy are lenses. They enable focusing, which is the standard approch at lower energies, also in the gamma regime. Compared to the previously presented concepts, they allow the separation of collection and detection area, and thus dramatically reduce the background.

1.2.3.1 Laue lens

Focusing gamma-rays can be achieved via Laue-diffraction on crystal planes. Compared to Bragg-diffraction, which happens on or near the surface of the material, Laue diffraction means that the gamma rays pass through the lens and are diffracted in the volume of the crystal — if they satisfy the Bragg-relation:

$$2d \sin\theta = n\lambda \tag{1.1}$$

Here d is the crystal plane spacing, θ the diffraction angle, n the reflection order and λ the wavelength.

Many such crystals are combined to form a gamma-ray lens. This technique has been initially demonstrated for astrophysics by the CLAIRE balloon-flight (*Halloin*, 2003) and is intended to be used on the envisioned MAX space telescope (*von Ballmoos et al.*, 2004). The Laue lens on MAX consists of a ring of crystals, which are oriented in a way that they diffract the radiation to a small focal spot on the detector. In order to increase the effective area, the lens has several rings, which differ in their material (different crystal plane spacings) and/or their orientation (diffraction of higher order) to focus more gamma rays of a given energy onto the detector. Figure 1.5 illustrates the basic concept.

Gamma-ray lenses have one important advantage over non-focusing telescopes: the detection volume, which is basically the focal spot, is much smaller than the collection area formed by the lens. Thus only a very small detector volume is necessary, which dramatically reduces the intrinsic background, which is a sensitivity-limiting factor for other gamma-ray telescopes.

But this advantage comes at the expense of a very narrow field of view (below one arcmin). Also, since the diffraction band width of any individual crystal is only a few keV, the instrument's energy range is roughly proportional to the number of crystals needed and thus to the overall instrument complexity. A viable mid-size instrument like MAX would be capable of viewing 2-3 energy bands, each of which would be roughly 100 keV wide. Moreover, such a lens has only limited imaging capabilities with its field-of-view. With current technology, lenses could be applied to photon energies up to a few MeV.

1.2.3.2 Fresnel lenses

Another approach that currently exists on paper only is to focus gamma rays using phase Fresnel lenses (*Skinner*, 2001). The refraction index for gamma-rays in matter is slightly lower than 1 and thus allows focusing. Besides the drawbacks already mentioned for the Laue lens, a Fresnel lens would require a large focal length around 10^9 m, depending on the energy of the photons. However, one would obtain a superior angular resolution near the diffraction limit in the μarcsec region, an efficiency close to 100%, and true imaging.

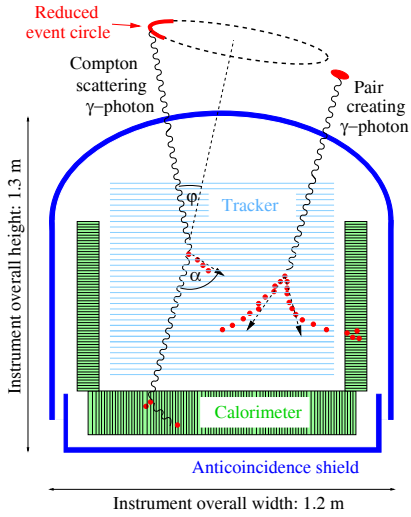

Figure 1.6: Baseline design and measurement principle of the full MEGA telescope. The recoil electrons from Compton scattering as well as the pair creation products are tracked in a stack of Silicon strip detectors and the secondary particles are stopped in the CsI calorimeter.

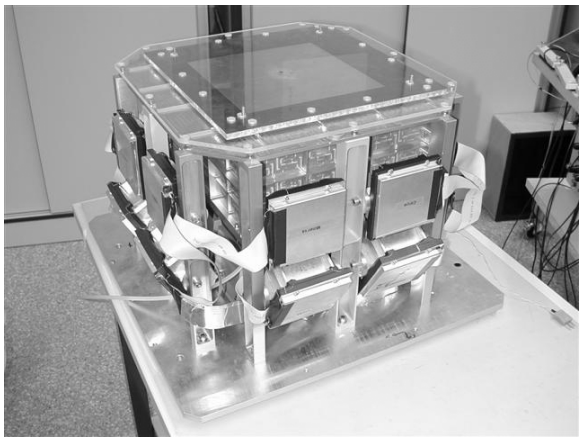

Figure 1.7: MEGA prototype: The tracker (central box) is surrounded by 20 calorimeters

1.3 MEGA - A telescope for medium-energy gamma-ray astronomy

Defining the medium-energy gamma-ray energy band from a few hundred keV up to tens of MeV, the number of available telescope candidates reduces: Coded mask systems would need massive masks to completely stop these photons and could probably only provide a very small field of view. Laue lenses have not been seriously considered above a few MeV. The natural candidates would be Compton-scattering or pair-creation telescopes. However, neither a Compton nor a pair telescope can cover the whole energy range, thus the perfect solution is a hybrid telescope: an electron-tracking Compton telescope which is automatically also a low-energy pair telescope (Figure 1.6).

The idea of constructing such a telescope as successor of COMPTEL and EGRET (low energies only) has been pursued at the Max-Planck-Institut für extraterrestrische Physik since the mid 1990s and culminated in the successful calibration of the MEGA prototype (Figure 1.7) in 2003, accompanied by detailed studies of a satellite version.

Like all previous successful Compton and pair telescopes, MEGA consists of three detector systems, a scatterer/converter/tracker, a calorimeter, and a surrounding anti-coincidence shield. The tracker has several tasks. First, it has to act as a Compton scattering and pair creation medium. Therefore the material requires a large cross-section for those interactions and low Doppler-broadening (details see 2.2.6) — for both reasons a low Z material is preferred. Second, it has to measure the direction of the secondary electrons and positrons as well as their energy very accurately. The logical choice, which provides good position and energy resolution is a stack of thin double-sided Silicon strip detectors. The prototype has 11 layers, each of which consists of nine 6×6 cm^2 wafers. The individual wafer is 0.5 mm thick and has 128 orthogonal p and n strips on opposite sides (0.47 mm pitch). A potential tracker for a satellite version would be a factor of four larger in area and a factor three deeper (32 layers with 36 wafers).

The lower hemisphere of the tracker is surrounded by calorimeters. Their main purpose is to stop all secondary particles and measure the interaction position as well as the deposited energy. Thus it should be built of high-Z material and have good position and energy resolution. The calorimeter of the prototype consists of 20 modules of three types: 8 cm deep ones at the bottom,

4 cm deep at the lower side and 2 cm deep calorimeters at the upper side. The depth corresponds to the necessary stopping power for on-axis incident photons: Small Compton scatter angles correspond to a high energy of the scattered photon and thus require more material for their absorption. Each module is built from 10×12 CsI(Tl) scintillator bars with a cross-section of 5×5 mm^2. The possible satellite version also uses such CsI modules, only the side walls have a uniform thickness of 4 cm.

Finally the whole detector is surrounded by an plastic anti-coincidence shield to reject charged particles of cosmic and atmospheric origin.

A more detailed discussion of the prototype and its calibration can be found in Chapter 6 and even more detail is given in *Andritschke* (2006). Additional information about a potential satellite version of MEGA can be found in Chapter 10.

Chapter 2

Interaction processes in a tracking Compton and pair telescope

In order to develop reliable and accurate reconstruction techniques for the measured events, it is essential to first gain a detailed understanding of the photons' possible interactions in the detector. In keeping with the type of instrument discussed in this work, photo absorption is mentioned only in the context of fully contained Compton scattering events, and Rayleigh scattering is ignored since its effects in a MEGA-type telescope are negligible.

All relevant photon interactions — photo-absorption, Compton scattering, and pair production — can be detected only via interactions resulting in energetic electrons and positrons in the instrument. Thus a detailed understanding of electron interactions constitutes the necessary foundation for a detailed discussion of the different photon detection processes (Section 2.1). Sections 2.2 and 2.3 discuss Compton and pair interactions. Using the idealized interactions of gamma-ray photons with matter as a starting point, each section subsequently describes the multitude of effects that occur in a real instrument.

2.1 Interactions of electrons with matter

When an electron (or positron) passes through matter, it interacts with the atoms' Coulomb potentials: It undergoes many small-angle scatterings (Molière scattering) and loses energy mostly via ionization and bremsstrahlung.

2.1.1 Molière scattering of electrons

The process of multiple small-angle scatters of electrons on Coulomb potentials is called Molière scattering. The change in the flight direction is described by Molière theory (for an overview see *Bethe*, 1953). The scatter angle distribution can be approximated by a Gaussian (*Particle Data Group*, 2004, see also Figure 2.1). The width of the angular distribution, projected on a scattering plane, is given by:

$$\delta_{0,proj} = \frac{13.6\,\mathrm{MeV}}{\beta cp}\sqrt{\frac{r}{R_0}}\left(1 + 0.038\ln\frac{r}{R_0}\right) \tag{2.1}$$

Here $\beta cp = \frac{E_e^2 + 2E_eE_0}{E_e + E_0}$ is the velocity times the momentum of the electron, E_e is the electron energy, E_0 the rest energy of the electron, R_0 the radiation length in the material (9.35 cm for Silicon), and r is the *straight* path length (i.e. the straight line between start and end points) of the electron in the material. The non-projected width of the angular distribution δ_0, which is basically given by $\sqrt{2}\cdot\delta_{0,proj}$, is shown for Silicon in Figure 2.2. The simulation was performed

with Geant3 for normal incidence and the electrons were passing through one slab of Silicon (500 μm thick). Profiles for 1 MeV and 5 MeV electrons are shown in Figure 2.1.

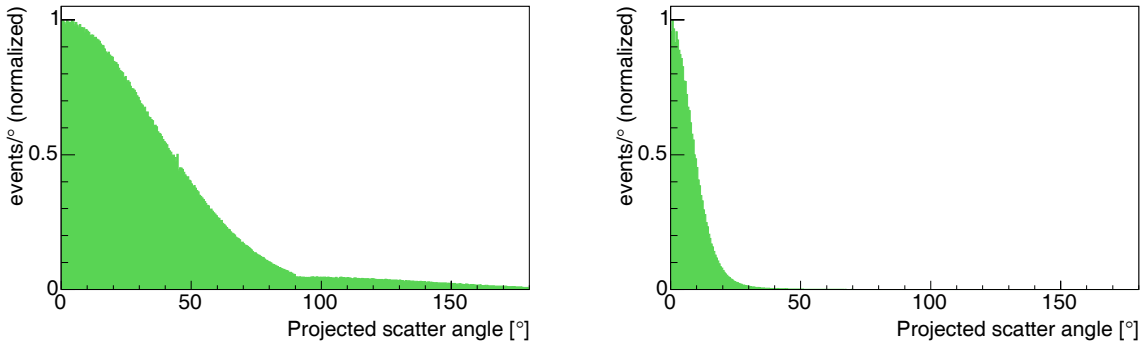

Figure 2.1: Typical Molière profiles at 1 MeV (left) and 5 MeV (right) as simulated with Geant3. After passing 500 μm of Silicon, the projected scatter angle of the electron has roughly a Gaussian shape. Only those electrons at 1 MeV which reverse their direction (scatter angles $> 90°$) do no longer follow the Gaussian approximation. They collect in a tail of the distribution at larger projected scatter angles.

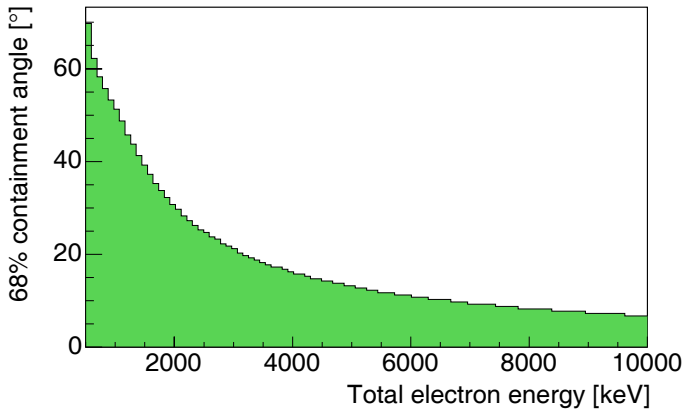

Figure 2.2: Geant3 simulation of the width of the angular distribution for electrons passing through 500 μm of Silicon (one tracker layer for MEGA). Given is the cone opening angle around the original direction, enclosing 68% of all events. This corresponds to $\sqrt{2} \cdot \delta_{0,proj}$ of the width given in Equation 2.1.

Considering electron tracks in MEGA's stack of Si strip detectors, Molière scattering has four consequences:

1. Given the geometry of the MEGA tracker (distance between layers 1 cm, pitch of the strip detector 470 μm), the directions of a track element (line between two interaction points) can be resolved up to 3° at normal incidence. This value is smaller than δ_0 for electron energies below 21 MeV. Thus almost all electron-direction measurements in the tracker are limited by Molière scattering. Of course switching to thinner Silicon layers would improve the situation a bit. But with e.g. 300 μm thick wafers, the limit is still at 15 MeV, which is not a significant improvement.

2. Since the electron deposits and thus loses energy along the track, and δ_0 increases with decreasing energy, the average scatter angle increases along the path of the electron. This is one criterion for determining the direction of motion of the electron.

3. The given widths of the angular distributions are for electrons which pass one layer of Silicon completely. This is normally not the case for the interaction in the first layer, where the Compton scattering happens. Here, the recoil electron does not need to pass the whole layer. As a consequence, the effect of Molière scattering is reduced by typically 50% for the electron emerging from the conversion layer. The same holds for pair creation.

4. Finally, from the above three points follows that the direction of the original electron in the MEGA energy range is best determined only from the first and the second interaction points.

2.1.2 Energy loss of electrons in matter

Six processes contribute to the energy loss of electrons and positrons, two of which dominate in a MEGA-type Silicon tracker: ionization at low energies, bremsstrahlung at high energies. The electron energy for which both loss rates are equal is called the critical energy. It can be approximated by $E_c = (800\ \text{MeV})/(\text{Z} + 1.2) \approx 53$ MeV for Si (*Berger and Seltzer*, 1964). Electron and positron interactions in MEGA are thus dominated by ionization. A welcome consequence of this is that MEGA tracks are not going to be "polluted" by a significant amount of additional bremsstrahlung hits, making the tracking much easier than for higher energy gamma-ray telescopes like GLAST. Other energy loss mechanisms are Møller scattering for electrons, Bhabha scattering for positrons respectively, positron annihilation before the positron is completely stopped, and δ-rays (knock-on electrons) (see e.g. *Particle Data Group*, 2004). None of the latter play an important role for MEGA.

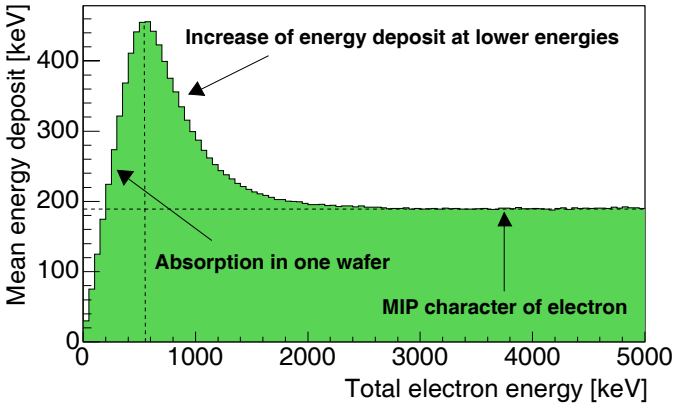

Figure 2.3: Mean energy deposit in 500 μm Silicon as function of electron energy. The direction of the incident electrons is isotropically distributed. The shape is described in terms of three regions: at high energies, the electrons are minimum-ionizing particles (MIPs) and their energy deposits are (within MEGA's energy range) almost independent of the incident energy. At medium energies (0.5 – 2 MeV) the electrons have lost their MIP character; a significant increase in the deposit of energy can be observed. Below 500 keV most electrons get stopped in the Silicon layer and deposit their complete energy.

Figure 2.3 shows mean energy deposits in 500 μm Silicon as a function of incident electron energy, as simulated with Geant3. This energy spectrum consists of three different regions. In the first one, up to roughly 400 keV, the electron is completely absorbed in the Silicon and deposits its complete energy. The second region around the maximum is characterized by electrons which have just enough energy to pass through the Silicon. At higher energies, the electrons behave like minimum ionizing particles, whose energy loss is almost constant. At even higher energies, beyond the range of Figure 2.3, the energy loss will increase again. A detailed quantitative description of this shape can be found in *Schopper* (2001).

For identifying the track direction this has one important consequence: For high-energy electrons above 2 MeV, the energy criteria alone can give almost no information about the direction of the track. At lower energies, however, the mean deposits increase significantly, which makes it easy to find the end of the track.

The actual energy deposit in one layer varies strongly (see Figure 2.4). The spectrum follows a Landau distribution, after Lev Landau, who made the first theoretical calculation of this energy distribution. There are no deposits below ~120 keV; the most probable deposit is ~175 keV for 1 MeV electrons (140 keV for 5 MeV electrons), and the long tail of the distribution leads to a high mean deposit around 250 (190) keV, as plotted in Figure 2.3. At 60 (40) keV FWHM this distribution is roughly three (two) times as broad as the energy resolution in MEGA's Silicon tracker.

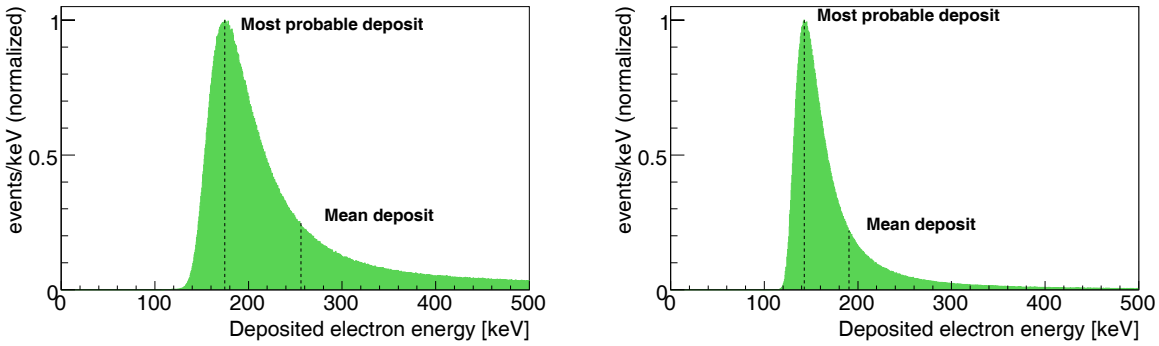

Figure 2.4: Deposit profiles for 1 MeV (left) and 5 MeV (right) electrons after passing 500 μm Silicon as simulated with Geant3. The direction of the original electron was isotropically distributed. The shape is a Landau-distribution, with a very long tail. Thus, the mean deposit with 256 (190) keV is significantly larger than the most probable deposit with 175 (145) keV.

2.2 Compton scattering

In 1923 Arthur H. Compton (1892-1962) discovered that X-rays can be scattered on electrons during their passage through matter and that there exists a relation between the scatter angle and the initial and final wavelength of the photon (*Compton*, 1923), which was later called *Compton equation* (Equation 2.6). A schematic drawing of the Compton effect is shown in Figure 2.5, which also serves as an illustration of notations used throughout this work[1].

In the following, first three fundamental aspects of (idealized) Compton scattering are described: Scatter kinematics, scatter probabilities as function of scatter angles, and the impact of photon polarization on the scatter cross-section are discussed in Sections 2.2.1 – 2.2.3. The latter includes an introduction to Compton polarimetry. These three sections are followed by detailed explanations of all the ways in which a real-life detector deviates from the ideal, and the consequences this has for the determination of the incident photons' direction and energy. Section 2.2.4 describes the consequences of incomplete or missing information about energies or directions, Section 2.2.5 introduces measures for the angular resolution of the instrument and discusses the impact of energy and position accuracy on the angular resolution. The influence

[1]For a complete list of frequently-used notations see also Appendix A.

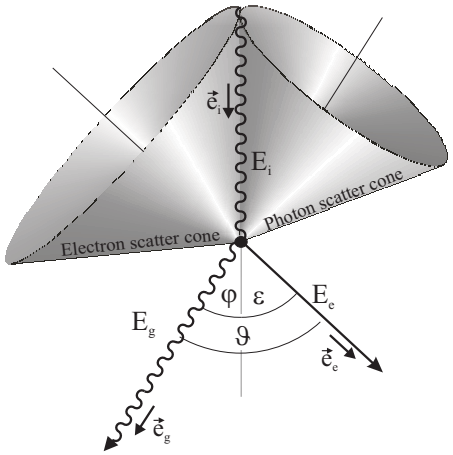

E_i	Energy of initial gamma ray
E_e	Energy of the recoil electron
E_g	Energy of the scattered gamma ray
E_0	Rest energy of the electron
E_e^{rel}	Total relativistic energy of the electron
φ	"Compton scatter angle" of the gamma ray
ε	"Electron scatter angle" of the recoil electron
ϑ	Total scatter angle
$\vec{e}_i$	Direction of the initial gamma ray
$\vec{e}_e$	Direction of the recoil electron
$\vec{e}_g$	Direction of the scattered gamma ray

Figure 2.5: Compton-scattering and all notations. Undulated lines represent photons, straight lines electrons. The photon scatter cone represents all possible origin directions of the photon in case the direction of the electron could not be measured, the electron scatter cone represents the possible origins in case the scattered photons' direction could not be measured.

of a bound electron's initial energy and momentum on the instrument's angular resolution is discussed in Section 2.2.6.

2.2.1 Kinematics

The underlying scatter problem can be described in terms of conservation of energy and momentum of photon and electron:

$$E_i + E_{i,e}^{rel} = E_g + E_e^{rel} \tag{2.2}$$

$$\vec{p}_i + \vec{p}_{i,e} = \vec{p}_g + \vec{p}_e \tag{2.3}$$

The initial energy $E_{i,e}^{rel}$ and momentum $\vec{p}_{i,e}$ of a bound electron are unknown. In the following it is assumed that the electron is at rest, i.e. its initial energy is its rest energy E_0 and its momentum $\vec{p}_{i,e}$ is zero. However, this unavoidable approximation has a consequence, the so-called *Doppler-broadening* limit to a Compton telescope's angular resolution, which is explained in Section 2.2.6.

Application of the relativistic energy-momentum-relation $E_e^{rel} = \sqrt{E_0^2 + p_e^2 c^2} = E_e + E_0$ and the relation between energy and momentum of photons $E_g = p_g c$ leads to the following equations for direction and energy of the initial photon:

$$\vec{e}_i = \frac{\sqrt{E_e^2 + 2E_e E_0}\vec{e}_e + E_g \vec{e}_g}{E_e + E_g} \tag{2.4}$$

$$E_i = E_e + E_g \tag{2.5}$$

In his original work of 1923 Compton could not measure the direction of the recoil electron — he could only measure the direction and energy change of the scattered gamma ray. He found the following relation between energies and scatter angle φ, which was later called *Compton equation*:

$$\cos\varphi = 1 - \frac{E_0}{E_g} + \frac{E_0}{E_g + E_e} \tag{2.6}$$

In order to get a mathematically valid Compton scatter angle φ — the arccos has the domain $[-1;1]$ — E_e and E_g have to comply with the following constraints:

$$\begin{aligned} \frac{E_0 E_i}{2E_i + E_0} < E_g < E_i \qquad & \text{for the scattered photon} \\ 0 < E_e < \frac{2E_i^2}{2E_i + E_0} \qquad & \text{for the recoil electron} \end{aligned} \tag{2.7}$$

These constraints correspond to backscattering of the gamma ray (energy of the photon reaches its minimum) and no scattering at all ($E_g = E_i$).

Equations similar to 2.6 exist for the scatter angle ε of the recoil electron and the total angle ϑ between the directions of scattered photon and recoil electron:

$$\cos\varepsilon = \frac{E_e(E_i + E_0)}{E_i\sqrt{E_e^2 + 2E_e E_0}} \tag{2.8}$$

$$\cos\vartheta = \frac{E_e(E_g - E_0)}{E_g\sqrt{E_e^2 + 2E_e E_0}} \tag{2.9}$$

Obviously, ε can take values between 0° (back scattering) and 90° (forward scattering, $E_e \to 0$) for fixed E_i. For the limit of (almost) no energy transfer to the electron, ϑ is equal to 90°. In the case of small E_i ($< E_0$), the total scatter angle rises monotonely with increasing E_e. If the incident photon's energy exceeds E_0, ϑ as a function of E_e first falls towards $\arccos\left(\frac{E_i - E_0}{E_i + 2E_0}\sqrt{\frac{E_i^2 - E_0^2}{E_i^2 + 2E_0 E_i}}\right)$ and then rises again. Finally, in the case of back scattering, ϑ is equal to 180°.

2.2.2 Cross-sections

A few years after Compton's discovery, *Klein and Nishina* (1929) derived the differential Compton cross section $\left(\frac{d\sigma}{d\Omega}\right)$ for unpolarized photons scattering off unbound electrons:

$$\left(\frac{d\sigma}{d\Omega}\right)_{C,\,unbound,\,unpol} = \frac{r_e^2}{2}\left(\frac{E_g}{E_i}\right)^2\left(\frac{E_g}{E_i} + \frac{E_i}{E_g} - \sin^2\varphi\right) \tag{2.10}$$

Here r_e is the classical electron radius. The above equation is also called the *unbound Compton* cross section since the electron is assumed to not be bound to an atom and therefore to be at rest. Because this is not the case for any detector material used in Compton telescopes today, the Klein-Nishina cross section constitutes an approximation. Figure 2.6 illustrates the angular dependence of the Compton cross section for 0.1, 1 and 10 MeV photons.

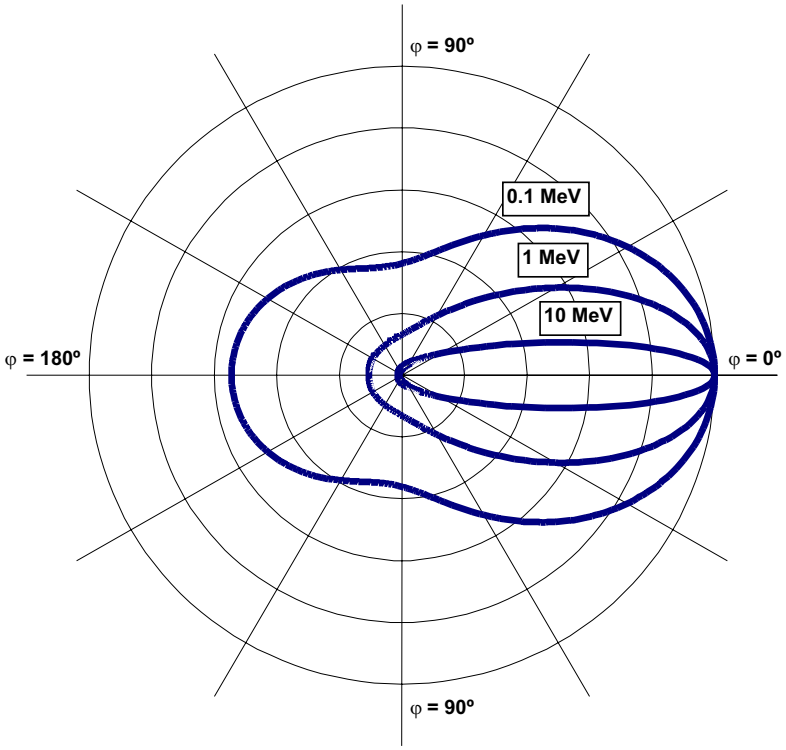

Figure 2.6: Klein-Nishina cross-section as a function of the Compton scatter angle φ for different energies: The higher the energy, the smaller the average Compton scatter angle — i.e. the stronger is the forward scattering.

2.2.3 Polarization

Compton scattering also preserves the polarization information of linearly polarized photons up to a certain degree. If the initial gamma ray is polarized, then the following differential cross section applies:

$$\left(\frac{d\sigma}{d\Omega}\right)_{C,\,unbound,\,pol} = \frac{r_e^2}{2}\left(\frac{E_g}{E_i}\right)^2\left(\frac{E_g}{E_i} + \frac{E_i}{E_g} - 2\sin^2\varphi\cos^2\chi\right) \tag{2.11}$$

Here χ is the azimuthal or polar scatter angle.

The polarization signature of the incident linearly polarized photons is reflected in the probability distribution of the azimuthal scatter angle, which can be derived from Equation 2.11:

$$P(\chi) = P_0 + A\cos\left(2\left(\chi - \chi_0 + \pi/2\right)\right) \tag{2.12}$$

Here χ_0 is the direction of the original polarization vector.

In qualitative terms, this polarization dependence can be described as follows (compare Equation 2.11):

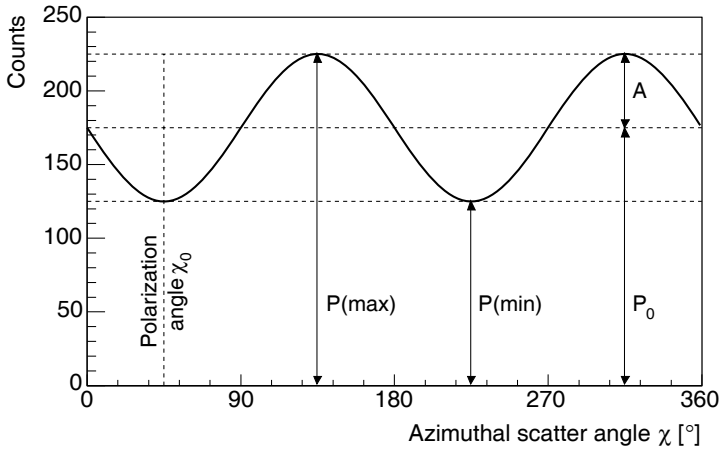

Figure 2.7: Expected polarization signal for a 100% polarized gamma-ray beam: The distribution of the azimuthal scatter angle χ is of the form $P(\chi) = P_0 + A\cos(2(\chi - \chi_0 + \pi/2))$ and $\mu = A/P_0$ is the modulation. The minimum of the signal defines the plane of polarization of the original photons.

- The scattered photons tend to scatter at right angles to the original polarization vector, minimizing the term $-2\sin^2\varphi\cos^2\chi$.
- At higher energies and therefore lower average Compton scatter angles, the modulation of the azimuthal distribution is reduced.
- For small and very large Compton scatter angles φ the detectable polarization signature is weak ($\sin^2\varphi$ is close to zero).

The polarization response of a detector can be described in terms of a quality factor μ (also called modulation). It is defined as the ratio between the amplitude A and the offset P_0 of the azimuthal scatter angle distribution. For a 100% linearly polarized beam of gamma rays, it is given by the following equation (see Figure 2.7 for a definition of variables):

$$\mu = \frac{P(max) - P(min)}{P(max) + P(min)} = \frac{A}{P_0} \tag{2.13}$$

The modulation as a function of incident energy E_i and scatter angle φ is shown in Figure 2.8. The maximum of the modulation shifts from $\varphi = 90°$ for low energies to $\varphi = 54°$ at 5 MeV and $\varphi = 45°$ at 10 MeV.

In a quest to detect polarization of e.g. gamma-ray bursts, of course special selection criteria must be applied to detected events to maximize an instrument's polarization sensitivity. The

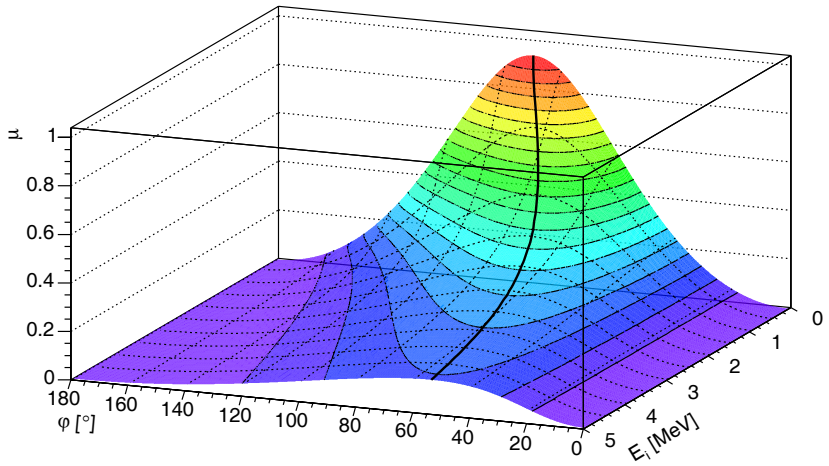

Figure 2.8: Modulation as a function of incidence energy E_i and Compton scatter angle φ as derived from the Klein-Nishina cross section. The thick black line indicates the maximum of modulation for a given incident energy. The thin lines indicate levels of constant modulation. Each real polarimeter aims at getting as close as possible to these ideal values.

Compton-scatter polarization signature is most pronounced at medium scatter angles and lower energies. For a deeper insight into the basic principles of Compton polarimetry, refer to *Lei et al.* (1997).

2.2.4 Incomplete measurement

In the previous sections ideal Compton telescopes have been discussed. However, when working with any real-life instrument, several additional aspects have to be taken into consideration. If the energies of the recoil electron E_e and the scattered photon E_g as well as their directions $\vec{e}_e$ and $\vec{e}_g$ are determined with high accuracy, the origin of the photon can be calculated using Equation 2.4. However, even if not all four parameters are measured (or only measured with a large error) it is still possible to constrain the origin and energy of the photon.

2.2.4.1 Missing or uncertain directions

COMPTEL, as a first-generation Compton telescope, was unable to measure the direction of the recoil electron. An equation describing the possible origins of the photon for this case can be derived. In the following, the z-axis is assumed to be parallel to the scattered photon's direction.

The Compton scatter angle φ can be written as:

$$\cos\varphi = \vec{e}_i \circ \vec{e}_g = e_{i,z} \cdot e_{g,z} = e_{i,z} \tag{2.14}$$

With the constraint $||\vec{e}_i|| = 1$ follows:

$$e_{i,x}^2 + e_{i,y}^2 = 1 - \cos^2\varphi = \sin^2\varphi \tag{2.15}$$

This equation describes a circle in the x-y-plane with radius $r = \sin\varphi$. With the reparametrization $e_{i,x} = r\sin t$ and $e_{i,y} = r\cos t$ one obtains for the origin of the gamma ray:

$$\vec{e}_i\,(t) = \begin{pmatrix} \sin\varphi\,\sin t \\ \sin\varphi\,\cos t \\ \cos\varphi \end{pmatrix} \forall\, t \in [0, 2\pi] \tag{2.16}$$

Thus the incident direction of the detected gamma ray can be restricted to a cone whose opening angle is the Compton scatter angle φ and whose axis points in direction of the scattered photon (Figure 2.5). However, the origin of the photon can no longer be determined uniquely. The resulting ambiguity has to be resolved by image reconstruction techniques (see Chapter 5) and is only possible if a sufficient amount of photons (depending on background conditions) has been measured. Such events constitute the majority of interactions in the MEGA telescope at low energies, where no electron tracks can be acquired.

An equation similar to 2.16 can be derived if the electron scatter angle is well known, but no information about the photon scatter angle is present. If the z-axis points in direction of the recoil electron direction, one gets:

$$\vec{e}_i\,(t) = \begin{pmatrix} \sin\varepsilon\,\sin t \\ \sin\varepsilon\,\cos t \\ \cos\varepsilon \end{pmatrix} \forall\, t \in [0, 2\pi] \tag{2.17}$$

Again the origin direction of the gamma ray can be restricted to a cone, now with opening angle ε (electron scatter angle) and pointing into the direction of the recoil electron (Figure 2.5). In the MEGA detector, the measurement of the energy of the scattered gamma ray is always accompanied by a measurement of its direction that is at least as accurately known as

the electron track direction. Consequently, this event type cannot be found in the data of the MEGA instrument and will not be discussed further.

Even if a photon has been completely absorbed and the electron's energy was sufficient to generate a track, the direction of the recoil electron can still only be measured to within the limit of Molière scattering (see Section 2.1). Combining the well-determined Compton cone and the less accurately known electron cone leads to the typical arc-like distribution of possible origins of such a photon on the sky (see e.g. Figure 5.3). This is the main event type of the MEGA detector at medium (2-10 MeV) energies.

2.2.4.2 Missing or incomplete energy measurements

If both the electron and the photon scatter angle — and thus the total scatter angle — and at least one energy (E_e or E_g) are known, then the missing energy can be computed from the Equation 2.9. However, in the case of MEGA most often no decision can be made whether E_e or E_g or both are incompletely absorbed. So this approach is not applicable for the recovery of the photon origin.

If no energies are measured or both energies only incompletely, but the electron and the photon scatter directions are well known, then it is still possible to partly retrieve the photon's origin. Due to momentum conservation, the photon must have originated from the scatter plane, somewhere between the (inverse) scatter direction of the recoil electron and the scattered photon (Figure 2.9). In spherical coordinates, the origin lies on a segment of a great circle described by:

$$\vec{e}_i = \|(1-t)\,\vec{e}_g + t\,\vec{e}_e\| \quad \forall\, t \in \left[\frac{\varphi_{min}}{\vartheta}, \frac{\varphi_{max}}{\vartheta}\right] \tag{2.18}$$

In most cases a partial measurement of the energies allows to further restrict this segment by determining a minimum and maximum possible Compton scatter angle (φ_{min} and φ_{max}). For a given ϑ the relation of the energies of recoil electron and scattered photon can be derived from Equation 2.9:

$$E_e = \frac{2\,E_0\,E_g^2\,\cos^2\vartheta}{(E_g - E_0)^2 - E_g^2\,\cos^2\vartheta} \tag{2.19}$$

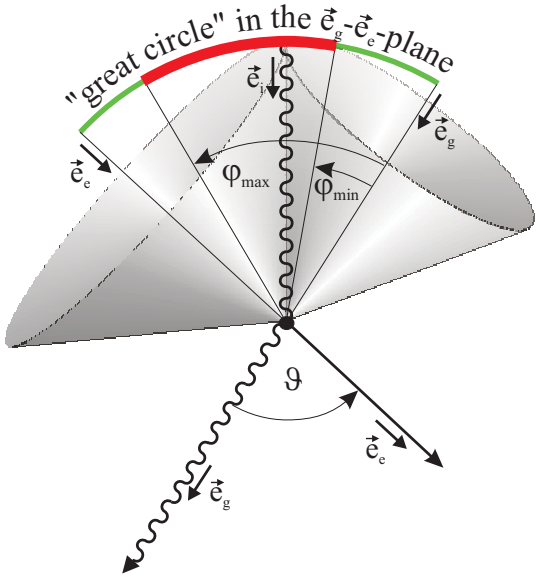

Figure 2.9: If neither the energy of the scattered gamma ray nor the energy of the recoil electron can be measured, but both directions are known, then momentum conservation requires that the photon's origin lies on the segment of the great circle defined by the direction of the recoil electron and the scattered gamma ray. If some partial energy measurements are given, a minimum and a maximum possible Compton scatter angle (φ_{min} and φ_{max}) can be calculated, further restricting the allowed segment of the great circle on the sky.

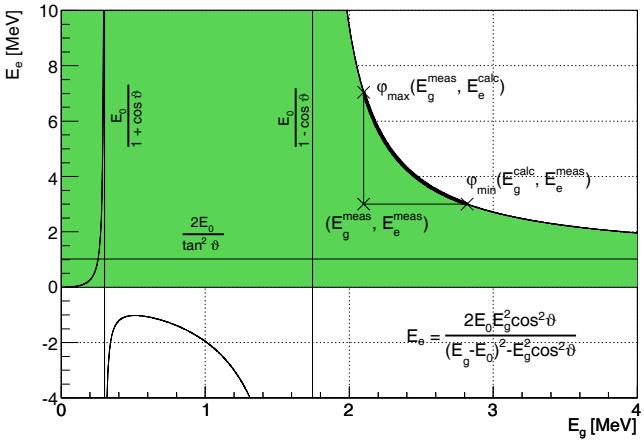

Figure 2.10: Energy of the recoil electron as a function of the energy of the scattered gamma ray for a fixed total scatter angle of 45°. Only the right branch constitutes a valid solution for the given ϑ angle (see text). All pairs of E_g^{meas} and E_e^{meas} left of the function (green area) are Compton-compatible with the given total scatter angle. If $E_g^{meas} > \frac{E_0}{1-\cos\vartheta}$, a φ_{max} can be determined; if $E_e^{meas} > \frac{2E_0}{\tan^2\vartheta}$, a φ_{min} can be calculated. Both further restrict the segment of the great circle from which the photon could have originated. Of course, if E_g^{meas} and E_e^{meas} lie on the function, the photon is completely absorbed and can be reconstructed into a point instead of a segment of a great circle (in absence of measurement errors).

Figure 2.10 illustrates this relation for an exemplary total scatter angle of $\vartheta = 45°$. The full mathematically allowed solution of Equation 2.19 is shown, regardless of its reflection in the actual physics for a scatter angle of $\vartheta = 45°$. The right branch ($E_g > \frac{E_0}{1-\cos\vartheta}$) corresponds to the actual physical solution for $\vartheta = 45°$, as can be demonstrated by Equation 2.9. The middle branch — requiring negative E_e — is clearly not a solution for the given problem. The left branch ($E_g < \frac{E_0}{1+\cos\vartheta}$) arises from the ambiguities introduced by the $\cos^2\vartheta$ terms in Equation 2.19. Using Equation 2.9 to discriminate the actual ϑ angles, it becomes clear that this part of the function is actually the physical solution of 2.19 for $\vartheta = 180° - 45°$, not for $\vartheta = 45°$.

Assuming ϑ, E_g^{meas}, and E_e^{meas} have been measured, the goal is to determine φ_{min} and φ_{max}.

- In the easiest case, E_g^{meas} and E_e^{meas} lie on the curve. Then the photon is completely absorbed and it can be reconstructed into a point (in absence of measurement errors).

- If $E_g^{meas} > \frac{E_0}{1-\cos\vartheta}$ and $E_e^{meas} > \frac{2E_0}{\tan^2\vartheta}$, and both values are below/left of the curve, for E_g^{meas} a corresponding electron energy E_e^{calc} can be calculated via Equation 2.19 and for E_e^{meas} a value E_g^{calc}. Since the Compton scatter angle is strictly monotone on the curve and the kinematically correct values have to lie *on* the curve, the values (E_g^{calc}, E_e^{meas}) define the smallest allowable Compton scatter angle φ_{min} and the (E_e^{max}, E_g^{calc}) define φ_{max} through the Compton equation.

- Some special cases have to be considered: If $E_g^{meas} < \frac{E_0}{1-\cos\vartheta}$ then no limit on φ_{max} can be given, thus $\varphi_{max} = \vartheta$. If $E_e^{meas} < \frac{2E_0}{\tan^2\vartheta}$ then no limit on φ_{min} can be determined, thus $\varphi_{min} = 0$.

- If (E_g^{meas}, E_e^{meas}) is above the right branch of the curve, then all possible total scatter angles of the incompletely measured energies would result in a smaller angle than ϑ and thus this region is kinematically impossible (in absence of measurement errors).

Figure 2.11 illustrates the angular extent of the great circle ($d\varphi = \varphi_{max} - \varphi_{min}$) for $\vartheta = 45°$ for the given partly measured energies.

In a real-life instrument, the electron has to travel through detector material in order for its direction to be measured. In this material, the electron undergoes Molière scattering and its direction changes (see Section 2.1). However, in order to restrict the origin of a photon to a segment of a great circle, the direction of the electron has to be known to a few degrees. Thus, this approach is only applicable at high energies, above 10 to 20 MeV, depending both on the amount of energy transferred to the electron and on the angle under which the electron passes

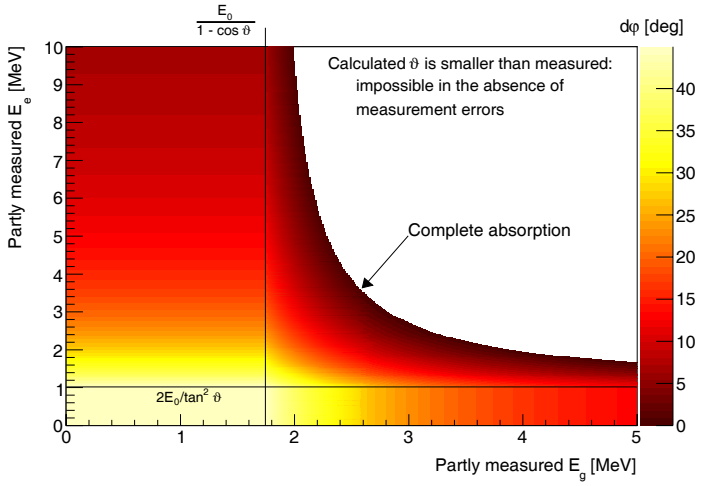

Figure 2.11: Angular extent of the segment of the great circle describing the possible origins of the Compton event in case of incompletely absorbed energies but well defined directions of the recoil electron and the scattered gamma ray for a fixed total scatter angle of 45°. Only those photons which lie on the line of complete absorption can be reconstructed to a point (in absence of measurement errors).

through the layers. Fortunately, it is in this same energy regime above 10–20 MeV were the approach is needed most, since here almost all Compton events are incompletely absorbed.

Of course, although it is possible to *image* such events, only lower and sometimes upper limits on the photons' incident energy can be given.

2.2.5 Angular resolution determination

No Compton telescope has perfect energy and position resolutions. Together with Doppler-broadening (Section 2.2.6), those measurement uncertainties limit the accuracy with which the origin of the photons can be determined. For an electron-tracking Compton telescope, this angular resolution can be described in terms of the angular resolution measure (ARM) and the scatter plane deviation (SPD). To determine these, the origin of the photons and thus their original direction $\vec{e}_i$ needs to be known.

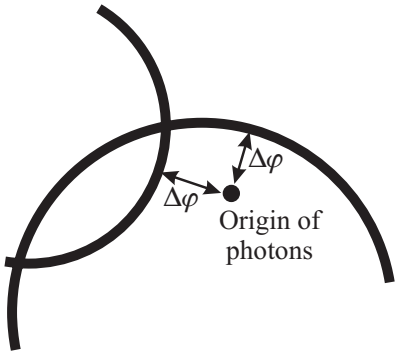

Figure 2.12: The angular resolution measure (ARM) is defined as the smallest angular distance between the known origin of the photon and the Compton cone. It is a measure for the width of the Compton scatter cone or arc. A real origin lying within the cone, which mostly implies that the scattered gamma ray is incompletely absorbed, results in a negative $\Delta\varphi_{ARM}$ value, a real origin outside the cone, i.e. an incompletely absorbed recoil electron, results in a positive $\Delta\varphi_{ARM}$ value.

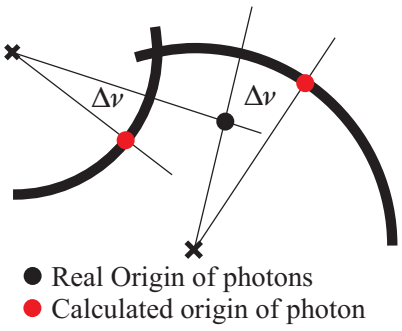

Figure 2.13: The scatter plane deviation (SPD) is defined as the angular distance on the Compton cone between the known origin of the photons and the calculated one. It is a measure for the length of the Compton scatter arc.

The ARM (Figure 2.12) for a reconstructed Compton event is defined by the shortest distance between the known initial photon direction $\vec{e}_i$ and the photon scatter cone defined by

the (measured) direction of the scattered gamma ray. This shortest distance is equal to the difference between the Compton scatter angle φ as calculated from the *measured* energies (φ by kinematics) and the angle between the *known* direction of the initial and *measured* direction of the scattered gamma ray (φ by scatter geometry):

$$\Delta\varphi_{ARM} = \arccos\left(\vec{e}_i \circ \vec{e}_g\right) - \varphi \tag{2.20}$$

In the case of an incompletely absorbed recoil electron, the ARM is shifted to positive $\Delta\varphi_{ARM}$; in the case of an incompletely absorbed scattered gamma ray, the ARM is shifted to negative values.

The *distribution* of ARM values obtained from a larger sample of Compton events provides a measure of the directional accuracy of the Compton reconstruction. Conversely, the width of the ARM *distribution* therefore describes the uncertainty in the opening angle of the Compton cone for each individual reconstructed Compton event.

From Figure 2.5, the analogy between electron and photon scatter cone is evident. Thus one can also define an "Electron-ARM" in analogy to the "Photon-ARM":

$$\Delta\varepsilon_{ARM} = \arccos\left(\vec{e}_i \circ \vec{e}_e\right) - \varepsilon \tag{2.21}$$

However, for the ultimate aim of Compton imaging, it is preferable to define the measurement accuracies of the photon's origin arising from both electron and gamma-ray scatter directions relative to the center of the photon cone — for the electron's contribution this is done via the SPD illustrated in Figure 2.13. The SPD describes the angle between the true scatter plane described by $\vec{e}_i$ and $\vec{e}_g$ and the measured one spanned by $\vec{e}_g$ and $\vec{e}_e$ assuming that $\vec{e}_g$ has been measured correctly:

$$\Delta\nu_{SPD} = \arccos\left((\vec{e}_g \times \vec{e}_i) \circ (\vec{e}_g \times \vec{e}_e)\right) \tag{2.22}$$

The SPD is relevant only if a measure of $\vec{e}_e$ exists. It is dominated by the accuracy with which the direction of the recoil electron can be measured and provides a measure for the length of the Compton scatter arc.

In the case of MEGA, for all but the highest energies the ARM is the key parameter to describe the angular resolution for a collection of Compton events, because the direction of the scattered gamma ray can be determined more accurately than that of the electron.

The ARM is influenced by most components of the measurement process, the accuracy of the energy of the electron and the scattered gamma ray as well as the accuracy with which the directions can be determined. The energy resolution determines φ in Equation 2.20, the quantity $\arccos\|\vec{e}_i \circ \vec{e}_g\|$ is influenced by the position resolution. The propagation of measurement errors for the Compton scatter angle φ (Equation 2.6) leads to the following equation:

$$d\varphi = \frac{E_0}{\sin\varphi}\sqrt{\left(\frac{1}{E_g^2} - \frac{1}{\left(E_e + E_g\right)^2}\right)^2 dE_g^2 + \frac{1}{\left(E_e + E_g\right)^4} dE_e^2} \tag{2.23}$$

Figures 2.14 and 2.15 illustrate the dependency of this uncertainty on the measurement accuracy of the electron's and the scattered photon's energy, each time as a function of Compton scatter angle.

Especially from Figure 2.15 it is obvious that a Compton telescope which intends to measure large Compton scatter angles needs to measure the energy of the scattered gamma ray to a very high precision to preserve its angular resolution.

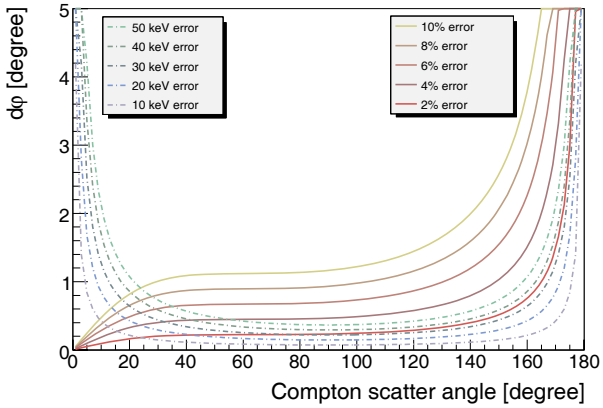

Figure 2.14: Measurement uncertainty of the Compton scatter angle $d\varphi$ as a function of the Compton scatter angle φ. Only the measurement uncertainty of the recoil electron is used. An initial energy of 2 MeV was assumed. The solid lines correspond to an error in percent of E_e, the dotted lines to a constant error. The energy uncertainty of the MEGA prototype is a combination of both.

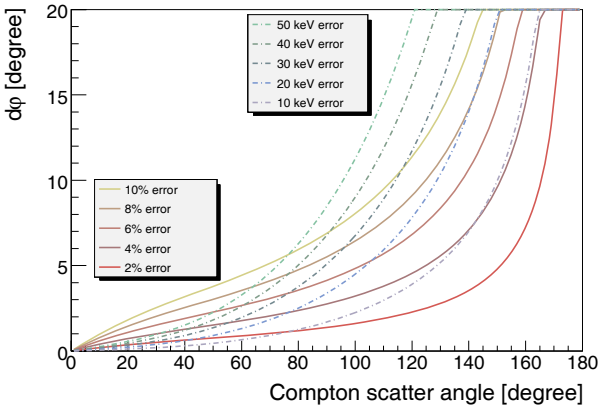

Figure 2.15: Measurement uncertainty of the Compton scatter angle $d\varphi$ as a function of the Compton scatter angle φ. Only the measurement uncertainty of the scattered gamma ray is used. An initial energy of 2 MeV was assumed. The solid lines correspond to an error in percent of E_g, the dotted lines to a constant error.

2.2.6 Doppler broadening as a lower limit to the angular resolution of a Compton telescope

In a real-life detector system the electrons are neither free nor at rest, but bound to a nucleus. In 1929 *DuMond* (1929) interpreted a measured broadening of Compton spectra as Doppler broadening induced by the velocity of the electrons. To describe this effect, a more sophisticated Compton cross section than the Klein-Nishina equation is required: the momentum distribution of the bound electrons must now be taken into account. A suitable expression has been derived by *Ribberfors* (1975) and called *bound* Compton cross section

$$\left(\frac{d\sigma}{d\Omega}\right)_{C,\,bound,\,i} = \left(\frac{d\sigma}{d\Omega}\right)_{C,\,unbound} S_i^I\left(E_i, \varphi, Z\right) \tag{2.24}$$

The S_i^I is called the incoherent scattering function of the i-th shell electrons in the momentum approximation; it has been calculated by *Ribberfors and Berggren* (1982). Z is the atomic number of the scattering material.

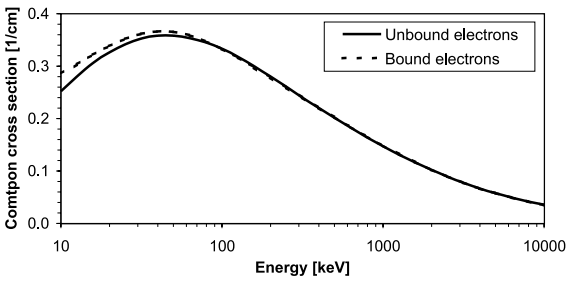

Figure 2.16: Compton cross section for bound and unbound Compton scattering in Silicon: While both curves are practically identical at energies above several 100 keV, for lower energies Compton scattering on bound electrons has a slightly higher probability than on unbound electrons.

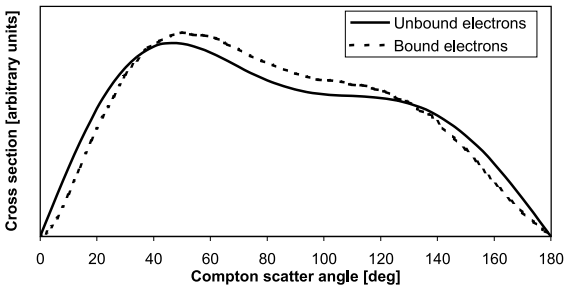

Figure 2.17: Cross section for bound and unbound Compton scattering in Silicon as a function of the Compton scatter angle at 100 keV. Both areas are normalized to 1 (arbitrary units, linear scale). In the bound case, small and large scatter angles are slightly suppressed.

Compared with Compton scattering on free electrons at rest three consequences arise:

- The total scatter probabilities change (Figure 2.16). Especially at lower energies, photons have a slightly higher probability to scatter than predicted by the Klein-Nishina equation (Equation 2.10) for unbound electrons.
- The scatter angle distribution changes (Figure 2.17): Compared to the Klein-Nishina equation small and large scatter angles are slightly suppressed. This effect is smaller at higher energies.
- The energy distribution between recoil electron and scattered gamma ray changes, while the sum of the interaction energies is still exactly equal to the total gamma-ray energy. As a consequence, the measured scatter angle and the one calculated using the standard Compton equation 2.6 differ. For a given point source location, an ARM distribution of the calculated origins shows a broadening (see Figure 2.18). Therefore this effect is widely known as *Doppler broadening*.

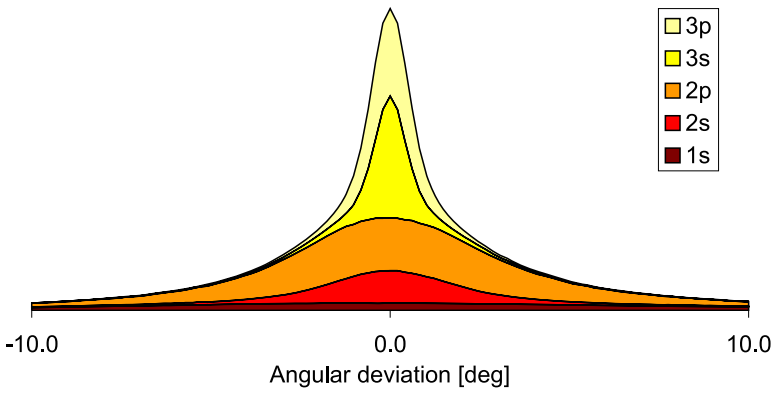

Figure 2.18: Cumulative ARM profile for Compton scattering of 200 keV photons in Silicon without scatter angle selections (based on simulations). The different areas represent the contributions of different shells of the Silicon atom: in the outside shells, the electrons are less energetic and closer to the "target-at-rest" assumption. Therefore the distribution is sharper. The effects shown are due to Doppler broadening only — all energy and position measurements are assumed perfect!

For a Compton telescope the first two points have little impact other than slightly modifying the event distributions and total sensitivity for lower energies. But since there is no way to determine the initial momentum of the electron, the third point gives rise to a lower limit for the angular resolution of Compton telescopes.

From the formulation of the incoherent Compton scatter function in Equation 2.24, it should be obvious that the Doppler-limited angular resolution depends on three parameters: the initial photon energy E_i, the Compton scatter angle φ and the atomic number Z.

An example for the shape of a Doppler-broadened ARM profile is shown in Figure 2.18. The total profile is composed of the profiles of the different shells: the innermost electrons (1s orbital) have the highest momentum, and therefore the widest distribution. The 2p orbital is populated by 6 electrons, whereas all other orbitals consist of two electrons. For this reason the 2p orbital contributes most to the width of the profile. The outermost electrons have the lowest momentum and therefore form the peak of the distribution.

Figure 2.19 shows the dependence of the angular resolution on the atomic number. On average, the angular resolution worsens with increasing Z. But it also strongly depends on the shell structure of the individual atoms. Up to Calcium (Z=20) the relationship is simple: it increases until it reaches a noble gas (He, Ne, Ar), then the FWHM decreases and reaches a minimum at the alkaline metals or alkaline earth metals. For higher atomic numbers the noble gases Krypton, Xenon and Radon are only smaller local maxima. The three highest local maxima around Z=30, Z=46 and Z=79 are reached when the 3d, 4d and 5d orbitals are filled

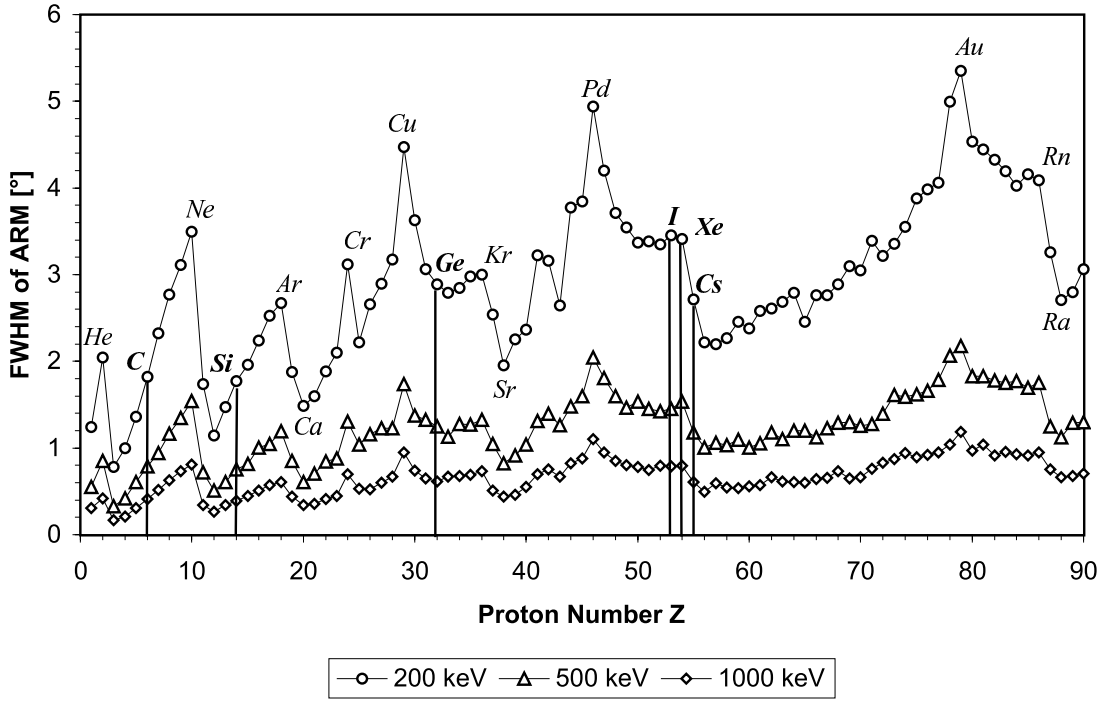

Figure 2.19: Dependence of the angular resolution on the nuclear charge. The best angular resolution is obtained for alkaline or alkaline earth metals. The worst FWHM is reached when orbitals are completely filled (e.g. for noble gases).

Material	Si	Ge	CdZnTe	Xe	NE213	CsI	NaI
FWHM at 200 keV [degree]	1.80	2.85	3.50	3.30	1.75	2.95	3.00
FWHM at 500 keV [degree]	0.80	1.25	1.55	1.45	0.75	1.25	1.40
FWHM at 1000 keV [degree]	0.40	0.65	0.85	0.80	0.40	0.75	0.85

Table 2.1: Doppler broadening in different semiconductor materials, Xenon, and scintillators.

for the first time. For example, ^{46}Pd is the maximum, not ^{48}Cd, because of its special electron configuration: the two electrons from the 5s orbital are filling the 4d orbital. Similar reasons can be found for other extraordinary local maxima, e.g. for ^{24}Cr the 3d orbital is half filled.

Of the Compton telescope materials currently under serious consideration, Silicon provides the best angular resolution assuming ideal detector properties, followed by Germanium and finally the noble gas Xenon. Table 2.1 summarizes the performance of different semiconductor and scintillator materials. Some hydrocarbon-based scintillators like NE213, which was used as the scatter material in COMPTEL, have a slightly better performance than Silicon due to their hydrogen component.

The angular resolution also strongly depends on the Compton scatter angle φ (see Figure 2.20). The FWHM worsens with larger scatter angles and therefore with smaller energies of the scattered photon. Since Doppler broadening results in a slightly different energy distribution between scattered gamma ray and recoil electron than would be observed in a Compton scatter on a free electron, its effects are similar to the energy measurement errors illustrated in Figures 2.14 and 2.15.

Figure 2.21 summarizes the relationship between the initial photon energy and the angular resolution: On average Silicon has a Doppler-broadening limit on the angular resolution roughly 1.6 times better than that of Germanium and roughly 1.9 times than that of Xenon. All three curves roughly follow a power law with $\alpha = -0.75$.

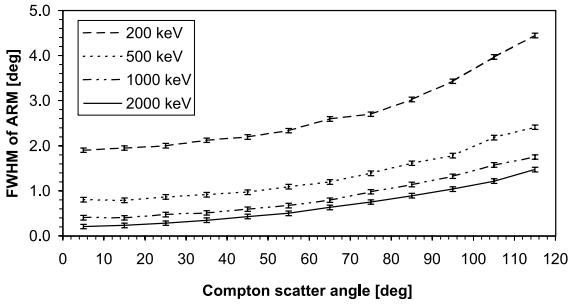

Figure 2.20: Dependence of the angular resolution on the Compton scatter angle φ for Germanium at four energies at the Doppler-broadening limit. All values are averaged within 10°-bins.

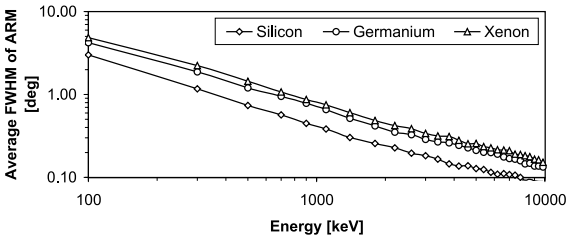

Figure 2.21: Dependence of the angular resolution on the energy of the initial gamma ray at the Doppler-broadening limit. The values are averaged in 200 keV intervals below 1100 keV and in 400 keV intervals above 1100 keV. No event selections were applied.

Doppler broadening constitutes a fundamental limit for the angular resolution of Compton scattering-based telescopes. Unfortunately, it makes several strategies to improve Compton telescopes at these energies futile:

Due to their superior stopping power, high Z materials (e.g. Ge, CdTe, Xe) are sometimes favored in gamma-ray astronomy. They guarantee a high efficiency; however, the associated angular resolution is fundamentally limited. In particular, Germanium Compton telescopes cannot take advantage of their good energy resolution to improve their angular resolution. They have already reached their Doppler limit (*Boggs et al.*, 2000b) at lower energies.

From the Doppler-broadening point of view, a Compton telescope based on semiconductor technology should use Silicon or Carbon detectors as scatterer since these promise the best angular resolution. However, they need much more material to achieve the same efficiency, and e.g. the energy resolution of Silicon is worse than that of Germanium.

For tracking Compton telescopes like MEGA, the scatter angle dependence of the Doppler broadening seems to be a disadvantage. An electron needs a certain amount of energy to pass through several layers of material, inducing a bias towards larger scatter angles for tracked events. Consequently, tracked events will tend to correspond to events where the role of Doppler broadening is more pronounced. However, since a reasonable amount of tracking sets in at incoming gamma-ray energies around 1-2 MeV, since the MEGA tracker is based on Silicon, and since other measurement errors dominate, Doppler broadening is not the limiting factor in the current implementation of MEGA.

Nevertheless, the wide tails of the Doppler-broadened ARM distributions constitute a significant problem. The events in those tails represent a background component for close sources, and thus make it more difficult to resolve sources in crowded fields, e.g. in the Galactic center region.

Doppler broadening is a fundamental limit for the angular resolution. Therefore below roughly 1 MeV Compton telescopes cannot give a better angular resolution than coded mask systems like IBIS (*Winkler et al.*, 2003) on board INTEGRAL, which has an angular resolution of roughly 0.2°. Even an ideal Silicon-based Compton telescope will not reach this value below $1 - 2$ MeV, with the exact angular resolution achievable depending on event selections.

2.3 Pair production

When the energy of the incoming gamma ray exceeds two times the rest mass of an electron, 1.022 MeV, another interaction mechanism starts playing a role: the conversion of the gamma ray to an electron-positron pair in the electromagnetic field of a nucleus. During this process

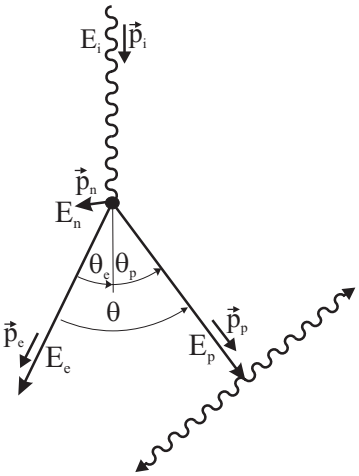

E_i	Energy of initial photon
E_e	Energy of electron
E_p	Energy of positron
E_n	Energy transferred to nucleus/electron
θ_e	Electron scatter angle
θ_p	Positron scatter angle
θ	Opening angle
$\vec{p_i}$	Momentum of the initial photon
$\vec{p_e}$	Momentum of the electron
$\vec{p_p}$	Momentum of the positron
$\vec{p_n}$	Momentum of the nucleus/electron

Figure 2.22: Pair production and all notations: When the energy of the gamma ray exceeds 1.022 MeV, it can be converted into an electron-positron pair. The positron later annihilates.

the photon gets completely absorbed and the nucleus takes over part of the photon momentum. This process is called pair production, pair creation, or gamma conversion and is described by the following equations of energy and momentum conservation:

$$E_i = E_e + E_p + E_n + 2E_0 \tag{2.25}$$

$$\vec{p_i} = \vec{p_e} + \vec{p_p} + \vec{p_n} \tag{2.26}$$

If the photon's energy exceeds four times the rest mass of an electron, pair creation can also happen in the field of an electron. Here the momentum is not transferred to the nucleus, but instead to the electron. While the recoil of the nucleus is converted to phonons and thus is not detectable by conventional means, the recoil of the electron generates a track signature — in theory three tracks might be visible in the MEGA detector. The ratio of the probability for pair production on an electron to that for pair production on a nucleus is given by:

$$p_{electron} = \frac{1}{CZ}\, p_{nucleus} \tag{2.27}$$

Here Z is the atomic number, which is 14 for Silicon, and C is a factor which depends on the incoming gamma-ray energy. At 100 MeV $C = 1.2$, at 6 MeV $C = 2.6$ (*Evans*, 1958). In the MEGA energy range the ratio of conversions on electron to the conversions on a nucleus is $\approx$ 1:30.

In all past and current gamma-ray telescopes the momentum transferred to the nucleus cannot be measured. Since the energy transfer is not very large ($\sim 511\,\mathrm{keV}/c$), an approximation of the original photon direction can be made by neglecting the nucleus' recoil:

$$\vec{e_i} \approx \frac{E_e\vec{e_e} + E_p\vec{e_p}}{E_e + E_p} \tag{2.28}$$

In the case of the MEGA prototype, even the energy of electron and positron can in most cases not be determined due to incomplete absorption. Thus an even more radical simplification is necessary:

$$\vec{e_i} \approx \vec{e_e} + \vec{e_p} \tag{2.29}$$

Pair creation telescopes, like Compton telescopes, are limited in their angular resolution by the interaction processes in a solid state detector. Ignoring instrument-specific uncertainties such as position and energy measurement accuracy, two uncertainties remain: the unknown

recoil of the nucleus and the small-angle scattering (Molière scattering) in the layers of the detector. Figure 2.23 summarizes these fundamental limits for a MEGA-like tracker consisting of layers of 500 μm thick Silicon. The most probable momentum transfer to the nucleus is close

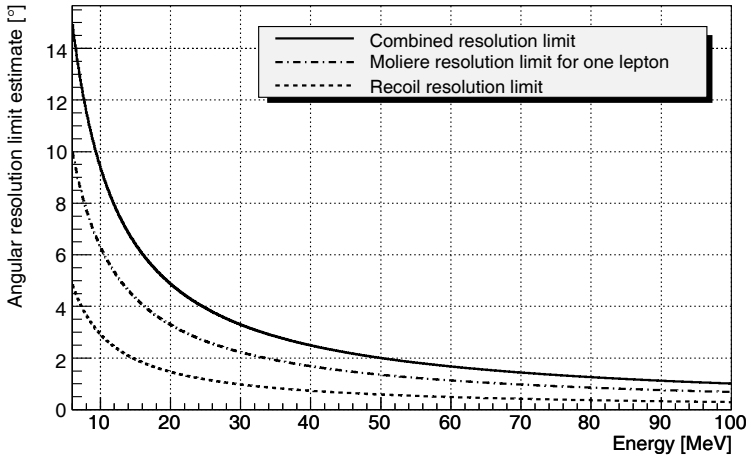

Figure 2.23: The fundamental angular resolution limit for pairs is determined by the unknown recoil of the nucleus and by the Molière scattering of electron and positron, while traversing through the initial layer. The impact of Molière scattering depends on the instrument's geometry (layer thickness in the tracker, 500μm Silicon in this case). It is assumed that the interaction occurs is the center of the layer.

to $0.511\,MeV/c$, with the nucleus most likely moving away at 80° to 90° from the photon's incident direction for photons of energies above 10 MeV (*Modesitt and Koch*, 1950). For Silicon, this results in an energy transfer of ∼5 eV which is 4 orders of magnitude below the detection threshold of MEGA. The angular resolution limit Δ_{recoil} can be estimated to be:

$$\Delta_{recoil} \approx \arctan \frac{m_e c^2}{E_i} \tag{2.30}$$

The Molière scattering limit is given by Equation 2.1 for one electron. In calculating the limit shown in Figure 2.23 it was assumed that the pair production happens in the center of the layer and the incoming photon's energy is shared evenly between electron and positron. The latter constitutes a rough approximation; 20% to 80% of the incoming photon's energy are transferred to the electron in the pair with about equal probabilities over the energy range of interest (see e.g. *Evans*, 1958). Consequently, the lower-energy particle's direction might have a rather large uncertainty, and the higher-energy particle a much smaller one. However, the combined resolution limit shown in Figure 2.23 — which is based on this assumption of equipartition of energy — turns out to be only 20% lower than the angular resolution obtained in full-fledged Monte Carlo simulations of the MEGA telescope (including energy and position uncertainties) in the energy range below 20 MeV where Molière scattering dominates the instrument's properties. A more detailed description for MEGA including all uncertainties is given in *Schopper* (2001).

Part II

New analysis techniques for the next generation of Compton and pair telescopes

Chapter 3

Simulation and data analysis overview

The next generation of tracking Compton and pair telescopes records significantly more information about the individual interactions of all particles involved than its predecessors COMPTEL and EGRET. This additional information has to be used in a completely different way to determine the sequence of the hits as well as the quality of the reconstruction. Since no time-of-flight information is available, mainly the kinematics and topology of the Compton interactions and of the electron and positron tracks can be used. In this context a completely new set of tools for data reduction and analysis had to be developed for this work. This toolset is bundled into MEGAlib — the Medium Energy Gamma-ray Astronomy library.

The MEGAlib software package encompasses the complete data analysis chain, which consists of four basic steps: (1) data acquisition, either by measurements with the real detector or via simulation, (2) calibration of real data or the introduction of measurement uncertainties to the simulations respectively, (3) event reconstruction and (4) high-level data-analysis including image reconstruction, polarization analysis, sensitivity calculation, etc. For all those steps different routines exist in MEGAlib. A schematic overview of the general data flow is shown in Figure 3.1.

This introductory chapter describes each of the four steps discussed above that are necessary to go from raw measurements or simulations to the lowest-level common data representations, hits in energy and position, and on to high-level data end products. In the following chapters the high-level processing steps, the event and image reconstruction, will be discussed in much greater detail as these comprise the heart of this work.

3.1 From detector measurements to hits

The data acquired by the read-out electronics of MEGA is expressed in detector units. These units are the ID numbers of the detectors and channels which have triggered and the output of the analog-digital-converters in ADUs (analog-to-digital converter units). Additional information available includes time of the trigger, the time gap between the first trigger in the tracker and the first trigger in the calorimeter, the trigger pattern, and more. All this data is acquired by the MEGAlyze program as seen in Figure 3.1. A detailed description of this program can be found in *Schopper* (2001).

The energy information of each channel is calibrated separately. The detector-specific information is converted into physical units: ADUs are transformed into energies and channel numbers into positions. In the case of a strip detector all signals of the x- and y-strips of one detector have to be combined into interaction positions. In the case of depth-sensitive

calorimeters the signal of both diodes is not only converted into energy but also into a depth measurement. After this step one event is represented by hits, each of which consists of energy and position in the detectors world coordinate system. An extensive overview of the single-hit calibration methods can be found in *Andritschke* (2006). Those hits are the input for the later event reconstruction.

3.2 From simulations to hits

The main purpose of Monte-Carlo simulations is to accurately predict the measurements and ultimately the performance of the detector — both on ground and in space. In the energy range of the MEGA telescope (from a few keV up to hundreds of MeV), the Geant Monte-Carlo software packages are widely used. For each of those packages exist simulation interface tools in MEGAlib. The workhorse is Geant3 (*CERN: Application Software Group and Networks Division*, 1993) with its MGGPOD extension (*Weidenspointner et al.*, 2005) for the simulation of orbital background environments. Geant3 is well tested in the MEGA energy regime and has given remarkable agreement between simulation and measurements of real satellites (*Weidenspointner et al.*, 2005). The object-oriented approach of Geant4 (*Agostinelli et al.*, 2003) makes the program more adaptable to the users' needs, and will in the future replace Geant3. Currently however, it is still in a rapid development phase, which turned out to make it less reliable than Geant3.

The foundation for a realistic simulation of a telescope is laid long before the simulation itself. First, one has to ensure that the simulation program contains all physical processes relevant for the telescope and the energy range. Especially the effect of Doppler broadening, which fundamentally limits the angular resolution of a telescope whenever it relies on Compton scattering, is not included in the default Geant packages. The GLECS extension package by *Kippen* (2004) addresses this problem for Geant3 and Geant4. Another important point is a realistic geometry description. In the Compton regime it is especially hard to stop the initial photon completely, because the result of Compton scattering still remains a photon, ready for the next Compton interaction, until it gets photo absorbed. Thus it is really important to include *absolutely all* passive materials at the right places, to allow for interactions in passive materials. This will result in incomplete absorptions, activations from protons and neutrons in a space environment, and thus the generation of secondary particles in passive material as seen in real detectors. In addition the correct isotopic composition of all materials and corresponding cross-sections for all particle types to be encountered must be implemented. Only if both, detector mass model and physics implementation in the Monte-Carlo code are realistic enough, the resulting detector performance parameters will truly reflect what a real detector would see.

When the simulation is performed, the output information is already in energies and positions, but highly idealized. Energy and position resolutions are perfect, no thresholds have been applied, etc. Ideally the correct measurement uncertainties should be introduced into the simulated data such that analyzing measurements and corresponding simulations gives the same results. This step relies on more detailed detector characteristics than are used in the simulation and are summarized as "simulation interface" in the overview diagram of Figure 3.1. For each single interaction in the detector, the simulation yields the exact amount of deposited energy and the exact interaction position. In real detectors, however, the position knowledge is noisy or restricted to voxels (e.g. strips in Silicon strip detectors and crystals in the CsI calorimeters) and the energy is noised by effects such as light yield, noise of read-out channels, etc. The "simulation interface" accounts for this by centering the positions in the individual voxel and applying a Gaussian noise to the energy measurement and the depth resolution of the 3D calorimeters according to the width of the expected/measured distributions.

No detector is perfect, but has a certain amount of not working pixels (dead, not connected,

deactivated, etc.). These pixels introduce additional dead material, which has to be accounted for. Thus, a certain percentage of all hits is rejected on a random basis.

Since a Compton telescope is a coincidence detector, at least two signals (for MEGA one from the tracker and one from the calorimeter), with a certain energy deposit (in the MEGA case measured as a voltage) are needed to trigger the read-out of the detector. This minimum energy deposit is called the trigger threshold. Since the threshold is constant neither in time nor for different channels in a real-life system, it is not implemented as a fixed energy but with a Gaussian width, which is determined by the expected/measured trigger threshold distributions. If a simulated event does not fulfill the trigger criteria, it is rejected.

After a coincident event has triggered the read out, all channels are analyzed to determine whether the energy deposit is more than $5\,\sigma$ above the average noise-level of this channel. All deposits below this noise threshold are rejected. Normally this noise threshold is smaller than the trigger threshold and is therefore important to detect additional small-energy hits beside the triggers. The noise threshold is implemented like the trigger threshold. However, of course the individual hit is only rejected if it lies below the noise threshold.

Each Compton detector has a coincidence window, during which it accepts events from the two detector systems. If during this time span another event interacts in the detector, a random coincidence occurs. Applying coincidence windows as well as readout and reset times is necessary to determine the dead time of the detector. Random coincidences constitute a source of additional background, especially in high-rate environments. The latter is not an issue for the MEGA measurements analyzed in this work, since they were all taken in the laboratory.

After the steps discussed in this and the preceeding section, the real and the simulated data should look very similar. The events are now represented by hits consisting of energy and position.

3.3 Event reconstruction and response generation

During the next step, the individual hits must be combined into events (Revan library in Figure 3.1) and the detector response matrices (Response generator in Figure 3.1) must be determined.

The methods of the event reconstruction are described in detail in Chapter 4. The basic idea is to look at the structure of the event, and from the kinematics, the topology and the detector geometry along the lines-of-travel of the photons, electrons or positrons, find out what happened in the detector: Did a Compton scattering occur or a pair creation, did a charged particle pass through or was a large shower created? At the end of the event reconstruction, the data is represented by event types and their associated information, e.g. a Compton event with given energy and direction of the recoil electron and the scattered gamma-ray, or a pair event with given direction and energy of electron and positron. All events are accompanied by a quality factor, which describes the probability that the event happened this way and is completely absorbed.

The second important task on this level of data analysis is to generate response matrices. A response maps the properties of the incoming photons to the detector measurement in a multi-dimensional data space. In order to determine the response, the information of the incidence photons from the simulation is compared with the characteristics of the reconstructed events. Since this data space is rather complex, different projections are made and optimized for special tasks, for example finding the correct interaction sequence (event reconstruction response see Chapter 4) or determining the origin of a photon in image space (imaging response see Chapter 5).

The result of this step of data analysis are events, and the description of how the detector reacts on well defined inputs, the response. The next step is to use this information to retrieve the parameters of the original source distributions.

3.4 High level data analysis

The last step, the high level data-analysis, tries to invert the measurement process and to determine the properties of the sources of the measured gamma rays.

The first crucial step is to find optimized selection criteria for "good" events. The main task of event selections is to exclude those bins of the data space that contain most of the background events. The high-level data analysis tools comprised in MEGAlib's Mimrec library allow event selection on basically all performance-relevant parameters of the Compton and Pair events. These include event type, start detector, energy, scatter angles, distance between interactions, event quality factors, earth horizon cut, number of hits, opening angle and initial deposit of the pair events, and many more.

Diagnostics tools assessing angular resolutions (ARM, SPD), energy dispersion, scatter angle (φ, ε, ϑ) distributions, etc. are necessary to determine the quality of the event selections as well as the performance of the detector. Moreover, it is possible to perform background corrected polarization studies, determine the effective area and sensitivity of a detector, and many more.

The most challenging step, however, is the image reconstruction itself, which is explained in Chapter 5. The list-mode likelihood image reconstruction algorithm allows to reconstruct sources in spherical as well as Cartesian coordinates (2D as well as 3D) from tracked and not tracked Compton as well as pair events and allows several different levels of response approximations to be applied to the data.

3.5 The scope of MEGAlib

MEGAlib is completely written in C++ and based on ROOT (*Brun and Rademakers*, 1997). It has accumulated over 300,000 lines of source code, most of which where written within the context of this work. Each result presented in this work has been achieved by using the MEGAlib software package. The software is designed to be easily adaptable to different detector designs, from tracking Compton and Pair telescopes, via time-of-flight based Compton telescopes to Drift chamber based Compton telescopes. The necessary changes are restricted to defining a new geometry and detector description.

The MEGAlib package has been considered the most versatile and state-of-the-art tool set available in 2004 by the ACT study team. Consequently it has been used for different Compton telescopes designs for the NASA Advanced Compton Telescope concept study (*Boggs et al.*, 2005).

The next two chapters are dedicated to the two most challenging tasks in the data analysis of tracking Compton and pair telescopes, the event reconstruction and the image reconstruction.

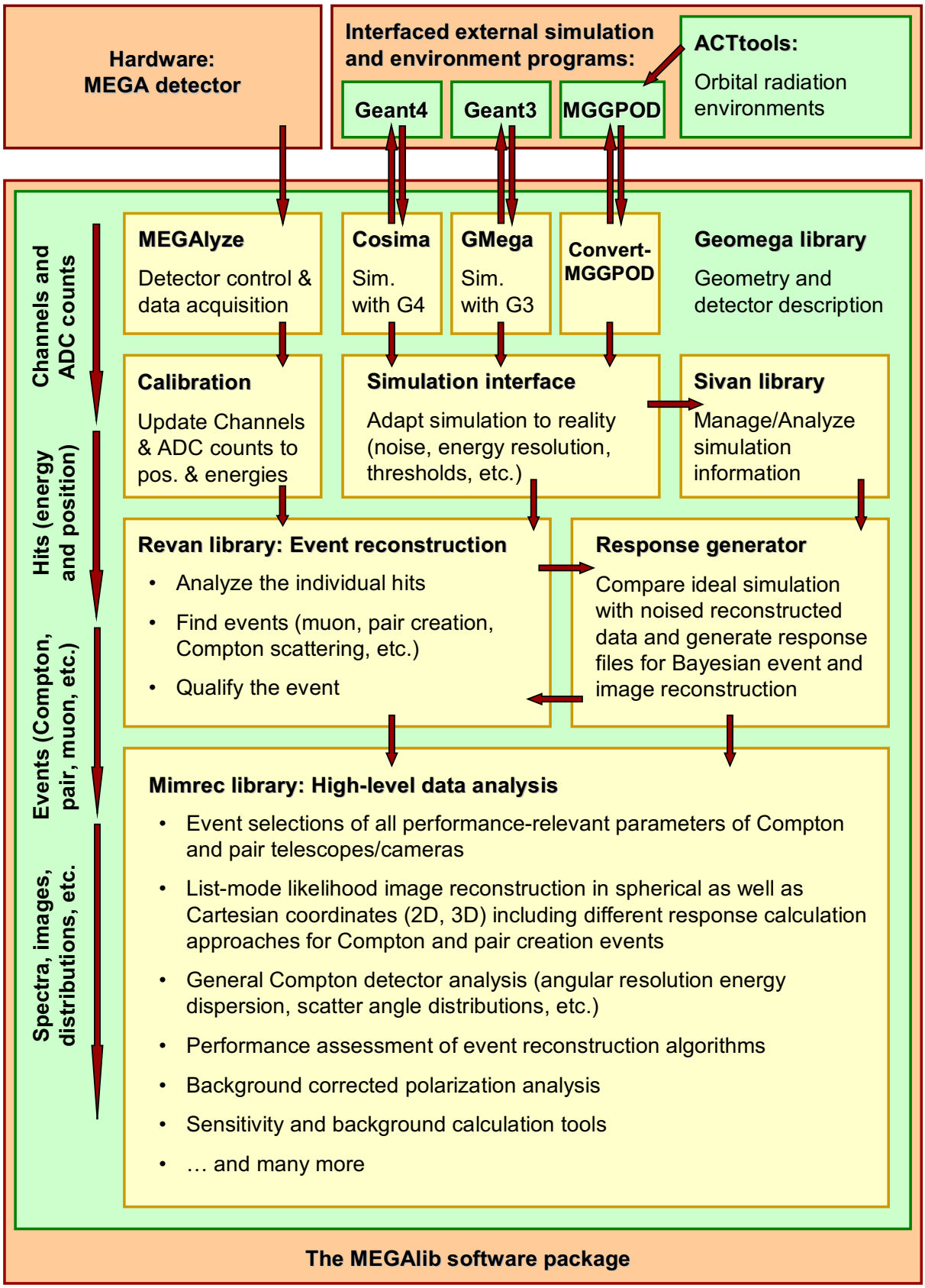

Figure 3.1: Basic layout of the MEGAlib software package. See the text for a detailed description.

Chapter 4

Event reconstruction

4.1 The basic idea

Valid events can generate a large number of different possible hit patterns in a combined Compton and pair telescope such as MEGA. The greatest challenge on the path from the hits making up a raw event to scientific results is figuring out what actually happened in the detector for each individual event. This process is called event reconstruction. Figure 4.1 illustrates a fraction of the variety of valid photon events, with lines illustrating the true sequence of event components. All shown events have been actually measured with the MEGA prototype.

While the following discussion is for the most part applicable to any modern-day Compton or pair telescope, the discussion is geared towards, and the choice of data space dimensions is optimized for, the MEGA instrument concept with its tracker consisting of thin Si layers.

4.1.1 Tasks and problems of the event reconstruction

The overall performance of a Compton and pair telescope is not only determined by its hardware but also by the performance of the algorithms which recover the original parameters of the incident photons from the measured data. Since each lost or not recognized event reduces the efficiency, and each incorrectly reconstructed event lowers the efficiency *and* increases the background, the performance of the data analysis has considerable influence on the final sensitivity of the telescope.

Before the event reconstruction, an event consists of nothing but a collection hits which all have position and energy information. The event reconstruction sorts those hits in the order in which the interactions of the original particle(s) inside the detector occurred. This is done by utilizing the laws of physics and statistical considerations. The result of this data analysis step is an event which describes the main interaction which happened in the detector, for example a Compton event with energy and direction of the scattered gamma-ray and recoil electron (including measurement errors), or a pair creation event with energy and direction of electron and positron. This information encompasses the parameters of the incident particle including energy and direction that are needed in the next step of data analysis.

Sequencing would be a trivial task if the hits had an accurate-enough time tag. But the compact design of the MEGA instrument and the slow response of its detectors and read-out electronics render this impossible. Thus the kinematics of the interactions, the topology of the event structure, and the geometry of the detector have to be used to deduce the parameters of the original photon.

During the event reconstruction numerous questions emerge and have to be answered: Are there tracks? Are there multiple tracks? Which hit belongs to which track? What end of the track is the starting point? Do all the other hits belong to the event? To which

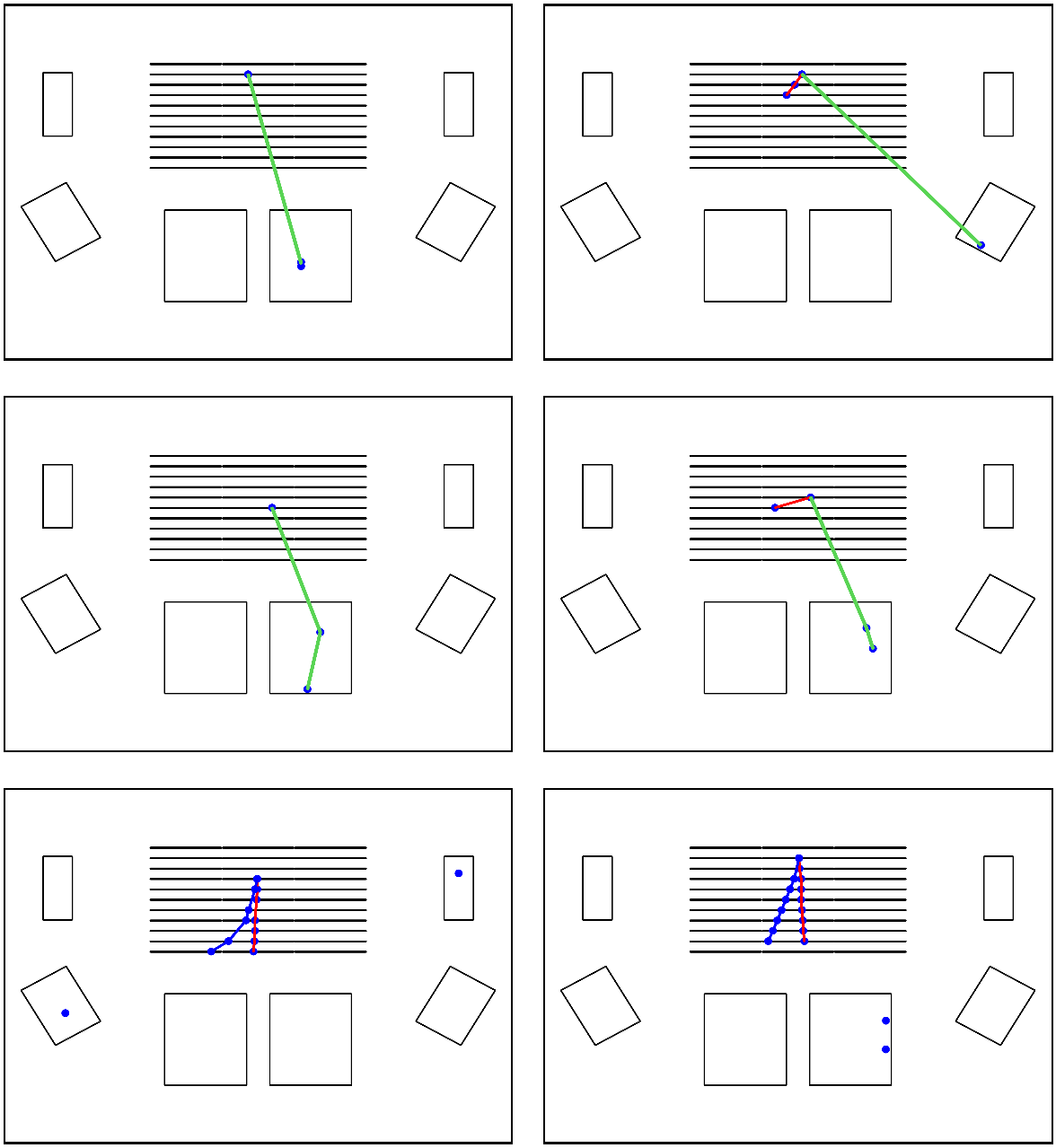

Figure 4.1: Event gallery. Top left: Compton event with two interactions without track (the classical COMPTEL event); Top right: Compton event with two interactions with track; Center left: Compton event with three interactions without track; Center right: Compton event with three interactions with electron track; Bottom: Pair event. The isolated hits in the left image have energies close 511 keV and probably originate from the positron annihilation photons. The two calorimeter hits in the right image sum up to 511 keV. The continuation of the tracks into the calorimeter is not shown. All events have been measured during the Duke calibration campaign, the top four events are from 2 MeV photons, the bottom 2 events are from 50 MeV photons.

track/sequence/event do all the other hits belong? Does a track continue down into the calorimeter? How much energy has been deposited in dead material? After answering those questions, the event type has to be determined: was it a Compton scattering event, or pair-creation, or simply an electron, positron, proton, muon passing through the detector — or even some decay process? Was it a "real" event or a random coincidence of several events? Is the event, especially the Compton event, completely absorbed? Did the event really start in the tracker? Did the event come from above? ...

While answering those questions, the event reconstruction has to cope with missing and surplus hits, which both significantly complicate things. The missing hits originate from interactions in passive material such as structure or dead voxels and from hits whose energy deposit is below the threshold. The latter proves especially problematic for Compton events with tracks where the electron did not deposit sufficient energy in the layer of the Compton interaction. This leads to missing energy as well as to a wrong start position of the track. Surplus hits are generated by general detector noise and random coincidences. At higher energies, bremsstrahlung from decelerated electrons also plays a role. Finally, the poor energy and position resolution in the calorimeters constitutes a definite handicap to determine the overall hit sequence of multiple Compton events.

4.1.2 Outline of the event reconstruction

The event reconstruction tries to identify the most simple structures like pair events and muons first. The remaining event are searched for the much more complex structures of Compton events, to which most of this chapter is dedicated. The individual steps are outlined below.

Step 1: Clusterize hits in adjacent bars and strips
When an electron passes through a Silicon wafer it might hit two or more adjacent strips. Those adjacent hits are combined into a cluster of hits. The energy of the cluster is the total energy of its hits and its position is the "center of energy". The detailed algorithm for the more complex case of several interactions in one Silicon wafer is described in Section 4.2. Under certain circumstances (high electron energies, interactions close to the border) electrons are also traveling from one CsI bar to the next bar in the calorimeter. In this case the two hits are combined into a cluster if the difference in depth position is not larger than 3 sigma of the bars' depth-position ("z") resolution.

Step 2: Search for a vertex to identify pairs
Pair events produce a very characteristic pattern in the MEGA detector, an inverted "V", which can be easily recognized not only by eye (see e.g. Figure 4.1) but also by a pattern recognition algorithm. If a vertex is found, the event is considered a pair event, and the corresponding reconstruction algorithm is applied (details see 4.3).

Step 3: Search for high energy charged particle events
High energy charged particles such as muons also create easily recognizable structures in the tracker: One rather straight track per particle passing through the tracker. If one (or more) of those signatures are found, the high energy charged particle reconstruction algorithm is launched, which fits a straight line to the pattern in the detector. Such muon events have been used in detector testing and calibration. Since this algorithm is rather trivial no individual section is dedicated to it in the later text.

After step 3, all easily recognizable patterns have been found. The remaining events are Compton events or "trash".

Step 4: Search for Compton electron tracks
The initial step in the focused search for good Compton events is the identification of any electron tracks and the determination their direction of motion. This is done by scrutinizing the

topology of the track and its kinematics, especially the energy deposits in the wafers and the change in direction during the passage through one wafer (see 4.4).

Step 5: Search for the Compton interaction sequence
This step aims to arrange all interactions (tracks are now one interaction with their start as position of the interaction) in their kinematically correct order. Keys are the direction of the electron track, and, if the event consists of three or more interactions, the available redundant information from the multiple Compton interactions, as well as the detector geometry, especially absorption probabilities along the path of the photon (see 4.5).

Step 6: Search for special beta-decays
The last step could be a search for characteristic signatures of beta-decays in the active material of the detector. Activation is a significant background source for a real satellite mission. Beta decays have a signature which might be partly identified by certain types of Compton telescopes: One hit is generated by the β^+ particle itself, other signatures by the released photons. In case some sub structures (sub collection of hits) of the event have the same energies as the (well-known) photon(s) produced by the decay and another hit is within the possible flight direction of that photon, then that event could be rejected. However, an excellent energy ($dE/E < 0.01$) resolution is necessary for this to be feasible. Thus this approach is not explored for MEGA.

The result
At the end of the event reconstruction process the events are described by their main interaction process: Compton, Pair, Muon, Shower, etc. Since it is not possible to uniquely reconstruct for example Compton events to a unambiguous position on the sky — one always has the Compton cone, an arc or a more complex structure, which is associated with the measurement uncertainties accompanied by the interaction process — it is important to keep the information about the main interaction process and not only the final information about the incoming particle. In addition, a quality factor resulting from the underlying statistical approach of sequencing is associated with each event. This quality factor can be used for event selections in the later analysis.

4.1.3 Approaches for complex reconstruction tasks

For all different event types one must sort and sequence hits, and decide on the best (i.e. most likely) order. The "rules" are provided by the underlying physics: the interaction of the electrons with the layers of the tracker, the kinematics of multiple Compton events, etc. However, for pairs and high energy charged particles this process is much easier: for pairs the start point can easily be found, and e.g. muons are only straight lines in the tracker. The main work has to be done for Compton events, to which the largest part of this chapter is dedicated.

While a number of different approaches have been investigated during the course of this work, those based on a real *statistical* quality factor, like correlations, χ^2 statistics, Bayesian statistics, etc., have proven to give the best performance for the general case of a tracking Compton and pair telescope and are the only ones discussed here. For each of the two most challenging reconstruction tasks (electron tracking and Compton sequence reconstruction) two methods will be discussed: A simple analytic approach which only uses the most important aspect of the data space, and a significantly more difficult approach based on a large data space, which uses as much information as can be retained.

The simple approach in both cases follows the following principles: It should be fast, there should be no extensive preparations necessary (e.g. calculation of response matrices) and it

should be largely independent of the geometry and the detectors' energy and position resolution. For the electron tracking, this is done by correlations (Pearson, Spearman-Rank) which are based on the fact that the angular deviation as well as the energy deposit per layer increase along the track. For the Compton sequence reconstruction, a simple χ^2 test statistics is used. It exploits the redundant information available in the case of a track or of multiple Compton interactions.

The more complex approach in both cases is implemented via Bayesian statistics. Interactions of the particles in the detector are described by probability density functions in many dimensions, and, after applying Bayes' theorem, one can calculate the probability of the found sequence being correctly ordered. This approach traces much better *what really happened in the detector* and can include all imperfections of the telescope, and thus will likely give better results. However, the underlying physics is described by many parameters, leading to a multi-dimensional probability density function. Taking into account the fine binning required to describe the physics in adequate detail, in the case of MEGA this results in response matrices with 10^8 bins and more. To obtain the necessary statistics, an average factor of $\sim$100 or more *good*, i.e. fully absorbed events in the correct sequence, are needed per bin to fill the matrix. Performing the necessary simulations required roughly one CPU year of simulation time on a 2.4 GHz Xeon CPU (of course a lot of CPUs were used).

As expected, the Bayesian methods result in a slightly better performance at the cost of significantly increased CPU consumption.

In the following sections all non-trivial algorithms of the outline in Section 4.1.2 will be discussed.

4.2 Clusterizing - multiple hit recognition in double-sided strip detectors

Most of the semiconductor detectors which are currently being considered for Compton telescopes are strip detectors, with the strips running perpendicular to each other on the top and bottom side of a wafer. The position of the interaction has to be recovered by finding the intersection of those strips which registered an energy deposit. Only after this step is completed the hits have positions which are needed for event reconstruction.

In the simple case of **Compton events**, where one traversing electron deposits energy in one or more neighboring strips on both (n and p) sides of the layer, the *single* position can simply be calculated via the energy-based center of gravity on both sides:

$$\vec{x}\,(\bar{i}^n, \bar{i}^p) = \left(\frac{\sum_{i^n} i^n E_i^n}{\sum_{i^n} E_i^n}, \frac{\sum_{i^p} i^p E_i^p}{\sum_{i^p} E_i^p} \right) \tag{4.1}$$

where the sum is over all hit, neighboring strips i^x in the cluster and E_i^x is the deposited energy in strip i^x.

For **pair events** the task of clusterizing is somewhat more complex. If multiple charged particles pass through one layer, the resulting position ambiguity cannot be resolved from the knowledge of the affected strips alone. Figure 4.2 illustrates an example of a pair creation in the field of an electron, which constitutes a worst case scenario: Two electrons and one positron pass through one Silicon layer. In addition to the three true interactions, there are 6 more intersection points of affected n and p strips that correspond to also-possible interaction sites. All $3 \times 3 = 9$ possible interaction sites are marked by an $\times$ in Figure 4.2. Thus $3! = 6$ permutations have to be considered: The strips (a_n, b_n, c_n) on the n-side can be combined with the permutations (a_p, b_p, c_p), (a_p, c_p, b_p), (b_p, a_p, c_p), (b_p, c_p, a_p), (c_p, a_p, b_p) and (c_p, b_p, a_p) of p-side strips. The energies on n- and p-side for each individual hit are in best agreement for the

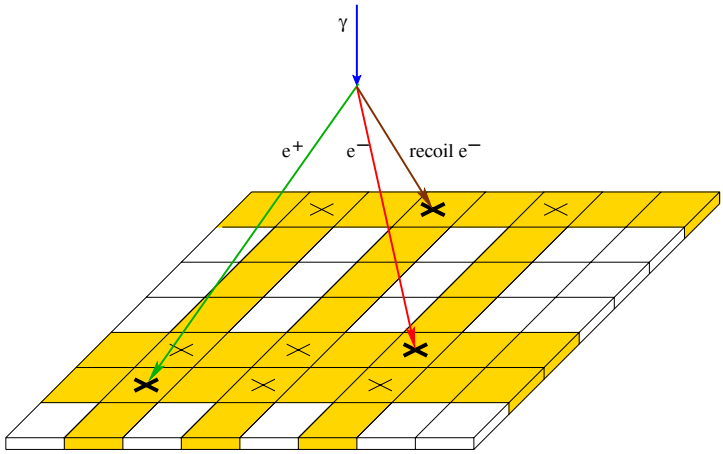

Figure 4.2: The rare pair creation on an electron produces three trackable particles, one positron and two electrons. In the simplest case, on p- as well as on n-side of the Silicon layer three strips are intersected, leading to nine possible interaction positions.

correct permutation, which can be found using a generalized form of a χ^2-statistics to compare all possible combinations:

$$Q_S = \frac{1}{N} \sum_{i,j=1}^{N} \frac{\left(E_i^n - E_j^p\right)^2}{\left(\sigma_i^n\right)^2 + \left(\sigma_j^p\right)^2} \qquad \forall \text{ permutations} \tag{4.2}$$

σ_i is the error of the energy measurement in strip i. The correct permutation is associated with the smallest quality factor Q_S, since then the E_n and E_p are in agreement within measurement errors.

For a real-life detector the algorithm has to cope with additional problems:

- In the case of the MEGA prototype a significant amount (typically 15%) of strips are dead. Thus it is likely that for one hit there will be a x-y-position but for the other only a x- or only a y-position.
- If on one side two well separated strips are triggering and on the other side only one strip, but with significantly higher energy, then two electrons passed through one strip one the second side. Those hits need also be separated by the algorithm.

The algorithm recognizes the correct interaction locations for roughly 90% of pair events recorded by the MEGA prototype. Unfortunately the expected energy deposit of an electron/positron passing through one wafer does not strongly dependent on the electron's energy and follows a fairly narrow Landau-distribution (see 2.1.2). Therefore it is likely that a similar energy within the energy resolution of n and p strips of the wafer will be deposited at the different interaction sites and thus the wrong permutation might be chosen. Nevertheless, even the 90% identification rate for the prototype is high enough to identify the topology of the pair-induced tracks. Thus the remaining wrongly identified interaction locations can be recovered during pair event reconstruction (details see 4.3.1).

From now on no distinction is made anymore between "hit" and "cluster". A "hit" might also consist of sub-hits in adjacent bars or strips, i.e. actually be a cluster.

4.3 Identifying and reconstructing pair events

Step 2 of the outline from Section 4.1.2 is the search for a vertex in the tracker to identify pairs. During gamma conversion an electron and a positron are created, the so called *pair*. A more detailed description of the pair creation process can be found in Section 2.3. Starting

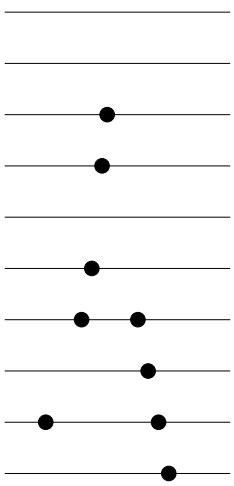

Figure 4.3: A worst case vertex which fulfills the minimum requirements: It starts with a layer with one hit, in one of the preceeding (seven) layers at least two have exactly two hits.

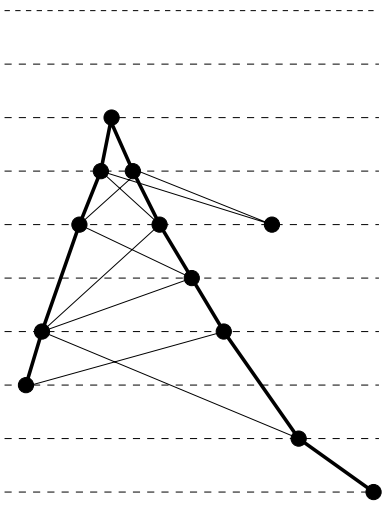

Figure 4.4: Illustration of the reconstruction of pair events. For details see text.

from their creation point, the electron and positron move in different directions. This creates a characteristic pattern in the MEGA tracker, an inverted "V": In most cases there is only one hit in the layer of the interaction, but two hits in the successive layers. In the following such a structure is called a *vertex*. It is the main characteristic for identifying pair events.

4.3.1 Method

The pair reconstruction algorithm consists of three main steps: identify the vertex, append all other hits to the electron or positron track, and finally do some post processing.

Step 1: Find the vertex
In a real-life detector, a pair must be allowed to have several missing interactions, either because electron and positron might have passed through dead material between the wafers or through dead strips. In addition, there might be several additional bremsstrahlung hits. Thus the definition of the vertex needs to be very fault-tolerant:

- One layer contains exactly one hit (the starting point)
- In the n following layers below the starting point at least two layers contain exactly two hits
- There is no hit in m layers above the starting point

An example which exactly fulfills the minimum requirements of this vertex definition can be found in Figure 4.3. The first question to ask is how easy it is to find a continuation of the vertex. In algorithmic terms, this comprises checking each consecutive layer of the tracker (top to bottom, after a first initial interaction is found) if it contains exactly two hits. The number (n) of consecutive layers of the tracker containing a total of two layers with exactly two hits each is a measure for track quality — the less layers have to be searched to find this pattern, the more reliably one can assume to be looking at a genuine vertex signature. In the case of MEGA, for a laboratory prototype in a strong beam no restriction on this parameter is necessary, while the simulated satellite performed best with n constrained to no more than four consecutive layers in the presence of background. The other parameter is the number of layers (m) above the start

point which may not contain any hits. Since the probability that two interactions happen in the whole tracker of the satellite geometry is on average 15%, this parameter is not critical and thus set to two.

Step 2: Append all hits

If a vertex is found (i.e. all 3 conditions above are fulfilled with a suitable n and m), then by definition the start position of the pair is known. Starting from this initial interaction position, the initially assumed directions of the electron and positron track are the directions to the hits in the first layer with two hits.

After the initial directions of the tracks are determined, each consecutive layer is searched for a continuation of the tracks. Whenever multiple combinations of measured hits into tracks are possible, the alternative resulting in the straightest tracks is chosen. "Straightest" here is defined as the assignment of hits to tracks, for which the following quality factor is smallest:

$$Q_D = \Delta\theta_{e,i}^2 + \Delta\theta_{p,j}^2 \tag{4.3}$$

where $\Delta\theta_{e,i}$ is the direction change of the electron track, if the track is connected to the ith hit in the next layer; similar for $\Delta\theta_{p,j}$.

The reconstruction accounts for missing hits as well as additional bremsstrahlung hits. The latter can result in more than two hits in one layer, or in a hit not consistent with either track. Whenever the energy of a hit is below the minimum energy deposit to be expected from the vertex electron or positron according to the Landau distribution, this hit is flagged as a bremsstrahlung hit and ignored in the search for the straightest vertices. After all tracks are found, the energy of all additional hits is added to the closest track's energy. This includes hits from the calorimeter. The energy of the first interaction, as well as the energy of hits after the starting point which are consistent with both tracks, is evenly distributed between the electron and positron.

Step 3: Post-processing

Although a vertex is a clear indication for a pair event, some of the tracks need post-processing. Sometimes the strip ambiguity discussed in Section 4.2 had not been correctly resolved, resulting in wrong intersection points. As consequence the tracks appear curved instead of straight (see Figure 4.5 for an example). To solve this problem, for each track a quality factor is calculated based either on a Pearson-correlation or on Bayesian statistics. The quality factors describes how good the tracks conforms with the expected physics. They are discussed in more detail in the context of Compton electron tracking in Sections 4.4.2.2 and 4.4.2.3. For the layer under investigation (3 in Figure 4.5), they are calculated without the hits of this layer but layer 2 and 4 directly connected — once in the given order, and once when the tracks below this layer are exchanged. If the quality factors for the exchanged tracks is better, this new direction is chosen as the correct one. The hit positions in layer 3 are ignored in this case and their energies are added in equal parts to the two tracks.

As a final step, one could in principle attempt to correct the measured energy by determining the incident photon's energy from the vertex opening angle as well as the change of the energy deposit and scatter angle along the tracks. The feasibility of such approaches has been demonstrated by e.g. *Fichtel et al.* (1975) for spark-chamber systems and higher-energy pairs. The same approach should be applicable to MEGA.

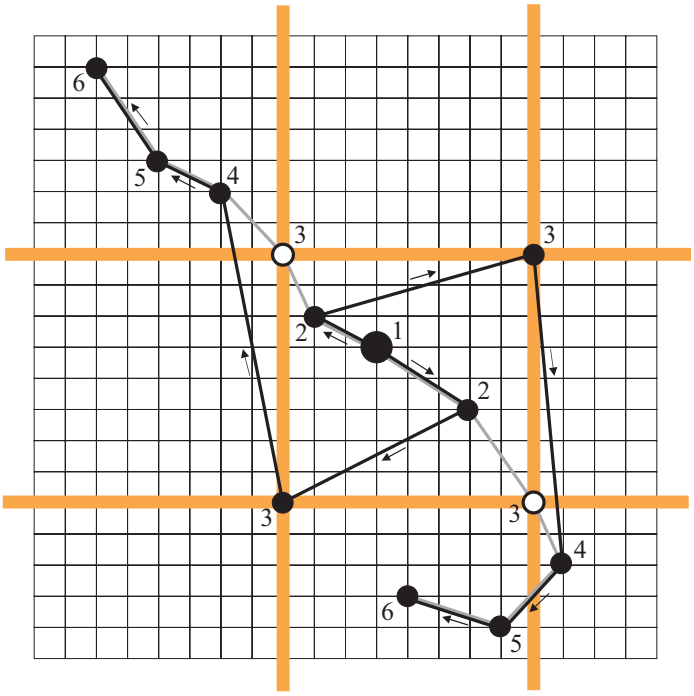

Figure 4.5: Illustration of the consequences of wrong interaction mapping during the clusterizing process. The figure shows a top view of the track, the numbers indicate the layer of interaction. In layer 3 the interaction mapping (see Section 4.2) is wrong. The white circles in layer 3 represent the correct interaction positions, the black ones are the wrongly mapped ones. As consequence the path of electrons/positrons is wrong: the black path is the wrongly reconstructed path, the grey path is the correct one. This problem is resolved during post-processing (details see text).

4.3.2 Performance

Figure 4.6 illustrates the direction-reconstruction performance of the pair tracking algorithm for 20 MeV photons (on-axis incidence, MEGA Satellite geometry). Considering only events which fulfill the requirements for an initial identification as pair event set forth in the previous section, the distribution of the deviation of the reconstructed from the true direction of incidence is shown.

Overall, it is evident that the vast majority of events is reconstructed correctly to within significantly better than 10°. 68% of directions are reconstructed to better than 5.75° which is mainly limited by Molière scattering. At small deviation angles, a smaller absolute number of events per angular bin are recorded. This is a purely geometrical effect — if counts/sr were shown instead, the distribution would continue to rise monotone towards smaller deviation angles.

For most events that appear at large direction deviations, the core of the pair recognition algorithm still worked. Multiple effects contribute to such large deviations; for the most part these could only be overcome in a different instrument geometry:

- If the energy of electron and/or positron are not measured correctly (due mostly to leakage from the instrument, sometimes due to wrong reconstruction of the later electron/positron path), applying Equation 2.28 will yield a wrong origin direction. This is especially pronounced for large opening angles. A larger instrument with thicker calorimeters would perform better in this respect.

- Strong Molière scattering within the layer of pair creation renders an accurate measurement of the electron's direction impossible. Thinner layers in the tracker could significantly reduce this effect.

- Especially for close tracks of electron and positron, the limited spatial resolution of the tracker limits the accuracy to which the incident direction can be reconstructed. Clusterization potentially compounds this problem — but the benefits of this approach far outweigh the disadvantage that comes to light in this particular case. A much finer strip pitch of the tracker would contribute to a better overall angular resolution especially for higher-energy pair events.

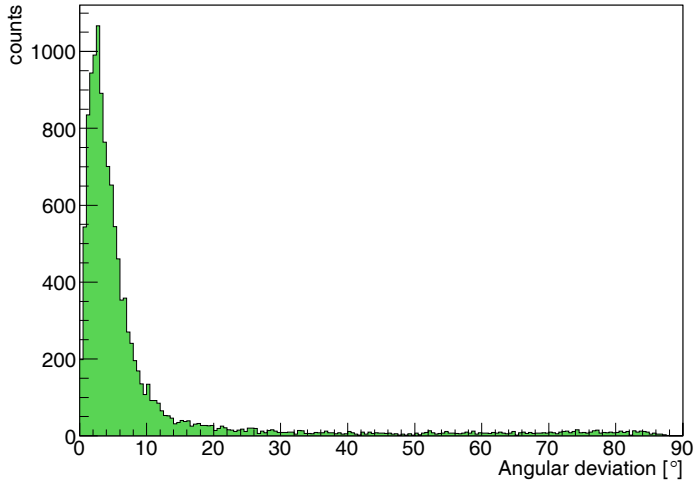

Figure 4.6: Angular deviation distribution of simulated, on-axis 20 MeV photons for the satellite geometry. While the majority of the events is correctly reconstructed into the peak (68% containment is 5.75°), a small background pedestal is visible. See the text for an explanation.

- If an initial Compton scattering occurs in passive material and the scattered photon then pair-produces in the tracker, this event cannot possibly be distinguished from an event consisting only of pair-production in the tracker. Further reduction of passive materials especially in the field-of-view of the tracker is the only method to reduce this component. Since the Compton cross-sections at higher energies are small such events do not occur frequently.

- The current algorithm does not allow for the possibility of a Compton interaction in the tracker followed by a pair-production event also in the tracker. Once the pair vertex is recognized, the event is treated as a pair-only interaction. However, again, such events do not occur frequently.

- Of course there are also some instances where the algorithm cannot correctly identify the vertex, e.g. because additional bremsstrahlung hits lie close enough to the vertex to cause confusion.

A first step is to assess the algorithm's capability to correctly recognize true pair events as such. Figure 4.8 shows the ratio of pairs found by the event reconstruction (i.e. which fulfilled the initial vertex criteria discussed in the previous section) to the number of pair interactions which actually happened in the tracker as known from simulation. While this ratio is 98% at 100 MeV, it falls to 79% at 20 MeV and 73% at 10 MeV. It should be pointed out that this number represents only the fraction of found pair events and is not a measure for the correct reconstruction of those events. Obviously, finding pair vertices is a simpler task at higher photon energies where the electron/positron tracks are guaranteed to traverse many layers. Towards lower photon energies, difficulties arise: Lower-energy electrons/positrons are more affected by Molière scattering, resulting in some case even in a particle bouncing back and forth between two layers. This is aggravated by the higher influence of the uneven distribution of the photon's energy between electron and positron on the track length and the larger opening angles which result in a track traversing less layers.

One approach to assess the quality of the achieved pair reconstruction is to measure the fraction of events contained in the pedestal below the peak corresponding to correctly reconstructed events from Figure 4.6. Fitting a constant to the distribution at angles greater than 30° and extending this over the whole span of angular deviations from 0° to 90°, one obtains a measure of the relative importance of this pedestal as a function of energy. The results are shown in Figure 4.8. The fraction of all events contained in the pedestal decreases from 16.8% at 10 MeV

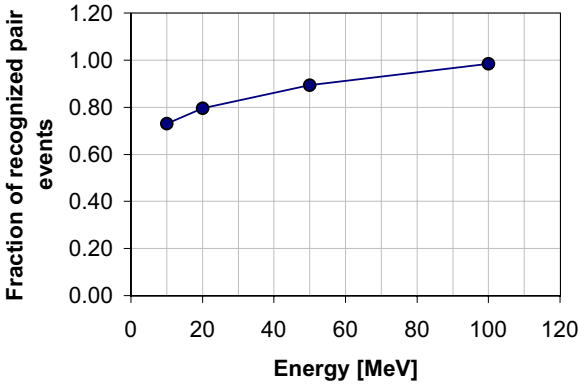

Figure 4.7: Fraction of pair events recognized as such. The true amount of pair creations in the tracker is known from simulations. The higher the energy, the easier the vertex signature can be found in the tracker. This number only describes how many pair events were recognized; no conclusions can be drawn about the accuracy of their reconstruction.

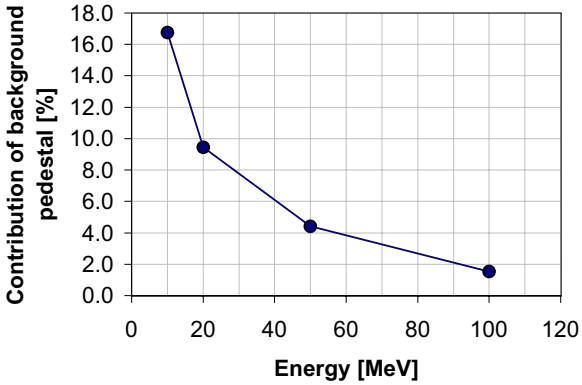

Figure 4.8: Contribution of the background pedestal from the angular deviation distribution (see Figure 4.6) the total number of identified pair events. The higher the energy of the incident photon the simpler is the reconstruction, the less likely large angular deviations appear. See the text for an explanation of all the reasons.

to 9.5% at 20 MeV and 1.5% at 100 MeV.

Besides the argumentation above, at lower energies the number of wrongly reconstructed events increases due to Compton tracks which are identified as vertices, when their tracks have sharp reverse points, i.e. switch from moving bottom-top to top-bottom. However, for on-axis incidence this happens mostly in cases, when the first interaction was not in the tracker, because Compton kinematics only allows for a maximum recoil electron angle of 90° (Equation 2.8). Finally most of the wrong reconstructions have larger opening angles. Only allowing an opening angle of 45° of 10 MeV pairs reduces the pedestal by a factor of 2 while reducing the overall number of detected pairs by only 22%. This will be one of the key event selections for background rejections for the final satellite simulation in Chapter 10.

4.4 Compton electron tracking

For the electron and positron tracks making up a pair event, the direction of motion is well defined by the vertex. For Compton electrons, finding the direction of motion is a much more difficult process which has to use the complete kinematics of the track.

4.4.1 The data space of electron tracking

An electron deposits its energy mainly via ionization and bremsstrahlung, and the deviation of its path through matter from a straight line is due to Molière scattering (see Chapter 2.1).

The underlying physics of the interaction process of electrons with matter determines the properties of a real electron track. They can be used to determine the direction of motion of the electron for a given measured track. These general properties of an electron track are:

1. The angular deviation $\Delta\alpha$ from layer to layer of the track increases according to Molière scattering.

2. The energy deposit E_{dep} in the wafer of the first interaction is lower than the average energy deposit since the initial Compton interaction takes place somewhere in the tracks' initial Si-layer and thus the electron only traverses a fraction that layer.

3. The energy deposit increases at the end of the path of the electron, but strongly varies, since it is Landau distributed (see Figure 2.4).

The following distinguishes between first, last, and so called central interaction points, which lie between the first and the last hit. In addition two-site tracks are treated separately. A suitable data space for describing the physical process in one central track point has five dimensions and is illustrated in Figure 4.9:

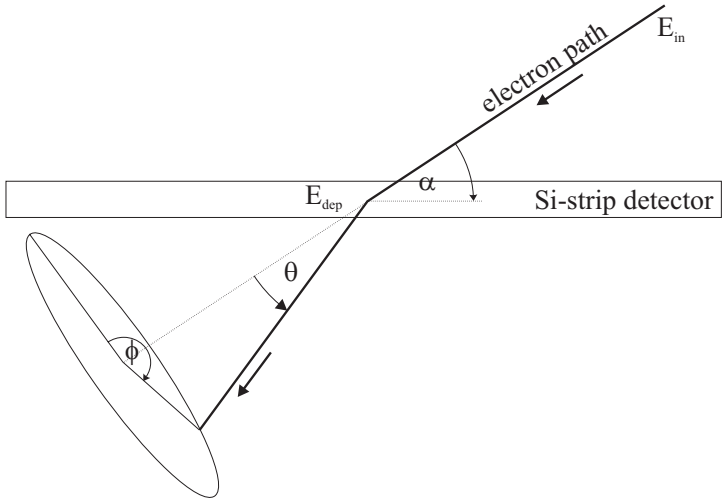

Figure 4.9: Five parameters span the data space $\mathcal{D}_{central}$ describing a central electron track point: the initial state is described by the total electron energy E_{in} and the incidence angle α on the Silicon, the final state is described by the deposited energy E_{dep} and the change of the direction of the electron relative to the original direction θ and ϕ.

The parameters are given by the initial and the final state of the electron. The initial state is described by the energy E_{in} and the direction of the photon. The only important component of this direction is the electron's incidence angle α on the Silicon layer. Instead of using the final energy and direction of the electron, the same information is better encoded in the energy deposit of the electron E_{dep} (Landau distributed) and the change of the electron's direction (expressed in terms of angles θ and ϕ).

Figure 4.10 shows two example slices of this five-dimensional data space $\mathcal{D}_{central}$, which has been filled with Geant3 simulations for the tracker of the MEGA satellite geometry. The tracker has been isotropically illuminated with photons uniformly distributed between 0 and 10 MeV. The left picture shows the deposited energy per layer as function of the incident energy of the electron before it enters the Si layer. The other dimensions are fixed to the bins around: $\alpha = 30°$, $\theta = 0°$, $\phi = 0°$, which corresponds to an incidence angle of 30 degrees and (almost) no change of flight direction. Under these special circumstances, the deposited energy only slightly increases with lower energy, but roughly conforms to a Landau-distribution. At lower energies the number of events which fulfill these criteria diminishes, because there are simply no more electrons which generate tracks of a length of three or more. The image on the right shows the change of flight direction as a function of the incident energy. Again the other dimensions stay fixed: The incidence angle at $\alpha = 30°$, the deposited energy around $E_{dep} = 200\ keV$ and the azimuthal outgoing angle at $\phi = 0°$. One clearly sees that with lower initial energy the average scatter angle increases — in accordance with Molière theory.

In addition to this data space, three others exist. The data space describing the start of the electron track $\mathcal{D}_{start}$ has only three dimensions: The initial energy E_i, the energy deposit E_{dep} and the outgoing angle α_{out}. The data space which describes the end point of the electron track $\mathcal{D}_{stop}$ is spanned by two parameters: the final energy deposit E_{dep} and the incident angle α.

For two-site tracks, i.e. tracks which consists of only two hits in adjacent layers, a special data space $\mathcal{D}_{dual}$ exists. It is spanned by the first energy deposit E_1, the second energy deposit E_2 and the track angle α between the hits.

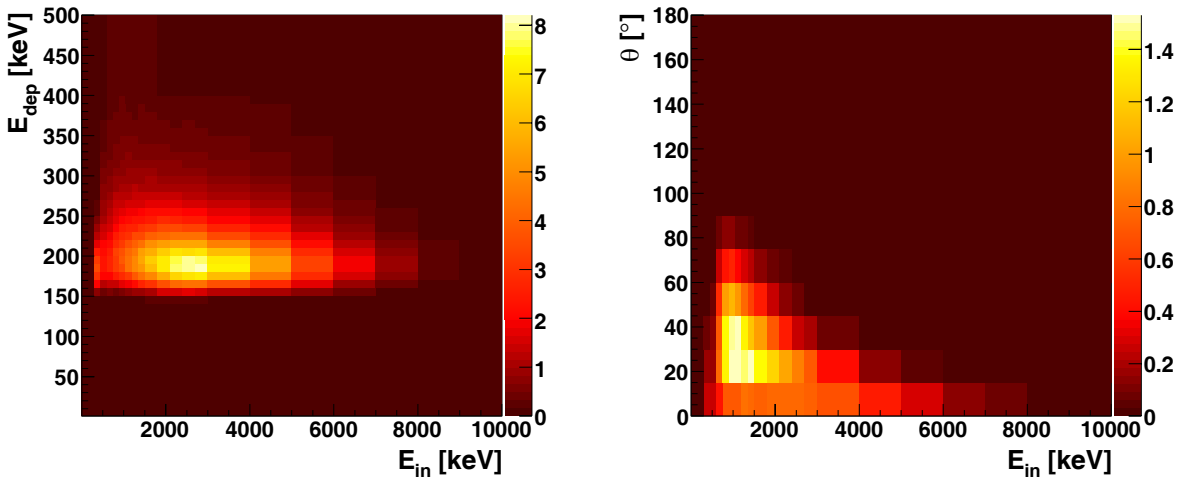

Figure 4.10: The above pictures show two-dimensional slices of the five-dimensional $\mathcal{D}_{central}$ data space of electron tracking. The left picture shows the deposited energy per layer as function of the incident energy of the electron before it enters the Si layer; the shape follows a Landau distribution. The right image shows the change of flight direction as a function of the incident energy. As expected, at high energies Molière scattering is significantly less pronounced than at lower energies. The data space has been generated by Geant3 simulations with the MEGA satellite tracker.

In section 4.4.2.3 an instrument response formulated in terms of those data spaces is used to determine the direction of motion of tracks via Bayesian electron tracking.

4.4.2 Identification of Compton electron tracks

The greatest challenge for electron tracking is the tracking of Compton electrons at low energies. In this regime, all tracks are short and are heavily influenced by Molière scattering. As a consequence, a lot of U-turns can be observed, and only a few tracks appear straight. This problematic domain ranges up to *electron* energies of 1–2 MeV. At higher electron energies, the tracks get longer and at least the start of the tracks is fairly straight. Thus, the direction can be found much more easily.

Compton electron tracking is a two-step process: The first step is to figure out all possible paths the electron might have taken (see 4.4.2.1), and in a second step the most probable combination and its direction have to be found (see 4.4.2.2 and 4.4.2.3).

4.4.2.1 Finding all possible track combinations

In order to develop an algorithm that is able to successfully operate on data from a complex real-life detector system, one must always keep in mind how various malfunctions and imperfections in the tracker influence the reconstruction. The MEGA prototype in particular has a significant amount of non-working strips, thus the track might have missing hits. A second problem are high thresholds leading to missing energy deposits. This is frequently the case at the start of the track, when the electron has passed only a small fraction of the layer. High thresholds are also problematic in the case of hits in one layer whose energy deposit is distributed over several strips, with resulting low deposits in *individual* strips. Finally, additional hits are another source of problems. They might originate from noisy channels, from bremsstrahlung emitted by the electron, or correspond to nearby Compton interactions without causal connection to the track under investigation. Figure 4.11 illustrates these issues.

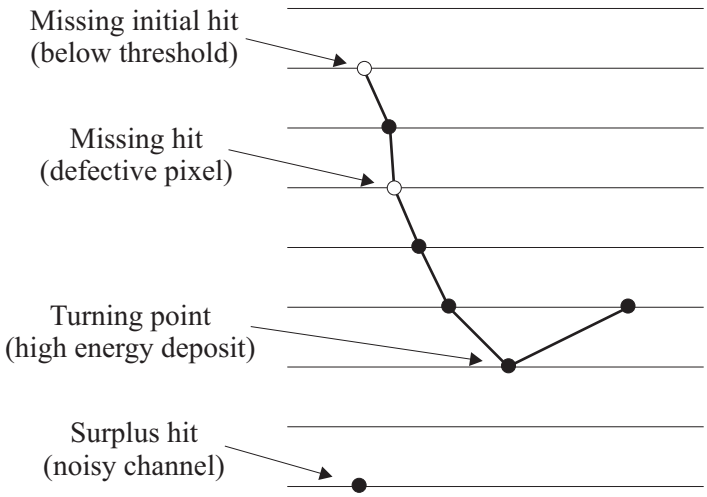

Figure 4.11: Summary of problems arising during electron tracking: Besides the challenges from the complex physics involved (especially Molière scattering), missing hits due to high energy thresholds and defective strips as well as additional hits (due to bremsstrahlung, noisy channels, or nearby additional Compton interactions) raise the demands on the tracking algorithm.

The following paragraphs describe the method used to search for all possible tracks that could conceivably be contained in a given event's recorded data. In a first step, all non-ambiguous track segments are identified. In the second step, an analysis of all ambiguities follows.

A track segment is called non-ambiguous when there is only one reasonable explanation for the observed hit distribution. This is the case for straight tracks, where only one hit per layer is present. Since the algorithm has to cope with non-working strips/layers, it is acceptable if every second layer is without a hit. Such single hits in (almost) consecutive layers are now assumed to belong together, i.e. to form a track segment. Such a segment is illustrated in Figure 4.12 a).

After this initial step, layers of the tracker remain which measured several hits in close proximity. No obvious solution for the corresponding track sequence exists; all possible combinations have to be investigated. For the example in Figure 4.12, the investigated possibilities are given in part b). They include U-turn tracks as well as additional hits.

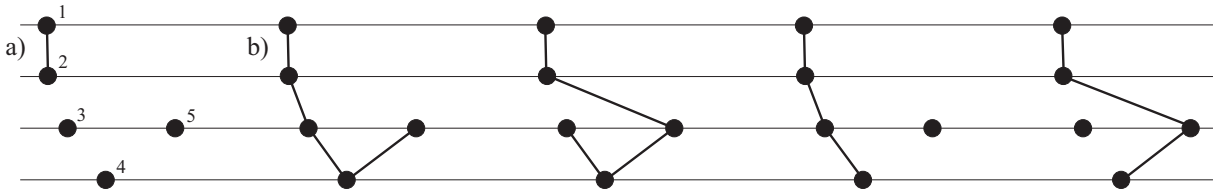

Figure 4.12: Low energy Compton tracking by example: The classical U-turn track. Step (a) is to find non-ambiguous track sequences. Non-ambiguous means this is the only reasonable path the electron could have taken, usually because one has nothing but one hit in two or more consecutive layers. In our example this is the case for the path $1 \rightarrow 2$. For the remaining *track elements* after step (a) several paths are thinkable, in our example $2 \rightarrow 3$ or $2 \rightarrow 5$. Afterwards all possible different paths are qualified. The event sequence which best matches the expected physics is chosen as the correct one.

The described algorithm is an exhaustive search — in case of ambiguous combinations every possibility is investigated. At low energies, this is the only way to find the most likely correct sequence. In addition, scatter angles as well as energy deposits vary so widely that only by incorporating all available track information an estimate for the correct sequence can be given.

This is different at higher energies where neither the angular change nor the energy deposits exhibit large variations and thus a subsequent hit can be reliably predicted from the previous

ones. The algorithm used in this case is basically the same as that for pair tracking. If the track is ambiguous, i.e. contains more than one hit per layer, the hit which has the smallest angular deviation from the direction of the unambiguous track segment is chosen. (In the example illustrated in Figure 4.12 a), this algorithm immediately prefers $2 \rightarrow 3$ to $2 \rightarrow 5$.)

For low-energy tracks now a host of possible sequences with two possible directions each (up or down) must be evaluated; in the case of high-energy tracks mostly one sequence with its two possible directions must be analyzed. In both cases all allowed sequence-direction combinations for a given event are now evaluated to find the correct sequence and its direction of motion. Two approaches are implemented: a fast, detector-independent figure-of-merits approach and a more sophisticated method based on Bayesian statistics called Bayesian Electron Tracking (BET).

4.4.2.2 Figures-of-merit tracking

Figures-of-merit tracking is a fast and simple approach to find the correct track sequence (including direction of motion) by calculating a set of quality factors for the track. Those quality factors are defined such that the smaller their value, the better the track complies with the physics of a correct track.

The most relevant indicators are the increase of the deposited energy E_{dep} at the end of the track and the increase of the change of the electron direction $\Delta\alpha$ along the track. One approach, which has been optimized for thinner layers, was introduced by *O'Neill* (1996). It is based on comparing measurements with their theoretically expected values. However, initial test have shown that this method cannot cope with U-turns very well and is thus not followed here. Another approach has been proposed by *Nefzger* (2000) and *Schopper* (2001), which suggests to use the covariances for E_{dep} and $\Delta\alpha$ to determine the direction of motion. In general, a non-zero covariance shows a relationship between two variables. In our case these pairs of related variables are (1) the deposited energy and the hit ID along the track and (2) the change in the scatter angle along the track and, again, the hit ID along the track.

For the energy increase the covariance is given by:

$$cov\left(E_{dep}, i\right) = \overline{E_{dep} \cdot i} - \overline{E_{dep}} \cdot \overline{i} \tag{4.4}$$

and for the angle by:

$$cov\left(\Delta\alpha, i\right) = \overline{\Delta\alpha \cdot i} - \overline{\Delta\alpha} \cdot \overline{i} \tag{4.5}$$

The bars indicate averages and the i is the hit number along the track.

A positive covariance means that an increase in the hit number is associated with an increase of the scatter angle or energy. For the correct sequence, we expect both $cov\left(E_{dep}, i\right)$ and $cov\left(\Delta\alpha, i\right)$ to be positive.

The covariance itself has a physical dimension which arises from the product of their variables, in our case keV or rad. To be able to later combine the two covariances into one figure of merit, the Pearson correlation (e.g. *Press*, 1992) is used instead of the covariance itself in this work. The Pearson correlation is defined as the covariance divided by the variances of the involved variables and can by definition only take values between -1 and $+1$.

$$c_{Pearson}\left(E_{dep}, i\right) = \frac{\overline{E_{dep} \cdot i} - \overline{E_{dep}} \cdot \overline{i}}{\sqrt{\overline{E_{dep}^2} - \overline{E_{dep}}^2}\sqrt{\overline{i^2} - \overline{i}^2}} \tag{4.6}$$

$$c_{Pearson}\left(\Delta\alpha, i\right) = \frac{\overline{\Delta\alpha \cdot i} - \overline{\Delta\alpha} \cdot \overline{i}}{\sqrt{\overline{\Delta\alpha^2} - \overline{\Delta\alpha}^2}\sqrt{\overline{i^2} - \overline{i}^2}} \tag{4.7}$$

Obviously $c_{Pearson}\left(\Delta\alpha, i\right)$ can only be calculated if the track consists of at least three hits. The single quality factor finally used to pick the most likely electron path is given by:

$$Q_{E,Pearson} = 1 - \frac{2 + c_{Pearson}\left(E_{dep}, i\right) + c_{Pearson}\left(\Delta\alpha, i\right)}{4} \tag{4.8}$$

The quality factor is normalized such that good tracks have a $Q_{E,Pearson}$ close to zero, bad tracks values close to one.

The Pearson correlation has one disadvantage: it assumes linear correlations between the two variables under consideration. This assumption of course does not hold for Compton electron tracks for either E_{dep} and i or $\Delta\alpha$ and i. The more general Spearman Rank correlation (e.g. *Press*, 1992) only assumes a monotone association between the variables and thus is more appropriate for the problem at hand. The Spearman Rank correlation coefficient is defined as:

$$c_{Rank} = 1 - \frac{6D}{N^3 - N} \tag{4.9}$$

Here N is the number of elements for which the difference can be calculated, i.e. for the correlation coefficient by energy deposit N is one smaller than the total number of track interactions, and for the angular change it is two smaller. D is the sum of the squared difference of the ranks either of E_{dep} and i or of $\Delta\alpha$ and i:

$$D\left(E_{dep}, i\right) = \sum_{n=1}^{N} \left(\mathrm{Rank}\left(E_{dep,n}\right) - \mathrm{Rank}\left(i_n\right)\right)^2 \tag{4.10}$$

Again the correlation coefficient c_{Rank} is close to one when the assumption of monotone association is true. Similar to the Pearson case, the sequence quality factor can be defined as:

$$Q_{E,Rank} = 1 - \frac{2 + c_{Rank}\left(E_{dep}, i\right) + c_{Rank}\left(\Delta\alpha, i\right)}{4} \tag{4.11}$$

A discussion of the performance of both approaches can be found in section 4.4.2.4.

4.4.2.3 Bayesian electron tracking

The previous approach has been optimized to be fast and simple. As a consequence, it completely ignores the complex, non-linear response of the detector and it does not use its full dimensionality. In addition, it does not result in a real probability, only in a figure-of-merit.

To assign each track a quality factor that *directly* reflects its probability of being correctly reconstructed, the probability $p\left(\mathcal{C}|\vec{m}\right)$ needs to be determined. This is the probability that the given sequence is correct $\mathcal{C}$ given the ordered measurements $\vec{m}$. Unfortunately, this value is not accessible via standard statistical methods — only $p\left(\vec{m}|\mathcal{C}\right)$, the probability to get the measurement $\vec{m}$ given that the sequence is correct, is accessible: This probability can easily be determined by simulation — or, given enough statistics, from instrument calibration measurements.

Bayes' theorem (*Press*, 1992) shows a way out of this dilemma: it allows to determine the needed $p\left(\mathcal{C}|\vec{m}\right)$ from $p\left(\vec{m}|\mathcal{C}\right)$ and additional prior information such as $p\left(\mathcal{C}\right)$, the probability to get a correct sequence, and $p\left(\vec{m}\right)$, the probability to measure $\vec{m}$. This information can also be obtained from calibration or simulation. This approach overcomes both fundamental problems of the correlation-based methods discussed in the last chapter: the actual probability of correct reconstruction is known, and it is possible to incorporate the full non-linear response of electron tracking through the probability $p\left(\vec{m}|\mathcal{C}\right)$.

For the probability $p\left(\mathcal{C}|\vec{m}\right)$ Bayes' theorem gives:

$$p\left(\mathcal{C}|\vec{m}\right) = \frac{p\left(\mathcal{C}\right) p\left(\vec{m}|\mathcal{C}\right)}{p\left(\vec{m}\right)} \tag{4.12}$$

In the case of several independent measurement points $\vec{m}_i$, this modifies to:

$$p\left(\mathcal{C}|\cup_i \vec{m}_i\right) = \frac{p\left(\mathcal{C}\right) p\left(\cup_i \vec{m}_i|\mathcal{C}\right)}{p\left(\cup_i \vec{m}_i\right)} = \frac{p\left(\mathcal{C}\right) \prod_i p\left(\vec{m}_i|\mathcal{C}\right)}{p\left(\cup_i \vec{m}_i\right)} \tag{4.13}$$

Since the denominator is not easily accessible, the following ratio

$$R = \frac{p\left(\mathcal{C}|\cup_i \vec{m}_i\right)}{p\left(\overline{\mathcal{C}}|\cup_i \vec{m}_i\right)} = \frac{p\left(\mathcal{C}\right) \prod_i p\left(\vec{m}_i|\mathcal{C}\right)}{p\left(\overline{\mathcal{C}}\right) \prod_i p\left(\vec{m}_i|\overline{\mathcal{C}}\right)} \tag{4.14}$$

plus the knowledge $p\left(\mathcal{C}|\cup_i \vec{m}_i\right) + p\left(\overline{\mathcal{C}}|\cup_i \vec{m}_i\right) = 1$ are used to obtain

$$p\left(\mathcal{C}|\cup_i \vec{m}_i\right) = \frac{R}{R+1} \tag{4.15}$$

Each measurement "point" $\vec{m}$ contains all relevant information about the interaction, expressed in terms of the best-suited parameters discussed in Section 4.4.1 above. For instance, for a central point of a track, total track energy E_{in}, deposited energy E_{dep}, incidence direction α_{in} of the track on the layer, and directional changes ϑ_{out} and φ_{out} make up the "point" $\vec{m}$ in the corresponding data space $\mathcal{D}_{central}$.

Based on Equation 4.15 a quality factor of a given track sequence can be determined:

$$Q_{E,Bayes} = 1 - p\left(\mathcal{C}|\cup_i \vec{m}_i\right) \tag{4.16}$$

To calculate this factor for a given possible sequence of measured track interactions, the probabilities $p\left(\vec{m}|\mathcal{C}\right)$, $p\left(\mathcal{C}\right)$ and $p\left(\vec{m}\right)$ have to be known. They are determined in advance by analyzing extensive simulations, storing each retrieved $\vec{m}_i$ element in one of two data spaces: The $\vec{m}_i$ elements are put into the so-called "correct" data space if they describe a directionally correct track segment, for which the sum of the present and subsequent energy deposits E_{dep} deviates from the known incident electron energy by less than 10% ("completely absorbed"). If the track segment under consideration is wrongly reconstructed or incompletely absorbed ($E_{dep} \geq 10\%$), the corresponding $\vec{m}_i$ go into the so-called "false" data space.

Of course it is important to fill the data space exactly the same way it is later accessed during event reconstruction. The first step is to do the track combination search described in section 4.4.2.1. Next, all single hits of each such track combination are checked to determine if they are part of a correct (sub-)sequence; the truth being known for this simulated data set. It is extremely important to completely analyze the given track combinations for correct subsequences: Not the correctness of the *complete* track is important for an entry in the correct data space, but the correctness of an individual sub-sequence. Examples are tracks which have an escaping bremsstrahlung photon at the beginning, but are correct after the emission point of the photon. All measurement points after the escape go into the correct matrix, the beginning, however, goes to the bad matrix due to missing energy. Another example is a wrongly reconstructed U-turn track: the start can be correct even if the U-turn at the end is wrongly reconstructed. The correct parts at the beginning are entered in the good matrix, the false ones into the other one.

The "correct" and "false" data spaces each contain the four electron-tracking data spaces $\mathcal{D}_i$ discussed in Section 4.4.1: one for dual hit tracks, one for the start point of long tracks, one for the central measurement points and one for the stop point of long tracks. Each $\vec{m}_i$ is of course expressed in the variables spanning the applicable data space. Additionally, the total number of correct or wrong sequences is stored to get $p\left(\mathcal{C}\right)$ and $p\left(\overline{\mathcal{C}}\right)$.

Once the above data spaces are populated, $p\left(\vec{m}_i|\mathcal{C}\right)$ can be determined for each $\vec{m}_i$ of any given $\vec{m}$ describing one possible ordering of a set of hits into a track. $p\left(\vec{m}_i|\mathcal{C}\right)$, the probability that $\vec{m}_i$ is measured when the sequence part is reconstructed correctly, can be calculated as

the number of entries for $\vec{m}_i$ in the "correct" data space ($N^{\mathcal{D}_i}_{m_i,\,correct}$) divided by the number of correct sequences in the data space ($N^{\mathcal{D}_i}_{all\,correct}$) where the data space $\mathcal{D}_i$ is of course the appropriate one for sequence part i (dual, initial, central or final) :

$$p\left(\vec{m}_i|\mathcal{C}\right) = \frac{N^{\mathcal{D}_i}_{m_i,\,correct}}{N^{\mathcal{D}_i}_{all\,correct}} \tag{4.17}$$

In order to get the correct normalization, all probabilities are determined in dependence of the input parameters (for instance for central interactions "all correct" means all correctly reconstructed elements with E_{in} and α as start parameters in the central data space). The ratio R is then given by:

$$R \approx \frac{N_{correct}}{N_{false}} \prod_{i=1}^{I} \frac{N^{\mathcal{D}_i}_{m_i,\,correct} \cdot N^{\mathcal{D}_i}_{all\,false}}{N^{\mathcal{D}_i}_{m_i,\,false} \cdot N^{\mathcal{D}_i}_{all\,correct}} \tag{4.18}$$

Since neither binning nor statistics are infinite, of course the ratio R is only an approximation. $N_{correct}$ is the total number of correct tracks found in the "training" data. $N^{\mathcal{D}_i}_{correct,i}$ is the number of entries in the cell of data space $\mathcal{D}_i$ which corresponds to the measurement point m_i, with m_i's parameters describing the interaction at measurement point i. $N^{\mathcal{D}_i}_{correct}$ is the total number of entries in the data space $\mathcal{D}_i$ relevant to measurement point i (start, central, stop, or dual). The variables for *false* are defined correspondingly.

4.4.2.4 Performance of the Compton electron tracking algorithms

This section is dedicated to analyzing the performance of the Compton electron tracking algorithm alone. It ignores the fact that such tracks are part of a Compton sequence, and that the kinematics of Compton scattering enables further improvement of the overall performance, especially through rejection of incorrectly reconstructed tracks.

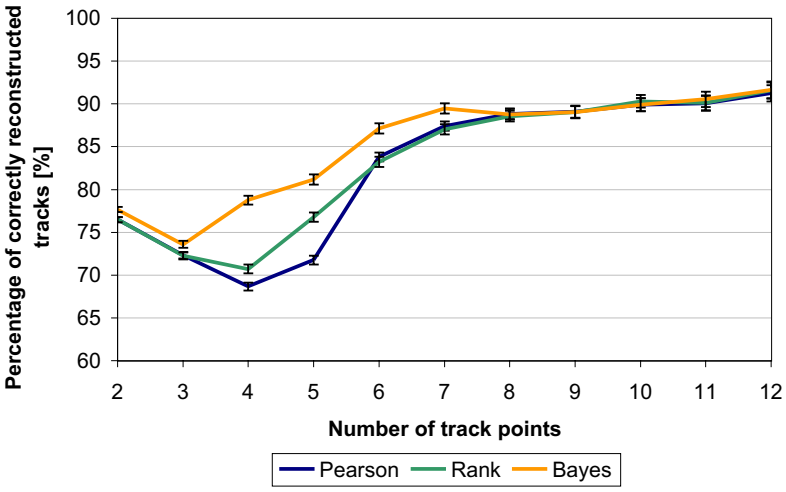

Figure 4.13: Comparison of the efficiency of the approaches based on correlations (Pearson, Rank) and Bayesian statistics. The underlying simulation was performed with the MEGA satellite geometry. It contains tracks from 100,000 triggered photons in the energy range from 0.5 to 5 MeV (flat spectrum), originating isotropically from the upper hemisphere. No event selections have been applied. While for longer tracks all approaches have the same performance, for shorter tracks the Bayesian approach, which uses the complete data space, performs best.

Figure 4.13 shows a comparison between the two correlation approaches (Pearson and Rank) from Section 4.4.2.2 as well as the Bayesian approach from Section 4.4.2.3. The fraction of correctly reconstructed tracks is shown as a function of the number of hits in the track. The analyzed data are from simulations of the MEGA satellite geometry; they contain tracks from 100,000 triggered photons in the energy range from 0.5 to 5 MeV (flat spectrum), originating isotropically from the upper hemisphere. No event selections have been applied to the data.

For tracks with eight or more interactions the performance of the three algorithms is roughly the same. It is limited by missing first interactions (below the threshold of the detector), escaping

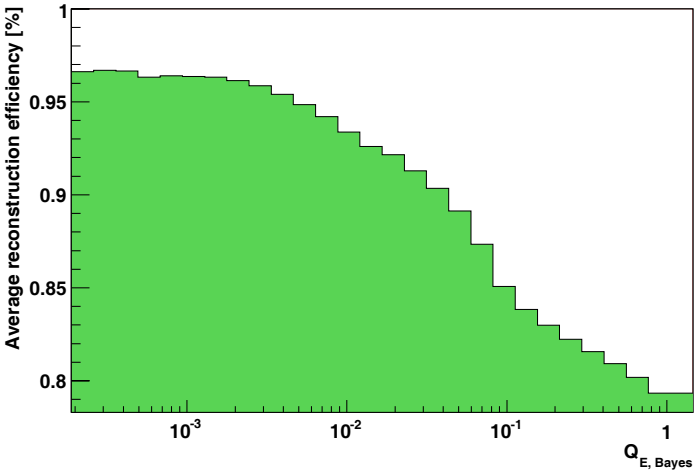

Figure 4.14: Average reconstruction efficiency up to a certain quality factor for Bayesian reconstruction: Using only events with a good (=low) quality factor allows to select high-quality events.

electrons at the end of the track (most directional information is encoded at the end of the track) and nearby additional hits close to the start of the track.

For shorter tracks (2-7), the Bayesian approach outperforms the correlation approaches, mainly because it uses the complete multi-dimensional track information and not only projections, as the correlation approaches do. For two-site tracks the performance is limited by the small amount of information which is available (two energy measurements and one angle). Between three and five interactions the performance is limited by tracks which reverse their direction, so-called "U-turn tracks". In the extreme case the electron bounces back and forth between two layers ("ping-pong tracks"). Those effects preferentially happen for low electron energies with pronounced Molière scattering. Due to the large scatter angles and the diversity of possible combinations, U-turn and ping-pong tracks are very hard to reconstruct (performance 50-60%). Since such tracks can be easily identified, they could be rejected during the analysis. But this path is not chosen, since more powerful tools exist to reject wrongly reconstructed tracks. The first one is the quality factor of the event, especially that of the Bayesian approach. One can select tracks according to their $Q_{E,Bayes}$ factor. The smaller the value, the higher the probability that the track is reconstructed correctly and completely absorbed.

Figure 4.14 shows the possible improvement in reconstruction efficiency if one selects only events with a small $Q_{E,Bayes}$ factor. The average reconstruction efficiency for events with a quality factor up to the given value is shown: $\sum_0^{Q_{E,Bayes}} N_{correct}(x) / \sum_0^x (N_{correct}(x) + N_{false}(x))$. If for example a specific data-analysis task requires a track reconstruction efficiency of more than 90%, then events with a $Q_{E,Bayes}$ smaller than ~ 0.04 could be selected. In the later analysis it will turn out that selecting only events with a track quality factor $Q_{E,Bayes} < 0.07$ will optimize the sensitivity of the MEGA satellite telescope; this cut rejects the 25% worst tracks.

As mentioned above, the reconstruction of the whole Compton sequence will provide an additional tool for rejecting wrongly reconstructed events: The redundant total scatter angle ϑ can be calculated via geometry and via kinematics. How a comparison of these two angles can be exploited will be explained in Section 4.5.1.2.

Of course, the above results are not independent of the characteristics of the tracking detector under investigation. While the general trend of longer tracks being equally well reconstructed using simpler algorithms should hold, the separation point of "longer" and "shorter" tracks as well as the reconstruction efficiency itself will depend on the tracker's properties.

For the analysis of the measurements of the MEGA satellite, the Bayesian approach is used, since it has a significantly better performance for low energy tracks. However, due to CPU-time limitations it was not possible to fill the necessary data space with simulation for the prototype.

4.4.2.5 Can electron tracking be improved further?

Especially the Bayes algorithm has already reached a high level of performance. Increasing the reconstruction efficiency by another few percent would certainly require exponentially more work than has been invested up to this point. Most failures are due to extreme measurements or unfortunate geometries (e.g. large electron incidence angles, tracks with U-turns, high energy deposits corresponding to the tails of the Landau distribution, etc.) and detector imperfections (escaping electrons, passive material, non-zero thresholds, etc.).

The most problematic category of events for the current algorithm are small U-turn tracks, i.e. tracks with have large initial incidence angles and move sideways through their "birth-layer" and return to their original layer. A possibility to improve their handling would be to give them their own data space in the Bayesian approach. Currently the central data space of Bayesian electron tracking is mainly filled with long straight tracks, where U-turns are unusual and thus have a lower probability. For four-hit tracks one could think of three data spaces: one where four layers are hit (straight tracks), a second where three layers are hit (circular tracks) and a third where two layers have been hit (ping-pong tracks). The same can be done for curling three-hit tracks. Due to the tremendous overhead and the large simulation runs required to get enough statistics, this remains a task for a future satellite mission.

In terms of detector design, thinner layers would be advantageous to address the problem of U-turn tracks. Less Molière scattering makes the tracks straighter. However, the problem is not eliminated, it is only shifted down to lower energies. In addition, one would need more layers to achieve the same scatter probability and consequently the energy measurement error would increase since the track of an electron with given energy would be recorded in to more measurement points.

The most relevant information for finding the direction of the track is encoded in the start point of the track. As already mentioned, the Compton interaction takes place somewhere inside the first layer and thus the electron deposits less energy than it would if it passed through the complete layer. As a consequence, it is extremely important to have low enough thresholds to measure the start point of the track — its low energy deposit distinguishes the start from the end of the track. In addition, if one does not measure the start of the track and thus not know the real location of the Compton interaction, the imaging of the whole Compton event is also deteriorated, because the direction of the scattered gamma-ray has a non-neglectable error.

Another important point is to build the tracker large enough that most electrons are contained in it. An ideal satellite tracker would contain thicker Silicon layers, or even Germanium or CZT layers, at the bottom to stop the electrons. This would also be relevant for the sides of the tracker.

For the energy measurement it is also necessary to have as little passive material and as few defective strips/pixels in the detector as possible. Both facts cause missing hits, thus leaks of energy and holes in the tracks.

4.5 Compton sequence reconstruction

In the preceding steps all easily identifiable structures in the tracker have been found: If pairs or high-energy charged particles were found then the event reconstruction never reached this step. In addition, all Compton recoil electron tracks have already been located and sequenced in the previous step. Tracks are now considered as one interaction whose position is the start point of the track. In order to successfully perform the next step, i.e. to identify and sequence Compton interactions, the reconstruction's focus must now broaden to also include all isolated hits recorded as part of an event. For MEGA, events are defined by trigger criteria to consist of at least one interaction in the tracker and at least one interaction in the calorimeter.

Compton sequence reconstruction searches for the true path of the initial gamma ray by analyzing all possible permutations of the recorded interactions and assigning a Compton quality factor to each permutation, which is based on the probability that an event actually occurred in this way. The permutation with the best quality factor is chosen as the correct sequence of interactions. If the best quality factor is not better than a certain value, the event can of course be rejected. This last decision, however, is not made during event reconstruction, but — as a cut on the Compton quality factor — in the later high-level data analysis.

The only outright event rejection happening in the present step concerns events for which the Compton kinematics are not correct for any one of the possible permutations or for which there are too many interactions to analyze: normally events with eight interactions or more are no longer analyzed, because it would require analyzing $8! = 40320$ possible permutations and thus far too much CPU time. The fraction of completely absorbed Compton events with more than seven interactions is negligible for MEGA.

In the following, first the basic principles for sequencing Compton interactions are presented. Afterwards, two different implementations of these principles are discussed: the *Classic Compton Sequence Reconstruction* (C-CSR) and the *Bayesian Compton Sequence Reconstruction* (B-CSR). The goal is again to have one fast approach, which can be applied to all geometries without preparations (C-CSR), and one optimized method, which considers the (almost) complete data space of the telescope but requires extensive simulations (B-CSR).

4.5.1 Characteristics of the data space

Compton scattering is described by the Klein-Nishina equation. A wide range of different energy transfers to the Compton electron is possible, and consequently the electron might or might not generate a track. The scattered gamma ray might undergo another Compton interaction, it might be stopped by photo absorption, if its energy is above 1.022 MeV it could undergo a pair creation, or it might even Rayleigh scatter. Since in the last process no energy is deposited, this is of course not detectable as interaction. Even leaving out the highly unlikely combination of a Compton scatter followed by a pair-creation event and ignoring Rayleigh scattering as both not significant and not detectable, a MEGA-style tracking Compton telescope measures a wide variety of different Compton event types which all require slightly different reconstruction approaches:

1. Simple COMPTEL-type events have one hit without a track in the first detector and another hit in the second detector. For most of these events it is impossible to determine the direction of motion of the photon since for MEGA the time of flight between the interactions cannot be measured.

2. If the event consists of one track and one hit in the calorimeter, then the redundant information provided by the track allows to determine the direction of motion of the photon.

3. The third type is characterized by multiple (3+) Compton interactions. Having several Compton interactions results in redundant information about the kinematics, which can either be used for determining the sequence of the interactions or — if the sequence is known or at least four interactions exist — of the total energy. This type can also have tracks, which further helps to find the correct sequence.

In general, the more information is available about the event, the higher the probability that the event can be reconstructed correctly.

4.5.1.1 Two interactions without track

When no additional information is available, the direction of motion of completely absorbed two-site events can only be retrieved unambiguously in rare cases. Those occur when the conditions of Equations 2.7 are met for one direction (top-bottom), but not for the other direction (bottom-top), i.e. when the energy transfer to the electron is smaller than the minimum allowed gamma-ray energy in case of backscattering. The small areas in the data space in which this holds are illustrated in Figure 4.15. The black area represents events going top to bottom and the dark gray line those going bottom to top. In all the unambiguous cases, there is only a very small energy transfer to the recoil electron. Thus this data space is partly complementary to the data space of tracked events.

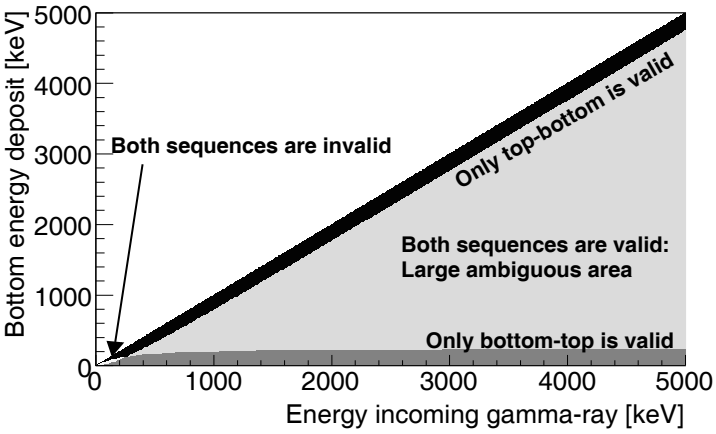

Figure 4.15: The black area is occupied by Compton interactions for which the direction of motion of the photon can be determined merely from the energy deposits as "top to bottom" and the dark gray area indicates photons moving unambiguously "bottom to top" – of course under the assumption of complete absorption. In the (light grey) space between those areas, both directions of motion are allowed. The area above the black line as well as a small area below $0.5E_0$ do not contain valid events. In the former case, a single energy deposit would already be larger than the energy of the incoming photon; the latter area is forbidden because of the constraints on allowable electron and photon energies resulting from Equations 2.7: For instance, for an incoming 100 keV photon, only 0–30 keV can be transferred to the electron.

The absolute positions of the interactions — as opposed to the angles between them — are another piece of information. These allow to determine the interaction probabilities of the photon on its path to the measured interaction locations. Due to the complexity of the geometry and the ambiguity in incident photon direction arising from the Compton cone, the absorption probability towards the initial interaction location is difficult and thus CPU-intensive to determine. Therefore it is not used in the current analysis. The absorption probability between the first and the second interaction is easily accessible. Successfully applying it to the event reconstruction, however, requires an excellent position resolution in both detectors in order to know the intervening material in the complex geometry of a real detector. Unfortunately, MEGA's calorimeters do not provide sufficiently fine position resolution. Thus, this information is only of limited use for MEGA and only included in the more complex Bayesian approach (see Section 4.5.3). In that section, it will also be shown that absorption probabilities are better suited to rejecting (strange) sequences (with e.g. random hits with low energy deposits) than to distinguishing between two equally valid sequences with roughly equal energy deposits in the two interactions points. Also the distribution of the Compton scatter angles according to the Klein-Nishina cross section encodes information about the direction of motion, even though this is also a weak criterion.

Finally, the available information about two-site events without track does not really allow to verify the quality of those events. In particular, it is not possible to determine if they are

completely absorbed or not. Only an approach which uses the complete information about the detection process in the instrument can make use of those events.

4.5.1.2 Two interactions with track

For two-site events with track MEGA can rely on the electron track to find the direction of motion of the gamma ray. The most frequent class of background events which have to be rejected in a satellite in low-earth orbit are gamma rays originating from the earth's atmosphere, so-called albedo photons. For a discussion of satellite background components and their origins, see Section 10.2.1. In the case of tracked two-site albedo-photon events, photons interact once in the calorimeter, then produce a track in the Silicon. Most likely, they then escape from the detector — if they are stopped in the tracker, they are unlikely to produce a track, because the necessary photo absorption happens only at very low photon energies. Figure 4.16 illustrates such an event.

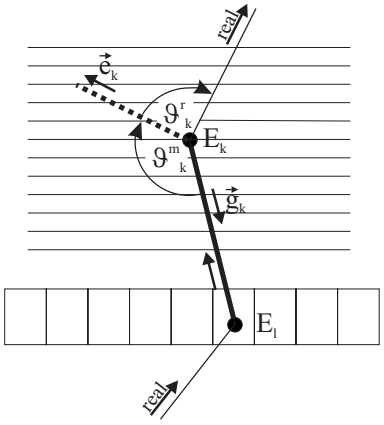

Figure 4.16: A typical upward-moving gamma ray in the MEGA detector: The first interaction (index l) happens in the calorimeter, a second one (index k) in the tracker, and the scattered gamma-ray escapes. Here $\vec{e}_k$ is the (correct) direction of the recoil electron, $\vec{g}_k$ is the (wrong) direction of the scattered gamma-ray, ϑ^m_k is the wrong and ϑ^r_k is the correct total scatter angle. E_l and E_k are the two measured energy deposits. It is assumed that the electron-tracking algorithm has identified the direction of motion of the electron correctly.

In the low-earth orbit forseen for a MEGA satellite, the albedo photons originate mainly from around 120 degree zenith distance, since they are generated in the earth's upper hemisphere. Thus, the originally envisioned approach of simply rejecting all events with upward-moving electron tracks — feasible for photons truly coming from the back of the instrument — will not reject albedo photons well; a more sophisticated approach is necessary.

The key to this is the total scatter angle ϑ, which is the angle between the direction of the scattered gamma-ray $\vec{g}_k$ and the direction of the recoil electron $\vec{e}_k$ (see Figure 4.16). This information is redundant — ϑ can be determined via kinematics (identical with Equation 2.8)

$$\cos\vartheta^{kin}_k = \frac{E_k(E_l + E_0)}{E_l\sqrt{E_k^2 + 2E_kE_0}} \tag{4.19}$$

and, using the information the electron track provides, also via geometry

$$\cos\vartheta^{geo}_k = \frac{\vec{g}_k \cdot \vec{e}_k}{|\vec{g}_k|\,|\vec{e}_k|} \tag{4.20}$$

If there is a large discrepancy $d\vartheta = \vartheta^{kin}_k - \vartheta^{geo}_k$ between the two angles, then the assumed ordering is likely to be wrong, or the event is incompletely absorbed. This is called the $d\vartheta$-criterion. Unfortunately, for the thick tracker layers of MEGA and for low electron energies it is also likely that the electron has simply undergone strong Molière scattering, which results in large $d\vartheta$ values as well, or that the electron track orientation has been determined incorrectly. Such events, however, will not appear in the center of the point spread function of a source and they should receive a bad quality factor for later rejection.

Similar values of ϑ^{kin} and ϑ^{geo}, however, do not automatically mean that the ordering is correct! Figure 4.17 shows values of $d\vartheta$ (z-axis, color) for upward moving gamma-rays at 2 MeV and at 10 MeV, based on the *wrong* assumption of a downward moving photon: the energy in the track is assumed as the initial deposit ("wrong electron energy") and the deposit in the calorimeter as the second deposit ("wrong gamma energy"). The main cause for $d\vartheta \neq 0$ in *correctly* reconstructed events is Molière scattering. In order not to reject too many valid events, only $d\vartheta$ values larger than $\sim$35° (for 2 MeV photos, depending of course on the electron energy, with smaller values for higher energies) can be considered a reliable indication that something is wrong with the event.

Note that there exists a large region with very small variations in $d\vartheta$ (at small E_g and/or E_e). In this region, both directions are valid within the limits of Molière scattering and thus one cannot distinguish between an incompletely absorbed upward-moving photon and a completely absorbed downward-moving photon. The ambiguity for low electron energies (small "wrong recoil electron energy") in the data space of two-site events with tracks is not relevant for MEGA — at those energies no tracks are generated. Ambiguities also exist for low deposits in the calorimeter (small "wrong scattered gamma-ray energy"); these can be eliminated by appropriate event selections.

Since the direction of motion cannot be determined uniquely everywhere in the data space, electron tracking — without additional information — is not as powerful a direction-of-motion tool as measuring the time-of-flight would be. However, electron tracking has of course another great advantage: it significantly reduces the size of the point-spread function, markedly improving a satellite instrument's sensitivity.

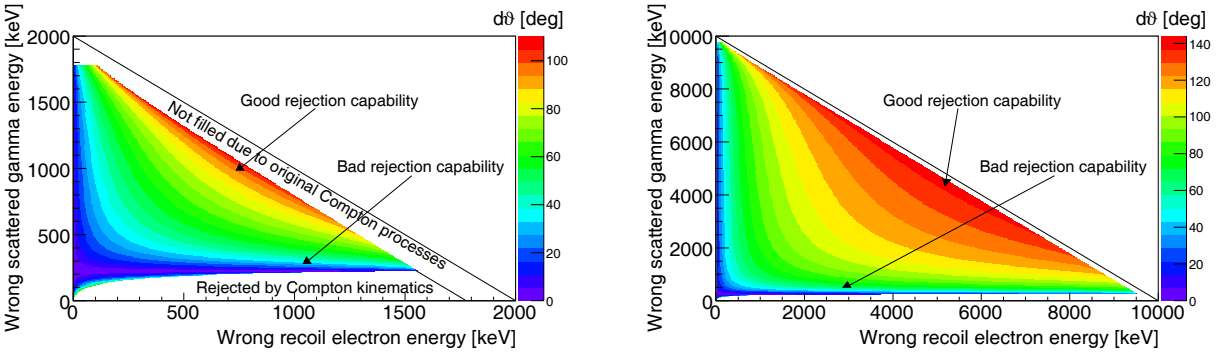

Figure 4.17: This figure shows the difference between the total scatter angle ϑ measured via geometry and via kinematics for an upward moving and escaping gamma ray which has its first interaction in the calorimeter for 2 MeV photons (left) and for 10 MeV photons (right). $d\vartheta$ is calculated (wrongly) assuming the first interaction happened in the tracker. For a large area in the data space such events can be rejected because they have large $d\vartheta$ values. However, low electron energies and/or low scattered gamma-ray energies also result in small ϑ values. Such wrongly reconstructed events cannot be distinguished from correct ones via the $d\vartheta$-criterion.

The track information cannot only be used to determine the direction of motion of the photon. Applying a $d\vartheta$ selection also serves to reject incompletely absorbed events which move from tracker to calorimeter, since ϑ_k^{kin} is wrong for such events. This is of course again limited by Molière scattering, and one therefore has to allow for a sufficiently large tolerance in $d\vartheta$. Figure 4.18 shows the theoretical variation in the difference of the two ϑ's when the scattered gamma ray is incompletely absorbed (left column) and when the recoil electron is incompletely absorbed (right column) for 2 MeV (top row) and 10 MeV (bottom row) incoming gamma rays which first interact in the tracker. In this context incomplete absorption means that not all energy is deposited in active material, i.e. the particle either escapes or deposits its energy in passive material.

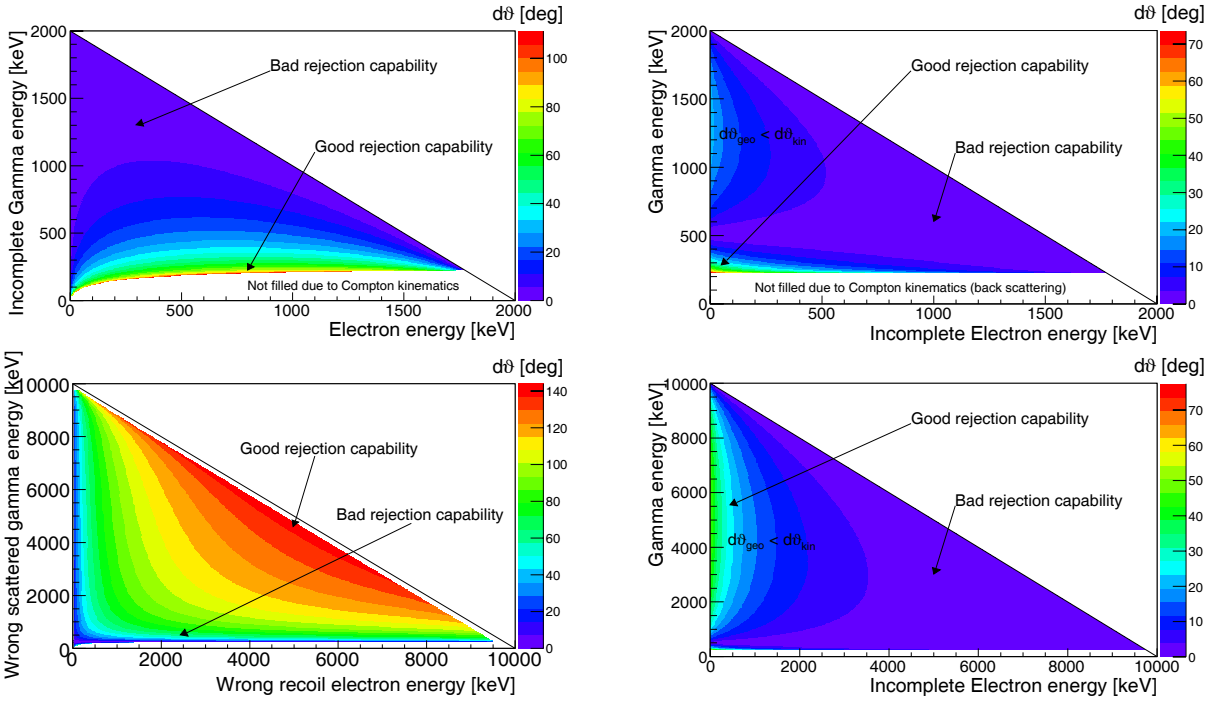

Figure 4.18: This figure shows the difference between the total scatter angle ϑ measured via geometry and via kinematics for downward-moving photons. In the left column, the scattered gamma ray is incompletely absorbed, in the right column the recoil electron is incompletely absorbed. Since Molière scattering induces significant $d\vartheta$ in good events, for MEGA at 2 MeV (top row) rejections are possible for $d\vartheta$ values above $\sim$ 35 degrees, and $\sim$ 10 degrees at 10 MeV (bottom row). Thus, it is only possible to reliably reject incompletely absorbed events in small portions of the data space. In the idealized, error and Molière-scattering free data space illustrated above, ϑ is exactly zero for the completely absorbed events (diagonal line).

Unfortunately, the total scatter angle ϑ changes only very slowly with decreasing energy of the scattered photon. This is the case because the calculated scatter angles of electron and photon move in opposite directions: the Compton scatter angle φ gets larger while the electron scatter angle ε gets smaller. As a consequence, the area for which there is a significant difference (relative to the effects of Molière scattering) between the geometrically determined (the correct) and the energetically determined total scatter angle is small. For the largest part of the data space it is impossible to flag incompletely absorbed events. Thus it is crucial to completely absorb most of the the incoming gamma rays: the detector must have a large active to passive mass ratio and must be thick enough to stop all photons.

A final remark: In theory it would also be possible to use the redundant track information to determine the original gamma-ray energy for incompletely absorbed events. However, for MEGA this would result in multiple problems: First, correcting the energy — without knowing the interaction sequence — would upgrade all upward-moving photons to energy-corrected downward-moving photons and thus dramatically increase the background. Second, this method would only work for the highest-energy photons (beyond 15 MeV) due to the limitation from Molière scattering. Finally, at those high energies in almost all cases the recoil electron as well as the scattered gamma-ray are not completely absorbed, finally rendering a correction impossible.

4.5.1.3 Multiple Compton interactions

The next level of complexity is reached when there are more than two interactions: at least two Compton interactions and one final complete (photo) absorption. Figure 4.19 illustrates such an event.

If one ignores tracks, then the complete data space for multiple Compton events consists of N

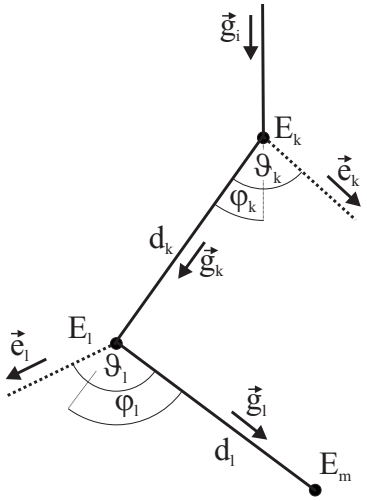

Figure 4.19: Multiple Compton interactions: In this example a gamma ray undergoes three interactions: Compton scattering at positions k and l, as well as a photo absorption at position m. The solid line corresponds to the path of the gamma ray, the dotted lines are the paths of the electrons. The plotted event contains several independent and redundant pieces of information. First, the second Compton scatter angle φ_l can be calculated in two ways: via Compton kinematics (Equation 4.21) and via interaction geometry as angle between $\vec{g}_k$ and $\vec{g}_l$ (Equation 4.22). In addition, two electron tracks also provide redundant information: Each of the total scatter angles ϑ_k and ϑ_l can be calculated via Compton kinematics and via the interaction geometry as angle between the photon direction $\vec{g}_k$ ($\vec{g}_l$) and the electron direction $\vec{e}_k$ ($\vec{e}_l$). This redundant information allows to determine the interaction sequence and (sometimes) whether or not the photon's energy is completely absorbed.

measurement points (with x, y, z and energy), which would lead to a $4 \cdot N$-dimensional data space matrix. The size of such a data space rapidly increases for Compton events consisting of several interactions. In addition, the absolute interaction positions x, y, z are not directly linked to the underlying physics. A well-designed data space thus is spanned by parameters that are directly connected to the underlying physics. The data space must be designed to conserve as much information as possible while not exceeding a manageable number of dimensions. Therefore, the parameters spanning the data space should be as independent as possible of one another. Particular care must be taken to conserve all information which is useful to discriminate between possible paths of the photon, and to determine the likelihood of an event being fully absorbed. Separate data spaces for first, central, and last interactions can be designed similar to the approach taken during electron tracking. In the following, parameters suited to these tasks are discussed; starting from these eventually a data space for Compton event reconstruction will be built.

As in the case of electron track reconstruction, in the process of reconstructing a Compton event one has to investigate all different paths (= sequences) the particle — in this case the photon — might have taken. In general, there exist $N!$ possible paths (= permutations). If one considers a triple interaction, 6 permutations have to be investigated to figure out the correct sequence.

For this task the Compton scatter angle φ_l of the central Compton interaction from Figure 4.19 has proven most valuable. Just like the total scatter angle (ϑ_k or ϑ_l) for electron tracking, this information can be calculated in two ways from the redundant information available: Via kinematics (similar to the classic Compton equation 2.6):

$$\cos \varphi_l^{kin} = 1 - \frac{E_0}{E_{l+}} + \frac{E_0}{E_{l+} + E_l} \tag{4.21}$$

and via geometry, as the angle between the photon direction before and after interaction l:

$$\cos \varphi_l^{geo} = \frac{\vec{g}_k \cdot \vec{g}_l}{|\vec{g}_k|\,|\vec{g}_l|} \tag{4.22}$$

Here E_l is the energy deposit at interaction site l, which corresponds to the energy of the recoil electron of the Compton interaction l, and E_{l+} is the energy of the scattered photon, which is defined as all energies deposits *after* interaction l in the sequence: $E_{l+} = \sum_{j=l+1}^{N} E_j$. For the example in Figure 4.19 this is simply E_m.

In the case of the correct permutation, $\cos\varphi_l^{kin}$ and $\cos\varphi_l^{geo}$ should be identical within measurement errors. Compared to electron tracking, where a large $d\vartheta$ ($\sim 35°$ at 2 MeV) had to be accepted because of the large uncertainty due to Molière scattering, the tolerated $d\varphi = \varphi_l^{kin} - \varphi_l^{geo}$ are much smaller: They correspond to the angular resolution, determined by energy resolution, position resolution and Doppler broadening. For MEGA, good $d\varphi$ values are a few degrees if the interactions happen in the tracker, but unfortunately the deviations are much worse in the calorimeter due to its limited position resolution (in the rare extreme case up to 90° in the side calorimeter).

The **$d\varphi$-criterion** — as the $d\vartheta$-criterion for electron tracks — cannot completely compete with time-of-flight information concerning the determination of the direction of motion: The direction of motion cannot always be determined uniquely from $d\varphi$. The most obvious example is the case of three hits with the same energy. For two of the calculated sequences — the original one and its reverse — the $d\varphi$ are zero. In this case only additional information such as absorption probabilities can help to determine the correct sequence.

Figure 4.20 shows $d\varphi$ for a 2 MeV photon which undergoes a triple Compton interaction as a function of the first and the third energy deposit. Only *one* of the five wrong sequences is considered, the reverse one. In case of very small second energy deposits as well as in the case of equal first and third deposits (within measurement errors and Doppler broadening), the reverse cannot be distinguished from the correct sequence: In both cases $d\varphi$ is close to zero for the true as well as the reverse order.

While for this figure only two sequences where considered, in reality all N! permutations have to be investigated. This further increases the risk that one wrong combination by chance is better than the original one due to the limited energy resolution.

Another illustration of ambiguous data space regions is shown in Figure 4.21. For given energy deposits (in the example $E_1 = 200\,\text{keV}$, $E_2 = 1200\,\text{keV}$, $E_3 = 600\,\text{keV}$) the distance of the interactions are varied and thus the φ_{geo} of a wrong sequence. Moving one position leads to a monotone increase (or decrease) of the φ_{geo} value (in the case of a wrong sequence — φ_{geo} of course stays constant for the correct sequence). Obviously if during this process φ_{geo} gets close to the value of φ_{kin}, determining the sequence is ambiguous.

While the $d\varphi$-criterion is the strongest for finding the true sequence of multiple Compton interactions, and therefore constitutes an obvious first choice of a parameter used to span the Compton reconstruction data space, it is not the only criterion which can be used — the events in ambiguous sections of the data space are not lost!

For MEGA the most obvious and strongest additional information is of course the electron track, which allows the application of the ϑ-criterion to 3+ interaction events in the same way as described in the last chapter for two-site interactions with tracks. If no tracks are measured, then still the **absorption probabilities on the paths between the interactions**, the distribution of φ according to the Klein-Nishina equation, as well as variations in the occupation of the data space induced by a particular instrument's geometry can be used to differentiate between the correct and wrong sequences.

Those features can best be shown in a data space filled by simulations of photons from all directions incident on a real-instrument geometry, in this case the MEGA satellite. The illustrations in Figure 4.15 through 4.21 were generated from analytic calculations. The full data space underlying the projections shown in the subsequent images is that used for the Bayesian event reconstruction discussed later in this Chapter (Section 4.5.3).

Figure 4.22 illustrates the dependence between gamma-ray energy and absorption probability en route towards the last interaction point in a Compton sequence. (Similar to the approach taken for electron tracking, the data spaces used for first and last interaction are somewhat

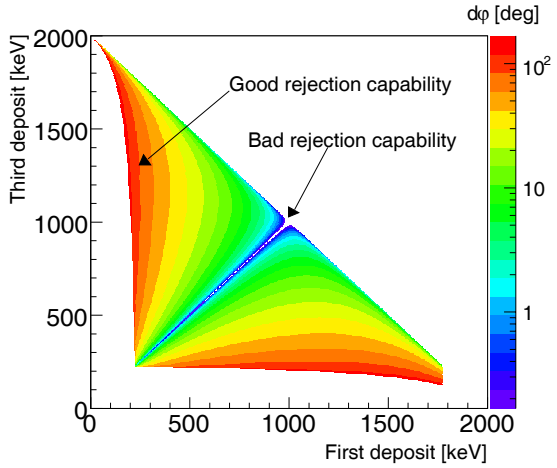

Figure 4.20: One of the regions in the triple Compton data space where calculating the Compton scatter angle difference $d\varphi = |\varphi_{kin} - \varphi_{geo}|$ is not sufficient to unambiguously determine the direction of motion of the gamma ray: the approach is in trouble when first and third deposit have equal energy within measurement errors or when the third deposit is very small. To calculate $d\varphi$ only one sequence has been considered, the one reverse to the correct one.

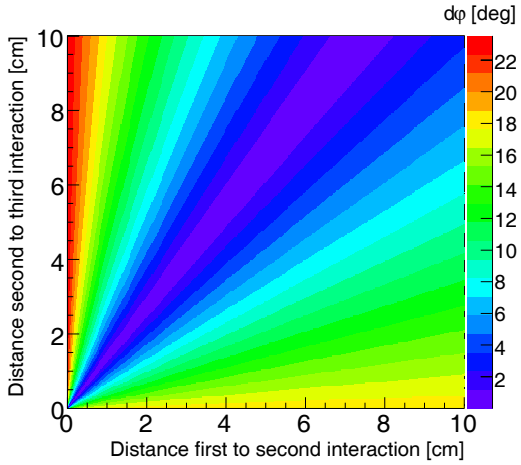

Figure 4.21: Another illustration of the limitations of the triple-Compton method: If one looks at one energy signature (in this case $E_1 = 200\,\text{keV}$, $E_2 = 1200\,\text{keV}$, $E_3 = 600\,\text{keV}$) and varies the distance between the interactions (which results of course in different geometrical scatter angles for the wrong sequences but does not vary them for the correct sequence), ambiguous data space regions become evident. The given example is a fairly bad case.

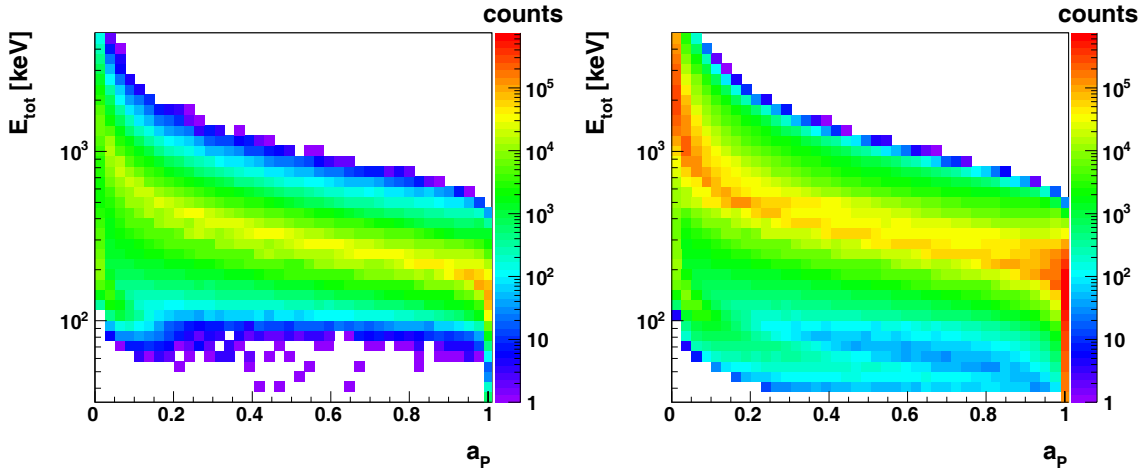

Figure 4.22: Remaining photon energy as a function of the absorption probability towards the last interaction point. The left image shows this distribution for correct sequences, the right image for all wrong sequences. The data spaces look rather similar, with one exception: the "false" one has some excesses at high energies and low probabilities as well as at low energies and high probabilities. The underlying simulation was performed for photons from all directions incident on the MEGA satellite geometry. Since this data space is generated as part of the Bayesian CSR, additional details can be found in Section 4.5.3.

different from that relevant to central interactions.) The left figure shows only the correct sequences, the right figure only the wrong sequences. Ideally, the good sequences would occupy completely different regions in the data space than the wrong sequences, and thus they could be easily distinguished. But partially due to the large position measurement errors of the MEGA detector, the differences are marginal. Clear excesses can only be found at high energies and low probabilities, as well as at low energies and high probabilities. In the first case the sequence had

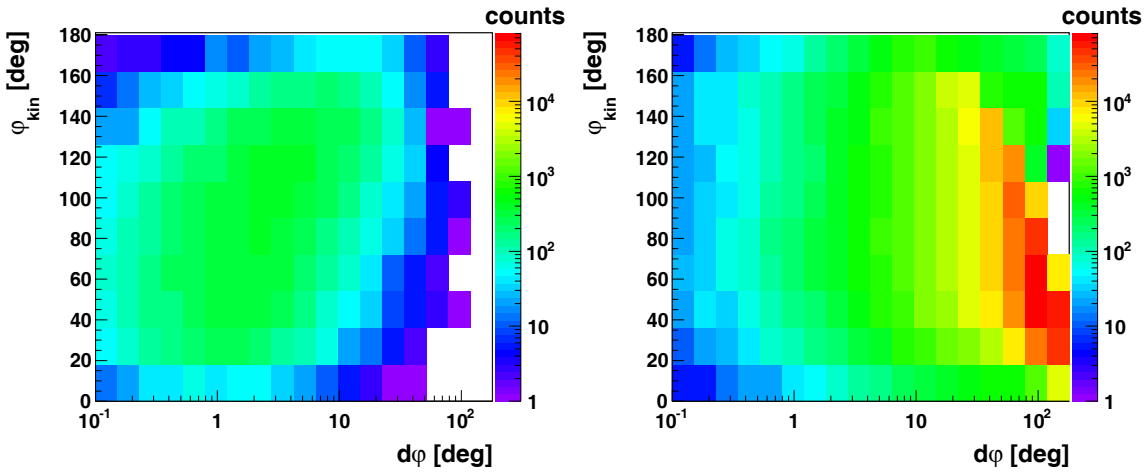

Figure 4.23: Compton scatter angle φ_{kin} as a function of the scatter angle difference $d\varphi$. Again, the image on the left shows only the correct sequences, the one on the right the all wrong sequences. The correct sequences gather at low $d\varphi$, but due to ambiguities resulting from the problems of the multiple Compton approach as well as the limited energy and position resolution of the simulated MEGA satellite, wrong sequences occupy that space as well. The distribution on the y-axis is determined by the Klein-Nishina distribution of φ and the geometry. The underlying simulation is a necessary ingredient to the Bayesian reconstruction; details can be found in Section 4.5.3.

a too-small interaction distance for a large photon energy, in the latter the sequence had a too-large distance for a small photon energy. Only wrong sequences with those characteristics can be rejected by an absorption probability criterion. Using this criterion for stricter event selections one would immediately risk to also reject good event sequences, because the corresponding data-space regions overlap.

The distribution of simulated events as a function of φ_{kin} and $d\varphi$ is shown in Figure 4.23. Again, the left image shows only the correct sequences, while the right image shows all other permutations. The first obvious finding is that the good sequences gather at low $d\varphi$ and their distribution is determined by the angular resolution of the telescope (large scatter angles result in worse angular resolution). The wrong sequences mainly gather at large $d\varphi$ values, but — due to the previously described ambiguities — stretch out to small $d\varphi$. In φ_{kin} the distribution of good sequences is modulated by the Klein-Nishina distribution of the Compton scatter angle and by the geometrical factors. Due to the large ambiguous regions it is not always possible to determine the correct sequence, since it is likely that by chance one of the wrong sequences has similar geometrical and kinematical Compton scatter angles and thus a small $d\varphi$.

In case of four (or more) interactions, in theory the redundant information could also be used to determine the energy of incompletely absorbed events. For each triplet of interactions the incoming energy in the triplet can be calculated independent of subsequent interactions or the total *deposited* energy:

$$E_{tot,1} = E_1 + 0.5E_2 + 0.5\sqrt{E_2^2 + 4E_0E_2/(1-\cos(\varphi_2))}. \tag{4.23}$$

In case of four interactions, for each possible sequence two triplets exist for which the total energy can be calculated. This results again in redundant information: $dE = E_{tot,1} - E_{tot,2}$ has to be $\sim$0 if the reconstructed sequence and the determined incoming photon energy are correct.

Unfortunately, the ambiguities in determining the total energy of incompletely absorbed events are large. An excellent position and energy resolution would be required to estimate the

total energy correctly. Since these requirements are not fulfilled by the present MEGA detectors this avenue is not explored further.

In summary, a good data space to describe Compton interactions should comprise the angles $d\varphi$ and φ as well as the photon energy E_i in order to allow use of the $d\varphi$-criterion as well as the distribution of the Compton scatter angle according to the Klein-Nishina equation. In addition, a distance factor d is needed, which describes the geometrical uncertainty influencing φ. If electron tracks are present, $d\vartheta$ and ϑ are needed as well. The absorption probability of the incident photon on its way to the interaction as a function of the photon energy adds a valuable tool to reject wrong sequences. In addition, of course the detector type (this encodes information about energy resolution, position resolution, Doppler broadening, etc.) as well as the number of interactions in the event must be retained. The exact layout of such a data space used for event reconstruction can be found in Section 4.5.3.

4.5.2 Classic Compton sequence reconstruction

The last section explained in detail the signatures of different event types — first for two-site interactions without tracks, then for two-site interactions with tracks, and finally for multiple-site interactions. This and the following section are now concerned with making use of the knowledge gained in order to reconstruct different types of Compton events as well as to determine the certainty with which a given event was reconstructed correctly. In this section, a straightforward, analytical approach is used — the "Classic" Compton reconstruction.

The part of the classic approach concerned with non-tracked, multiple-Compton events has already been described in the literature by different authors for different applications, for e.g. nuclear spectroscopy (*van der Marel and Cederwall*, 1999; *Schmid et al.*, 1999) as well as gamma-ray astronomy (*Oberlack et al.*, 2000b; *Boggs et al.*, 2000a). In this work it has been extended to electron tracking.

Two-site events without track Without the information of time-of-flight and under high-background conditions, determining the order of two-site events is a non-trivial task. No single parameter allows reliable discrimination; the complete data space would be required. According to 4.5.1.1, for only a small part of these events the order can be unambiguously identified. In all cases, it is impossible to determine if the photon has been completely absorbed. For any analysis in high-background conditions, at most those events for which only one order is allowed can be used; otherwise too many background events would be selected. In the case of laboratory measurements, however, events from the ambiguous section in Figure 4.15 are used and are assumed to start in the tracker as long as this is kinematically possible. Although there exist other, weak criteria for finding the most likely order of those events, like the Compton scatter angle distribution according to the Klein-Nishina equation, or absorption probabilities, they are not used in the classic approach since there is no way to combine all those pieces of information into a single quality factor — which also must remain compatible with all other event types. This will be the task of the approach discussed in the next section. Since there is no reasonable quality factor $Q_{C,Classic}$ for two-site events without track which is compatible with that defined for all other event types, $Q_{C,Classic}$ is set to zero if the event is assumed to have started in the tracker.

Two-site events with track If a track is present, ordering the hits is much easier. As long as it is kinematically possible that the event started in the tracker, this assumption is made. In the later stages of the analysis, the $d\vartheta$-criterion (4.5.1.2) is used to select only those events, which are kinematically correct. A maximum allowed value of $d\vartheta$ is chosen to select the good

events. This cut achieves a significant reduction of background and wrongly ordered events. The quality factor for events starting in the tracker is set in the same way as for two-site events without track ($Q_{C,Classic} = 0$).

Multiple interactions Multiple interactions in the MEGA instrument generally consist of one track or hit in the tracker, and several hits in the calorimeter. All $N!$ sequences have to be considered to find the correct order. The key is the redundant Compton scatter angle φ ($d\varphi$-criterion see 4.5.1.3). A generalized χ^2 approach is used to find the correct ordering. Since no a-priori assumption about the first interaction can be made, the following quality factor has to be calculated for all possible $N!$ permutations:

$$Q_{C,Classic} = \sum_{i=2}^{N-1} \frac{\left(\cos\varphi_i^{kin} - \cos\varphi_i^{geo}\right)^2}{\Delta\cos^2\varphi_i^{kin} + \Delta\cos^2\varphi_i^{geo}} \tag{4.24}$$

where the measurement errors $\Delta\cos^2\varphi_i^{kin}$ and $\Delta\cos^2\varphi_i^{geo}$ are derived via Gaussian error propagation.

The sequence with the smallest $Q_{C,Classic}$ complies best with expectations for a correctly sequenced and completely absorbed gamma ray and out of all $N!$ sequences under consideration it is most likely the correct one. The deviation from zero of the quality factor of the best sequence is a criterion for the goodness of compliance of the sequence with multiple Compton interactions — for incompletely absorbed events or for non-Compton events the quality factor has a larger value. Therefore, selecting only events below a certain $Q_{C,Classic}$ value can discriminate against background and incomplete absorbed events.

If the best sequence found has tracks, then again the ϑ-criterion can be used to verify the ordering and to reject impossible sequences (e.g. track at the end, electron scatter angles larger than 90° within the sequence, etc.).

This "classic" approach has several fundamental problems:

- It ignores the multi-dimensionality of the Compton measurement process: it only uses two one-dimensional projections — the φ-criterion and the ϑ-criterion. Given the variety of events, it is impossible to integrate all information and end up with one single, analytically-determined quality factor for all event types in this classic approach.

- It ignores the known relations between different quantities in the data space. For example, the value $d\varphi$ is expected to be smaller for small scatter angles (less Doppler-broadening, less influence of measurement errors) than for large scatter angles.

- For a Compton telescope, background suppression is vital; it has to be enabled by the event reconstruction. The current approach, however, does not incorporate knowledge about where in the data space the background events will accumulate.

- Finally, the classic approach results only in a figure-of-merit, the $Q_{C,Classic}$ quality factor, instead of a real probability. Such a probability should describe the likelihood that the selected sequence belongs to a completely absorbed and correctly ordered gamma-ray event.

The following section describes an algorithm which eliminates all of the above shortcomings — at the price of significantly higher requirements on CPU resources.

4.5.3 Bayesian Compton sequence reconstruction

In order to incorporate the full dimensionality of the measurement process and its asymmetry, to identify those data space cells where the background accumulates, and to obtain a quality factor based on a probability as the result of event reconstruction, again a multi-dimensional instrument response based on Monte Carlo simulations in conjunction with Bayesian statistics is used. The key dimensions enabling event reconstruction are those defined in Section 4.5.1: the difference of the Compton scatter angle as calculated by energy and by geometry $d\varphi$, the difference of the total scatter angle as calculated by energy and geometry $d\vartheta$ and the absorption probabilities towards the currently investigated interaction position.

Ideally, of course, only a single data space per interaction encompassing all relevant aspects should be used. However, the resulting size of the data space — and thus the response matrix — would make it impossible to perform the necessary simulations to determine the instrument response on current hardware (Beowulf cluster with 32 × 2.4 GHz Xeon CPUs) within a reasonable time span (weeks). Since the key dimensions of the data space discussed above are (almost) independent from each other, but depend on common basic parameters like total energy, Compton scatter angle, etc., the consolidated data space can be split into smaller sub-spaces, which correspond to different aspects of the individual interactions. For instance, information related to electron tracks is stored in a separate data sub-space, then used in the evaluation of initial as well as "central" Compton scatters. This approach results in lower-dimension data spaces that are easier to sufficiently fill with Monte Carlo simulations. The data sub-spaces used and their dimensions are:

Initial interaction point

Without track

1. The cosine of the Compton scatter angle as calculated by kinematics $\cos\varphi^{kin}$. Larger scatter angles result in larger measurement errors and increased Doppler-broadening.
2. The energy E_{in} of the photon before the Compton interaction. The distribution of $\cos\varphi$, given by the Klein-Nishina-equation, depends on the total energy of the photon. E_{tot} and $\cos\varphi^{kin}$ completely describe the interaction process.
3. The detector in which the interaction happened. It influences Doppler-broadening (via the material) as well as energy and position resolution. (For MEGA, currently no distinction is made between the different calorimeter types).
4. The number of interactions contributing to the whole event. This determines the number of combinations which have to be investigated and thus the final normalization.

If the first interaction has a track, the data sub-space describing electron tracks is relevant:

With track – ϑ-criterion:

1. The difference between the total scatter angle ϑ as calculated by energy and geometry: $d\cos\vartheta = \cos\vartheta^{kin} - \cos\vartheta^{geo}$
2. The total scatter angle as determined by kinematics $\cos\vartheta^{kin}$
3. The energy of the recoil electron E_e. The last two again describe the complete Compton process.
4. The detector of the interaction
5. The number of interactions

Central interaction point

φ-criterion:

1. The difference between the central Compton scatter angle as calculated by energy and by geometry: $d\cos\varphi = \cos\varphi^{kin} - \cos\varphi^{geo}$
2. The Compton scatter angle as calculated by kinematics $\cos\varphi^{kin}$
3. The energy E_{in} which the photon had before the Compton interaction. E_{in} and $\cos\varphi^{kin}$ again describe the complete Compton kinematics.
4. A distance factor, which determines the geometrical error of $d\cos\varphi$: $d_E = min\,(d_-, d_+)$. d_- and d_+ are the distances to the interactions before and after this one.
5. The detector of the interaction
6. The number of interactions

Compton-absorption criterion:

1. The *Compton* absorption probability a_C from the last to this interaction for the relevant photon energy (E_{in}).
2. The energy E_{in} of the photon which traveled the distance from the last to this interaction position.
3. The detector of the interaction
4. The number of interactions

In addition, when the interaction produced an electron track (this is the same data space as for the initial data point):

ϑ-criterion:

1. The difference between the total scatter angle ϑ as calculated by energy and geometry: $d\cos\vartheta = \cos\vartheta^{kin} - \cos\vartheta^{geo}$
2. The total scatter angle as determined by kinematics $\cos\vartheta^{kin}$
3. The energy of the recoil electron E_e. The last two again describe the complete Compton process.
4. The detector of the interaction
5. The number of interactions

Final interaction point

Photo-absorption criterion:

1. The *photo* absorption probability a_P from the last to this interaction for the relevant photon energy (E_{in}).
2. The energy of the fully absorbed photon E_{in}.
3. The detector of the interaction
4. The number of interactions

Of course the simulation-based instrument response must treat events the same way that actually measured interactions in the detector are treated by the event reconstruction algorithm. For instance, if a photon Compton scatters and subsequently is photo absorbed, and the two interactions happen within one voxel of the detector, then the combination of the two energy deposits will be treated as one photo-absorption interaction.

Once the data space is selected, the Bayesian approach can be set up: The property of the event which has to be determined is the probability that the considered sequence is correctly

ordered and belongs to a completely absorbed gamma-ray ("$\mathcal{C}$"), given the measured parameters $\vec{m} = \cup_i \vec{m}_i$: $p\left(\mathcal{C}|\cup_i \vec{m}_i\right)$, where $\cup_i \vec{m}_i$ is the measurement transformed and split into the above data spaces, i.e. i stands for a sequence part such as the electron-tracking aspect of a central Compton interaction. The following discussion summarizes in the context of Compton reconstruction of events the application of Bayesian methods that has already been discussed in detail in Section 4.4.2.3 in the context of Bayesian electron tracking.

Bayes' rule gives:

$$p\left(\mathcal{C}|\cup_i \vec{m}_i\right) = \frac{p\left(\mathcal{C}\right) p\left(\cup_i \vec{m}_i|\mathcal{C}\right)}{p\left(\cup_i \vec{m}_i\right)} = \frac{p\left(\mathcal{C}\right) \prod_i p\left(\vec{m}_i|\mathcal{C}\right)}{p\left(\cup_i \vec{m}_i\right)} \tag{4.25}$$

The denominator cannot be determined with the above data space, thus the following ratio is used:

$$R = \frac{p\left(\mathcal{C}|\cup_i \vec{m}_i\right)}{p\left(\overline{\mathcal{C}}|\cup_i \vec{m}_i\right)} = \frac{p\left(\mathcal{C}\right) \prod_i p\left(\vec{m}_i|\mathcal{C}\right)}{p\left(\overline{\mathcal{C}}\right) \prod_i p\left(\vec{m}_i|\overline{\mathcal{C}}\right)} \tag{4.26}$$

Obviously $p\left(\mathcal{C}|\cup_i \vec{m}_i\right) + p\left(\overline{\mathcal{C}}|\cup_i \vec{m}_i\right) = 1$ has to be fulfilled and the final solution is:

$$p\left(\mathcal{C}|\cup_i \vec{m}_i\right) = \frac{R}{R+1} \tag{4.27}$$

The given task now is to determine $p\left(\mathcal{C}\right) \prod_i p\left(\vec{m}_i|\mathcal{C}\right)$ and $p\left(\overline{\mathcal{C}}\right) \prod_i p\left(\vec{m}_i|\overline{\mathcal{C}}\right)$ from the data spaces.

Again, two data spaces need to be filled to calculate all involved probabilities: one for the correct sequence parts and one for the wrong sequence parts. From the simulation, the correct sequencing of the photons is known. With this knowledge, for each event all possible sequences are investigated. All correct parts of a given sequence are entered into the "correct" data space, all other sequence parts into the "wrong" data space. A sequence part is considered correct if the involved particles move in the correct direction and have – within a 3 sigma measurement error limit – the correct energy. Figure 4.24 illustrates the filling process.

The data spaces now contain information about how often a sequence part with a given set of parameters is part of a correct sequence, and how often it is part of a wrong sequence. Analog to equation 4.18 the ratio R can be determined:

$$R \approx \frac{N_{correct}}{N_{false}} \prod_{i=1}^{I} \frac{N^{\mathcal{D}_i}_{m_i,\,correct} \cdot N^{\mathcal{D}_i}_{all\,false}}{N^{\mathcal{D}_i}_{m_i,\,false} \cdot N^{\mathcal{D}_i}_{all\,correct}} \tag{4.28}$$

The final quality factor of the event for the Bayesian Compton sequence reconstruction is defined as:

$$Q_{C,Bayes} = 1 - p\left(\mathcal{C}|\cup_i \vec{m}_i\right) \tag{4.29}$$

As mentioned before, filling the above-discussed data spaces with simulations is a major task. In order to obtain reasonable statistics using the minimum amount of bins which guarantee to improve the performance compared to the classical approach would have taken one CPU year on a single 2.4 GHz Xeon processor and was still a challenge on a 32-CPU Beowulf cluster. In order to correctly train the algorithm, the simulation used to generate response matrices must be as close as possible to the measurements (or simulations of measurements) which will finally be reconstructed: same detector geometry, same energy and position resolution, similar input spectra, particles and geometries, etc. For the simulations with the MEGA satellite it was not possible to include the activation-induced background components in the simulations for the response matrices — this would have greatly exceeded the available computing resources. Thus only photons have been used, with angular distributions similar to earth-albedo and cosmic-diffuse background components, only with a significantly flatter spectrum to achieve enough statistics at higher energies.

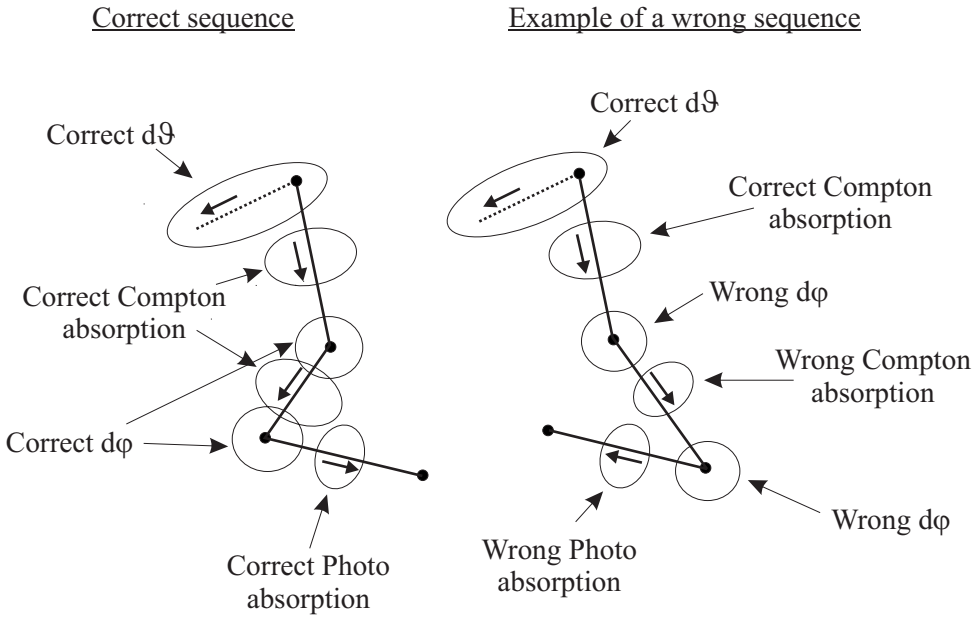

Figure 4.24: Filling the Bayesian data space: For each event each possible sequence is considered. For each sequence each part is checked whether the photon (and electron) direction is correct and whether they have — within measurement errors — the correct energy. If this is the case, the sequence part is added to the "correct" data space, otherwise to the "wrong" one. This figure illustrates which data space each sequence part belongs to: the sequence illustrated on the left is the correct one, the sequence shown on the right is one of the 23 wrong sequences. Note that the latter is only *partly* wrong.

The amount of simulations required to obtain a response is governed by the need to fill the "correct" data space with enough good events. Thus, due to the low efficiency and the correspondingly low rate of fully absorbed events of the MEGA prototype, the required computing time for a Bayesian data space for the prototype is even higher than for the MEGA satellite. Therefore only the classical approach could be used for the prototype data analysis in Chapters 7 to 9.

4.6 Combined electron tracking and Compton sequence reconstruction performance evaluation

For real measured events, the only way to access the reconstruction performance are the ARM distributions for the photon and electron cone, which have been introduced in Section 2.2.5. Thus those are also used here. Correctly reconstructed and fully absorbed events contribute to the peak of those distributions, incorrectly reconstructed events (including incompletely absorbed ones) pile up off-peak.

An example of the photon ARM for both classic and Bayesian electron-track and Compton-event reconstruction can be seen in Figure 4.25. Correctly reconstructed events comprise the peak. The distributions are plotted on a logarithmic scale to make the off-peak components visible. The underlying simulation has been performed with the MEGA satellite geometry and an on-axis narrow-line 2 MeV source at infinity. Both ARMs contain all reconstructed events, regardless of sequence length, start detector (tracker or calorimeter), or if an electron track exists — no event selections have been applied, except for a restriction to photopeak events (total energy deposit 1974–2026 keV). The white area below the thick curve corresponds to data analyzed with the classic algorithms (Spearman-Rank Correlation and Classic Compton sequence reconstruction) and the dark area to the same data analyzed with the Bayesian algorithms. Using the Bayesian algorithm reduces the number of incorrectly reconstructed events by a factor of

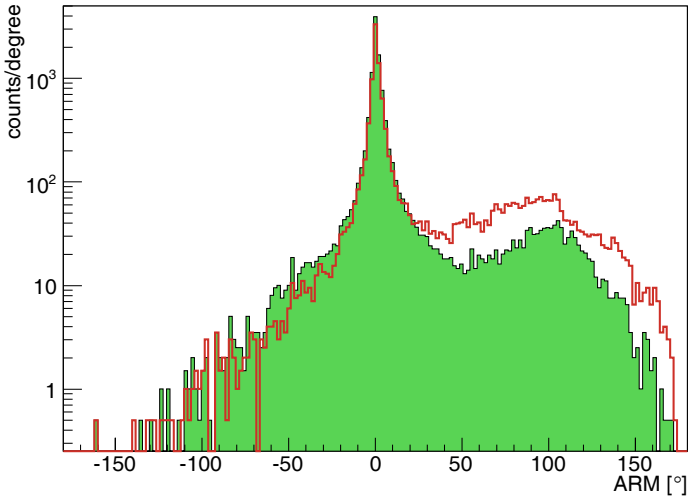

Figure 4.25: Comparison of photon ARM distributions illustrating the reconstruction performance of the Classic (thick red line) and the Bayesian approach (dark area). The extreme background events which accumulate beyond 50° are significantly reduced by the Bayesian approach, resulting in an overall reduction of off-ARM-peak events by a factor of two and a corresponding increase in events in the ARM peak. The simulation was performed with 2 MeV photons (far field, on axis). All photo-peak events are used.

two, and correspondingly increases the number of events in the ARM peak. Since background reduction is vital for a Compton telescope the following performance analysis will concentrate on the better approach, the Bayesian algorithms.

Figure 4.26 shows an example of the photon ARM for tracked events with an energy of 2 MeV (again far field, on axis). Besides only using photo-peak events, no event selections have been applied. It is obvious that the majority of these events is correctly reconstructed to within a few degrees. Figure 4.27 shows the electron ARM for the same events. Incorrectly reconstructed tracks accumulate at large angles ($> 50°$); short tracks (2–4 interactions) constitute the majority of these events.

Due to the long distances between interactions in the tracker and the calorimeters in MEGA, wrong *short* electron tracks only result in a small error (few degrees) in the direction of the scattered gamma ray $\vec{e}_g$. As a result, these events result in a broadening of the main photon ARM peak rather than an increase of clearly off-peak background. The same holds for most of the wrong sequences inside a MEGA calorimeter. Due to the high Z of the material, multiple hits occur close together, resulting again only in a few-degree change in $\vec{e}_g$ in the case of a wrong reconstruction as long as the direction of motion of the photon can still be determined correctly. As in the case for wrongly-reconstructed electron tracks, such events result in a broadening of the main (photon) ARM peak rather than an increase of clearly off-peak background in the distribution.

The fact that certain classes of wrongly reconstructed events contribute to the (broadened) ARM peak rather than resulting in a clearly off-peak component makes quantifying the number of correctly reconstructed events a non-trivial task. The method chosen first determines the "acceptance interval" around the ARM peak containing 95.5% of all events (2σ containment) — assuming perfect event reconstruction. The latter can be achieved using auxiliary information from the simulation: While detector energy resolution, Doppler broadening, Moliere scattering, etc. are taken into account, the ordering of the interactions and their characterization as e.g. either close Compton interactions or electron track is taken from the simulation knowledge. This optimum-case ARM is now compared to the true ARM obtained from the same data using the real event reconstruction — i.e. without additional knowledge. The fraction of events that lie outside the (ideal) ARM's acceptance interval is determined for the true ARM. The difference between this exclusion fraction and the 4.5% excluded in the ideal case is a measure for the fraction of wrongly reconstructed events. Figures 4.28 and 4.29 illustrate the overall efficiency of the reconstruction algorithm in terms of both photon and electron ARM. An algorithm that

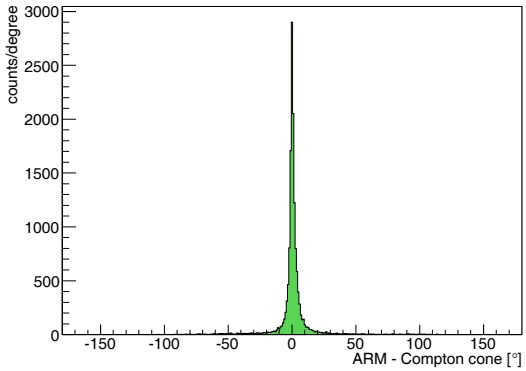

Figure 4.26: Photon ARM of tracked events with 2 MeV incidence energy. Almost no wrongly reconstructed events are visible because they mainly accumulate in the (broadened) peak of the distribution.

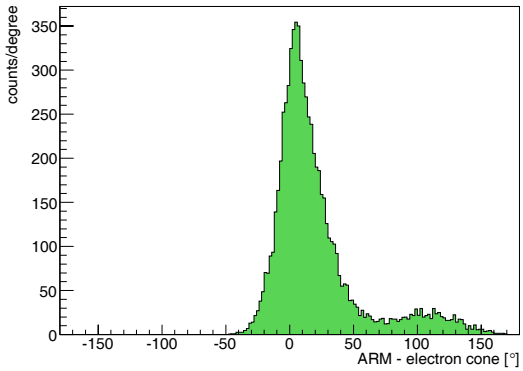

Figure 4.27: Electron ARM of tracked events with 2 MeV incidence energy. Wrongly reconstructed tracks result in large electron ARM values; they can be rejected by applying the $d\vartheta$-criterion.

would achieve 2σ containment in the "acceptance interval" defined above would reconstruct all of its events correctly — so such an ideal algorithm would achieve 100% correctly reconstructed events.

The average number of correctly reconstructed events is around 90% for tracked as well as untracked events in the photon ARM. For not-tracked events, at higher energies the performance decreases somewhat. This is mainly due to multiple interactions in the calorimeter — these are not easy to reconstruct given MEGA's energy and position resolution which lead to the large areas of overlap in the data space as visible in Figure 4.23. The large size of the CsI bars not only worsens the position resolution, but for events with several interactions it is also likely that for example in a sequence of four interactions, interaction two and three are in the same voxel. The result is a large $d\varphi$ value and a likely wrong reconstruction.

The number of correctly reconstructed events as determined via electron ARM is illustrated in Figure 4.29. As expected, the reconstruction efficiency increases with increasing photon (and thus electron) energy, from below 80% at 500 keV to above 90% for 1.5 MeV and more.

Figure 4.30 illustrates the power of one tool to reject wrongly reconstructed events, the $d\vartheta$-criterion (see Section 4.5.1.2). For 2 MeV photons and different $d\vartheta$ selections, it shows how large the excess of photons outside the original 95.5% acceptance interval of the electron ARM is. The

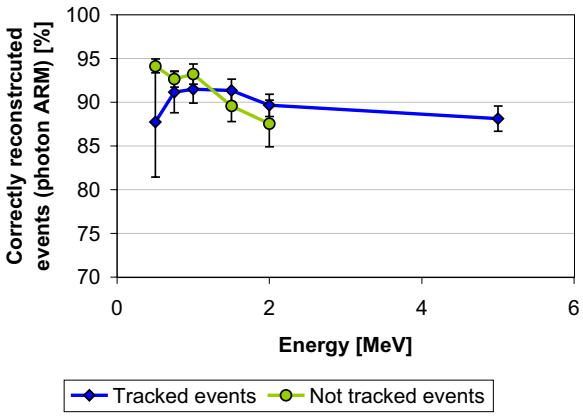

Figure 4.28: Overall performance of the event reconstruction in terms of the photon ARM for various energies. The average reconstruction efficiency is around 90%. For a detailed explanation see text.

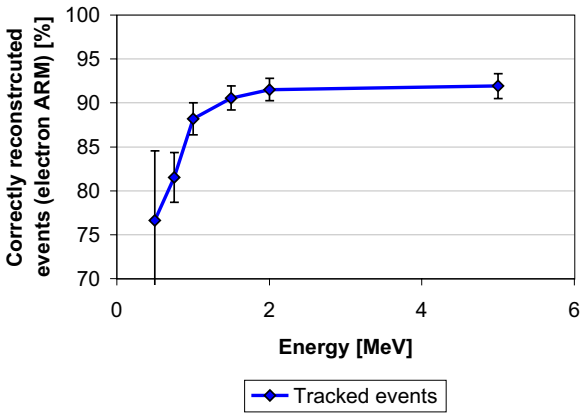

Figure 4.29: Overall performance of the event reconstruction as seen by the electron ARM for various energies. The reconstruction efficiency increases with increasing electron energy. For a detailed explanation see text.

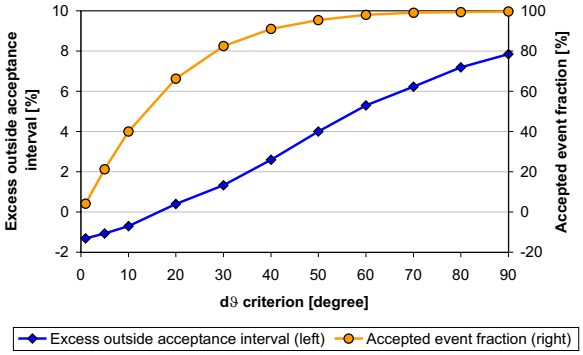

Figure 4.30: Effects of the $d\vartheta$ event selection criterion on the fraction of events outside the acceptance interval of the electron ARM distribution. The ideal cut is around $d\vartheta = 35°$. See text for details.

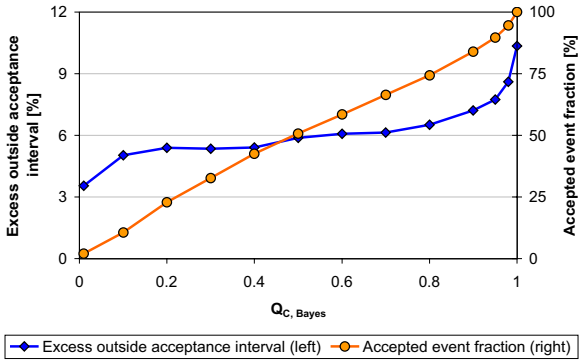

Figure 4.31: Effects of using the Bayesian event reconstruction quality factor as event selection criterion on the fraction of events outside the acceptance interval of the photon ARM distribution. The ideal cut is around 0.95. See text for details.

overall fraction of events accepted by the dϑ-criterion is also shown. For $d\vartheta = 180°$, when all events are accepted, roughly 8.5% are outside the acceptance interval — in addition to the 4.5% which are expected there in the case of ideal reconstruction. Around $\sim$40°, rejecting 70% of the wrongly reconstructed events (decrease from 8.5% to 2.5%) means rejecting 9% of all events, i.e. even for completely absorbed source photons more incorrectly than correctly reconstructed events are rejected. Applying a $d\vartheta$-limit below $\sim$40° results in rejecting mainly good events. Since the $d\vartheta$-criterion is a measure of the directional quality of the electron track, such a strict $d\vartheta$-criterion results in a significantly narrower electron ARM. This reduces the fraction of (non-rejected) events outside the acceptance interval below that for an ideal reconstruction but no $d\vartheta$-cut (4.5%) — resulting in the negative values. The optimum $d\vartheta$-criterion value, which is best empirically derived by optimizing the narrow line sensitivity of the instrument, lies between 30° and 40° in the case of the MEGA satellite instrument.

Figure 4.31 illustrates a second tool to reject wrongly reconstructed events, the quality factor derived from Bayesian event reconstruction. Some of the wrongly reconstructed events in the photon ARM peak accumulate at large $Q_{C,Bayes}$ values. For example, using only events with $Q_{C,Bayes} \leq 0.95$ rejects 25% of the wrongly reconstructed and 10% of the correctly reconstructed events, again using the measure of the photon ARM acceptance interval discussed above. While this does not seem to be too promising (10% of valid source photons would be rejected), considering the total expected background in a low-earth orbit still some advantages arise. A large $Q_{C,Bayes}$ value has two possible origins: Firstly, the event might be barely compatible with Compton scattering, probably because it is incompletely absorbed or does not originate from a (single) photon event. Secondly, these events might originate from data-space cells which are heavily background dominated. In both cases the $Q_{C,Bayes}$ is extraordinary helpful to reject background events. $Q_{C,Bayes}$ is one of the main event selection criteria used to optimize a MEGA satellite's performance (see Chapter 10).

The final proof that the event reconstruction works reliably can only be brought by a full-blown simulation and subsequent rejection of the orbital backgrounds as expected for the MEGA satellite in low-earth orbit. This will be shown in Chapter 10.

Chapter 5

Image reconstruction for a combined Compton and pair telescope

The effects of imperfect measurements of Compton interactions described in Section 2.2.4 lead to large ambiguities in the determination of the origin of each individual photon. The main objective of image reconstruction is to resolve this ambiguity and to recover the origin (sky) distribution of the photons. The leverage available to achieve this goal is the knowledge that *all* photons observed reflect *one* common origin distribution.

5.1 Selecting an algorithm

The measurement process of any gamma-ray telescope can be described in the following way:

$$D(\vec{d}) = T(\vec{d}; \chi, \psi) \times J(\chi, \psi) + B(\vec{d}) \tag{5.1}$$

Photons emitted from a sky intensity distribution $J(\chi, \psi)$ undergo the measurement process T and, together with some background B, are measured in the data space D. The measurement process T completely describes the detector (absorption probabilities, etc.) as well as the physical process (photo effect, Compton scattering, pair creation).

The task of image reconstruction is to invert the measurement process and to determine the image $J^{rec}(\chi, \psi)$ from given measurements $D(\vec{d})$. Since no unique solution for this inversion problem exists, iterative approaches for the reconstruction of the image have to be chosen.

The parameters necessary to properly characterize a telescope's imaging process are very different from those optimized for the reconstruction of individual tracks or Compton events — even though each set of parameters, and thus each data space, constitutes a reduction of the same *complete* data space.

For a modern tracking Compton telescope, the *imaging* data space D consists at least of the following dimensions: the direction of the scattered gamma ray (χ_g, ψ_g), the Compton scatter angle φ, as well as the direction of the recoil electron (χ_e, ψ_e) and its scatter angle ε. The two scatter angles have been chosen instead of the energy of the scattered gamma ray E_g and recoil electron E_e since they constitute a description of the measurement in terms which directly relate to possible origin directions of a photon. For a pair telescope the minimum data space only needs two dimensions, the measured energy E_i and the reconstructed origin $\vec{e}_i$. Table 5.1 gives the minimum number of bins required for a measurement data space and response matrix for the MEGA telescope in Compton mode. Reducing the number of bins further would lead to the loss of a significant amount of information.

The required size of the imaging data space ($\sim 10^{14}$ bins) and the response matrix T ($\sim 10^{19}$ bins) are far beyond the possibilities of any state-of-the-art personal computer – neither can

Measured parameter	Size [bins]	
	MEGA (Satellite)	COMPTEL
Direction of scattered γ (χ_g, ψ_g)	$2 \cdot 360 \times 2 \cdot 180$	360×180
γ scatter angle φ	4×120	25
Direction of recoil electron (χ_e, ψ_e)	180×45	1
Electron scatter angle ε	90	1
Sum data space	$\sim 10^{14}$	$1.6 \cdot 10^6$
Field of view ($\leq 2\pi$ sr)	$2 \cdot 180 \times 2 \cdot 180$	60×60
Sum response matrix	$\sim 10^{19}$	$5.8 \cdot 10^9$

Table 5.1: Minimum size of the MEGA data space and response matrix for a sky image (far field). The number of bins for the measured parameters is the *minimum* number which does not lead to the loss of a *very significant* amount of information. Note that the factor "2" in scattered photon direction angles and field of view corresponds to an accuracy of 0.5°.

it be filled via simulations, nor kept in RAM for image reconstruction (the data space would need $\sim$ 100 TB). Moreover, the proposed data space already constitutes a strong simplification of measurements with a real modern-day Compton detector: it does not take into account the different calorimeters with their different energy resolutions, it ignores multiple interactions, and it ignores the distance between the two interactions which influences the angular resolution through the spatial detector resolution.

Therefore all types of imaging algorithms which use a binned data space, like they have been used for COMPTEL or INTEGRAL, are completely ruled out. As a consequence a list-mode based algorithm has to be used. In this type of algorithms no binned data space is used, but a mere list of events (*Barrett et al.*, 1997). Thus the size of the data space is no longer fixed, but proportional to the number of measured events. As long as the number of events is significantly smaller than the number of data-space bins, list-mode algorithms are preferable. For the MEGA telescope as well as for the prototype this is obviously the case. For example, during the calibration of the MEGA prototype $15 \cdot 10^6$ events have been measured (*Andritschke*, 2006).

But list mode has further advantages: Since no binned data space is used, *all* information can be used with full precision as it has been measured for each event. In addition to the information contained in the data space discussed above, for MEGA this means using the position of the first and the second interaction of the gamma ray, the number of interactions, etc. Furthermore, it is easy to integrate different event types like untracked Compton events, tracked Compton events, and pair events into one image. Finally, the detector geometry can easily be changed, which is especially useful for a prototype system under construction. Nevertheless list-mode also has one disadvantage: A pre-calculated response matrix does not exist. Instead the response has to be calculated for each event individually during image reconstruction, which is a time consuming task depending on how accurate the response should be determined.

The selected imaging algorithm for the MEGA telescope is called List-Mode Maximum-Likelihood Expectation-Maximization (LM-ML-EM). Is has been originally developed for medical imaging (*Wilderman et al.*, 1998). Its binned version is similar to Richardson-Lucy-type algorithms (*Richardson*, 1972; *Lucy*, 1974).

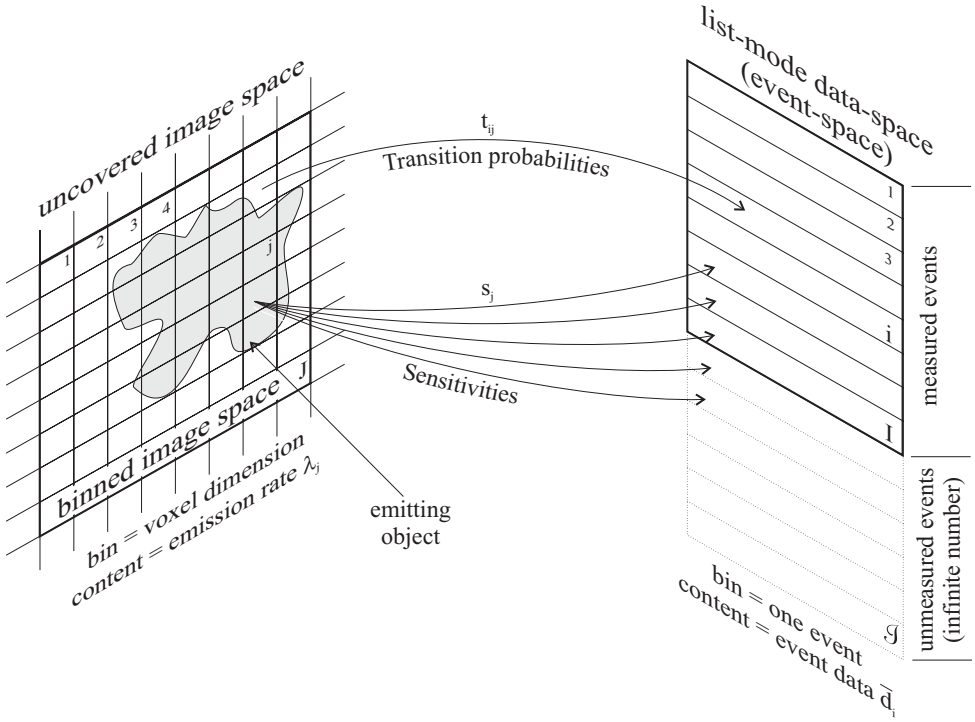

I	data space with all measured events
$\mathcal{I}$	data space of all not measured events
i	event index
J	image space
j	image-bin index
$\lambda_j^{(l)}$	image-bin content at iteration level l
v_i	probability that the event i came from within the image-space ("visibility")
t_{ij}	probability that a photon emitted from j is measured with the parameters of event i ("transition matrix" or "response")
s_j	probability that an event emitted from j is measured ("sensitivity"): $s_j = \sum^{I+\mathcal{I}} t_{ij}$ — note that sensitivity as used here in the context of LM-ML-EM imaging is not identical to the sensitivity of a telescope to an astrophysical source

Figure 5.1: The data spaces and their relations

5.2 The list-mode maximum-likelihood expectation-maximization algorithm

The goal of image reconstruction is to determine the origin of the photons, the image J, from all the measurements I. The likelihood function $\mathcal{L}$ describes the probability that the individual measurements $D = \{y_i\}$ have been generated by the image J with the emissions $\lambda = \{\lambda_i\}$.

$$\mathcal{L}(\lambda) = \prod_i p(y_i, \lambda) \tag{5.2}$$

Since the events (with a few exceptions such as decay cascades) are independent from each other, i.e. the occurance of any event has no effect on the occurance of any other event, Poisson statistics can be applied (with $\bar{y}_i$ as the expectation of the Poisson distribution and Y_i is the number of entries in data space bin i):

$$\mathcal{L}(\lambda) = \prod_i p(y_i, \lambda) = \prod_i \frac{\bar{y}_i^{Y_i}\, e^{-\bar{y}_i}}{Y_i!} \tag{5.3}$$

or in logarithmic description:

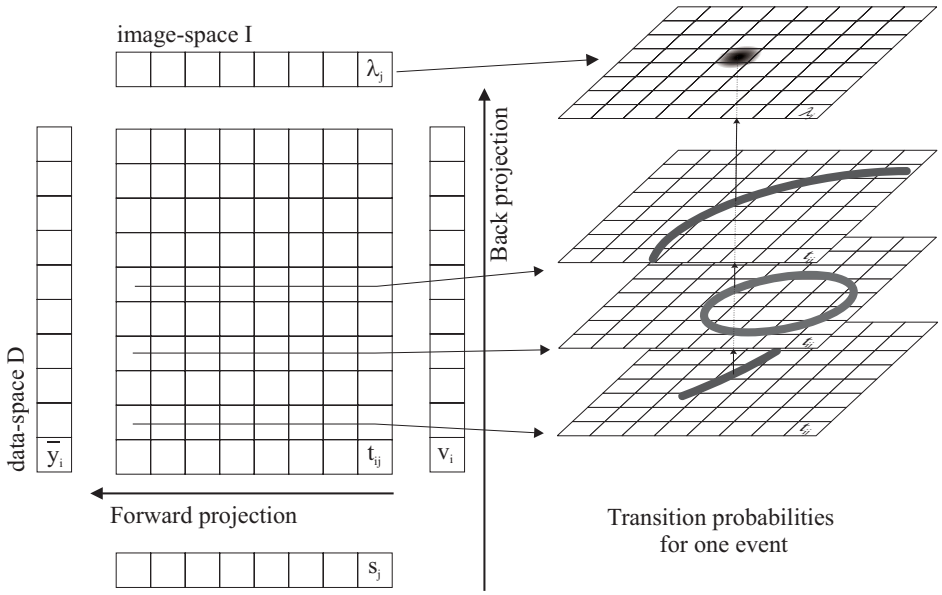

Forward projection (calculate expectation):

$$\bar{y}_i = \sum_k t_{ik}\lambda_k$$

Back projection (maximization of expectation):

$$\lambda_j^{(l+1)} = \frac{\lambda_j^{(l)}}{s_j}\sum_i \frac{v_i t_{ij}}{\bar{y}_i}$$

Figure 5.2: How the algorithm works. Five matrices are used by the algorithm, the image λ_j, the response of the individual events t_{ij}, the efficiency s_j, the expected data space content $\bar{y}_i$ and for Compton events the visibility v_i. The rows of t_{ij} represent in each bin the probability that the event originates from the given bin. In a visual representation, Compton cones and arcs would appear. The iterative algorithm maximizes the expectation in two steps. First, given the current estimate of the image λ_j and the response t_{ij}, the expectation that this event is measured, $\bar{y}_i$, is calculated. This step basically is a forward projection from image into data space. The second step maximizes the expectation and corrects the old image. This step is basically a backprojection from data into image space.

$$\ln \mathcal{L}(\lambda) = \sum_i \left[-\bar{y}_i + Y_i \ln \bar{y}_i - \ln Y_i!\right] \tag{5.4}$$

The goal is now to find that source distribution (image) which has the highest probability to generate the data D, i.e. one has to find the maximum of the likelihood function, by solving $\frac{\partial \ln \mathcal{L}}{\partial \lambda_i} = 0$. Since this is not possible in the general case, *Lange and Carson* (1984) suggested to maximize the expectation of the likelihood function instead. They derived an iterative algorithm to reconstruct the image. Translating their algorithm into list-mode (*Wilderman et al.*, 1998) results in the following equation:

$$\lambda_j^{(l+1)} = \frac{\lambda_j^{(l)}}{s_j}\sum_i^I \frac{v_i \cdot t_{ij}}{\sum_k t_{ik}\lambda_k} \qquad \forall j \in J \tag{5.5}$$

A derivation as well as an explanation how and why the algorithm works and variations of it can be found in *Zoglauer* (2000); an illustration and brief summary is given in Figure 5.2.

Compared to the formulation in *Wilderman et al.* (1998), Equation 5.5 contains the additional factor v_i, the visibility of event i. It stands for the probability that the event came from the selected image space. This factor is in principle a reinterpretation of the original Y_i factor from the unbinned ML-EM algorithm (*Lange and Carson*, 1984), which represented the number of bins in the data space element i: Especially for Compton events with large cone sections in combination with small image spaces, the event has a non-zero probability that it came from

outside the image space. Consequently, only a fraction of the event is seen in the image, the fraction v_i.

The original list-mode algorithm (*Wilderman et al.*, 1998) did not contain any criteria to stop the iterations. It simply converges asymptotically. The best images, however, are obtained shortly before convergence, when the width of the point sources corresponds to the intrinsic angular resolution of the detector. At this point the iteration is stopped by hand.

In the following section the determination of the response T is discussed in more detail.

5.3 Imaging response of a Compton and pair telescope

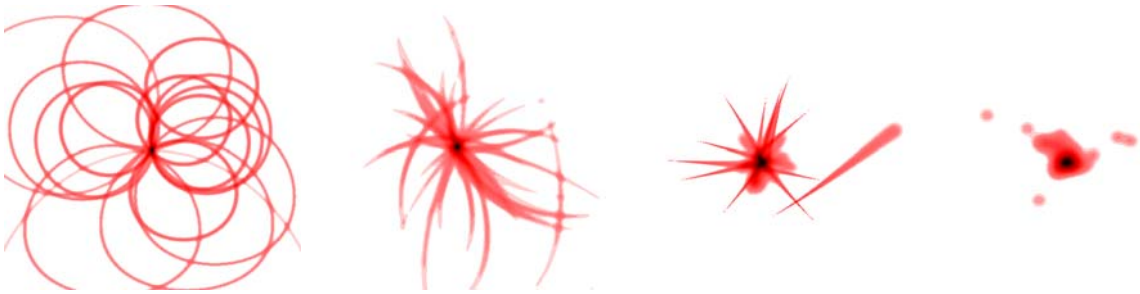

Figure 5.3: The 4 different event types of a tracking Compton and pair telescope. Left to right: Untracked Compton events; tracked Compton events; high-energy tracked Compton events with incomplete absorption; pair events.

Figure 5.3 illustrates the four basic event types of a MEGA-type instrument: For most interactions below 2 MeV, the kinetic energy of the Compton recoil electron is not sufficient to produce a track. Therefore the photon's origin can only be restricted to a cone (see Section 2.2.4.1 and Figure 5.3, left). Its width is determined by the accuracy of energy and position measurements. Between 2 and 10 MeV most events have an electron track and a reasonable amount is completely absorbed (at least in the MEGA satellite geometry). Thus, their origin is restricted to an arc, a section of the cone (Figure 5.3, middle left), whose length is determined by Molière scattering. Above 10 MeV most of the Compton scatter events are incompletely absorbed, but the direction of electron and scattered photon is well defined. Therefore, the origin of the photon can be restricted to the great circle between (reverse) electron and photon direction (Figure 5.3, middle right). Since the direction of the scattered gamma ray can be determined more accurately than the direction of the recoil electron (Molière scattering), the origin distribution has a drop-like shape. Measured energies can further restrict this arc (details see Section 2.2.4.2). The origin of pair events (Figure 5.3, right) can be calculated from electron and positron direction and energy (see Section 2.3). The main uncertainties are due to Molière scattering of electron and positron in the Silicon layers.

Two parameters describe the imaging response in Equation 5.5: the event response t_{ij} and the sensitivity s_j (Note that the word "sensitivity" denotes a quantity here that is different from the sensitivity describing the overall performance of an astrophysical telescope). Figure 5.4 summarizes all probabilities which contribute to these parameters for Compton events.

The easiest way to determine the sensitivity s_j are Monte-Carlo simulations. This avoids the analytic calculation of all the probabilities of Figure 5.4. The determination of the response t_{ij} is less straightforward: it is calculated by looping over all image-space bins and describes the probability that the measured photon was emitted from any one given image bin. The calculation has two steps: determine the absorption probability and multiply by a normalized response which basically represents the Compton cone/arc or pair origin distribution.

Using list mode allows to strongly simplify the large response matrix required for a binned-mode approach (see Table 5.1) — given the case of a very sparsely populated data space, as

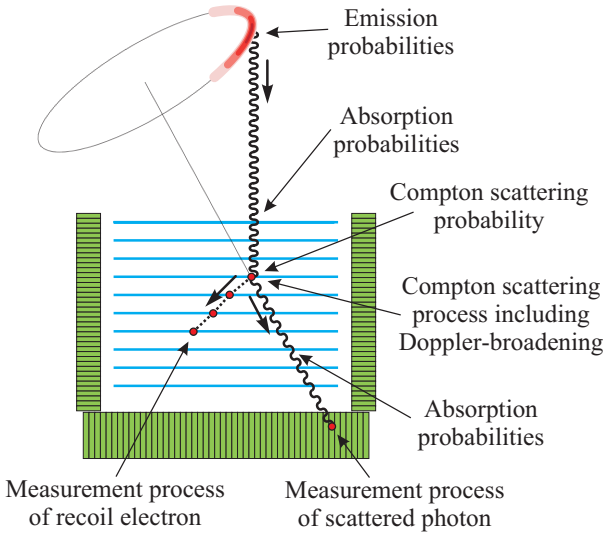

Figure 5.4: Illustration of the processes and associated probabilities which have to be considered during calculation of t_{ij} and s_j, for the case of a Compton-scatter event.

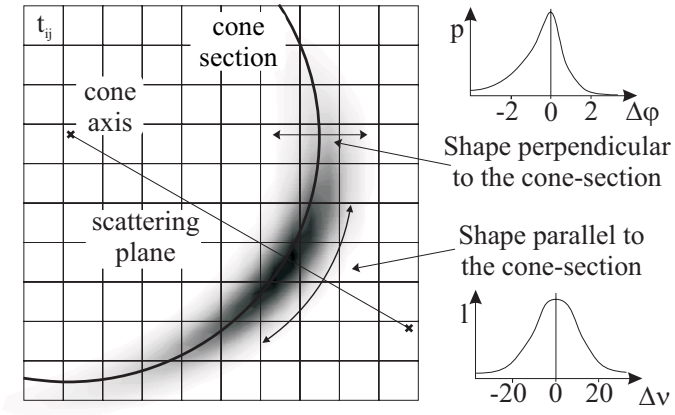

Figure 5.5: Modeling the measurement process: The cone-section is filled perpendicular to and along with two profiles: the first depends mainly on the energy measurement and the second on Molière scattering.

is the case for the type of telescope discussed here. Using only the measured events as data space is obviously accompanied by a reduction of the size of the response matrix, since then the response is only needed for the measured events. The matrix is now small enough that generating the t_{ij} corresponding to the measured events is feasible and drastically reduces the amount of storage space. However, since the t_{ij} have not been previously stored for all possible events, they have to be calculated on-the-fly. This can be done using simpler response matrices, because the matrix does not need to encode the complete Compton scattering — this information is already contained in the event list. Knowing the properties of the Compton event y_i currently under consideration (scatter angle and direction, recoil electron angle and direction), the profile $p\,(\Delta\varphi)$ of the cone section and, in case of tracked events, the length $l\,(\Delta\nu)$ of the arc (see Figure 5.5) are sufficient to create the single-event image responses illustrated in Figure 5.2 on the right as transition probabilities for one event. The profile p of the cone-section is dominated by the energy measurement of electron E_e and scattered gamma-ray E_g, by Doppler-broadening, and by the spatial resolution of the detector. The length l of the arc is mainly determined by direction and energy of the recoil electron.

Two ways are used to determine the exact shape of the Compton cones and arcs. The simplest form uses a Gaussian approximation for p and l, with widths corresponding to the values derived from ARM and SPD. The more complex approach relies on predetermined response matrices. From a large set of simulations the profiles are determined as a function of the measured parameters: perpendicular to the cone $p = p(\varphi_{kin}^{meas}, E_i^{meas})$ and perpendicular to the scatter plane $l = l(\varepsilon_{kin}^{meas}, E_e^{meas})$, where the profile represents the distribution of possible true

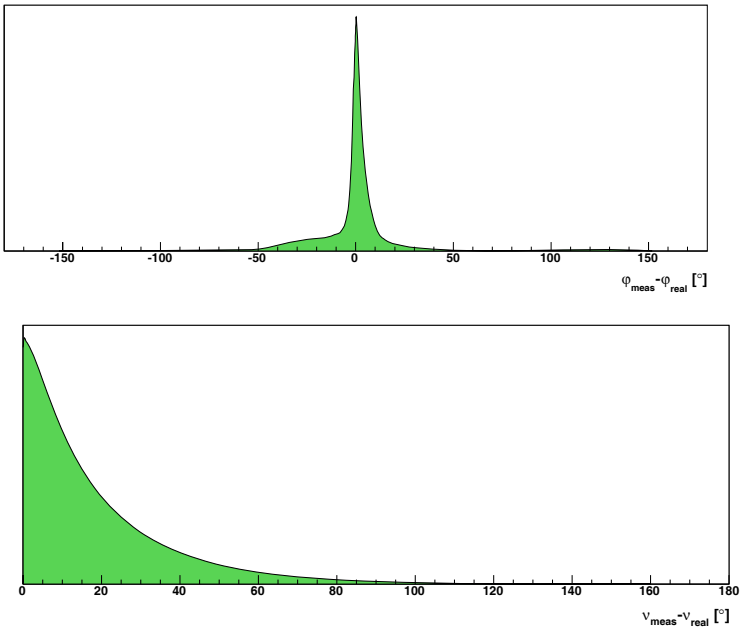

Figure 5.6: Examples of the profiles used for reconstructing Compton events. The top figure shows a p profile for tracked events with 2 MeV measured total energy and 60° scatter angle for the MEGA satellite geometry. Obviously, the shape resembles the ARM. The wings, however, originate from incompletely absorbed events of higher energy. The bottom figure shows the corresponding l profile, which is mainly determined by Molière scattering. It resembles the SPD. During image reconstruction those simulated profiles are smoothed and interpolated.

event cones for the given measured cone, and the distribution of possible true scatter planes for the measured scatter plane, respectively (examples are given in Figure 5.6). Figure 5.5 illustrates how both factors model the Compton response. For each event the t_{ij} are calculated by combining the event cone with the p profile perpendicular to the cone and the l shape perpendicular to the scattering plane. The combined shape is normalized in a way that if the shape would be completely contained in the image, integrating over the image would give 1.

For low energies this response calculation gives the Compton circles/arcs of Figure 5.3, left. With increasing energy, the length of the arc gets smaller, since the Molière scattering decreases, but the profile gets broader due to energy leakage. At high energies, when the energy measurement is rather incomplete, but the direction of the recoil electron is well known, the events have shapes like in Figure 5.3, middle right.

Compared to Compton events, pair events are trivial. The image response description relies on just one parameter to describe the angular extent of possible origins. Start point for the determination of the t_{ij} is the calculated origin. The applied profile is again either a 2D Gaussian fit, where the width corresponds to the angular resolution, or as a more advanced approach, using a profile $p = p(E_i^{meas})$, which describes the distance to the measured origin of the photon. A future expansion of the handling of pair events should contain not only a 1D profile, but a 2D profile as a function of the incidence angle, since for large incidence angles a slight shift of the reconstructed positions towards smaller incidence angles can be observed; this so called fish-eye effect, which has also been found in other pair telescopes like EGRET (*Thompson et al.*, 1993), is currently not taken into account.

The performance of the image reconstruction is best demonstrated through the images obtained for a variety of sources. Several examples can be found in Chapters 8 and 10.

While list mode allows the most accurate description of the response within the limits of available computing resources and thus probably produces the best images, it has also some disadvantages. First, it is extremely difficult to get an absolute normalization, i.e. intensity/flux as a result of the image reconstruction process. For this, all normalizations have to be correctly determined for each event. While this is no problem for 1D problems such as spectral deconvolution, for Compton imaging in list-mode is would be extremely time consuming. Consequently,

this has not been done for any images in this work (i.e. all s_j are assumed to be one, and no absorption probabilities are calculated). Secondly, for a real space mission even only having a list of all events will require extreme computer resources. In this case (all-sky image including all events), probably some type of simplified binned mode algorithm might be necessary.

Part III

The MEGA prototype and its performance

Chapter 6

The MEGA Prototype

When the completed MEGA prototype achieved its first light in February 2003 at MPE, an important step towards the next generation of Compton telescopes was taken: MEGA added a new dimension to the measurement of gamma rays in the Compton regime, the direction of the recoil electron. This chapter is dedicated to the setup and the calibration of this unique instrument.

6.1 Setup of the prototype instrument

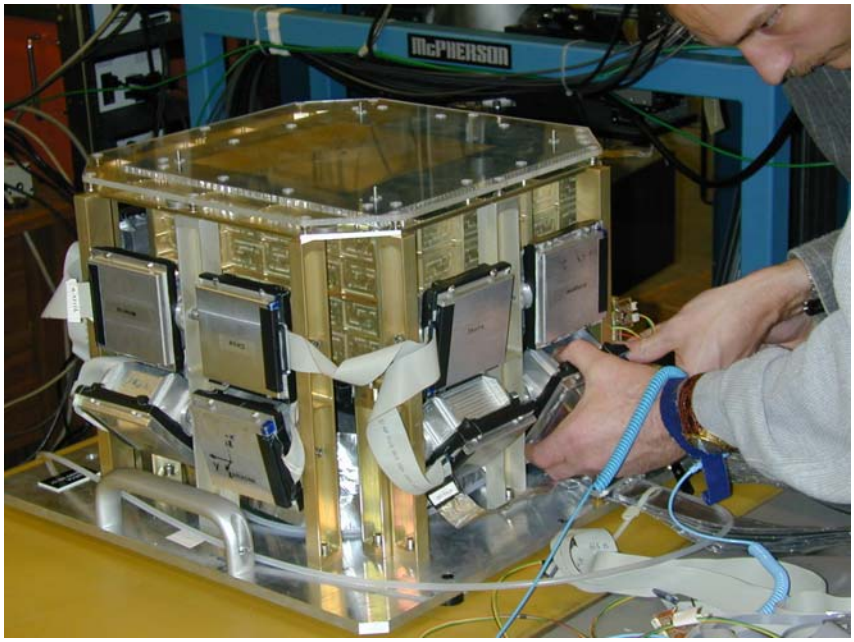

Figure 6.1: MEGA prototype detector: The tracker is housed in the central gold-colored box. It consists of 11 layers; each is made up of a 3×3 array of double-sided Silicon strip detectors. The lower hemisphere of the tracker is surrounded by 20 CsI calorimeter modules, which are housed in the aluminum boxes.

Each new measurement concept, such as adding electron tracking to a Compton telescope, needs to be proven before it is applied to a full-scale gamma-ray astronomy mission. This validation involves several steps, including extensive simulations as well as the construction and calibration of a prototype. The latter's performance of course must be verified against the simulations. This is the level MEGA has reached. In the future, the MEGA prototype probably

will be flown on a balloon mission to prove its background rejection capabilities. This would be an essential step before implementing an astrophysical mission.

The construction of the MEGA prototype, which started in the mid 1990s, was completed in February 2003. Since then, extensive calibration measurements have been performed. The prototype consists of three detector sub-systems: A tracker in which the primary Compton scatter or pair creation process takes place, a calorimeter which stops and measures all secondary particles, and finally, for measurements in a real astrophysical environment, an anti-coincidence shield which encloses the detector and rejects charged particle events.

Table 6.1 summarizes the main properties of the three MEGA detectors subsystems, which will be described in detail in the next sections. An overview of the data acquisition system, including electronics design and trigger processing scheme, can be found in *Kanbach et al.* (2005) and in more detail in *Andritschke* (2006).

	Si-strip layer	Calorimeter (one unit)			ACS
		2 cm	4 cm	8 cm	
Number of units	11	8	8	4	1
Material	Si	CsI(Tl)	CsI(Tl)	CsI(Tl)	BC412
Density $[g/cm^3]$	2.33	4.5	4.5	4.5	1.0
Active mass $[g]$	37.8	250	500	1,000	17,000
Avg. energy res. 1σ $[keV]$	9.7 @ 122	38 @ 662	38 @ 662	38 @ 662	n/a
Spatial resolution $[mm^3]$	0.47×0.47×0.5	5×5×20	5×5×40	5×5×27 (FWHM)	n/a
Avg. timing resolution $[\mu s]$	1	5	5	5	0.05
Avg. noise threshold $[keV]$	51	181	181	221	90
Channels	768	120	120	240	6
Avg. defective channels [%]	10	8	8	12	0

Table 6.1: Summary of the properties of the different detector sub-systems of MEGA.

6.1.1 Tracker

The most innovative part of MEGA is the tracker, also called "D1". It has two main purposes: First, the D1 serves as scatterer or converter for the Compton and pair interactions, respectively. Second, this tracker records energy and trajectory of all generated charged particles. For each charged particle, the interaction position and the deposited energy in each layer of the tracker is measured with high accuracy.

These main requirements demand a tracker with a high probability for Compton scattering or pair production, low Doppler-broadening in the case of Compton scattering, and a reasonable range of the created electrons: The electrons need to pass through enough layers to allow a measurement of their direction, but they also need to be stopped within the tracker. Furthermore, a high pixelation and good energy resolution is crucial for the determination of the trajectory and the energy of the electrons and to allow the reconstruction of the origin of the photons. Considering all requirements, Silicon-strip semiconductor detectors are the best choice for the tracker of a combined Compton and pair telescope.

The prototype tracker is a stack of eleven layers of double-sided Silicon strip detectors, which have a separation of 1.0 cm (Figure 6.2). Each layer consists of a 3 × 3 array of Silicon wafers (Figure 6.3). Each wafer has a sensitive area of 6 × 6 cm^2, is 500 μm thick, and has a strip pitch of 470 μm for a total of 128 strips per wafer side. Strips on one side of the wafer determine the x-position of an interaction, orthogonal strips on the other side of the wafer determine the corresponding y-position. The strips of 3 adjacent wafers in each layer are interconnected ("daisy-chained"), and the signals are read out by the front-end chips at the edge of the layer. In each layer, 3 × 128 strips are read out on each side. The tracker consists of a total active Silicon mass of 415 g, read out by a total of 8448 channels.

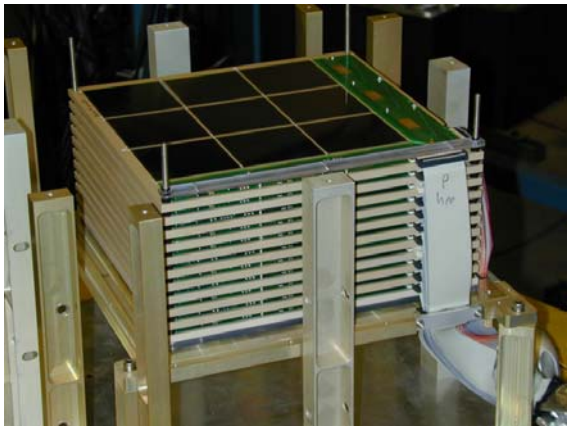

Figure 6.2: The complete tracker is a stack of 11 layers which are spaced 1 cm from each other.

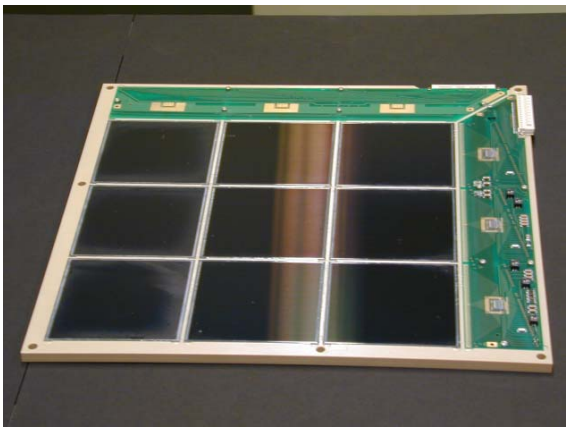

Figure 6.3: One layer of double-sided strip-detector. It has a size of roughly 23 × 23 cm^2 and consists of 3×3 Silicon wafers.

The achieved energy resolution varies from layer to layer and strongly depends on the temperature and on the quality of the individual wafers. Moreover, top and bottom sides of the wafers, called p- and n-side according to the doping required in the semiconductor, have different properties: The energy resolution on the p-side of the strips is roughly a factor of two better than the resolution on the n-side. For the p-side the average FWHM at 122 keV (^{57}Co) is 23 keV, where the best layer has 15 keV and the worst ∼30 keV for room temperature. On average, the trigger threshold is 60 keV and the noise threshold 51 keV. The achieved position resolution as measured by muons is 290 μm and the time resolution is close to 1 μs.

A detailed characterization of the strip detectors can be found in *Schopper* (2001) and *Bloser et al.* (2003). The performance of the complete tracker is described in *Andritschke* (2006).

6.1.2 Calorimeter

The purpose of the second detector ("D2"), the calorimeter, is to stop and measure all secondary particles: the electrons and positrons from pair-creation as well as the scattered Compton photons. Especially for the reconstruction of Compton events, it is crucial to know the energy and direction of the scattered gamma-ray to a very high accuracy in order to obtain well-defined event cones. In addition, in a satellite instrument in low-earth orbit, the calorimeter also (at least partly) shields the tracker from the dominant background component, atmospheric photons. Consequently, a high stopping power is required and thus high-Z materials are preferable. In addition, the detector material must allow for a high pixelation and have a good energy resolution.

At the time the MEGA prototype was designed, the scintillator CsI(Tl) was the material of choice. It provides a high light yield and therefore an acceptable energy resolution, and can be cut into small bars to allow a relatively high pixelation. Moreover, it is available in sufficient quantities for a reasonable price.

The MEGA calorimeter is assembled of 20 individual modules of different depth: At the bottom the blocks are 8 cm thick, the lower side walls have a depth of 4 cm and the upper side walls 2 cm. Each block consists of an array of 12 × 10 CsI crystals which have a cross-section of 5×5 mm^2; their length corresponds to the block thickness. The crystals in each block are separated by several layers of Millipore paper, which provides a high reflectivity. For light readout the crystals are coupled to an array of Si-PIN-diodes via Silicone cushions. The thinner side calorimeters have PIN diodes only on the side facing away from the tracker in order to minimize the passive material between tracker and calorimeter. The large bottom calorimeters, however, do have double-sided readout. This allows the measurement of the interaction depth

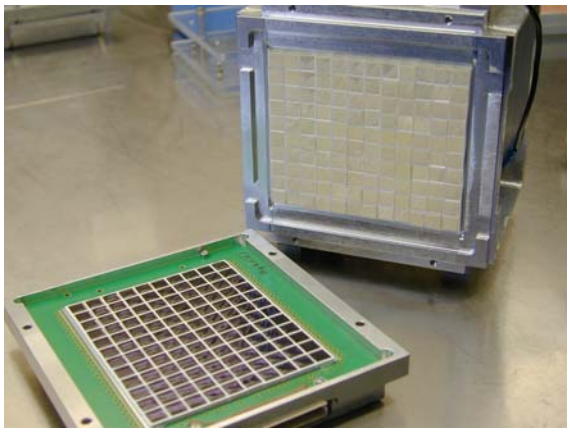

Figure 6.4: One partially disassembled 8 cm calorimeter module. The 120 CsI crystals surrounded by Millipore and enclosed in the Aluminum housing are visible at the top right. The removed PIN diode array, with the Silicone cushions coupling the CsI crystals to the diodes, is lying at the bottom left.

in the crystal, but has the disadvantage that electron/positrons moving from the tracker to the calorimeter generate a signal in the diodes, complicating the determination of the total energy of these particles. On average, a depth resolution of 2.7 cm FWHM is reached for large energy deposits. The total active CsI mass is 10.8 kg and the calorimeters have 2880 readout channels.

The moderate energy resolution of the prototype's calorimeter is one of the major drawbacks of the whole prototype and is the limiting factor for its angular resolution: The side calorimeters achieve only ∼13 % FWHM. Improvements in the performance of the calorimeter are mandatory for a final satellite version. Improving the readout from PIN to drift diodes, and probably exchanging the scintillator material for the newer $LaBr_3$, would allow for significantly improved energy resolution, lower thresholds, and shorter coincidence windows.

Detailed descriptions of the MEGA calorimeter can be found in *Andritschke* (2000) and *Andritschke* (2006).

6.1.3 Anti-coincidence shield

The third detector subsystem is the anti-coincidence shield ("ACS"). Its purpose is to allow discrimination against all events in the detector induced by charged particles. While this system was not employed during the laboratory or accelerator calibrations of the MEGA prototype discussed below, the ACS is an intrinsic part of the whole detector system for a prototype balloon flight and eventually for a space instrument. Charged particles of solar and cosmic origin, as well as charged particles trapped in the earth's magnetosphere in case of a satellite, or secondary charged particles generated in the earth's atmosphere in the case of a balloon experiment, are detected in the instrument along with the gamma rays of interest. Reliable rejection of charged-particle events improves the instrument's signal-to-background ratio and lowers the demands on data acquisition and telemetry.

The MEGA ACS, built in the form of a house, almost completely encloses the detector head (see Figure 6.5). Its walls consist of 1.27 cm thick BC-412 scintillator. Embedded into the scintillator are wavelength-shifting fibers (Figure 6.6) to propagate the photons to the photo multipliers.

6.1.4 Setup of the prototype

The arrangement of the individual modules has to fulfill certain criteria: most of the scattered gamma-rays should be stopped, and the instrument should achieve a wide field of view. In addition, given the relatively small number of calorimeter modules available, these should be placed such that a minimum amount of passive material lies between the CsI and the tracker's Silicon layers. The current setup of the prototype has been optimized using extensive simulations to achieve the best possible sensitivity for a detection of the Crab during a future MEGA balloon

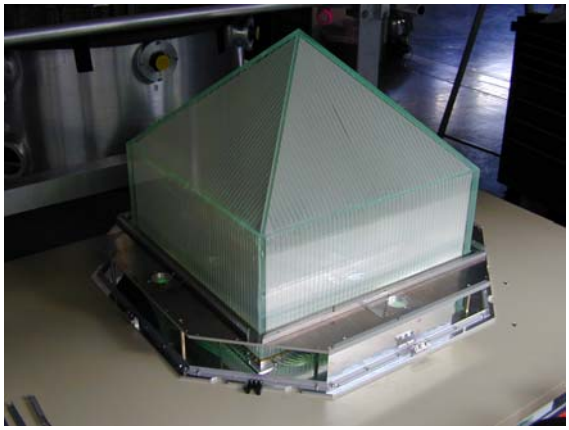

Figure 6.5: The ACS dome without light shields.

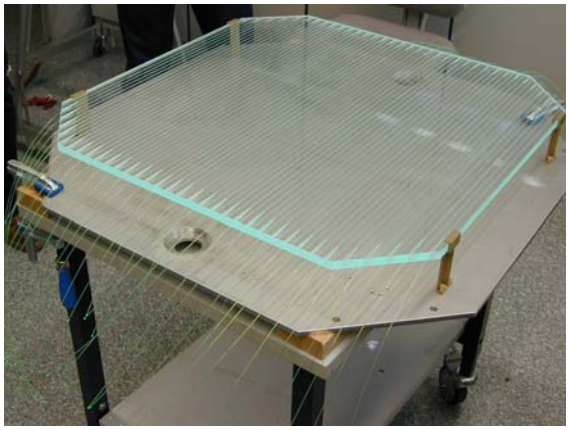

Figure 6.6: Wave-length shifting fibers glued into the lower ACS plate.

flight. The resulting geometry is basically a half-open sphere; in the bottom hemisphere the calorimeters are packed as closely as possible. The distance between tracker and calorimeter modules turns out to be crucial: Putting the calorimeters too close to the tracker maximizes the efficiency, but lowers the angular resolution and thus the achievable sensitivity. The optimum distance between bottom calorimeter and bottom layer of the tracker was determined to be 5 cm — however, at the time of this calculation a significantly better energy resolution in the calorimeters was expected than what was later achieved. The thinner calorimeter modules are arranged according to the stopping power needed for on-axis incidence of photons: small scatter angles correspond to a larger energy of the scattered gamma-ray, which need more stopping power. Thus the the 4 cm calorimeters where placed at the lower side, the 2 cm calorimeters at the sides — both as close as mechanically possible to the tracker. The final setup can be seen in Figure 6.1.

6.2 Calibration measurements

The calibration of a Compton and pair telescope is a two-step process: The first step is to determine the correlation between detector signals, which are measured in ADUs (analog-digital-converter units), and energy for each individual detector channel. Since the prototype has 11328 individual channels and the response of the detector is non-linear and different for each individual channel, the analysis of the calibration data is a lengthy process. This first step is from now on referred to as "single-channel" calibration; details can be found in *Andritschke* (2006).

While in the first step the response of single detector elements to a well-defined source is established, the second step focuses on the response of the detector as a whole. Here, parameters such as overall energy resolution, angular resolution, field of view, efficiency, and polarization and their dependence on energy, scatter-angle, etc. are determined. The evaluation of these parameters for the MEGA prototype is discussed partly in this work and partly in *Andritschke* (2006). In Chapter 7, the overall energy resolution achieved with the prototype is presented. Chapters 8 and 9 discuss the angular resolution of the MEGA prototype and its capabilities as a polarimeter.

The calibration of the MEGA prototype is comprised of two phases: measurements with laboratory sources at MPE in Garching (February to March 2003) and beam measurements at the High Energy Gamma Source at Duke University, Durham, NC (April/May 2003).

The beam measurement was intended to explore the complete energy range of the prototype up to 50 MeV and to determine the response of the detector to linearly polarized photons. The laboratory measurements with radioactive sources were only used for test and verification

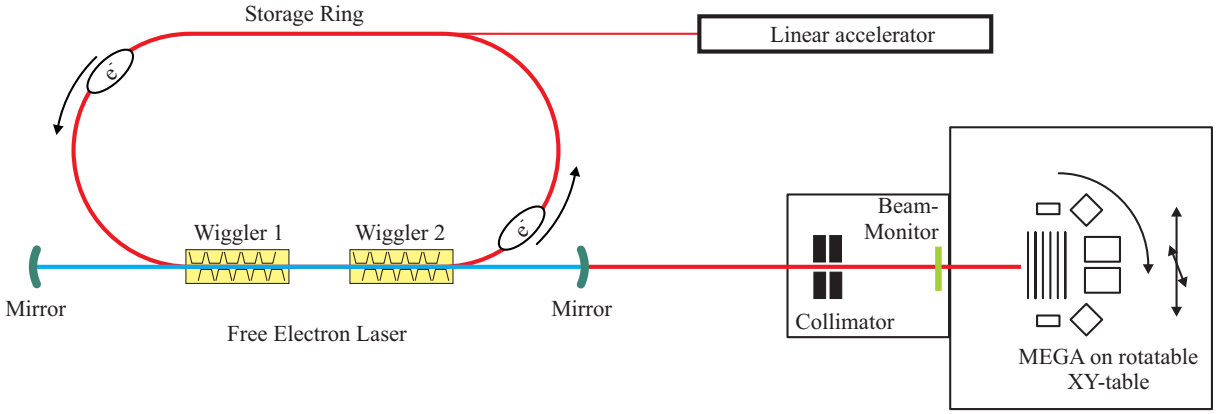

Figure 6.7: Schematic drawing of the setup at HIGS. See text for details.

purposes before the Duke measurements. In the following, emphasis is put on the Duke measurements, since the initial lab measurements were taken under still changing measurement settings, and consequently no complete single-channel calibration exists. Only specific measurements for multiple and extended sources, which were not repeated at Duke and only require a rough calibration, are included here.

The detailed calibration of the MEGA prototype has been performed using data acquired with the High Energy Gamma Source HIGS (*Litvinenko et al.*, 1995, 1997) of the Free Electron Laser Laboratory (FELL) at Duke University. HIGS produces 100% polarized, monoenergetic (energy spread 1-2%) gamma rays in the energy range from ∼0.7 up to ∼50 MeV via Compton backscattering.

A schematic of the setup of the free electron laser and MEGA can be found in Figure 6.7. The generation of gamma rays at HIGS is a two-step process: First monoenergetic photons (IR – UV) are produced by a free-electron laser. Then those photons are Compton backscattered through head-on collisions with the electrons and thus reach MeV energies.

For this purpose a bunch of electrons is injected into the storage ring from a linear accelerator. A section of the ring contains wigglers, a set of magnets which generate an alternating magnetic field. The electron bunch is forced on a sinusoidal trajectory, and as a result the electrons start emitting synchrotron radiation in the IR to UV regime — depending on electron energy and wiggler parameters. The forward component is captured in a laser cavity, which is formed by two mirrors at the beginning and end of the wiggler-section of the storage ring. All beam and wiggler parameters are chosen such that electron and photon bunch are moving through the wigglers simultaneously. For certain resonance energies of the electrons, they interact with the electric field of the previously generated photons. As a result the electrons emit in phase, which leads to resonant amplification of the photon bunch — the free-electron laser, producing monoenergetic and 100% polarized photons.

When the facility is not only used as a free electron laser, but as a gamma-ray source as during the MEGA calibration, a second electron bunch is injected in the storage ring. This bunch is stretched compared to the first one, to prevent stimulated emission (lasing). It hits the photon bunch head-on in the field-free zone between the wigglers. The photons are inverse-Compton scattered on the electrons and boosted to gamma-ray energies. During the backscattering process of low energy photons with high energy electrons, the original polarization is almost 100% conserved (*Park et al.*, 2001) — this is not to be confused with the distribution of photon scatter *directions* described by the Klein-Nishina Equation 2.11. Lead collimators, which are located ∼60 m from the collision area, select the backscattering component of the beam, which then interacts in the MEGA detector. The opening angle of the collimator determines the energy

Figure 6.8: Setup of MEGA at Duke: The MEGA prototype (1) is located below a Styrofoam housing to regulate the temperature via an air-conditioning system (4). MEGA is mounted on an XY-table (2) to scan the detector with the narrow pencil beam. To verify the field of view,, the whole XY-table assembly can be rotated (3) around the center of the tracker. The data acquisition system (front-end (5), ADCs (6), CPU (7)) is also shown.

spread and the beam width. For the MEGA calibrations the latter was either 0.5 or 1 inch (1.27 or 2.54 cm), corresponding to an energy spread of roughly 1-2%. To record the intensity of the beam as a function of time, between MEGA and the collimator a beam monitor was installed. A detailed description of the beam monitor can be found in *Andritschke* (2006).

Figure 6.8 illustrates the MEGA setup. The detector was mounted on an XY-table, which allowed to illuminate different positions of the MEGA tracker with the gamma-ray pencil beam. Eleven positions were illuminated: the centers of all nine wafers, the electronics and the calorimeter. The latter two measurements were intended to verify the background rejection capabilities. To scan the detector at different incidence angles and determine the field of view of the detector, the XY-table was mounted rotatable around the center of the tracker.

The original calibration plan was to cover the whole beam energy range from 0.7 to 50 MeV with at least 7 data points (710 keV, 2 MeV, 5 MeV, 8 MeV, 12 MeV, 25 MeV and 50 MeV) and to sample the field of view — at least for energies not accessible with laboratory radioactive sources (5 MeV and higher) — with at least four angles: 0°, 30°, 60°, and at least one incidence at 180° to determine the background rejection capability of the event reconstruction algorithms. The calibration schedule was divided into two sections, up to 8 MeV and above 8 MeV, due to a necessary change of mirrors for higher energies which took 72 h and had to be performed during the weekend. Unfortunately, at lower energies the beam flux achieved was significantly lower

Energy [MeV]	0.7	2	5	8	10	11.9	17	25	37	49
0°	270	216	315	225	405	405	405	315	405	1035
30°	216	0	315	0	495	495	495	360	450	360
60°	0	0	450	0	540	675	540	540	540	540
80°	0	0	0	0	0	350	0	540	450	450
120°	0	0	90	0	0	135	0	90	90	135
180°	0	0	90	0	135	90	0	0	90	90

Table 6.2: Matrix of all measurements as a function of energy and incidence angle. Table entries represent thousands of triggered events recorded in a given configuration.

than expected so that significantly more time per energy and incidence direction was necessary to achieve the minimum number of photons. In addition, the beam showed stronger contamination than expected, so that only the minimum requirements were achieved below 10 MeV. At higher energies, the beam flux was significantly higher, and an unexpected time extension was granted. As a result, at energies above 8 MeV MEGA recorded significantly more events at more angles and energies than were required to determine the energy, angular and polarization response of the prototype.

A complete list of measurements performed, as well as the number of triggered events recorded in each run, is given in Table 6.2. These number, however, are not equal to the number of valid photon events detected, as later chapters will show. The following three chapters are dedicated to the analysis of different aspects of this data.

Chapter 7

Event characteristics and spectral properties of the MEGA prototype

This and the following two chapters describe the recovery of the three main photon properties from MEGA prototype calibrations: energy, direction, and polarization. Note that these chapters are not intended to fully characterize the prototype, instead they focus on the recovery of the original photon parameters from and the performance of the reconstruction and imaging algorithms on real data. Other key parameters of the prototype such as efficiency, etc. are discussed in *Andritschke* (2006). This chapter is based exclusively on the on-axis beam-calibration data from the Duke campaign, for which the finest sampling of the spectral domain is available.

7.1 Event statistics

Compared to the event reconstruction of the MEGA satellite geometry — which thus far exists in simulations only, the actual prototype provides a variety of challenges: Non working channels, channels providing fake signals, high and varying thresholds, capricious energy resolutions as well as position resolutions in the large bottom calorimeters, etc. Moreover, the relatively small prototype with its large amount of passive material is severely handicapped by incomplete energy measurements.

For the event reconstruction, the classic approach has been used (Spearman-Rank correlation for tracking, Classic Compton Sequence reconstruction for the Compton interactions), because the Bayesian approach would have required more CPU resources than available. The event reconstruction as described in Chapter 4 did *not* use any prior knowledge about the input photons, such as their energy or the path of the beam within the prototype. This event statistics is intended to provide an overview of the characteristics of the data. Thus no event selections have been applied except where explicitly noted, and wrongly reconstructed events are part of the data set.

Figure 7.1 shows the distribution of the different event types as a function of the incident photon energy. According to their cross-sections (see Figure 1.1), the fraction of Compton events is expected to decrease with increasing energy, while the number of pair events should increase. Contrary to this expectation, especially at 710 keV a high fraction of pair and charged-particle (e.g. single straight paths from the tracker into the calorimeter or showers) events has been detected. Since such events could not possibly have been induced by 710 keV photons, this indicates a significant contamination of the beam with high energy photons.

This can easily been shown by imaging these events. Figure 7.2 prove that the pair-producing photons originate from the beam. Direct energy measurements at tens of MeV are not possible with the small prototype (see next section), but the achieved angular resolution and the opening

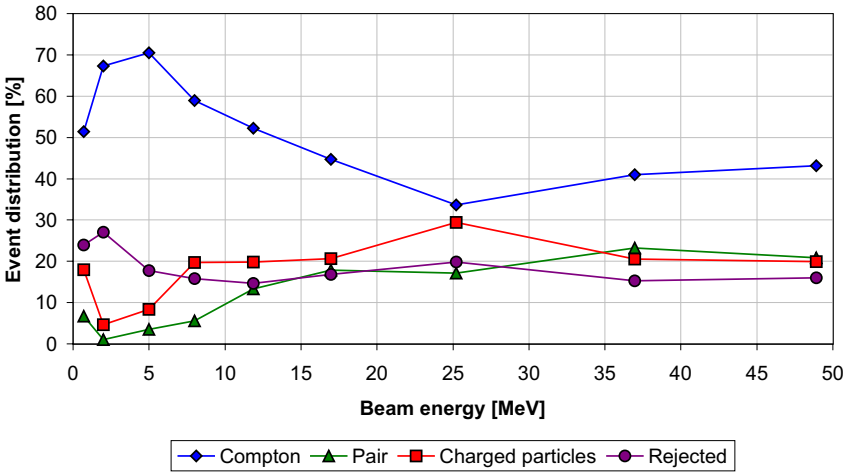

Figure 7.1: Distribution of reconstructed event types as function of the incidence energy for all on-axis Duke measurements. See the text for more details.

angle for these pairs indicates a high-energy component in the beam with an average energy around 20 MeV (compare Figure 8.11).

The cause of this "pollution" is not completely understood. However, since this was the first measurement, the vacuum in the storage ring might not yet have been optimal. In addition, at 710 keV it was extremely difficult to get sufficient gamma-ray flux. Thus it was necessary to keep the electron current in the storage ring at a rather high level (20 mA). All facts together might have resulted in more bremsstrahlung photons than in later measurements.

At 25 MeV a slight overall reduction of Compton and pair events is visible, together with an increase of rejected and charged-particle events. The 25 MeV measurement was the first measurement after the mirror change. Here, pair-creation is the dominant interaction process. If a pair creation occurs outside the sensitive material, above the tracker, for example in its protective cover, then two separate charged particle tracks are visible. Since the vertex of these pair events is not located in the tracker, they are classified as showers. To reject such events, in all later high-energy measurements (10 – 50 MeV) the first layer was used in anticoincidence — this explains the inconsistency of the 25 MeV data point. Even with the first layer used as anti-coincidence, the fraction of charged-particle events remains constant at 20%, between 10 and 50 MeV.

Figure 7.3 splits the rejected events into their main sub-categories. The largest fraction are events which have not at least one complete interaction in the tracker and one in the calorimeter; all of them are due to malfunctions in the prototype: At smaller energies, for most of them only one strip — not two orthogonal strips — measured an energy deposit. Thus those events may trigger, but the position in the tracker cannot be recovered. In addition events exist for

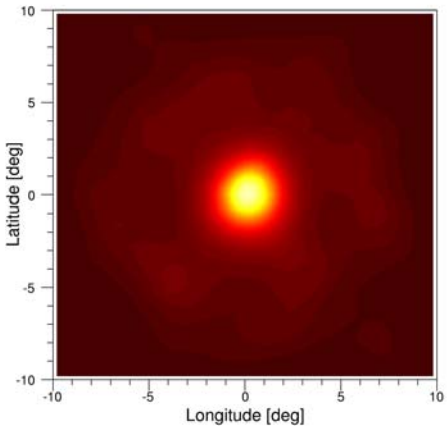

Figure 7.2: Image of the contamination component (only pair events in the data are imaged here!) in the 710 keV measurement. Imaging unambiguously reveals its origin from the beam (at 0°,0°).

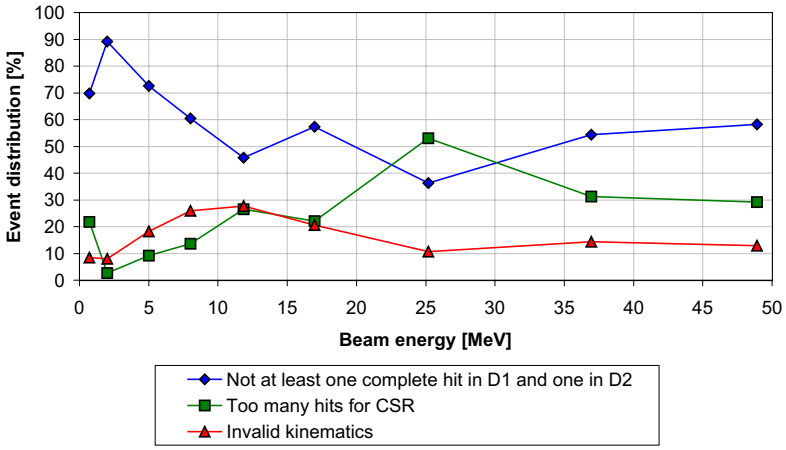

Figure 7.3: Rejection reasons for events during the event reconstruction (100% ≙ all *rejected* events). A detailed description can be found in the text.

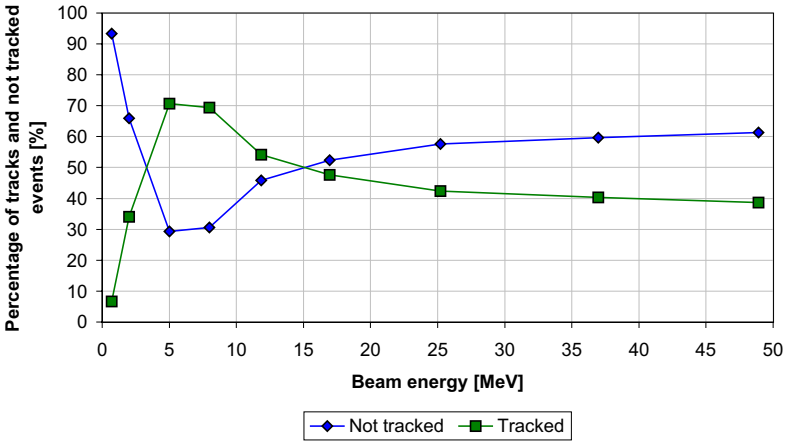

Figure 7.4: Distribution of tracked and not tracked events as a function of energy (100% ≙ all *Compton* events). The large fraction of not tracked events at higher energies originates from photons which have their first interaction in the calorimeter and a secondary particle interacting in the tracker.

which the trigger hardware was influenced by electrical inference, resulting in events which have only hits in the tracker or only hits in the calorimeter. The second category are events where no sequence of the recorded interactions is compatible with Compton kinematics. The final rejection category are events with too many individual hits. Since Compton sequence reconstruction is an algorithm of order $\mathcal{O}(n!)$ (Section 4.5.2), computational demands become too high if the number of individual interactions exceeds a certain threshold. This cut-off is set to seven interactions (using the definition of Chapter 4.5), i.e. an electron track is counted as one interaction).

Figure 7.4 shows the break-down of Compton events into events with and without track, restricted to events which the algorithm determined to have started in the tracker. Up to 5 MeV, the fraction of tracked events increases as expected. However, then the trend reverses and the fraction of untracked events increases again. Simulations show that almost all of these Compton events without track above 5 MeV truly had their first interaction in the calorimeter before some secondary produces a hit in the tracker. They typically have one hit in D1 and one cluster in D2 and are incompletely absorbed. They fall in the "two interactions without track" category of Chapter 4.5.1.1 for which no good rejection possibility exists in the context of Classic event reconstruction. Given the simulation-based knowledge that they are mostly wrongly reconstructed events, this class of events is not included in the subsequent analysis.

Figure 7.5 illustrates the average track and Compton sequence length. Up to 8 MeV the average track length increases, then it deceases again. The explanation for the decrease at higher energies are again wrongly reconstructed and incompletely absorbed events. However, these wrongly reconstructed events *with tracks* can be nicely rejected using the $d\vartheta$-criterion from Section 4.5.1.2. As expected, the average number of (separable) Compton interactions increases with the total energy.

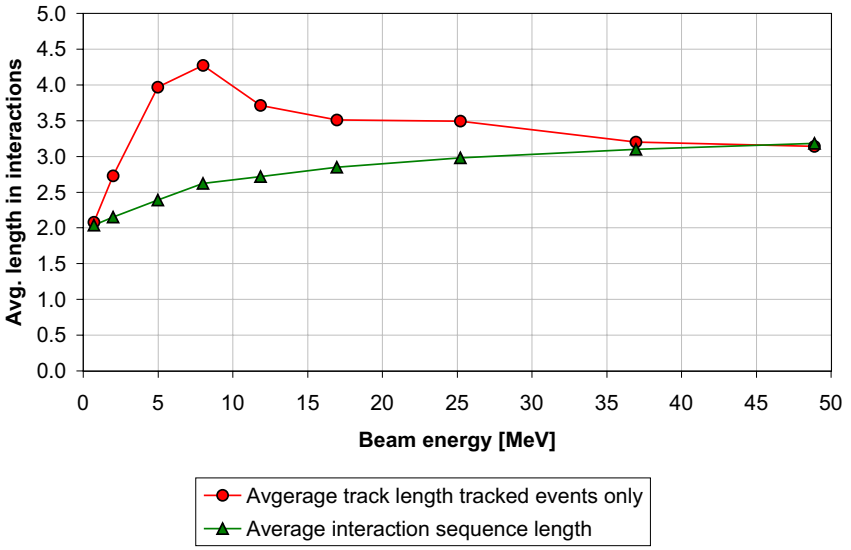

Figure 7.5: Average Compton track length and average Compton sequence length as a function of energy. In contrast to expectations, above 8 MeV the track length decreases with increasing energy. The reason are events which interact in the calorimeter first and then a bremsstrahlung photon produces a track. They can easily be rejected by the $d\vartheta$-criterion.

7.2 Spectral response

One important task of a telescope is to measure the energy of the detected photons. In this respect, the Compton regime presents an extraordinary challenge, since the photons have the least probability to interact (see cross-sections Figure 1.1), and if they interact via Compton scattering, the scattered photon nevertheless might escape the detector.

Figure 7.6 shows the measured spectra after the event reconstruction for five different on-axis measurements. The left image shows all events (no event selections have been applied), the right image shows only events for which the minimum distance between cone and origin (i.e. incident beam direction) is less than 10°.

Only at 710 keV the MEGA prototype has sufficient active mass to stop enough photons completely to generate a photo peak despite the mediocre energy resolution of the prototype. For this beam energy the combined energy resolution of the prototype is (41±4) keV (one sigma). At 2 MeV, the suboptimal energy resolution smears out a possible photo peak. At even higher energies, the total energy cannot be measured: If the photon interacts via Compton scattering, the scattered photon probably escapes. If the photon interacts via pair creation, likely most of the energy is deposited in passive material; moreover, if the electron or positron does hit the CsI, the energy deposited is high enough to lie in a domain for which no calibration for the crystals exists — as a result, the recovered energy is most likely wrong.

Again, the term “incompletely absorbed events”, as used in this work, refers to all photon interactions which fulfilled the instrument’s trigger criteria but where the photon’s energy could not be retained in the active material of the detectors — be it that particles escape from the detector, that energy is deposited in passive material or dead voxels, or that an energy deposit is below the relevant detection threshold.

Reproducing these measured spectra in simulations is a daunting task, because too many properties of the individual detectors are not well known.

- One set of problems arises from the instability of the system: Thresholds and energy resolutions vary with time and temperature. Only the time-averaged system properties are roughly known, and corresponding (large) uncertainties are introduced into the simulation. To include for example the noise threshold in the simulation, the overall distribution of the thresholds is determined for all channels of e.g. the tracker and fitted by a Gaussian. During simulation a random threshold is determined for each individual hit, given the mean

710 keV

2 MeV

8 MeV

17 MeV

50 MeV

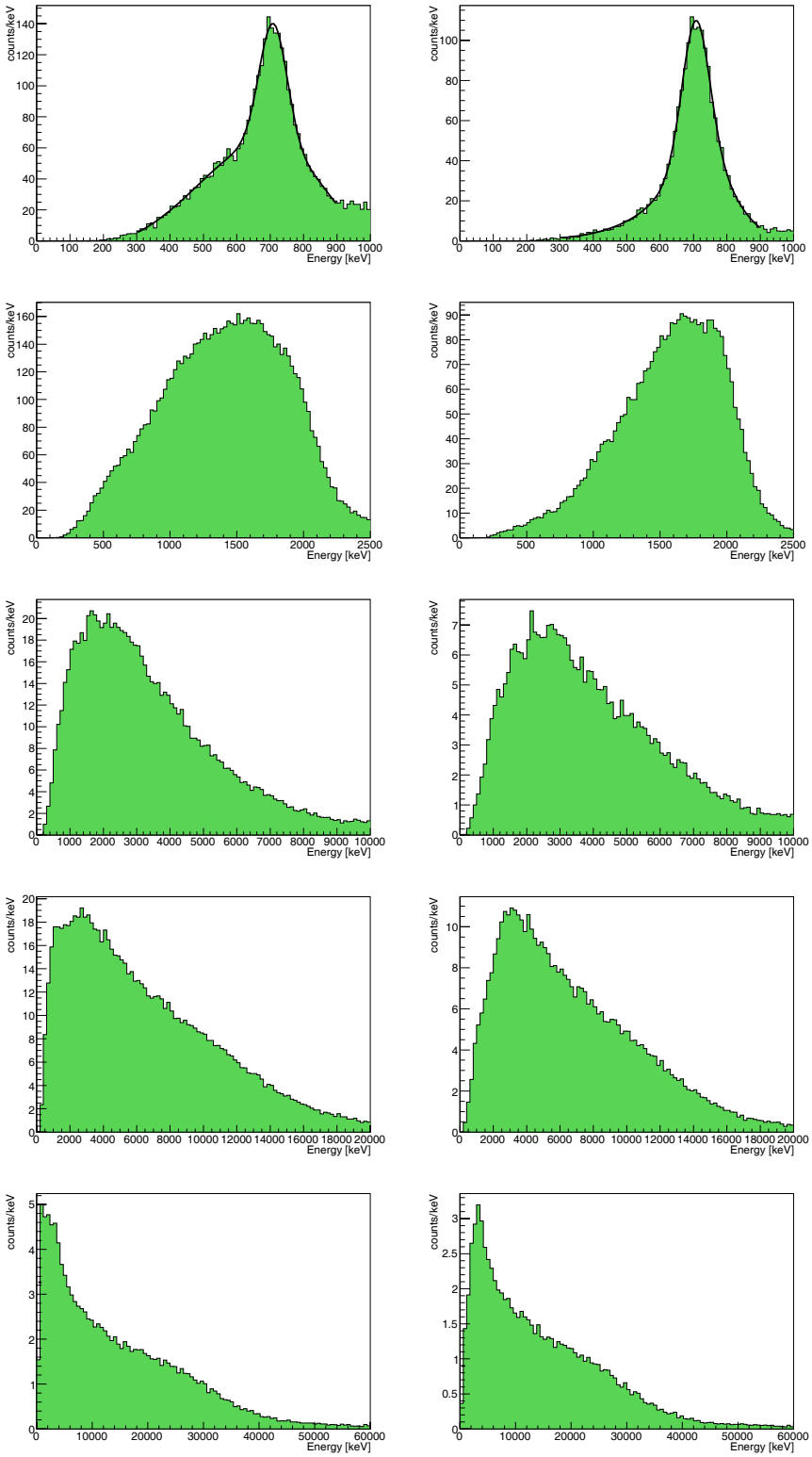

Figure 7.6: Measured spectra after the event reconstruction: Left, the spectra are shown without selections; on the right side only those events are selected which originate from the beam direction (radius: 10°). The MEGA prototype is only at 710 keV capable to completely stop the majority of its events. All other energies are dominated by incompletely absorbed events.

and the sigma of the Gaussian fit. The same procedure is applied to all other detector properties.

However, most system properties were determined in the dedicated "single-channel" calibrations and constitute short-term snapshots of the instrument relative to the 2-week calibration campaign; each parameter may have varied more widely over the whole time span. In addition, variations of individual system properties, such as thresholds or gains in different channels, may well be correlated. The simulation, however, for lack of more detailed information must assume that each parameter such as threshold, measured energy, etc. varies according to a certain distribution and independent of variations in other measured quantities for a given event.

- The energy calibration of the tracker is also problematic: The highest energy calibration source, which was available at Duke, was ^{57}Co with its 122 keV line. However, the mean energy deposit of an electron passing through one tracker layer is Landau-distributed with a mean value around 200 keV and a very long tail. Consequently, no calibration for the mean energy deposit exists! The low-energy calibration of the tracker is extrapolated to higher energies. Thus comparing the measured energy deposit with the simulated ones reveals certain differences: The peak energy of the measured Landau distribution is roughly 15% lower than that of the simulated distribution, but the measured distribution has a significantly stronger high-energy tail. Overall, this results in a roughly 7% higher average deposited energy for the 2 MeV measurement compared to the simulation. The reason is probably non-linearities in the electronics which cannot be adequately calibrated given the available source calibration data.

- A similar problem exists for the calorimeter. It was not possible to calibrate the detector with sources below 511 keV, because no suitably strong sources were available at Duke. This is a problem because higher-energy photons can interact deep in the calorimeter, depositing — in a Compton interaction — less than 511 keV in one CsI crystal. Furthermore, the highest-energy calibration (1275 keV of ^{22}Na) was rather difficult to evaluate; in particular a calibration was not possible for all channels (*Andritschke*, 2006). Charged particles, such as the electrons from e.g. 25 MeV and higher photons, can deposit several MeVs in one crystal. Again, for such events an extrapolation of the low-energy calibration had to be used.

- Another problem arises from the trigger threshold in combination with the coincidence window. To reduce the amount of chance coincidences, the trigger signals of tracker and calorimeter must be detected within a 2.2 μs time window. Unfortunately, CsI calorimeters have a slow response, i.e. for weak signals the threshold level might have not been reached before the end of the coincidence window. For low-energy events, this effect introduces an additional threshold to the one set by the hardware, and is expected to raise the hardware threshold by roughly 100 keV.

- A final problem arises from the differences between the calibration and measurement mode. In calorimeter-calibration mode, the front-end chip holds the signal a certain time after the trigger has been raised. In measurement mode, the signals of the calorimeters are held a certain time after the *tracker* has triggered. This results in two problems: A larger D1 signal generates a trigger signal faster than a small one, varying the trigger time and thus the height of the calorimeter signal at the time the signal is held. The second problem is that the delay between D1 trigger and D2 readout is fixed; the delay time has been optimized for the 662 keV measurement. Just how accurately the single-channel calibration obtained in calibration mode reflects the behavior of the instrument in

measurement mode for other photon energies remains unknown. The fixed-delay readout, however, is expected to introduce some additional energy measurement uncertainty in the calorimeters.

The 2 MeV Duke measurement is least influenced by the problems detailed above and thus is best suited for a comparison between measurements and simulations: the measured events — at least those close to the "photo-peak" — are above all trigger threshold effects, and the total energy at least of the calorimeter hits is mostly within the calibration range. Figure 7.7 shows the influence of the different detrimental effects on the 2 MeV spectrum. The first figure shows the ideal beam spectrum, which has an intrinsic width of roughly 1%. In the next step all geometrical effects are activated: photons/electrons escape from the detector or deposit energy in passive material. The majority of all events (82%) are incompletely absorbed. Technically, one would have to consider all tracked events in the MEGA prototype to be incompletely absorbed events: The electron loses energy in the air between the layers of the tracker; this shifts the photopeak slightly to lower energies. The third spectrum includes the effects of thresholds (noise as well as trigger) and not-working channels of the active material. The total number of photo peak events is reduced to 7%. In the final step, the MEGA prototype's energy resolution is applied to the simulated data — and completely smears out the photo peak. Although several details of the detector's behavior remain unaccounted for in the simulation — as discussed above — the final simulated spectrum resembles the measured one (thick line) quite nicely.

Figure 7.8 shows where the energy is lost. On average, for the 2 MeV measurement for each triggered event 2/3 of the incident photon's energy is detected. 19% is lost in passive material, 9% is carried away by escaping particles, and on average 5% is not recorded due to threshold effects.

The spectral resolution of the MEGA prototype is significantly below the performance needed for a space mission. In addition, several of the detector's shortcomings are hard to correctly calibrate and consequently cannot be fully incorporated into a simulation of the detector. Thus the following recommendations have to be made for future developments:

- The single most important improvement recommendation concerns the calorimeters and its electronics, to improve the energy resolution and the stability of the prototype as well as to lower its thresholds.
- Additionally, the calorimeter needs to completely enclose the tracker and be as compact as possible, in order to significantly reduce the number of escaped photons.
- Furthermore, the amount of passive mass needs to be minimized, especially between tracker and calorimeter.
- Finally, the tracker must be large enough to accommodate even high-energy tracks in the Compton regime. Assuming that at least 14 MeV photons have to be stopped (at this energy Compton and pair cross-section have equal energies), assuming that 50% of the energy is transfered to the electron and that on average 200 keV are deposited per layer, around 35 layers are necessary to stop this electron. Consequently, a significantly larger tracker is necessary. Alternatively, the tracker might be enclosed by thicker Silicon layers at the bottom and the sides (or even Germanium or CZT).

Given the current spectral response of the MEGA prototype with its strong energy dispersion above $\sim$1 MeV where no photo-effect is visible, the original spectral information can only be

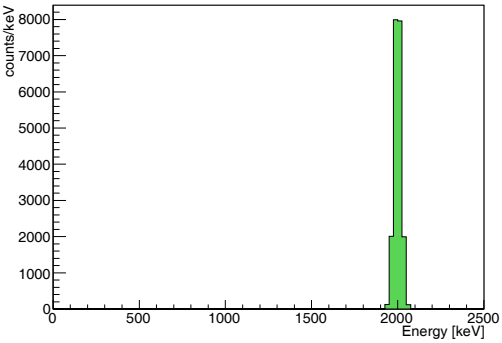

(A) Incident beam spectrum of the 2 MeV Duke measurement with a 1% energy resolution of the beam itself. Only events are shown which in the simulation interact in both D1 and D2 detector material.

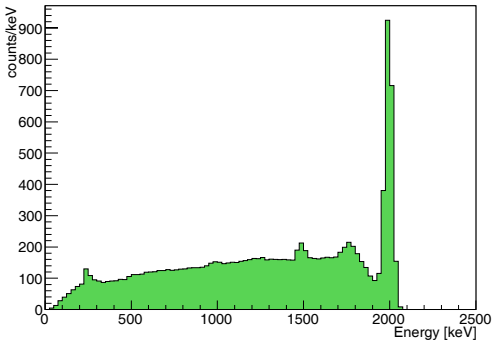

(B) Reconstructed beam spectrum using an idealized detector. Energy resolution (and correspondingly calorimeter depth resolution) is assumed perfect, and all thresholds are assumed at 0 keV. However, escaping photons and electrons as well as deposits in passive material are considered. The Compton edge, backscatter peak, and first escape peak are clearly visible. The photo peak is slightly shifted towards smaller energies, due to the energy loss of electrons in air while traveling from layer to layer.

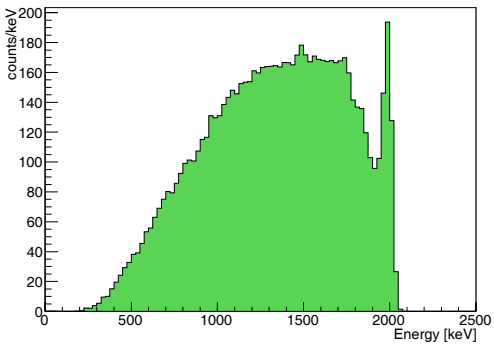

(C) Reconstructed beam spectrum including losses induced by trigger and noise thresholds as well as not working pixels/strips strongly reduces the photo-peak as well as the total number of detected events.

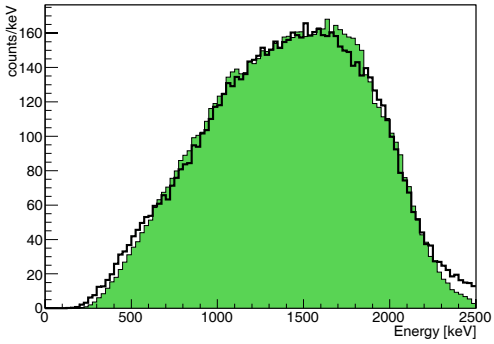

(D) Final reconstructed beam spectrum. Adding the appropriate energy resolution completely smears out the photo peak. Although there are still several uncertainties in the simulation (see text for details on detector properties that cannot be incorporated), the final simulated spectrum resembles the shape of the measurement (thick line, normalized to same total number of counts in the spectrum) quite closely.

Figure 7.7: The effects of the measurement process on the simulated 2 MeV spectrum. (A)-(D) show the increasing energy dispersion due to the measurement process and the instrumental function.

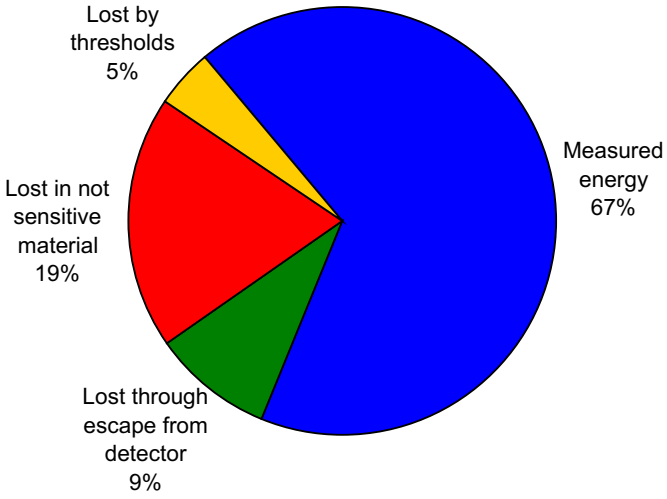

Figure 7.8: Average distribution of energy deposits/losses of the *triggered* events as determined by simulations of the 2 MeV Duke measurement. For the average measured photon 1342 keV of the 2000 keV are measured. On average 380 keV are lost in passive material, 185 keV carried away by escaping particles, and on average 90 keV are lost due to threshold effects.

retrieved via deconvolution. This would require determining a complete energy response, a data space with the dimensions incident and measured energy, and applying similar algorithms to the spectral response as used for image reconstruction in Chapter 5. However, a significantly better approach would be to improve the detector.

Chapter 8

Imaging properties of the MEGA prototype

One key functionality of a telescope is its ability to retrieve the origin of the measured photons. For telescope designs that do not directly yield a sky image, but instead require reconstruction, two sets of properties need to be examined: the quality of information contained in individual events, discussed in the first part of this Chapter, and the accuracy with which the imaging algorithm can retrieve input sky (or laboratory source) distributions from the data. For a tracking Compton telescope two parameters are critical for its imaging performance: the accuracy with which the width and the length of the arcs of the Compton cone can be determined — these determine the size of the point-spread function of the telescope. For a pair telescope's imaging performance, the critical parameter is the direction accuracy of each photon's point of origin as determined from the electron's and positron's tracks (and energies). In the second part of this Chapter, the LM-ML-EM-Algorithm described in Chapter 5 is applied to laboratory and beam data of the MEGA prototype to evaluate the full imaging system's response to point sources on and off axis as well as to illustrate its response to multiple sources and extended emission regions.

8.1 Angular resolution

8.1.1 The Compton regime

The size of the point-spread function, and thus the angular resolution of a tracking Compton telescope, is determined by the shape of the arcs of the Compton cones. As described in Chapter 5, this shape can be described by two parameters: the width of the arc (ARM), which is mainly determined by the energy and position measurements, and of course influenced by Doppler-broadening, and the length of the arc (SPD), which is determined by the accuracy with which the direction of the recoil electron track can be measured.

8.1.1.1 Width of the Compton cone

The width of the Compton cones and arcs is measured by the Angular Resolution Measure (ARM) as defined in Section 2.2.5. It is a complex function of several parameters of Compton scattering such as scatter angle and total energy, but also background suppression cuts like those detailed in Chapter 4 (cuts on the quality factor of the electron track, of the Compton sequence, and of course the $d\vartheta$-criterion). The ARM distributions shown here have been obtained from MEGA beam measurements using the following event selections:

710 keV

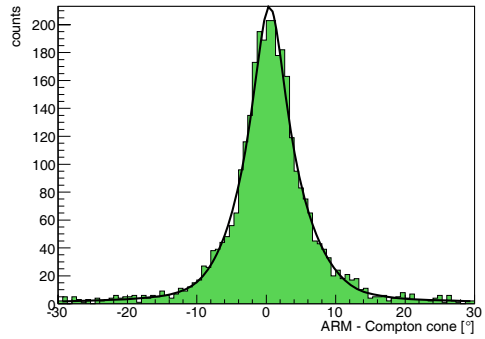

Figure 8.1: Right column: ARMs of tracked events from 2 to 8 MeV: At 2 MeV the ARM is dominated by the energy resolution in the calorimeters; contributions from the other effects (position resolutions, energy resolution in the tracker) are a factor of three smaller (compare Table 8.1). At higher energies the angular resolution improves. The fits, consisting of a combination of Lorentz aus Gauss functions, are only used to determine the FWHM of the distribution.

2 MeV

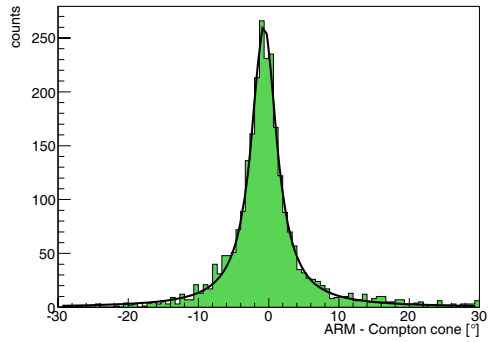

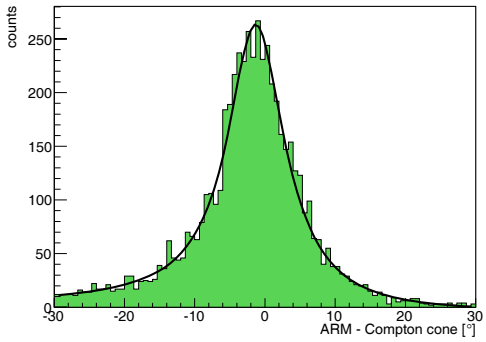

Figure 8.2: Left column: ARMs of not tracked events at 710 keV to 2 MeV. While at 710 keV the angular resolution is dominated by energy resolutions, at 2 MeV the contribution of energy and position resolution are rather similar.

5 MeV

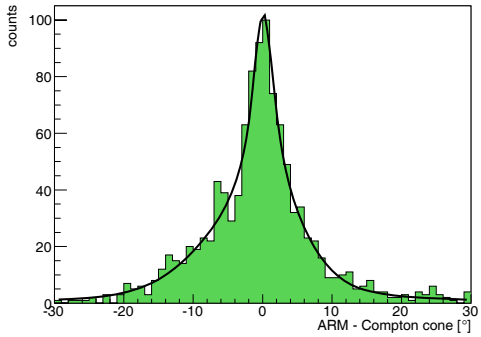

8 MeV

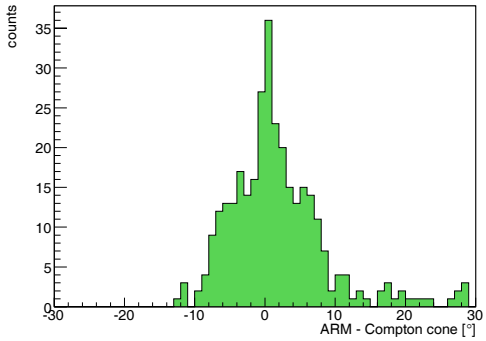

- The event has to pass the event reconstruction as a kinematically correct Compton event, which can be uniquely identified as moving from tracker to calorimeter. Ambiguous two-site events without track (Section 4.5.1.1) have been rejected.

- Due to the lack of a photo peak above 710 keV, an energy window of ±5% around the known source energy has been applied. For comparison, the energy resolution (one sigma) of the beam was 1-2%.

- The Compton scatter angle φ has to be larger than 7° and smaller than 90°. Both cuts eliminate wrong Compton events — eliminating small-angle scatters avoids second interactions close to the beam path, and true backscattering is very unlikely given the detector geometry.

- Only events were used whose reconstructed start point is consistent with the beam path. This eliminates background, but has *no* effect on the angular resolution.

Since the background can be rejected sufficiently well by only using events first interacting in the beam path, no additional background rejection cuts, such as cuts on the quality factor of the reconstruction or on the $d\vartheta$-criterion, are necessary. Reasonable cuts here would not have a significant influence on the angular resolution of the MEGA prototype; they would only reject significantly wrong reconstructed events.

Figures 8.1 and 8.2 show the ARM for the 0.71, 2, 5 and 8 MeV measurements at Duke. The left column shows not-tracked events, the right column tracked events. Ignoring the 8 MeV measurement for the moment, the angular resolution improves with increasing energy. This is expected, because at higher energies the relative energy measurement uncertainties decrease and along with a smaller average Compton scatter angle the angular resolution improves (details see Section 2.2.5) — as long as the photon is completely absorbed and correctly reconstructed. Similar arguments hold for the difference between tracked and not tracked events at 2 MeV: In order to generate an electron track, a sufficient amount of energy needs to be transferred to the electron. This results in large Compton scatter angles, where energy measurement uncertainties, especially those of the calorimeters, have a larger influence on the angular resolution than at small Compton scatter angles (Figure 2.15).

While the ARM distributions up to 5 MeV are smooth functions, MEGA's ARM distribution at 8 MeV has a peculiar shape: It has a strong central peak and then the distribution broadens abruptly. It turns out that the peak corresponds to two-site events with track, and the broad distribution to multiple Compton interactions (details see Chapter 4.5.1.3) with several interactions in the same calorimeter module. While the track defines the start of the sequence rather nicely, the lack of a good energy calibration at high energies in combination with a very moderate position resolution makes it difficult to find the correct sequence, particularly if several interactions occur in close proximity. Simulations have shown that in order to reliably distinguish between different possible Compton interaction sequences in the case of multiple interactions in a single calorimeter module, energy resolutions of a few percent at most, not ∼13% as in the prototype are required. Similarly, position resolutions corresponding to geometrical Compton scatter angles of several degrees, and not a few tens of degrees, are necessary. Another reconstruction approach would be to use the energy-weighted center of interaction in a calorimeter module in case of multiple hits. However, in the energy regime under consideration, the distances between interactions are large enough that no improvement is possible.

Figure 8.3 summarizes the achieved angular resolution. The left figure includes all events which comply with the above event selections, the right figure only two-site events. As explained above, two-site events are expected to give a better resolution than multiple events, given the performance characteristics of the MEGA prototype. Overall, in terms of angular resolution below 10 MeV, the *prototype* has a hard time competing with COMPTEL (smooth line in the figures). Since it *is* possible to build an improved calorimeter, the satellite instrument will have a significantly better angular resolution (Figure 10.5).

Reconstructing the origin of Compton events requires knowledge of interaction positions as well as deposited energies. Thus the angular resolution is influenced by most of the imperfections of the prototype, with contributions from energy and position resolutions, thresholds, as well as non-linearities and time-variabilities. Table 8.1 illustrates how activating the individual imperfections in the simulation, one after the other, influences the final angular resolution of

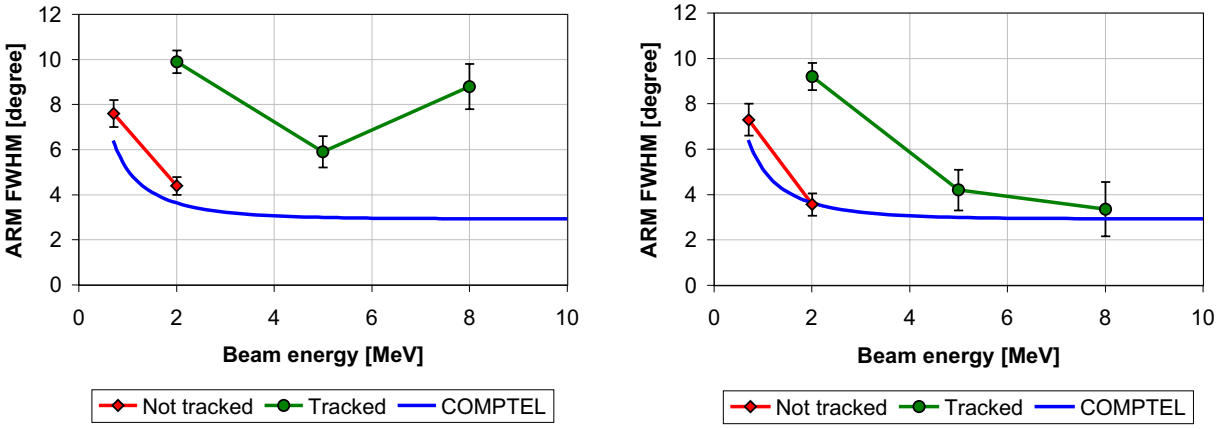

Figure 8.3: Angular resolution as a function of energy for tracked and not tracked events as measured during the Duke calibrations. The left plot is based on all data fulfilling event selection criteria, the right-hand plot is based only on two-site events. For comparison, the COMPTEL angular resolution fit from *Schönfelder et al.* (1993) is shown. For a discussion of these plots see text.

Imperfection	FWHM ARM at 2 MeV [°] for	
	not tracked events	tracked events
Doppler broadening	0.18 ± 0.02	0.25 ± 0.02
Plus voxelization D1/D2 & incomplete absorption	1.5 ± 0.2	1.1 ± 0.1
Plus thresholds & defective pixels	1.7 ± 0.2	1.3 ± 0.1
Plus energy resolution D1	2.8 ± 0.3	2.7 ± 0.3
Plus energy & depth resolution D2	3.4 ± 0.5	9.7 ± 1.1
Plus energy shift	3.7 ± 0.6	10.8 ± 1.3

Table 8.1: Activating one detector imperfection after the other in the simulation reveals the impact of each on the MEGA prototype's angular resolution.

both tracked and not tracked Compton events for an on-axis 2 MeV photon beam. The angular resolution is fundamentally limited by Doppler broadening (Section 2.2.6), which results in a limit close to 0.2° for MEGA's Silicon tracker. On average, the consequences of Doppler broadening are slightly worse for tracked events because these events have larger scatter angles.

The simulation automatically voxelizes the positions in the strip detectors and calorimeters (depth resolution is still perfect) and incorporates incomplete absorptions. Especially the voxelization results in a significant broadening of the angular resolution. Not tracked events have smaller Compton scatter angles and predominantly interact in the bottom calorimeters. Thus, for these events the average distance between first and second interaction (12 cm) is smaller than for tracked events which predominantly are stopped in the side calorimeters (16 cm) — and consequently the finite voxelization of the detectors has a larger impact on not tracked events. The resulting angular resolution limit for perfect detectors with the given voxelization is 1.5° for not tracked and 1.1° for tracked events.

Thresholds and defective pixels only have a small influence on the angular resolution, i.e. the ARM *width* — on average they worsen it by 0.2°. They are, however, responsible for a shift of the ARM peak *position* to positive values. One must keep in mind that the event selections applied demand that the total measured energy be no more than 5% below the incident beam's photon energy. Since a missing calorimeter hit likely would correspond to a loss of more than 100 keV of the total incident photon energy (2 MeV), the impact of thresholds on ARM width (rather than overall photopeak efficiency) evaluated here mainly reflects the impact of missing small energy deposits (e.g. start of track) in the tracker.

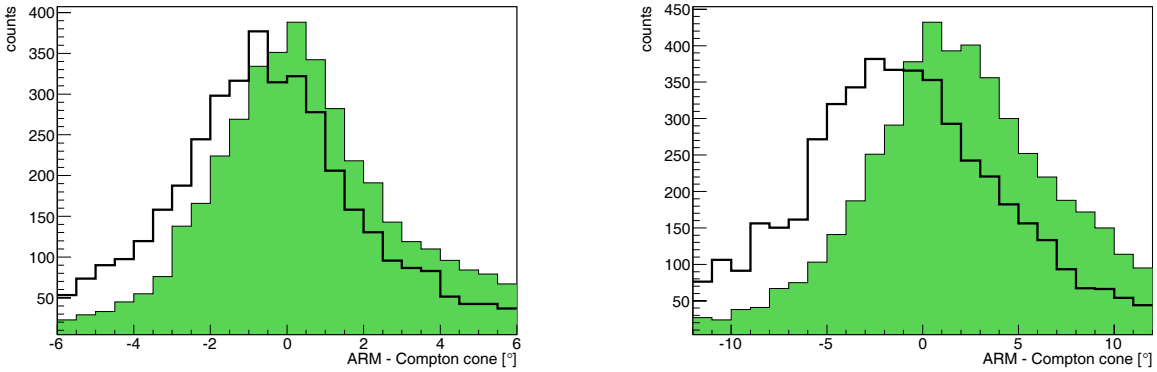

Figure 8.4: Comparison of the angular resolution resulting from simulations of not tracked (left) and tracked events (right) at 2 MeV — including voxelization, thresholds, dead pixels/strips, and energy resolutions — with the measured distributions. The black line reflects measurements, the filled histogram simulations. For a possible explanation of the differences see text.

Activating the energy resolution in the tracker in addition to voxelization and thresholds in tracker and calorimeter results in an angular resolution just below 3° for both event types. Activating the energy and depth resolution in the calorimeters worsens the angular resolution for tracked events by a factor of three; for not tracked events the resulting ARM deterioration amounts to only ∼20%. This can be explained by revisiting Equation 2.23 and Figure 2.15: The larger the Compton scatter angle φ and thus the lower the fraction of the incident photon's energy carried by the scattered gamma ray (E_g), the larger is the influence of the measurement uncertainty in E_g on the angular resolution! As consequence, especially a *tracking* Compton telescope requires an excellent energy resolution in the calorimeter to achieve a good angular resolution.

Before the last line in Table 8.1 is discussed, an initial comparison of the simulated ARM shapes (including effects of voxelization, thresholds, dead pixels/strips, and energy resolutions) with the measured ones should be made. Figure 8.4 shows this comparison. While the width of simulated and measured ARM distributions is roughly the same for both tracked and not tracked events, the measured distributions are slightly shifted towards lower ARM values, the simulated distributions slightly shifted towards higher ARM values. The shift in the simulated distributions indicates either too high energy measurements in the calorimeter or too low energy measurements in the tracker. The latter can easily be explained by energy losses of the electrons in the tracker that remain undetected mainly due to thresholds.

The measured distribution, however, shows a contrary trend: The too-small ARM values observed indicate either too high energy measurements in the tracker or too low measurements in the calorimeter. Both options constitute viable possibilities in the context of the MEGA prototype detector and its calibration: First, as explained in Section 7.2, comparing the energy deposit for tracked events in one layer as a function of the incidence angle reveals that the average measured energy deposit is higher than the average simulated one, especially in the long higher-energy tails of the distribution where no calibration points exist. Second, the difference between calibration and measurement mode of the detector for the calorimeters (details see again in Section 7.2) is likely to result in underestimated energies especially of small deposits in the calorimeter. Adding a crude estimate of these two effects into the simulation (increase of the average deposited energy in the tracker by 7% and an underestimate of the calorimeter energies below 511 keV by 10%) results in the simulated ARM distributions shown in Figure 8.5 and the simulated ARM width given in the last line of Table 8.1. The combination of these two assumptions bring simulated and measured ARM distributions into good agreement. Shifting the energy deposits of individual hits according to the two corrective steps outlined above has

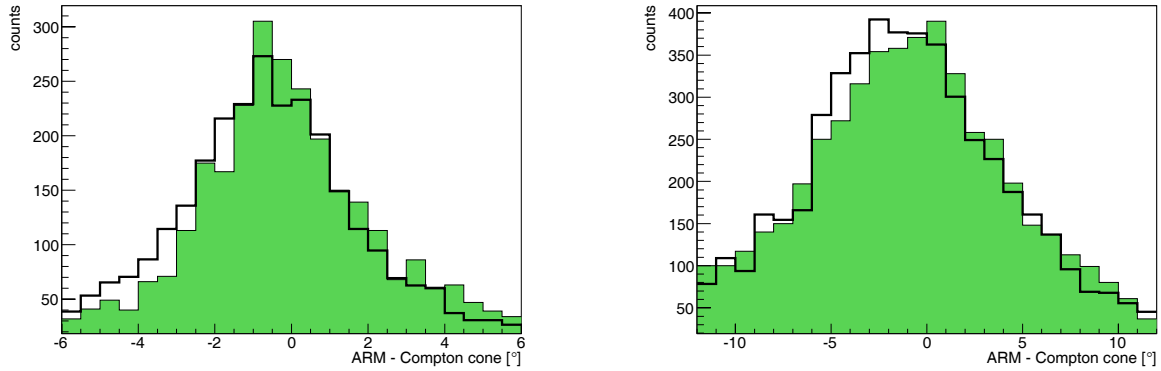

Figure 8.5: Comparison of the angular resolution of not tracked (left) and tracked events (right) with the measured distributions at 2 MeV after accounting for an average overestimate of the energy in the tracker and a potential underestimate of the deposited energy in the calorimeter. The two corrections combined would explain the discrepancy in the ARM peak positions between simulation and measurement evident in Figure 8.4. Again, the black line reflects measurements, the filled histogram simulations.

no significant influence on the total simulated energy spectrum because the two effects almost cancel each other.

Much more detailed calibration measurements with the prototype would be required to quantitatively assess these two effects from measurements and to correct the calibration for both effects. Since the combination of both calibration deficiencies only shifts the ARM from the right to the left side of the axis, and since the shift is still small compared to the width of the ARM distribution, no significant net effect on the width of reconstructed sources is expected. Thus the following discussion is using the original calibration obtained from *Andritschke* (2006).

8.1.1.2 Length of the Compton arc

For a tracking Compton telescope, the second characterizing feature is the length of the Compton arc, either represented by the scatter plane deviation (SPD) or the electron ARM. In the Compton energy regime of the prototype, it is completely dominated by Molière scattering.

Determining the electron ARM or SPD only for "photo peak" events of the Duke measurements is a drastic event cut: For the electron to be fully absorbed in the MEGA tracker, it must have a low energy (< 2 MeV) — if the track is too long, the electron might escape from the tracker. In addition, the probability that at least one hit is missing from the track is increasing with the track length. Selecting only events with electron tracks < 2 MeV, however, will result in an electron ARM or SPD much broader than what would be observed for the *average* tracked

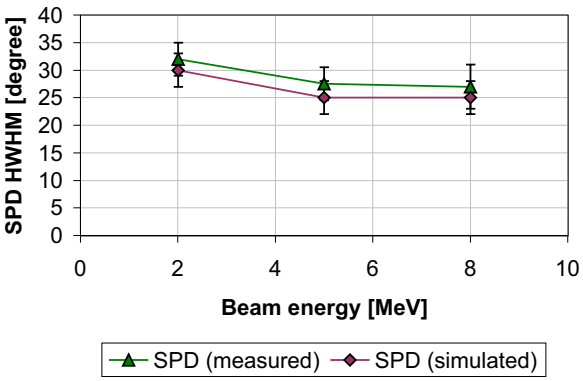

Figure 8.6: SPD: Comparison between simulation and reality.

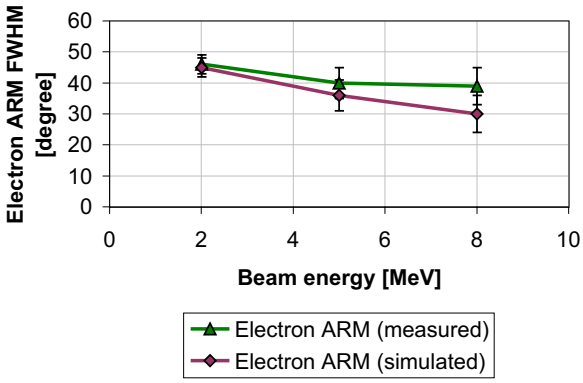

Figure 8.7: Electron ARM: Comparison between simulation and reality

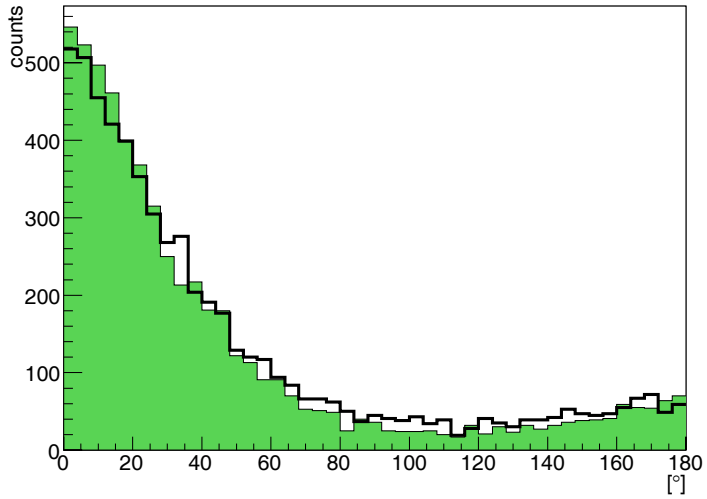

Figure 8.8: Comparison of the scatter plane deviation of the 2 MeV measurement (thick line) with the simulation. Both are in agreement within measurement and simulation uncertainties.

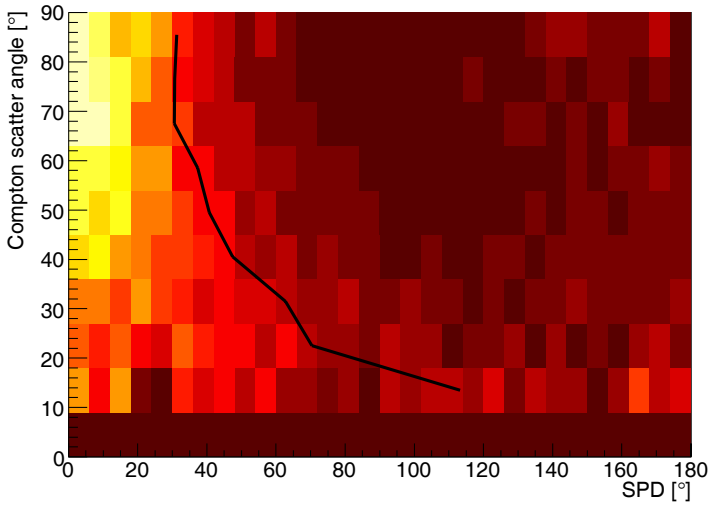

Figure 8.9: Distribution of the scatter plane deviation versus the Compton scatter angle for the 2 MeV run. The colors indicate a linear scale and each horizontal line has been normalized in the sum to one, to better show the shape of the scatter plane deviation.

Compton event at high energies: Small electron energies correspond to large *electron* scatter angles. For on-axis incidence, the scattered lower-energy electrons therefore must pass through more Silicon in one layer, increasing the effects of Molière scattering.

Figure 8.6 shows the HWHM of the scatter plane deviation of tracked events for the Duke measurements at 2, 5 and 8 MeV, and Figure 8.7 shows the FWHM of the electron ARM, each compared to simulations. For both measures of the Compton arc length, simulation and measurement are in good agreement. The largest deviation appears at 8 MeV where measurement statistics are lowest; within errors all measured electron ARM and SPD widths are in good agreement with simulations.

Figure 8.8 illustrates the good agreement between simulation and measurements (thick line) of shape and width of the scatter plane deviation for the Duke 2 MeV on axis measurement.

Figure 8.9 shows the scatter plane deviation for "photo peak" events observed in the 2 MeV on-axis run as function of the Compton scatter angle. Two effects lead to an overall distribution which narrows with larger scatter angle: First, a large Compton scatter angle corresponds to a larger energy transfer to the electron, making Molière scattering less influential. Second, large Compton scatter angles lead to smaller electron scatter angles, which for on-axis photons means that the electron has to pass less material per layer and thus gets scattered less. The same

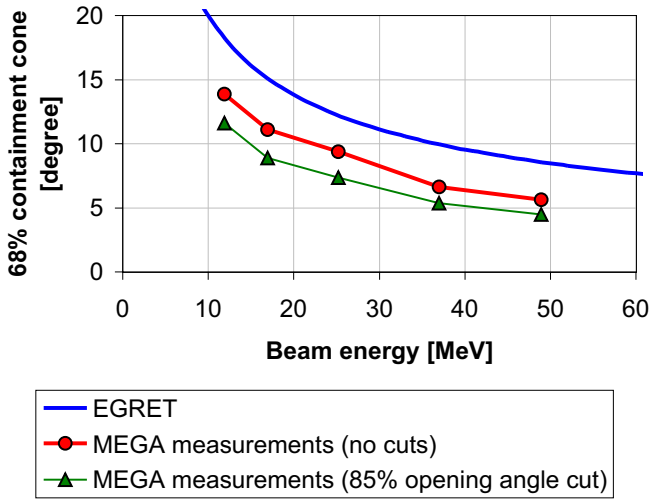

Figure 8.10: Comparison of the achieved angular resolution of the MEGA prototype and EGRET: At 49 MeV, MEGA's angular resolution is almost a factor of two better than EGRET's.

applies at higher energies, of course; however, not enough photo peak events have been collected during the Duke runs to compile a similar 2D scatter plot.

8.1.2 The pair regime

Pair events — previously discussed in Section 2.3 — have some advantages over Compton events. They can be directly reconstructed without the necessity to measure the energy to a very high accuracy, and their response is in first order symmetric around the incident photon's direction. Consequently, the angular resolution can be determined simply from the deviation of the calculated from the real origin. The angular resolution of the MEGA prototype in the pair regime, given as the half-angle of a cone containing 68% of all reconstructed events for a given Duke run, is shown in Figure 8.10.

The angular resolution of the MEGA prototype for pair events is dominated by the unknown recoil of the nucleus and Molière scattering in the Silicon layer of the pair creation. The influence of both effects reduces with increasing photon energy (see also Figure 2.23). Thus the angular resolution improves with higher energies.

Figure 8.10 shows the angular resolution without and with cuts on the pair opening angle. No cuts on the measured photon energy were applied. The 68% containment has been determined in each case from an angular resolution plot such as that shown in Figure 8.11.

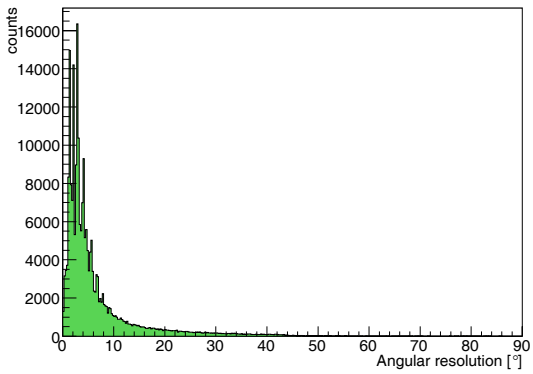

Figure 8.11: Distribution of the angular deviation between the measured and real origin of the pair photon.

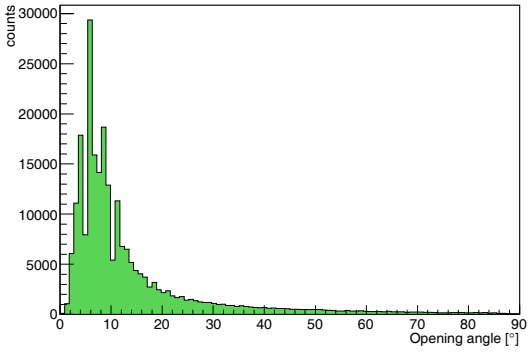

Figure 8.12: Opening angle distribution of all pair events recorded in the 49 MeV on-axis measurement.

Between the opening angle and the probability that the pair has been reconstructed correctly exists a correlation: Larger opening angles correspond to a more uneven distribution of the photon's energy to the pair's electron and positron. The more the electron and positron angles differ, however, the more significant the energy correction to the reconstructed photon direction becomes (compare Equation 2.28). Since the majority of pair events is not even marginally contained in the prototype, the simpler direction reconstruction based on Equation 2.29 results in a better angular resolution than those using the energies. As a consequence, the incident photon direction of pairs with large opening angles is not correctly reconstructed. Moreover, events in the tail of the distribution of reconstructed opening angles (see Figure 8.12) are partly reconstructed incorrectly — for example when the true vertex start point is missing, and a hit lower in one of the two particle tracks is used as vertex start point. This can be verified both using simulations and by backprojecting such events onto the sky. Both effects results in a fairly random distribution on the sky for large opening angles (e.g. $> 50°$ for the 49 MeV measurement), rather than one clustered around the incident photon direction. Consequently, using only the 85% of events with the smallest opening angles results in a significant improvement (on average 20%) of the angular resolution for pair events. This opening angle cut rejects all angles larger than 23° at 49 MeV and all larger than 45° at 12 MeV. It will be used as one of the background rejection cuts for the MEGA satellite in Chapter 10.

At 49 MeV the MEGA prototype's angular resolution is roughly a factor two better than EGRET's (top graph in Figure 8.10). MEGA will also surpass the expected angular resolution performance of GLAST and AGILE since they — same as EGRET — contain converter foils which increase the angular dispersion due to Molière scattering.

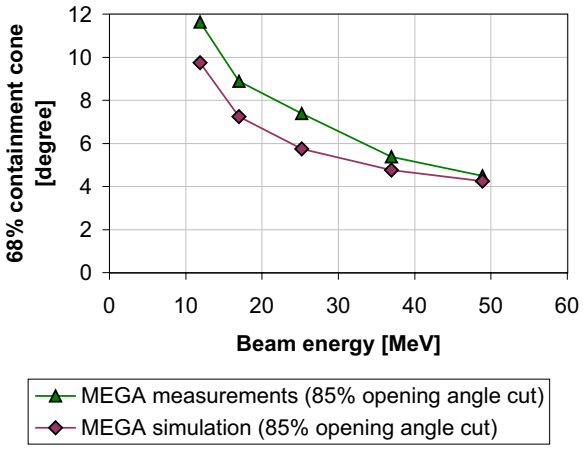

Figure 8.13: Comparison of the simulated angular resolution in the pair regime with that achieved analyzing MEGA prototype measurements.

Figure 8.13 compares the simulated angular resolution with the measured one. Generally, the simulated angular resolution is slightly better than the measured one. The difference is more pronounced at lower energies. The simulation does not take into account the recoil of the nucleus, and so a slightly better performance of the simulation is expected. A larger fraction of the total photon momentum is transferred to the nucleus at lower energies. Therefore, the resulting discrepancy between simulation and measurement is largest in this regime. However, the missing energy transfer to the recoil nucleus cannot fully explain the observed deviation. The remainder of the discrepancy is likely caused by problematic events in the Duke measurement data — arising either from contamination of the beam by charged particles and/or higher-energy photons, or from interactions of the photon beam in a cover above the tracker that was left in place during the high-energy beam runs and whose honeycomb structure could not satisfactorily be represented in the model geometry.

8.2 List-Mode Likelihood imaging of the prototype data

Up to this point, the imaging properties discussed were based on the angular deviations of reconstructed events from the true photon (and electron) directions *for individual events*. From this point on, the iterative methods introduced in Chapter 5 are utilized to obtain the best possible images from *the ensemble of observed events* from a given source.

8.2.1 Multiple sources

A telescope, especially one with a large field of view, of course has to be able to detect and distinguish between multiple sources observed simultaneously. A measurement with five sources of different energies, different intensities and at different positions placed simultaneously in the field of view of MEGA has been performed. The positions relative to the detector as well as

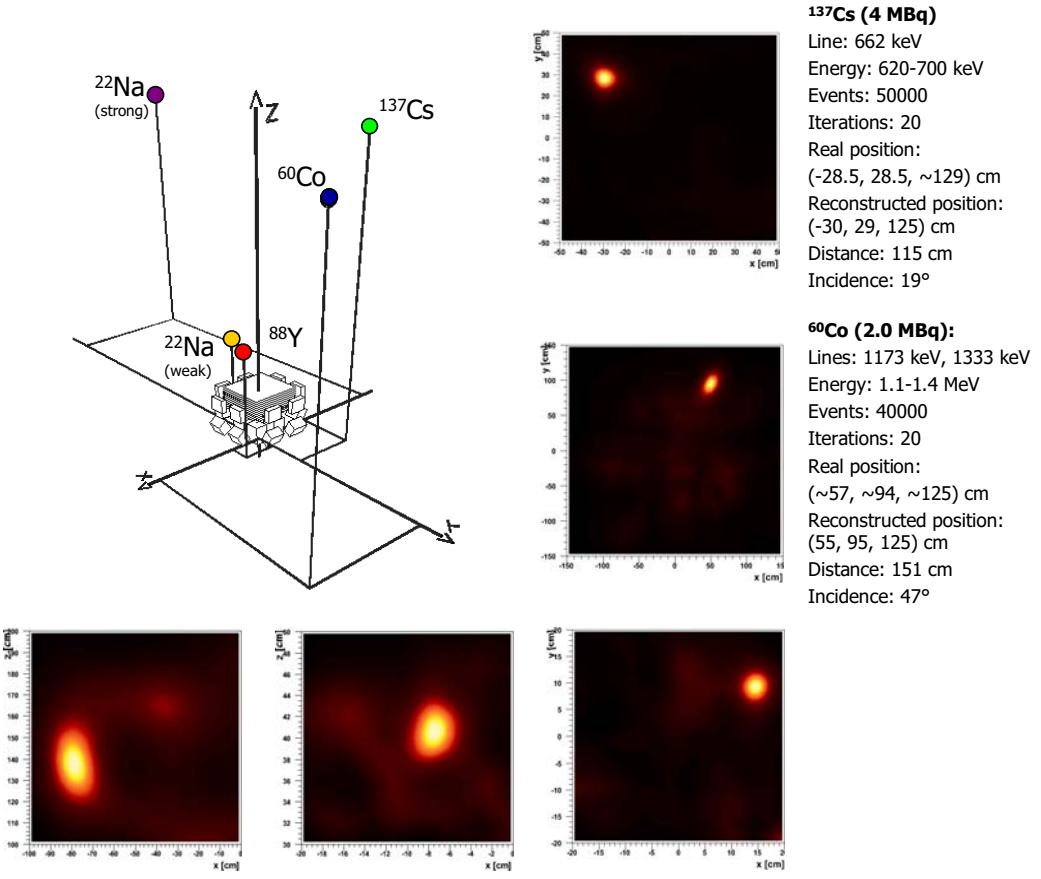

^{137}Cs (4 MBq)
Line: 662 keV
Energy: 620-700 keV
Events: 50000
Iterations: 20
Real position:
(-28.5, 28.5, ~129) cm
Reconstructed position:
(-30, 29, 125) cm
Distance: 115 cm
Incidence: 19°

^{60}Co (2.0 MBq):
Lines: 1173 keV, 1333 keV
Energy: 1.1-1.4 MeV
Events: 40000
Iterations: 20
Real position:
(~57, ~94, ~125) cm
Reconstructed position:
(55, 95, 125) cm
Distance: 151 cm
Incidence: 47°

^{22}Na (1.9 MBq):
Line: 1275 keV
Energy: 1.2-1.35 MeV
Events: 7200
Iterations: 20
Real position:
(~-70, ~-175, ~135) cm
Reconstructed position:
(-80, -170, 137) cm
Distance: 226 cm
Incendence: 52°

^{22}Na (51 kBq):
Line: 1275 keV
Energy: 1.2–1.35 MeV
Events: 8600
Iterations: 20
Real position:
(-7.5, -28.5, ~41) cm
Reconstructed position:
(-7.5, -28.5, 40.5) cm
Distance: 35 cm
Incidence: 57°

^{88}Y (70 kBq):
Line: 1836 keV
Energy: 1.6-2.0 MeV
Events: 21000
Iterations: 20
Real position:
(~16, ~10, ~51) cm
Reconstructed position:
(15, 9, 51) cm
Distance: 35 cm
Incidence: 32°

Figure 8.14: Multiple sources in the near field of MEGA. Since only projections of the source images onto vertical and horizontal planes have been used in this near-field reconstruction, some sources appear non-circular. "Energy" denotes the energy-based event selection applied.

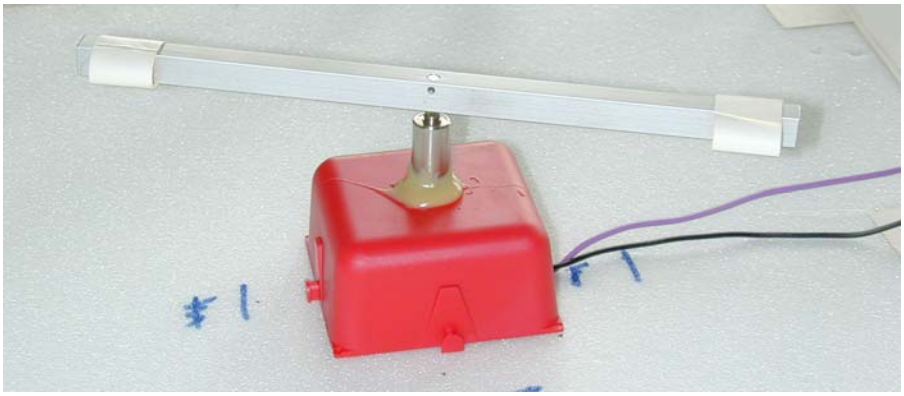

Figure 8.15: The propeller on top of the MEGA Styrofoam housing.

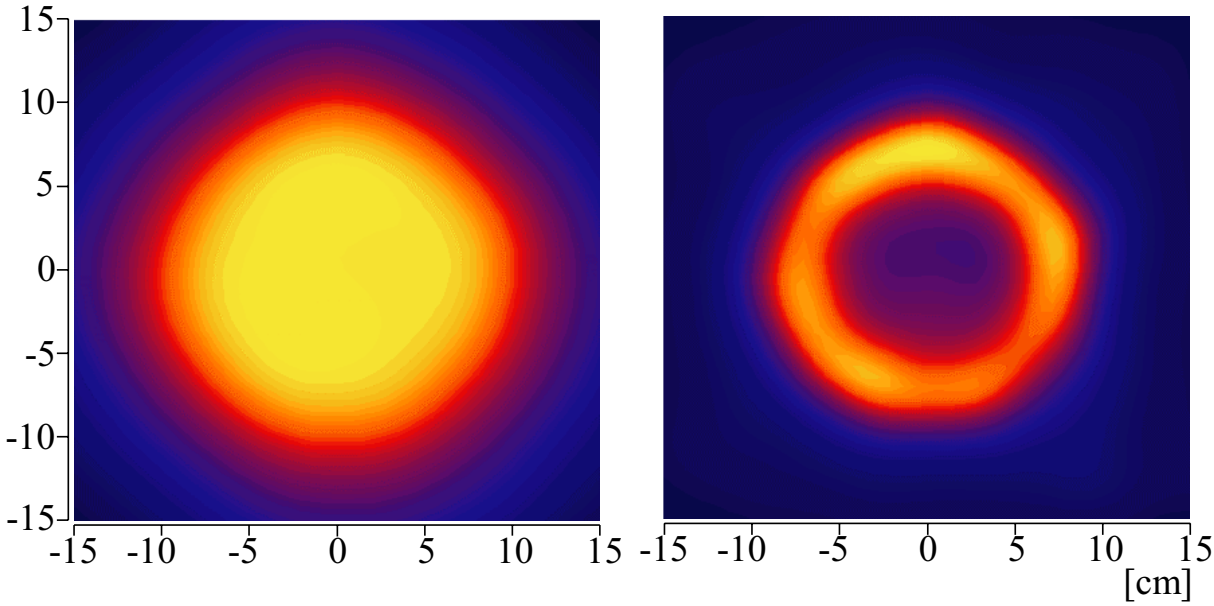

Figure 8.16: "Radioactive ring": In the image at iteration 0 (left), which is only a simple back projection of the events, the ring structure is hidden by cone circles and arcs. The ring structure is clearly visible after 50 iterations with the list-mode algorithm (right).

the reconstructed near-field images are shown in Figure 8.14. All five sources have been imaged to their correct positions. This measurement proves MEGA's capability to disentangle multiple sources and also serves to illustrate its large field of view at low energies.

8.2.2 Extended sources

The sky in the MeV regime contains a host of extended source regions, from supernova remnants and OB-associations to our Galaxy as a whole, in addition to a multitude of point sources. Therefore the ability to image extended sources is a key requirement for any telescope for medium-energy gamma-ray astronomy. The capability of the MEGA prototype in conjunction with the List-Mode Maximum-Likelihood Expectation-Maximization algorithm to image extended sources can be illustrated using laboratory measurements. Two ^{88}Y sources (34 kBq and 36 kBq) have been mounted on a rotating propeller located 27 cm above the center of the MEGA prototype's tracker on the Styrofoam cover of the detector. The propeller swept out a circle with radius 7 cm, which corresponds to a diameter of $\sim$29°. The setup is illustrated in Figure 8.15.

The reconstructed image (left 0th iteration, right 50th iteration of the LM-ML-EM algorithm) can be found in Figure 8.16. It contains $\sim$138,000 Compton events in the energy range from 0.8

710 keV

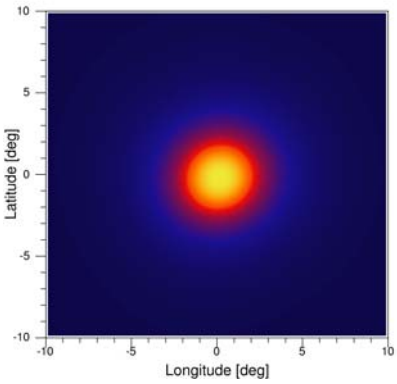

Figure 8.17: Right column: Images of tracked events from 2 to 8 MeV: At 2 MeV the image is dominated by the energy resolution in the calorimeters, which dominates all other resolutions by roughly a factor 3. At higher energies, this factor becomes less important, and the overall angular resolution improves significantly. The deviation of the shape of the source from perfect symmetry is due to the low statistics at 5 MeV and 8 MeV (187 events at 8 MeV).

2 MeV

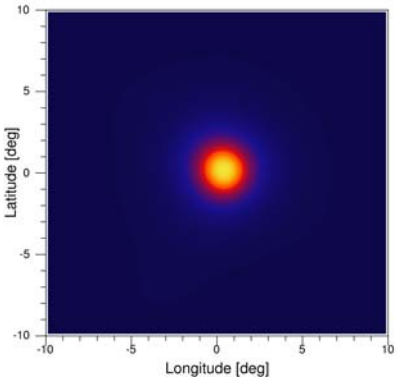

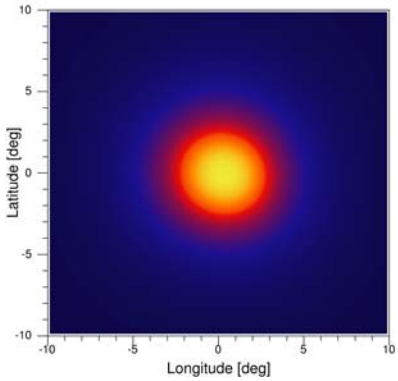

Figure 8.18: Left column: Images of not tracked events at 710 keV and 2 MeV. While at 710 keV the angular resolution is dominated by the energy resolution in the calorimeters, at 2 MeV it is dominated by the position resolution in the calorimeters, which contributes ∼60% to the angular resolution at this energy.

5 MeV

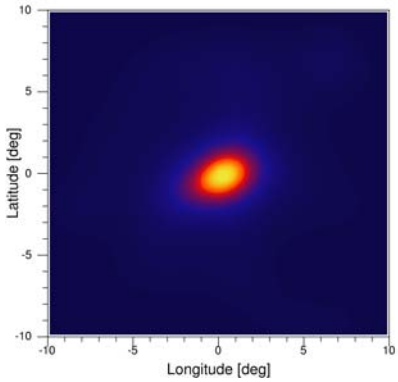

8 MeV

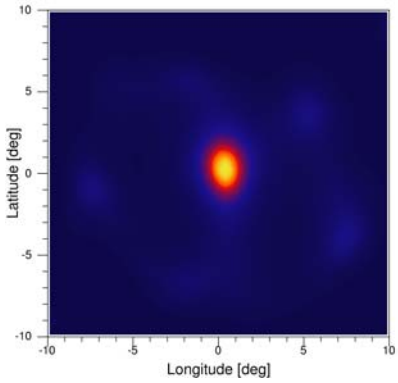

to 1.0 MeV. The minor irregularities in the imaged circle result from the assumption that all detectors have the same efficiency.

This measurement constitutes a perfect demonstration of the performance of the imaging algorithm: The left image shows the zeroth iteration of the list-mode maximum-likelihood expectation-maximization algorithm. The overlapping raw Compton cones let the source appear disk-like. With higher iterations, the ring structure becomes visible. The algorithm was halted when the width of the ring roughly corresponded to the angular resolution achieved by the MEGA prototype.

8.2.3 On axis imaging as a function of energy

Figures 8.17 and 8.18 show the reconstructed Duke images in the Compton regime from 710 keV up to 8 MeV for on-axis measurements, split into tracked and not tracked events. Only two-site events were used to generate the images, which nicely illustrate the improvement in angular resolution towards higher energies promised by the decreasing ARM width illustrated in Figure 8.3.

Figure 8.19 shows reconstructed images for on-axis incidence in the pair regime (12 to 49 MeV). With increasing beam energy, the reconstructed source image becomes sharper, because the influence of both the unknown recoil of the nucleus and Molière scattering weaken.

8.2.4 Field of view

One large advantage of both Compton and pair telescopes is their large field of view. Figure 8.20 contains reconstructed images at incidence angles from 0° to 60° at 5 MeV and from 0° to 80° at 49 MeV, demonstrating the large field of view of the MEGA prototype in the Compton and pair regimes.

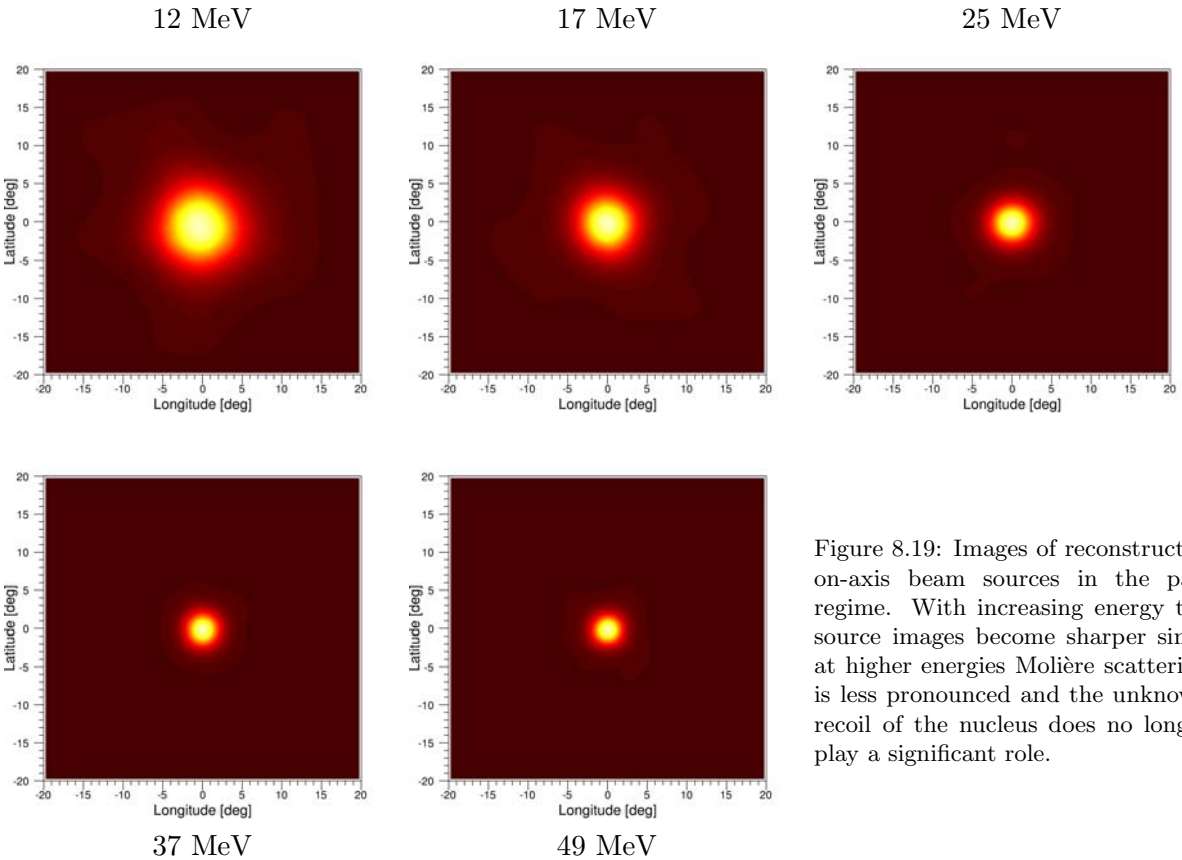

Figure 8.19: Images of reconstructed on-axis beam sources in the pair regime. With increasing energy the source images become sharper since at higher energies Molière scattering is less pronounced and the unknown recoil of the nucleus does no longer play a significant role.

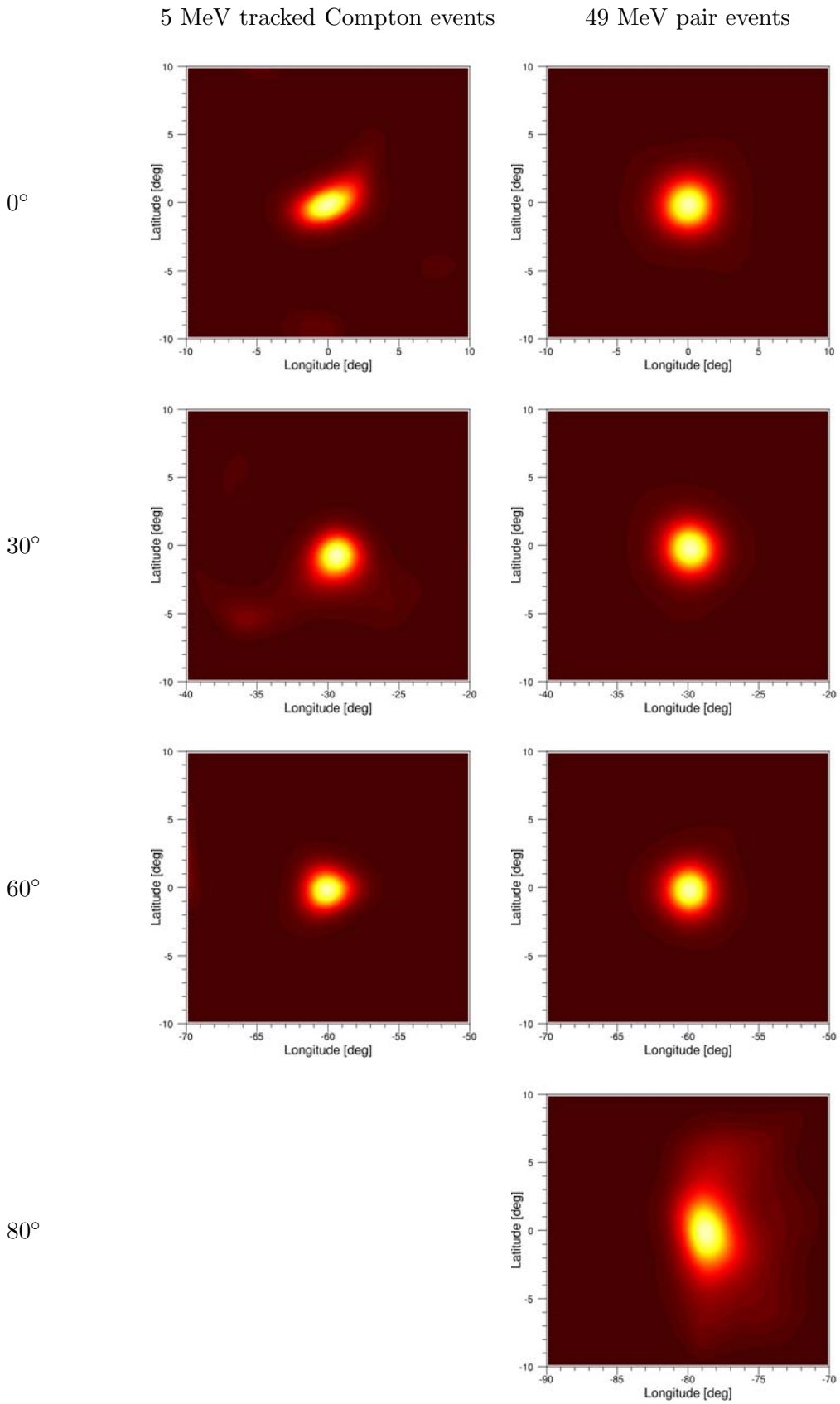

Figure 8.20: Field of view of the MEGA prototype for tracked Compton events at 5 MeV and pair events at 49 MeV.

Compton reconstruction of MEGA prototype 5 MeV data in combination with subsequent Maximum-Likelihood imaging yields point sources at the expected locations. All three imaged sources appear slightly less circular than their pair-event counterparts. A deeper analysis of the on-axis beam data indicates either beam instabilities or detector performance instabilities during the measurement. As a result, only ∼5 of the 9 nine scanned positions on the tracker, which were illuminated by the beam, can be reconstructed. This leads to the elongated shape of the reconstructed beam image. At 30° the image is based on only ∼200 events, at 60° on only 60 events. Thus low statistics are the likely cause for both the ∼1° off-beam reconstruction at 30° and the not-quite-circular shape of both off-axis beam images.

As for the Compton images, pair reconstruction of MEGA prototype data with subsequent Maximum-Likelihood imaging also yields point sources at the expected locations. For the 49 MeV pair events, like for all lower pair energies, the reconstructed image loses its nicely circular shape for the largest incidence angle, 80°, because of the longer path of the electrons in the layer of the pair creation. Simulations show that electrons which move almost horizontally through a layer are likely either stopped or leave the layer significantly closer to normal to the layer surface than they entered it. This creates a preference for tracks from electrons/positrons which underwent Molière scattering into a particular direction. In the reconstructed images this leads to a reconstruction of the sources too close to the instrument axis as seen in Figure 8.20 at 80°. This phenomenon is called "fish-eye" effect, and has also been measured with EGRET (*Thompson et al.*, 1993). Further improvements in the imaging response such as taking into account the incidence angle 5.3 could correct for this effect.

The accuracy to which the location of the beam source can be determined from the 5 MeV data is likely dominated by beam contamination effects for the on-axis measurement and certainly by the small number of events contributing to the off-axis images. The 49 MeV beam images contain several tens of thousands of events each — the point source location accuracy achieved here reflects remaining systematic uncertainties rather than consequences of source statistics. Figure 8.21 illustrates the accuracy to which the location of a very strong 49 MeV point source can be retrieved as a function of the incidence angle. While the on-axis performance is 0.15°, the location accuracy slightly deteriorates off-axis as the Fish-eye effect becomes more important.

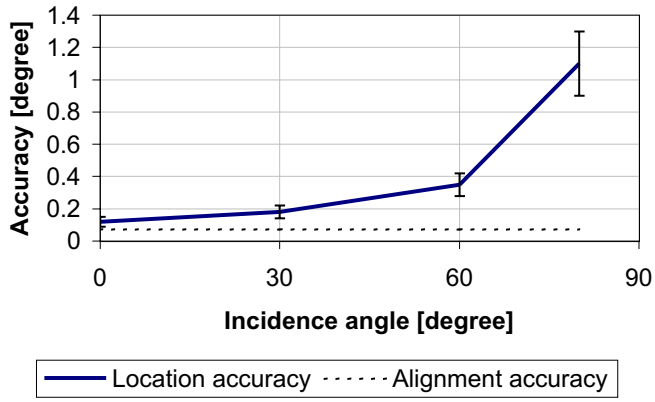

Figure 8.21: Location accuracy for pair events. 25000 events are used at each position.

Chapter 9

The MEGA prototype as Compton polarimeter

Most processes in high energy astrophysics, such as synchrotron radiation, bremsstrahlung, or Compton scattering, generate polarized gamma rays. All past and present gamma-ray telescopes, however, have at best limited capabilities to detect this polarization. A MEGA-like telescope, ideally suited to detect polarized gamma rays in the Compton regime, would provide a valuable tool for constraining emission geometries and source magnetic field configurations and thus enable a better understanding of the source emission mechanisms.

As described in section 6.2, all measurements during the Duke campaign were performed with monoenergetic 100% polarized pencil beams of gamma rays with a fixed, horizontal polarization vector. This beam is well suited to determine the polarization response of the MEGA prototype.

9.1 Data correction

To retrieve the expected polarization signal (see Chapter 2.2.3) from the raw azimuthal scatter angle distribution, three corrections have to be applied: for individual detector module efficiency, detector geometry, and background.

In the ideal case one measurement with a 100% linearly polarized photon beam and one with a non-polarized beam under otherwise identical would be required to allow optimum correction for efficiency and geometry. Due to the production process of the gamma rays (100% linearly polarized IR or UV photons are Compton backscattered), it was not possible to turn off the polarization of the beam at Duke. Other simple correction techniques, like rotating the detector or the polarization vector to effectively remove the polarization could not be applied either.

Measurements with radioactive laboratory sources, which are of course unpolarized, at energies similar to the Duke beams are one possibility for the corrections. However, due to (1) detector efficiencies strongly varying between the measurements in Garching and in Duke, (2) problems correcting far-field (Duke) with near-field (Garching) measurements and (3) not 100% identical energies (710 keV beam vs. 662 keV line of ^{137}Cs and 2.0 MeV beam vs. 1.8 MeV line of ^{88}Y), the laboratory measurements *alone* are not sufficient to perform all necessary corrections.

Consequently a more complex approach had to be chosen to correct the data. It relies partly on event selections, partly on laboratory calibrations, and partly on simulations: The most disturbing problem is caused by time-varying trigger and read-out thresholds in the calorimeters (see Chapter 6) which effectively result in time-variable efficiencies of the calorimeters. To overcome this problem, only those events were selected which have at least a deposit of 300 keV in one single crystal. Since low energies of the scattered gamma ray correspond to large scatter angles, this selection leads to a restriction to smaller scatter angles and thus the detected

polarization signature decreases. After this selection, all remaining differences are expected to be time invariant, like defective pixels or the coupling between crystals and PIN-diodes. So the remaining *efficiency* correction can be applied using previous lab measurements.

The largest influence on the azimuthal shape is due to the geometry. At low energies the holes between individual calorimeter modules are visible in the azimuthal scatter angle distribution. At higher energies the four edges of the bottom calorimeter are visible. Since no suitable unpolarized measurement was available, the *geometry* correction was taken from simulations.

The background does not need a correction since it can be easily suppressed by data cuts: Firstly, selecting only events from the known path of the tightly collimated beam eliminates practically all of the room background (especially the 1.461 MeV line of ^{40}K). Secondly, incompletely absorbed events and chance coincidences are eliminated (1) by the event reconstruction, (2) by selecting only events originating from the known source direction and (3) by using only events with the correct energy.

Thus the final correction applied to the data was:

$$P_{corr}(\chi) = \frac{P_{meas}(\chi)}{\mathcal{P}_{geo}(\chi)\mathcal{P}_{eff}(\chi,\varphi)} \tag{9.1}$$

where P_{meas} is the raw, measured and P_{corr} is the corrected azimuthal scatter angle distribution (details see Section 2.2.3) as a function of the azimuthal Compton scatter angle χ. $\mathcal{P}_{geo}(\chi)$ is the geometry correction discussed above, and $\mathcal{P}_{eff}(\chi,\varphi)$ is the described efficiency correction.

9.2 Polarization response of the prototype

As explained in Section 2.2.3 and illustrated in Figure 2.8, the polarization response of a Compton telescope has two main properties which of course should be visible in the MEGA measurements: The modulation as a function of energy has to increase towards lower energies. As a function of Compton scatter angles it has to reach its maximum at medium scatter angles (below 90°, depending on energy).

The measured energy dependence of the modulation for the Duke measurements at 0.71, 2 and 5 MeV is illustrated in Figure 9.1. If no Compton scatter angle selections are applied, the modulation decreases from 0.17 at 0.71 MeV to 0.12 at 2 MeV down to 0.06 at 5 MeV. At 8 MeV no significant modulation is seen. All these values are in good agreement with simulations.

The polarization vector of the Duke beam was horizontally aligned in the room and therefore the maxima of the measured modulation are expected in the vertical direction. Thus the minima, which correspond to the polarization angle, have to be found at 90° in Figure 9.1. The measured values, $82° \pm 24°$ at 0.7 MeV, $86° \pm 11°$ at 2 MeV and $74° \pm 18°$ at 5 MeV, are all compatible with a 90° polarization vector within measurement errors. At 2 MeV, measurement errors are smallest and the measured polarization angle agrees well with the beam's polarization vector. The large error — and large deviation of the measured polarization angle — at 5 MeV can be explained by the weak polarization signal and the poor statistics. At 0.71 MeV the deviation is mainly due to varying efficiencies of individual detector modules.

Since the source signal dominates the background and since only one source is present, for these measurements it is also possible to do a polarization calculation without the necessity of imaging the event into the source location and without restricting the energy. For example, ∼50% of the events at 710 keV cannot be imaged into the point source, although their first interaction is within the beam path. The reasons are mainly incomplete absorption in the tracker or calorimeter, but also problems measuring the correct energy for small hits in the calorimeters. Events with low-energy calorimeter hits carry most of the polarization information, but no correct calorimeter calibration below 511 keV exists. Moreover, due to the difference between the calibration and measurement mode (details see 7.2 and *Andritschke*, 2006) it is likely that

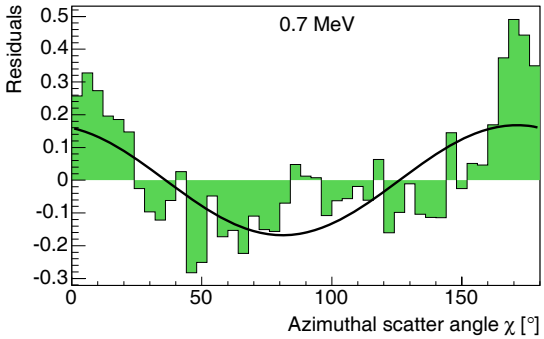

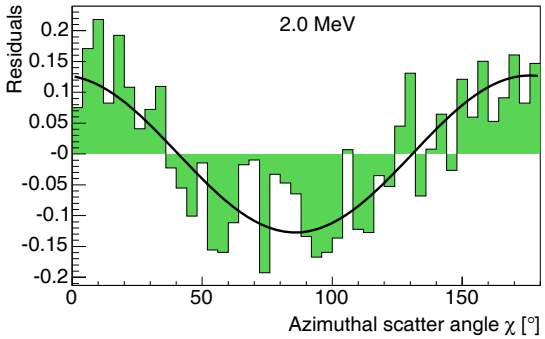

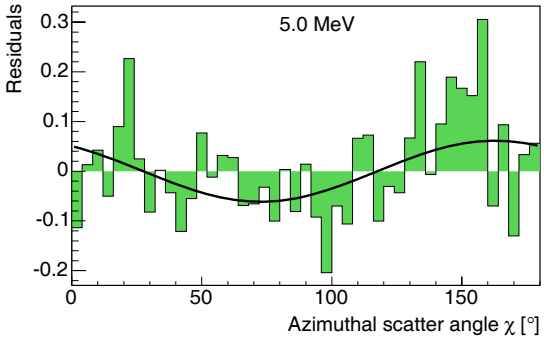

Figure 9.1: Polarization response as a function of energy: The black line indicates the best fit with a cosine. The origin of the scatter angle x-axis corresponds to the vertical direction as MEGA is mounted at HIGS. Within measurement errors and statistics, all values are in agreement with the simulations (see table below).

Energy [MeV]	Modulation μ		Polarization angle [°]	
	measured	simulated	measured	simulated
0.71	0.17 ± 0.04	0.19	82 ± 24	90
2.0	0.13 ± 0.03	0.14	86 ± 11	90
5.0	0.06 ± 0.03	0.03	74 ± 18	90

the total measured energy is lower than the real one. The latter is easily verified by looking at the spectrum for the 710 keV measurement when only energies of the scattered gamma-ray below e.g. 450 keV (scatter angles larger 54°) are allowed. There no photo-peak is visible.

If no kinematics restrictions are applied, and only the azimuthal scatter angle is determined geometrically from the two interaction positions, the modulation can also be determined. Only an upper energy cut has to be applied to suppress background from the beam itself as well as from the concrete walls (^{40}K).

This method results in a modulation of 0.30 ± 0.08 at 710 keV, which is almost a factor 2 higher than that obtained using the initial event selections, but suffers from a much higher uncertainty. Since at higher energies the suppression of larger scatter angles does not play a dominant role, at 2 MeV and above the two methods yield the same results within measurement errors.

The modulation as a function of the Compton scatter angle is shown in Figure 9.2 for the 2 MeV measurement. As expected, the modulation reaches its maximum around 66°; the measurement is in good agreement with the simulations.

The prototype clearly demonstrates that MEGA is a perfect polarimeter in the Compton regime. The well-chosen geometry of MEGA allows it to detect Compton events with large scatter angles; these carry most of the polarization information. An envisioned MEGA satellite telescope will probably be able to measure photons down to ∼300 keV, where the polarization

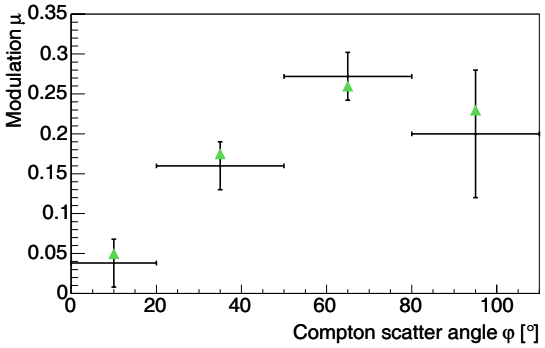

Angle φ [°]	Modulation μ	
	measured	simulated
10	0.04 ± 0.03	0.05
35	0.16 ± 0.03	0.17
65	0.28 ± 0.03	0.26
95	0.20 ± 0.08	0.23

Figure 9.2: Dependence of the modulation on the Compton scatter angle for 2 MeV photons. The triangles represent the values from Geant4 simulations, which are in good agreement with the measurements. The maximum is reached as expected around 66°. At 95°, poor statistics lead to a larger measurement error.

information of the original photons is best preserved through the Compton scatter process. While MEGA will not be able to distinguish these low energy photons from background in normal operation mode, for special sources such as gamma-ray bursts or solar flares the polarization properties can be easily determined: They are short and strong events for which the background does not play a dominating role. MEGA will add a new dimension to gamma-ray astronomy — polarization!

Part IV

Steps towards a MEGA space mission

Chapter 10

Expected performance of a MEGA satellite mission

Building, testing and calibrating the MEGA prototype was a crucial step towards a MEGA space mission. In order to make significant contributions to answering many of the most pressing questions in medium-energy gamma-ray astronomy the MEGA satellite instrument has to provide at least a factor 10 sensitivity improvement over COMPTEL, needs to operate in the energy band from at least 0.4 to several tens of MeV, requires a wide field-of-view, needs to be sensitive to polarization, and must have an excellent energy, position and time resolution. Therefore, significant performance improvements compared to the prototype are mandatory. In this chapter the performance of one possible incarnation of a MEGA instrument, which is loosely based on the MEGA pre-phase A study (*Wolter et al.*, 2000), will be presented.

10.1 Necessary design improvements towards a satellite mission

Although the MEGA prototype demonstrated adequate performance during its calibration, the prototype's energy and angular resolution in the Compton regime are mostly inferior to the performance of its satellite predecessor COMPTEL. A MEGA satellite mission, however, aims at a sensitivity improvement of a factor of 10 over COMPTEL with a significantly more compact instrument, requiring powerful background rejection capabilities which in turn depend on the instrument's energy and especially angular resolutions. The desired sensitivity improvement over COMPTEL translates into at least ∼5% energy resolution in the photo-peaks in the nuclear line regime, at least ∼2° angular resolution, and a photopeak efficiency of a few percent. Some feasible improvements comprise the energy and angular resolution, efficiency and methods for background rejection.

The overall **energy resolution** is obviously determined by tracker and calorimeter together, which both need to be enhanced for a satellite mission (a detailed discussion of all technical aspects of the necessary improvements summarized below can be found in *Andritschke*, 2006):

- The calorimeter modules' energy resolution can be improved by replacing the PIN diodes with drift diodes; improved signal to noise ratio and on-chip amplifiers would enable a factor of 2–3 improved energy resolution.

- The energy resolution of the Si-strip detectors can be enhanced by reducing the leakage current This should be easy with today's production techniques. Additionally the tracker can be cooled moderately. Decreasing the temperature from 21°C to 8°C yields an improvement in energy resolution of 30% (*Bloser et al.*, 2003).

- In a future read-out system temperature instabilities, varying trigger thresholds, systematic errors due to delicate timing, etc. will be significantly reduced to improve the energy resolution.

The **angular resolution** is influenced by detector position resolution and Doppler broadening as well as energy resolution. While a Silicon tracker is already the best choice of currently available semi-conductor materials as far as Doppler-broadening is concerned, the following improvements are possible:

- For tracking Compton telescopes, which predominantly track Compton events with large Compton scatter angles, the energy resolution of the second detector system is more important than that of the first one (compare Figures 2.14 and 2.15 for large scatter angles). Therefore, more efforts should be devoted to improving the calorimeter modules' energy resolution.

- While the position resolution of the tracker is more than sufficient, the position resolution of the calorimeter, especially the depth resolution, is not. For a much larger satellite detector, the average distance between the tracker and calorimeter interactions increases and the problem partly resolves itself. In addition, switching from PIN to drift diodes in the calorimeter would not only improve the energy resolution but also the depth resolution. Moreover, a careful roughening of the surface of the crystals would lead to an increased light output gradient along the CsI bars. Since this sacrifices part of the light yield and thus energy resolution, a detailed trade-off analysis is required.

The **efficiency** of a detector is determined by the fraction of incoming photons whose incident direction and energy is correctly reconstructed to within the instrument's angular and energy resolution.

- The first measure to increase the number of photons detected in a D1-D2 hit sequence is to build a deeper tracker in which significantly more photons have their first interaction. Currently only 0.7 percent of all on-axis 2 MeV photons, which generate a D1-D2 trigger have their first interaction in the tracker.

- As a second step, the calorimeter has to be constructed in a more compact fashion: While the calorimeter of the prototype covers only $\sim$30% of the lower hemisphere, the final version should cover $\sim$100%.

- Additionally, reducing the amount of passive material inside the detector head results in an increased number of events completely absorbed in active detector material. Thus it is very important to reduce as much as possible all materials on the path of the photons to their interaction in the tracker and on their way to the calorimeter (minimize mechanical structure of D1 and its surrounding electronics, make a thin entry window into the calorimeter, etc.).

- One of the limiting factors for the prototype's efficiency is the high dead time of the readout, which limits the detectable event rate to roughly 130 cts/s. A simple advance would be to read out all chips in parallel instead of in series, and/or to read out only channels with signals above the noise threshold.

- Due to the high thresholds in the detectors a lot of interactions with small energy deposits are lost. This is particularly problematic for the start point of a Compton electron track, which has a probability of $\sim$25% percent to go undetected in the prototype — only the passage of the electron through the next layers is detected, leading to missing energy, decreased position resolution, and a higher risk of wrongly reconstructing the event. Most of the strategies to improve the energy resolution will also enable lower thresholds.

Ultimately, the sensitivity of a detector system including event reconstruction is determined by its source detection and its background rejection capabilities as well as the **background prevention measures** implemented in the instrument's design. The first two, background rejection and source detection capabilities, are mainly determined by energy and angular resolution (the smaller the point spread function the better) as well as detector efficiency and the performance of the event reconstruction. The detector design considerations listed below would constitute measures that prevent or at least reduce certain types of background events through optimized detector design:

- A calorimeter that completely covers the lower hemisphere would not only increase the source detection efficiency, but also shield the tracker against photons from the Earth's atmosphere (albedo photons).
- Less passive material, especially within the detector head, and the selection of structural materials which have lower probability to get activated in reactions with protons and neutrons can reduce the background.
- A shorter coincidence window will reduce the number of chance coincidences.
- Thinner wafers would reduce the effects of Molière scattering and thereby reduce the length of event arcs and thus the size of the point spread function. However, since this would also result in a higher energy consumption of the tracker (more channels) and worse energy resolution for the tracks (more measurement points), this path is not followed for the satellite detector. Detailed tradeoff studies between energy resolution and electron-tracking performance should be performed.
- An additional possibility not incorporated into the instrument simulated here would be to replace the CsI calorimeter with a calorimeter built from $LaBr_3$ or a high-density semiconductor like Germanium or CZT. The resulting improved energy resolution of the calorimeter would allow to apply the triple Compton approach with a significantly better accuracy than is possible with a CsI calorimeter. Moreover, the potentially higher pixelation and the slightly lower Z of e.g. Germanium detectors would allow to measure and resolve more interactions of the initial photon. The more parameters of the initial photons are measured, the better the chances to reject background. However, the more interactions occur on average, the more pressing is the need for an outstanding energy resolution as well as for minimal amounts of passive material in which those interactions could also occur.

10.2 A potential MEGA satellite

The baseline geometry for the MEGA telescope has been defined by the Pre-Phase A study (*Wolter et al.*, 2000). The tracker consists of 32 Silicon layers, each of which consists of 6×6 wafers of the size 6×6 cm^2. Their thickness (0.5 mm), and pitch (0.47 mm), as well as the layer distance (1.0 cm) are the same as for the prototype. For the simulation, an uniform energy resolution of 10 keV FWHM has been assumed as well as a trigger threshold of 50 keV and a noise threshold of 30 keV.

The lower hemisphere is completely surrounded by a CsI calorimeter which has a thickness of 8 cm at the bottom and 4 cm on the sides. Replacing the PIN with drift diodes should lead to an energy resolution of 5% at 662 keV (8% at 350 keV, 3% at 2000 keV) in each crystal. A uniform depth resolution of 0.5 cm FWHM was assumed in the large 8 cm crystals. The 4 cm crystals at the side do not have a depth resolution.

A sophisticated model of the geometry has been built. Great care has been taken to model the spatial distribution as well as the isotopic composition of all materials correctly. The satellite

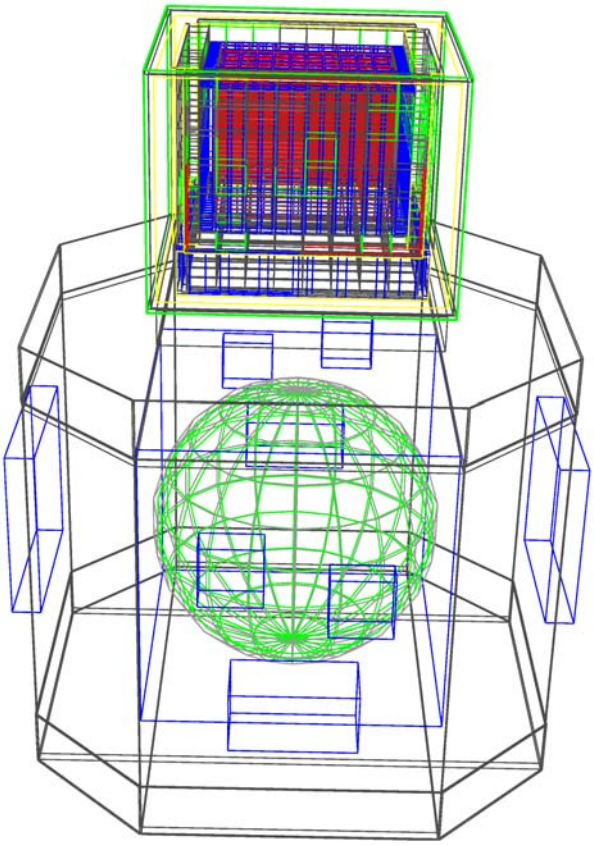

Figure 10.1: Wire-frame representation of the MEGA satellite as used for simulations. The spacecraft has a total mass of 850 kg. The overall height of the whole spacecraft is 1.8 m; length and width of the spacecraft bus are 1.4 m.

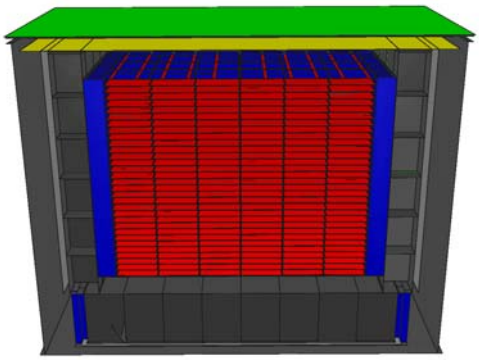

Figure 10.2: Cutaway view of the detector head. The central structure represents the Silicon tracker (red). It is surrounded on the sides by 4 cm deep calorimeters and on the bottom by 8 cm deep calorimeters (grey housing visible). The whole structure is surrounded by an anti-coincidence shield. It has a height of 55 cm and a width of 65 cm.

consists of 850 kg of material, of which 5.3 kg are active Silicon, 183 kg CsI, and 16 kg plastic scintillator (anti coincidence). Drawings of the complete spacecraft as well as a cross section through the simulated detector head are shown in Figures 10.1 and 10.2.

10.2.1 Simulation and orbital background

The simulation follows the approach explained in Section 3.2: The simulations were performed with MGGPOD, and the input background spectra have been generated with the environment component of the ACTtools (*Wunderer et al.*, 2006). The simulation assumed an equatorial orbit at 525 km altitude to avoid passage through the South Atlantic Anomaly (SAA) and thus prevent activation of the detector material by trapped protons. The simulated input spectra comprise cosmic photons, protons, electrons and positrons as well as albedo photons and neutrons. For hadron environment components, detector and spacecraft activation and subsequent radioactive decays have been included in the simulations. The input spectra for the different components are shown in Figure 10.3. The cosmic particle distributions are isotropic where they are not shielded by Earth; albedo photons are not evenly distributed but exhibit a significant concentration around zenith angles of $\sim$120°. It should be noted that the Cesium and Iodine neutron cross sections currently included in MGGPOD are only estimates.

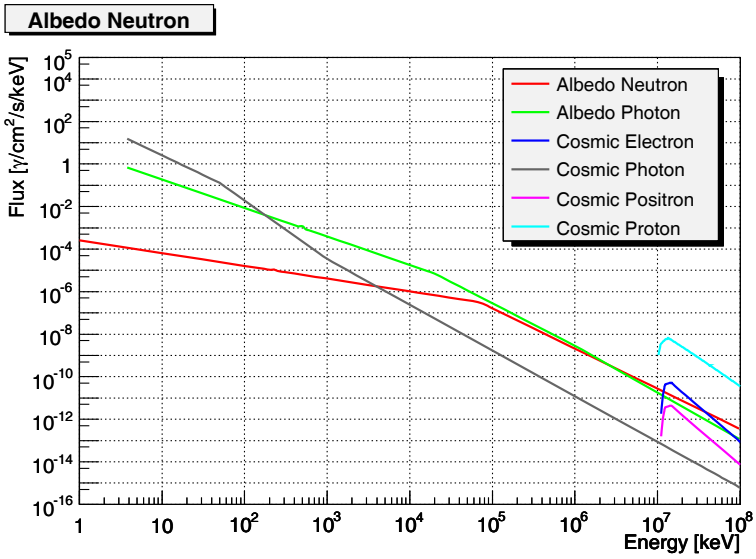

Figure 10.3: Integrated input spectra for the background simulations. Due to the geomagnetic cutoff, charged particles need at least an energy of 10 GeV to reach the spacecraft.

10.2.2 Event selections

For the event reconstruction of the simulated MEGA satellite data, the Bayesian approach has been used. Detailed response matrices for electron tracking and Compton sequence reconstruction as described in Chapter 4 have been calculated to enable this elaborate event reconstruction approach and consequently provide the best background rejection available.

However, having used this elaborate event reconstruction approach does *not* imply that all reconstructed events should be used in the analysis. For the ultimate goal, determining the best point-source sensitivity achievable with the MEGA instrument, several key background rejection cuts have to be made. Evaluating the instrument's point source sensitivity necessitates a selection on a "resolution element window" around the (assumed known) source position. For not tracked events this window constitutes an ARM window, for tracked events an ARM and SPD window. For the case of gamma-ray line sources, an energy window is also necessary as part of this basic set of selections. A second class of event cuts chooses only the "best" events, i.e. those defined by small Compton scatter angles, good Compton and track quality factors, as well as a not too large $d\vartheta$ value.

In addition, measures must be taken to reduce as much as possible the largest background component which are photons generated by cosmic-ray interactions in the Earth's atmosphere. To achieve this, a so-called Earth horizon cut is introduced: For each event the probability is calculated that it originates from the Earth's atmosphere. The current algorithm determines the fraction of the event origin probability distribution (the Compton circle or arc) which is compatible with an origin in the Earth's atmosphere. If this value is too large, then the event is rejected.

For pair events, two selection criteria are implemented: one on the opening angle (angle between the direction of electron and positron), the other on the energy deposit in the first layer — the higher the energy deposit, the longer was the electron/positron path in the first layer; the resulting more significant Molière scattering finally results in a larger angular deviation from the true origin.

Most of the cuts are a function of energy, thus their optimum values have to be determined for each nuclear line of interest or, for continuum sensitivity calculations, for each energy interval. Moreover, it is not obvious what the ideal values — i.e. those which optimize the sensitivity — are for e.g. a given astrophysical line and the background below this line. Thus a 13-dimensional event selection data space has to be searched for the optimum selections. This is accomplished by calculating the sensitivity for each bin in this data space. Some selected results, for narrow

Event selections	511 keV	1809 keV	50 MeV
Event types included in analysis	not tracked Compton	tracked Compton	pair
ARM-window around the source location	0–2.8°	0–2.2°	0–2.8°
SPD-window around the source location	n/a	0..32°	n/a
Energy window	±18 keV	±20 keV	25–75 MeV
Maximum Compton quality factor	0.8	0.97	n/a
Maximum Track quality factor	n/a	0.04	n/a
Maximum Compton scatter angle	90°	160°	n/a
Maximum $d\vartheta$-criterion	n/a	42°	n/a
Earth horizon cut (angle determined from zenith)	0–90°	0–80°	0–50°
Maximum allowed probability that the event came from below horizon	0.0	0.7	n/a
Minimum track length	1	2	n/a
Minimum length of Compton sequence	2	2	n/a
Maximum angle between electron and positron of pair events	n/a	n/a	20°
Maximum deposit in first layer of pair creation	n/a	n/a	600 keV

Table 10.1: Event selections optimized for point source sensitivities in scanning mode; for details see text.

lines at 511 keV (not tracked Compton events) and 1809 keV (tracked Compton events) as well as for a continuum sensitivity bin around 50 MeV (pair events), can be found in Table 10.1

10.2.3 Instrument resolutions and efficiency

The following section describes the main instrument characteristics for the detection of point sources: energy and angular resolution as well as effective area. To derive each data point, the event selections resulting in optimum *sensitivity* at that energy — derived in the fashion described above — were used.

Figure 10.4 illustrates the expected photo-peak **energy resolution** of the telescope, shown in terms of the peak's full width at half maximum. For all figures, nuclear-line energies of particular astrophysical interest have been chosen as the data points: the 511 keV positron annihilation line, the 847 keV line from ^{56}Co decay, which originates e.g. from SN Ia, 1157 keV from ^{44}Ti, a tracer for young supernova remnants, 1809 keV from ^{26}Al, a tracer for e.g. star

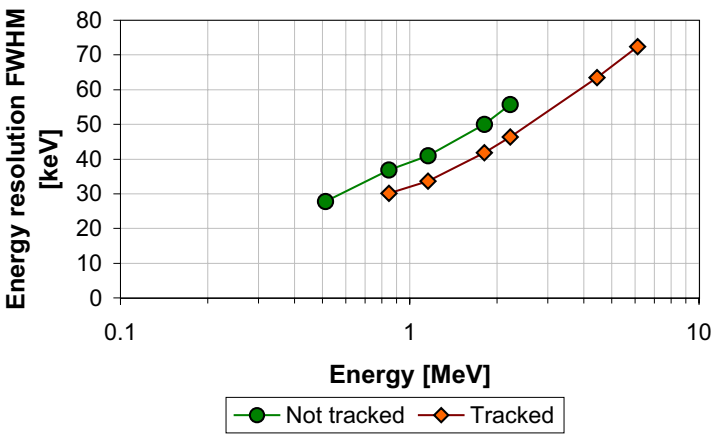

Figure 10.4: Energy resolution for tracked and not tracked events. Since not tracked events deposit more energy in the calorimeter and the calorimeter's energy resolution is worse than the tracker's, not tracked events have a worse energy resolution.

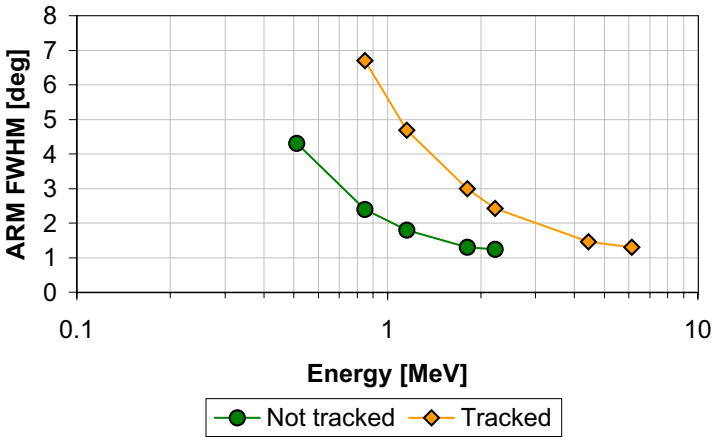

Figure 10.5: Angular resolution for tracked and not tracked events. As already seen with the MEGA prototype, not tracked events have a better angular resolution (FWHM of ARM) than tracked events. Since the accuracy of the energy measurement of the scattered gamma ray is more important for larger scatter angles than for smaller scatter angles, the energy resolution in the calorimeters influences the angular resolution of tracked events most.

formation regions, 2223 keV from neutron capture, as well as the nuclear excitation lines of $^{12}C^*$ (4.44 MeV) and $^{16}O^*$ (6.13 MeV). All performance values are quoted for ideally narrow lines, irrespective of likely-to-be-expected line shapes of actual astrophysical sources.

Since the tracker has a better energy resolution than the calorimeter, tracked events — which deposit a larger fraction of their overall energy in the tracker — have a better energy resolution than not tracked events. Unfortunately, above ∼6 MeV the satellite has similar problems as the prototype: Particles escape or deposit energy in passive material and thus no (significant) photo peak at higher energies is achieved for either Compton or pair events.

Two key parameters describing the **angular resolution** of a tracking Compton telescope are ARM and SPD: in combination they define the size of the point spread function in the imaging data space. Figure 10.5 gives the ARM width for tracked and not tracked Compton events over the full energy range for which the instrument detects a significant photo peak. Since the influence of the energy measurement error (including Doppler broadening) of the scattered gamma ray dominates the angular resolution (see Section 2.2.5, especially Figure 2.15), tracked events have roughly a factor two worse resolution than not tracked events. At higher energies, the angular resolution converges towards the position resolution limit close to 1° for both tracked and not tracked events. Compared to the prototype, the MEGA satellite instrument's angular resolution is roughly a factor of three better. This is to a large extent due to the improved energy resolution in the calorimeter; the larger distance between the interactions — which lowers the position resolution limit — also contributes significantly.

The scatter plane deviation, which describes the length of the Compton arcs, as a function of energy is plotted in Figure 10.6. With higher energies, the effect of Molière scattering is less pronounced; consequently the arcs become smaller. In contrast to the prototype, selecting only photo-peak events does not pose a significant restriction on the amount of energy transferred to

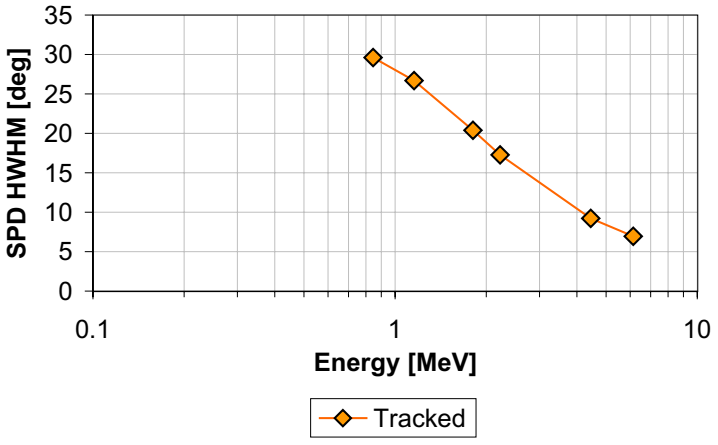

Figure 10.6: Scatter plane deviation as a function of energy.

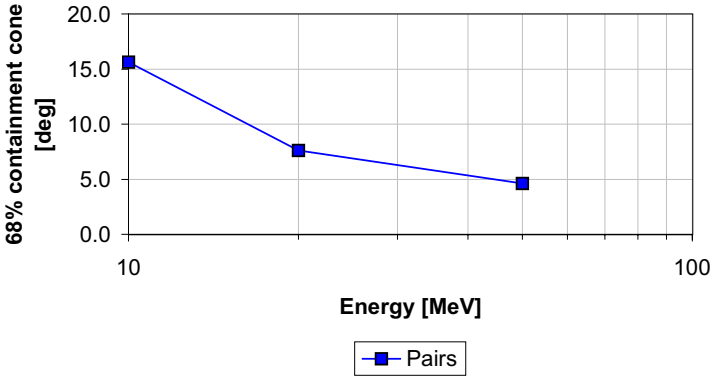

Figure 10.7: Angular resolution of pair events; defined as a 68% containment cone.

the recoil electron: the tracker is large enough to also fully absorb high-energy recoil electrons.

In the pair regime, no significant differences in the angular resolution exist between prototype and the satellite instrument discussed here. The unknown recoil of the nucleus as well as Molière scattering becomes less influential at higher photon energies, and thus the angular resolution improves (Figure 10.7). Although these high energy photons are almost never completely absorbed in active material, the energy containment in the case of the satellite is good enough so that the application of the energy-dependent equation 2.28 for the calculation of the origin of the photon gives slightly (20%) better results than the energy-independent equation 2.29.

No real-life telescope can detect all gamma rays which pass through its surface area. The **effective area** of a telescope is defined as the geometrical front area a corresponding *ideal* telescope would require in order to record the same number of valid counts. The effective area of the satellite instrument can be calculated based on simulations according to the following equation:

$$A_{eff} = A_{start} \frac{N_{detected}}{N_{started}} \tag{10.1}$$

$N_{started}$ photons of identical incident direction are started from the area A_{start}, which is chosen large enough so that photons impinge on the complete telescope, and $N_{detected}$ photons pass the given event selections.

The effective area for the MEGA telescope in the photo-peak domain for not tracked events is given in Figure 10.8 as a function of different energies and event selections.

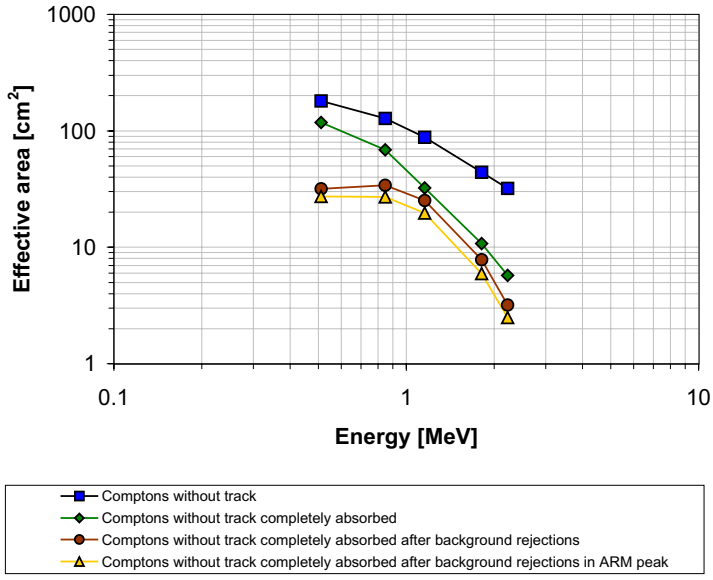

Figure 10.8: Effective area for not tracked events as a function of the series of event cuts applied to obtain optimum sensitivities. For an explanation of the different cuts see text.

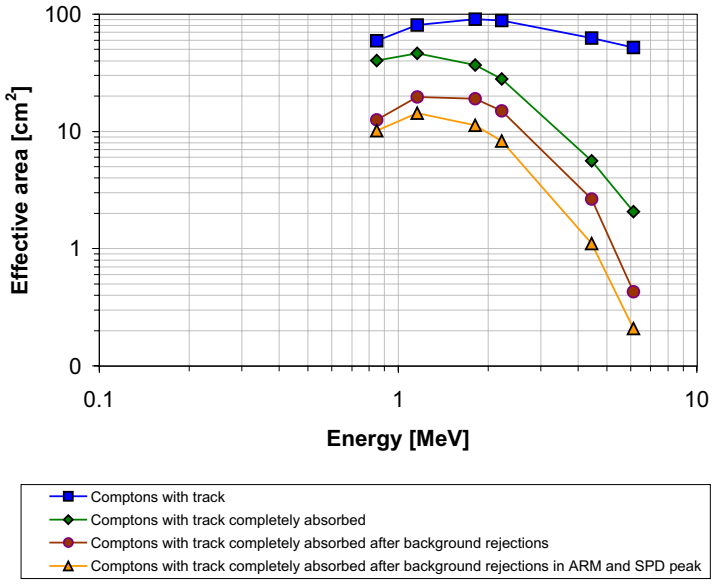

Figure 10.9: Effective area for tracked events as a function of different event cuts. See text for a discussion of the cuts applied.

The first curve (squares) shows all kinematically correct Compton interactions starting in the tracker which do not produce a track.

The second curve (diamonds) represents all events within a roughly $\pm 1.4\sigma$ energy-resolution window around the simulated narrow-line energy, i.e. the photo-peak events. Since above $\sim$1 MeV most not tracked events are incompletely absorbed, this results in the largest reduction of events at higher energies.

The third curve shows all events which pass the event selections, i.e. the background rejection criteria, which are chosen to optimize the narrow-line point source sensitivity at each energy. For not tracked events those comprise cuts on the Compton scatter angle, the Compton quality factor, and an Earth horizon cut. The positron annihilation line at 511 keV is a strong background line — as well as a very interesting astrophysically emitted line — due to positrons from beta decays. Thus very strict cuts are necessary. They reduce the source signal significantly — but still result in the optimum narrow line point source sensitivity achievable.

The last curve (triangles) shows only events which are compatible with the position of the tested point source given the instrument's angular resolution, i.e. which lie within the selected ARM window.

Below 511 keV, the achievable instrument effective area will be strongly influenced by the in-orbit trigger regimes and trigger thresholds whose settings will have to be selected partially in response to telemetry availability. Thus the effective area of the satellite instrument at low energies is hard to realistically predict. Generally, the effective area below 500 keV falls as Compton scatter events depositing enough energy for a trigger in both tracker and calorimeter become less likely. Below $\sim$100 keV, photo-effect dominates the interactions in the tracker.

The impact of similar event selections on the effective area is shown for tracked events in Figure 10.9. The increasing number of rejected events in the second curve (diamonds) reflects the decrease of full absorptions at higher energies. At 6 MeV only 4% of all triggered events are fully absorbed. The third curve shows again the effect of event selections optimized to reject background. For tracked events, the maximum allowed difference between the total scatter angle calculated via geometry (angle between scattered gamma ray and recoil electron) and via Compton kinematics ($d\vartheta$-criterion) is most important, because it eliminates most of the wrongly-reconstructed or upward-moving events. Another cut is performed using the quality factors of the event reconstruction. Events which might have been reconstructed incorrectly, or occupy data space cells which are dominated by background, are suppressed. Finally, an Earth horizon cut rejects events originating from the lower hemisphere (in detector coordinates;

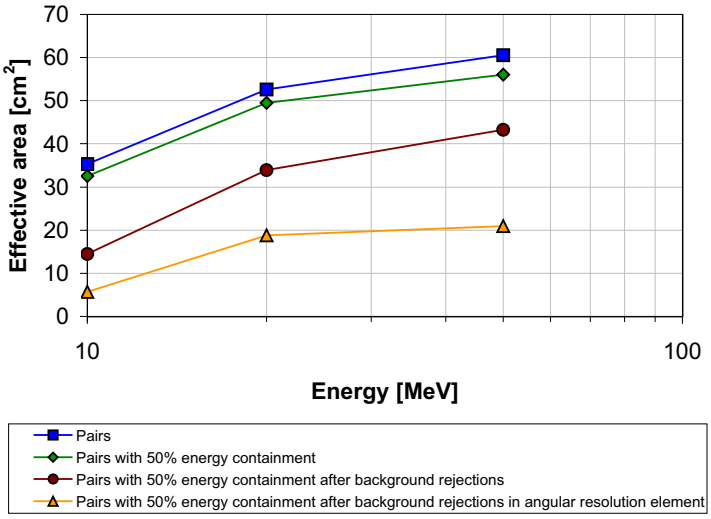

Figure 10.10: Effective area for pair events after applying different levels of data cuts to optimize the point source sensitivity.

mainly photons from the Earth's albedo and from detector activation). Omitting these event selections optimized to improve sensitivity would worsen the instrument's on-axis narrow-line point-source sensivitiy by roughly a factor 2.5 at 1809 keV.

In the pair regime the influence of event selections on the effective area is a little bit more complicated. A complete energy measurement is not necessary to determine the origin, thus a restriction on the (not prominent) photo-peak is not required. The only relevant event selections are those on the opening angle of the pair and on the energy deposit in the first layer of interaction. The sensitivity optimization is done within continuum energy bands rather than for a single line energy. The corresponding values can be found in Figure 10.10. The first curve shows all pair events, the second only those with at least 50% energy containment in the active detector material. The third curve includes background rejection selections, like a cut on the opening angle, on the energy deposit in the layer of pair creation and an Earth horizon cut, which basically only allows incidence angles smaller than 60°. The last curve contains only events which are compatible with the source location. For the last two curves the values of the cuts correspond to those which optimize the continuum sensitivity. Depending on the different scientific tasks, different, less restrictive event selections could be chosen.

Another key parameter for a MEGA satellite instrument is the **field of view** of the telescope. MEGA is intended to scan the whole sky and to detect variable sources. The larger the portion of the sky it can see during a scan the more photons it collects over time from any given region. Therefore a large field of view improves the total exposure, even if the absolute effective area far off-axis is fairly small. In addition, the resulting all-sky exposure becomes fairly uniform and thus easier to handle during data analysis. Finally, the chances of detecting variable sources such as gamma-ray bursts or flaring AGNs is much larger with a large field of view.

The field of view of the MEGA satellite for tracked events is shown in Figure 10.11. The HWHM in instrument effective area for tracked events, after all cuts illustrated in Figure 10.9, is reached around 40° incidence angle. For not tracked events and pair events the HWHM is between 40° and 50°.

10.2.4 Sensitivity

The most important performance parameter for any (gamma-ray) telescope is its sensitivity. It describes the weakest source which can still be detected with a certain significance z (in units of σ), e.g. $z = 3$. For point sources the following equation holds:

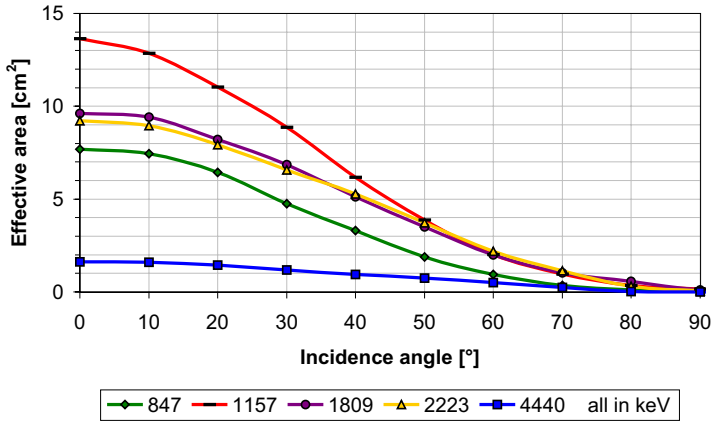

Figure 10.11: Field of view (expressed as an effective area) for tracked events after all event selection cuts. The HWHM is reached around 40°.

$$F_z = \frac{z\sqrt{N_S + N_B}}{T_{eff}\, A_{eff}} \tag{10.2}$$

Here F_z is the $z\sigma$ sensitivity limit, expressed in terms of the flux a source must have to be detected at this sensitivity limit, N_S the number of source photons, and N_B the number of background photons in the resolution element, A_{eff} the effective area of a telescope, and T_{eff} the effective observation time. The resolution element describes the complex point spread function of the telescope. In this work it is defined by an ARM, SPD and energy window around the known source position.

The number of source photons for a source at the sensitivity limit is given by $N_S = F_z\, T_{eff}\, A_{eff}$. Solving for F_z, Equation 10.2 can be rewritten as:

$$F_z = \frac{z^2 + z\sqrt{z^2 + 4N_B}}{2\, T_{eff}\, A_{eff}} \tag{10.3}$$

Three types of sensitivities are most relevant for a Compton and pair telescope: the continuum sensitivity, the (narrow) line sensitivity, and the polarization sensitivity.

In contrast to COMPTEL and EGRET, MEGA is not intended to be operated in pointing mode, but in scanning mode: instead of being oriented at one section of the sky while circling in low-earth orbit, MEGA will always point away from Earth and scan the complete sky. This approach maximizes the sky exposure over the mission (a target-pointed instrument in low-earth orbit looks at Earth a significant amount of its observation time) and simplifies mission operations (no repointing at chosen targets required). To correct for the resulting uneven exposure, MEGA will probably be tilted from time to time by ±25° towards the Earth's poles.

As a consequence of this scanning scheme, all sources are observed under constantly changing background conditions and with changing effective areas. To determine the sensitivity in scanning mode given a total observation time, first the effective area after event selections as a function of the incidence angle has to be determined. From an integration over the sphere and total observation time the average exposure in the source element can be retrieved. Similarly, the number of background events in the resolution element can be obtained. Since MEGA constantly looks away from Earth and in its low-earth equatorial orbit would not suffer from passages through radiation belts or the South Atlantic Anomaly, it will be able to perform science observations at least 90% of its actual time in orbit. 10% are assumed to be needed for instrument health checks and calibration.

Figure 10.12 shows MEGA's average **continuum sensitivity** for point sources after five years all-sky survey compared to the nine-year COMPTEL mission. The latter values were taken from *Schönfelder et al.* (2000) for the average exposure, corrected for $\Delta E = E$ (assuming

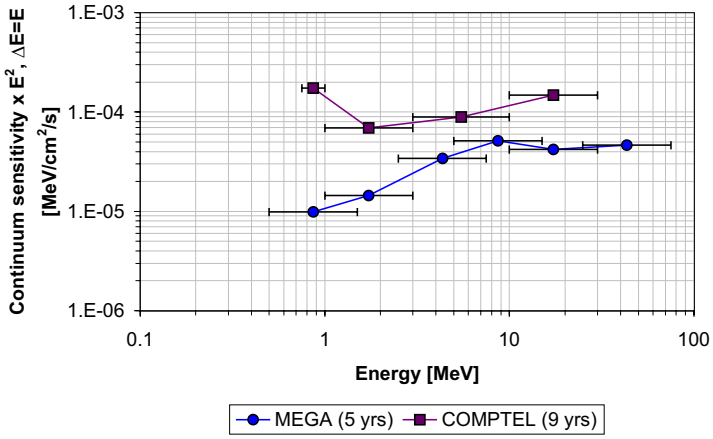

Figure 10.12: Average MEGA continuum sensitivity after five years all-sky survey compared to the average sensitivity of COMPTEL after its nine-year mission. A power-law source spectrum ($\alpha = -2$) was assumed for the simulations of MEGA. The energy error bars for the COMPTEL values show the original energy bins. The sensitivity however has been determined for an $\Delta E = E$ window.

an E^{-2} slope), and scaled to an observation time of nine years (assuming 52 days average effective observation time).

Below one MeV, MEGA will achieve the goal of 10 times better sensitivity than COMPTEL. Below 750 keV as well as at high energies, between 30 and 50 MeV where neither COMPTEL nor EGRET had a reasonable sensitivity, MEGA will provide evenly exposed all-sky maps with unprecedented sensitivity. Between 1 and 30 MeV a five-year MEGA mission as outlined in the Pre-Phase A study still provides a factor 2 to 5 improvement over COMPTEL's nine-year mission sensitivity. Between 5 and 15 MeV, MEGA's sensitivity is limited by incompletely absorbed Compton events; pair events at these energies are still fairly well contained but the pair angular resolution at these energies is too coarse to further improve the sensitivity (Figure 10.7). Basing the sensitivity calculation on a combined spectral and directional deconvolution might improve the performance especially in the 5–15 MeV Compton regime. However, a more efficient instrument, i.e. one with a thicker tracker and a better energy resolution in the calorimeters, would constitute a much more promising approach. A spectral deconvolution can never compete with an instrument efficiently containing the full photon energy in the first place.

MEGA's **sensitivity to nuclear lines** constitutes a significantly greater improvement over COMPTEL than its sensitivity to continuum sources. Figure 10.13 shows the estimated average 3σ sensitivity of the MEGA telescope to narrow lines after five years of scanning observations compared to COMPTEL at 1.809 MeV (*Oberlack et al.*, 2000a) and 2.2 MeV (*McConnell et al.*, 1997). After the same observation time (here five years) MEGA will exceed COMPTEL's narrow-line point-source sensitivity by a factor of 10. Due to the associated larger effective area and better angular resolution, untracked events yield a better sensitivity for MEGA below 1 MeV than tracked events. However, for the current geometry and with optimized event selections, measuring electron tracks reduces the number of background counts in a given angular resolution

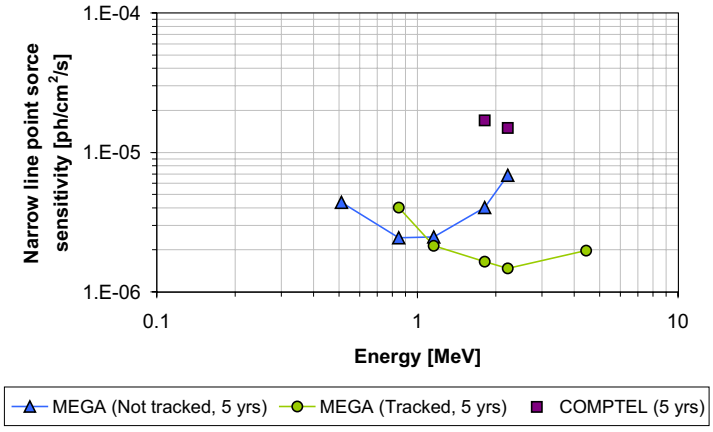

Figure 10.13: MEGA narrow line sensitivity in scanning mode after 5 years of operation compared to two selected COMPTEL results also after 5 years of operation.

element by roughly a factor of eight at 1.809 MeV (averaged over the whole sky) compared to not tracked events. This is the case despite the fact that the angular resolution for tracked events is roughly a factor of two worse than that for not tracked events, i.e. the ARM resolution element is significantly larger. The superior performance is both due to having a slightly better energy resolution, and to only dealing with event arcs instead of circles. After factoring in the different instrument effective areas for the two Compton event types, a net sensitivity improvement of 2.6 of tracked events compared to not tracked events remains at 1.809 MeV (1.7 at 1.157 keV, 3.0 at 2.223 keV).

Given the moderate energy resolution of the MEGA detectors, switching from narrow to broad lines does not effect the sensitivity significantly. For a 3%-broadened 847 keV line — expected from the decay of ^{56}Co produced during SN Ia — the sensitivity worsens only by ∼10%.

Another important feature of the MEGA telescope is its **polarization sensitivity** (see Section 2.2.3 and Chapter 9). The key parameter to judge an instrument's capabilities in this regard is the minimum detectable polarization (MDP), which is defined as follows (compare *Lei et al.*, 1997):

$$\mathrm{MDP} = \frac{z}{\mu_{100}\, R_S} \sqrt{\frac{R_S + R_B}{T}} \tag{10.4}$$

Here, R_S is the source count rate and R_B is the background count rate (after all relevant cuts are applied) in the time interval T. z is again the significance and μ_{100} the detected modulation (see Equation 2.13) for an 100% linearly polarized beam.

For example, for a Crab-like source the minimum detectable polarization with MEGA is ∼0.5% after five years mission time in the energy interval 0.4 to 2 MeV (*total* Crab flux in this energy band: 0.0095 $\gamma/\mathrm{cm}^2/\mathrm{s}$ derived from *Sizun et al.*, 2004). A 10 mCrab source's MDP after the same time is still ∼42%.

10.2.5 Background rejection

The background level for not tracked events at 1809 keV is roughly a factor of 8 higher than that for tracked events — although tracked events have a factor of two larger ARM. The crucial step from event circles to the event arcs reduces all background components, but especially those from the lower hemisphere (Figure 10.14) such as e.g. albedo photons, and those with a track direction hardly compatible with Compton kinematics ($d\vartheta$-criterion). In addition, the fraction of the total background contributed by cosmic photons is significantly larger in the case of tracked events. This is to be expected, since these photons are valid events incident from all directions including that of the instrument's resolution element around the source in question.

A spectrum of each of the individual background components before event reconstruction and without any event selections (other than the trigger criterion) is illustrated in Figure 10.15. In equatorial low-earth orbit contributions from albedo photons dominate, followed by cosmic photons and activation from cosmic protons. Figure 10.16 shows the background rates after the reconstruction. The event selections optimized for the 1809 keV narrow line have been applied — with the exception of the energy window — and only those events are included which originate from the given ARM and SPD window. On average less than 1/2500 of all originally triggered background events are reconstructed as tracked events into the angular resolution element. For example at 1809 keV, ∼99.96% of the background is rejected. The same event selections result in a rejection of "only" ∼82% of the photo-peak events — improving the signal-to-background ratio by a factor of ∼450 relative to the originally triggered events. After the event selections, ∼18% of the photo peak but only ∼8% of the *total* source signal remain —

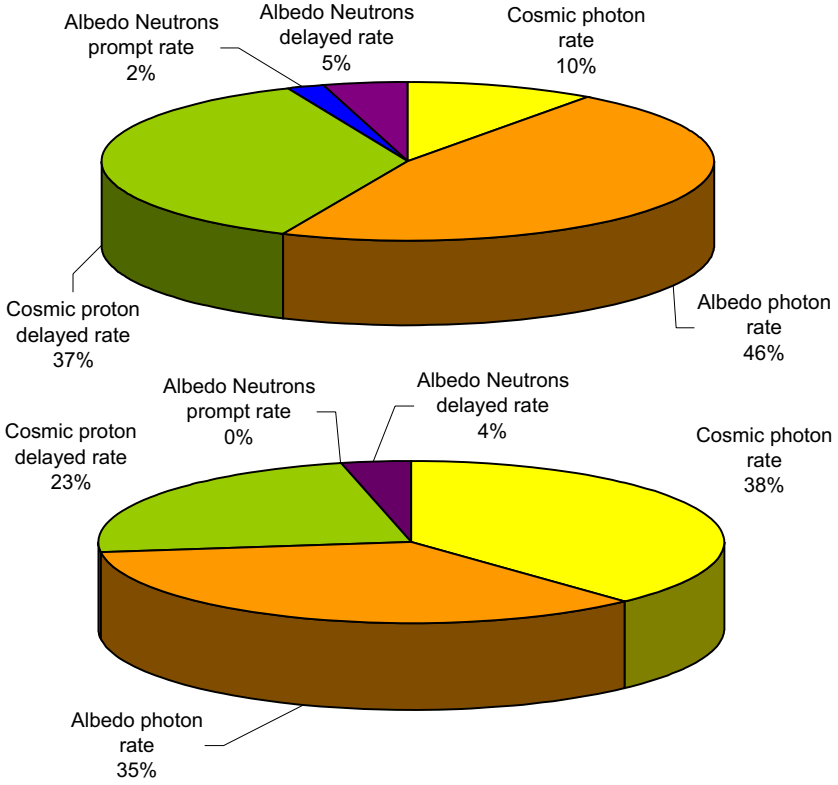

Figure 10.14: Relative contributions to the background at 1809 keV for both not tracked (top) and tracked (bottom) events for a narrow-line on-axis source. The prompt component of the cosmic protons, as well as cosmic electrons and positrons have negligible contributions, because with exception of some secondary bremsstrahlung photons, those particles are vetoed in the anti-coincidence. See the text for more details.

indicating a significant suppression of incompletely absorbed events. Suppressed source events include not reconstructable events, not tracked events and some pairs, events starting in the calorimeter, and events rejected by all other cuts defined in Section 10.2.2.

At this point, **Classic and Bayesian event reconstruction** can be compared using the ultimate measure: their capability to extract weak sources from astrophysical data. The obtained sensitivity describes the performance of a telescope in conjunction with the algorithm used to retrieve the source information from the raw data. Applying different data analysis algorithms to the *same* simulated or measured instrument data allows to compare the performance of the algorithms — and again the ultimately obtained instrument sensitivity constitutes the best available measure to compare them. Thus the obtainable sensitivity can be used to compare the Classic event reconstruction algorithm, used for the prototype, with the Bayesian approach, used as baseline for the satellite geometry. All background components have been reconstructed with both algorithm categories and the *optimum* on-axis narrow line sensitivity has been determined for some selected energies. As expected, on average the Bayesian algorithm results in a factor of 1.5 better sensitivity, with optimum performance at 1809 keV (1.7 improvement), but only a factor of 1.2 better results at 511 keV.

10.2.6 Comparing the MEGA satellite instrument to COMPTEL

After an *equal* mission time, MEGA would have a factor of 10 better narrow-line sensitivity and a factor 3 – 20 better continuum sensitivity compared to COMPTEL over COMPTEL's entire energy band — even though it cannot measure time-of-flight and only has ∼5 kg active tracker material. Moreover, MEGA is sensitive down to below 511 keV and up to ∼100 MeV. The achieved sensitivity improvements over COMPTEL have several reasons:

- The larger amount of measured information for a single event enables better rejection of background events. For example, events with multiple Compton scatters can be resolved,

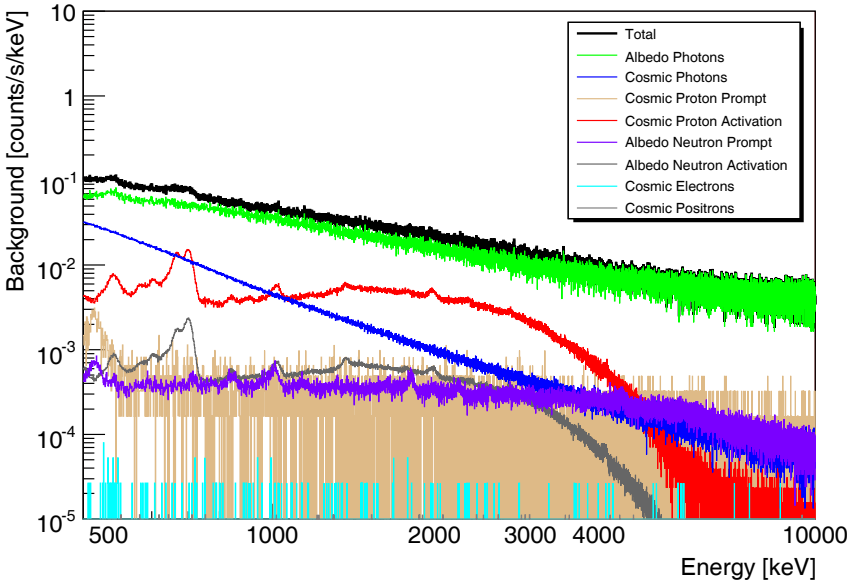

Figure 10.15: Spectral distribution of background event rates separated by component; all events generating a trigger are included. The largest contribution in equatorial low-earth orbit originates from albedo photons, followed by cosmic photons and activation from cosmic protons.

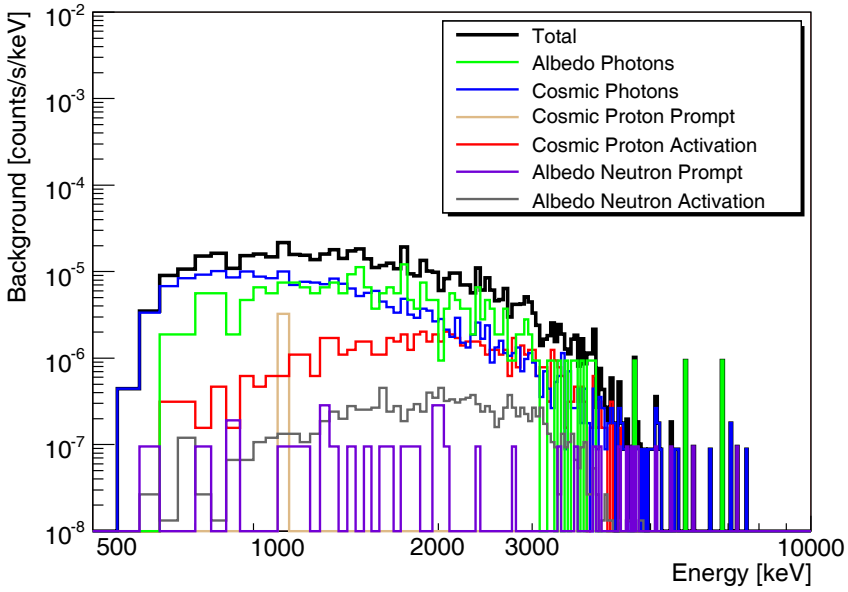

Figure 10.16: Remaining rates of all background components for tracked events after reconstruction and event quality cuts. The events have been reconstructed with the Bayesian event reconstruction algorithm as tracked Compton events, and fall within an on-axis angular resolution element. The event selections of the 1809 keV line have been applied, with exception of the energy window. On average less than 1/2500 of all originally triggered background events remain.

and absorption probabilities can be used for background rejection.

- Electron tracking in particular enables a sensitivity improvement compared to untracked events in MEGA. The effect depends on the photon energy. At 1.809 MeV the effective area-corrected sensitivity improvement amounts to a factor of 2.6.
- Better angular and energy resolution yield a narrower point spread function and thus fewer background events in the resolution element used for sensitivity calculations.
- Moreover, MEGA has a larger field-of-view (half width ∼40°), enabling a significantly larger sky exposure than COMPTEL's.
- Operating in zenith-pointed scanning mode results in a significantly higher fraction of usable observation time per orbit compared to pointing mode (COMPTEL had roughly one third effective observation time, MEGA should have at least 90%).

- The choice of an *equatorial* low-earth orbit also constitutes a significant improvement. COMPTEL had a 28°-inclination low-earth orbit, passing through the South Atlantic Anomaly and suffered from the consequences of the resulting spacecraft activation. Initial tests have shown that the choice of an equatorial orbit alone results in at least a factor of two sensitivity improvement.

10.3 Selected science simulations with a MEGA satellite instrument

Simulating actual observations is completely infeasible for most of the mission's science objectives, because the generation of the corresponding background components would require the simulation of far too many particles. Only some smaller problems such as gamma-ray bursts or narrow-line emission from a limited sky region are within reach of the available computing resources.

Figure 10.17 shows a reconstructed image from a simulation of the Cygnus region in the light of radioactive ^{26}Al (1.809 MeV) based on a 3-year all-sky survey. The input source distribution contains all sources of ^{26}Al which have been identified in *Plüschke* (2001) for the Cygnus region as well as the appropriate amount of background photons. Only those tracked events have been used which fulfill the event selection criteria for an 1809 keV narrow line defined in Table 10.1 excluding ARM and SPD selections. The reconstructed image is overlaid with symbols representing the source distribution used as input to the simulation: Wolf-Rayet stars are represented by dots, OB associations and supernova remnants by open circles which reflect their extent. All extended sources have been assumed circular and simulated as discs. Since an extreme amount of CPU time would be required to correctly simulate the hadron-induced background components in particular, the total background rate *after event selections per angular resolution element* has been determined for a smaller run. Then the total number of background events expected for the given exposure *after event selections per angular resolution element* has been simulated using only an up-scaled cosmic photon spectrum as input.

While the structures that appear clearly discernible in the reconstructed image correspond nicely to the strongest sources in the region, most of the sources are either too close together or too weak to be resolved by the MEGA telescope. The brightest central spot is dominated by Cygnus OB2 and some WR stars (e.g. WR145). Together they represent roughly one third of the total flux expected from the Cygnus region. The circle at (-76°,-8°) represents the Cygnus Loop supernova remnant. Since the 3σ point source sensitivity limit is at $\sim 2.2 \cdot 10^{-6}\,\gamma/\mathrm{cm}^2/\mathrm{s}$ after 3 years and the Cygnus loop has a total assumed flux of $\sim 1.7 \cdot 10^{-6}\,\gamma/\mathrm{cm}^2/\mathrm{s}$, the visible weak signature corresponds to a $\sim 2.3\sigma$ source signal.

According to standard models, gamma rays are emitted closer to the central engine of a gamma-ray burst than photons at longer wavelengths. Thus they likely carry most of the information about the progenitor. One key to understanding the emission mechanisms of those gamma-rays is their polarization, which depends on source emission geometries as well as magnetic field configurations.

The high-energy burst GRB910814 has been used as template for this simulation. This was the second brightest burst observed in the first year of the CGRO mission and had a fluence of 123 MeV/cm^2 in the simulated energy band (50 keV - 10 MeV). The spectrum followed a broken power-law ($\alpha_{min} = -1.0$, $\alpha_{max} = -2.57$, $E_b = 1070$ keV) (*Schaefer et al.*, 1992). The short duration and the strength of the burst result in measurements that are nearly free of background. Therefore the only significant background consists of chance coincidences, incompletely absorbed, and falsely reconstructed events. The restriction to events originating from the recon-

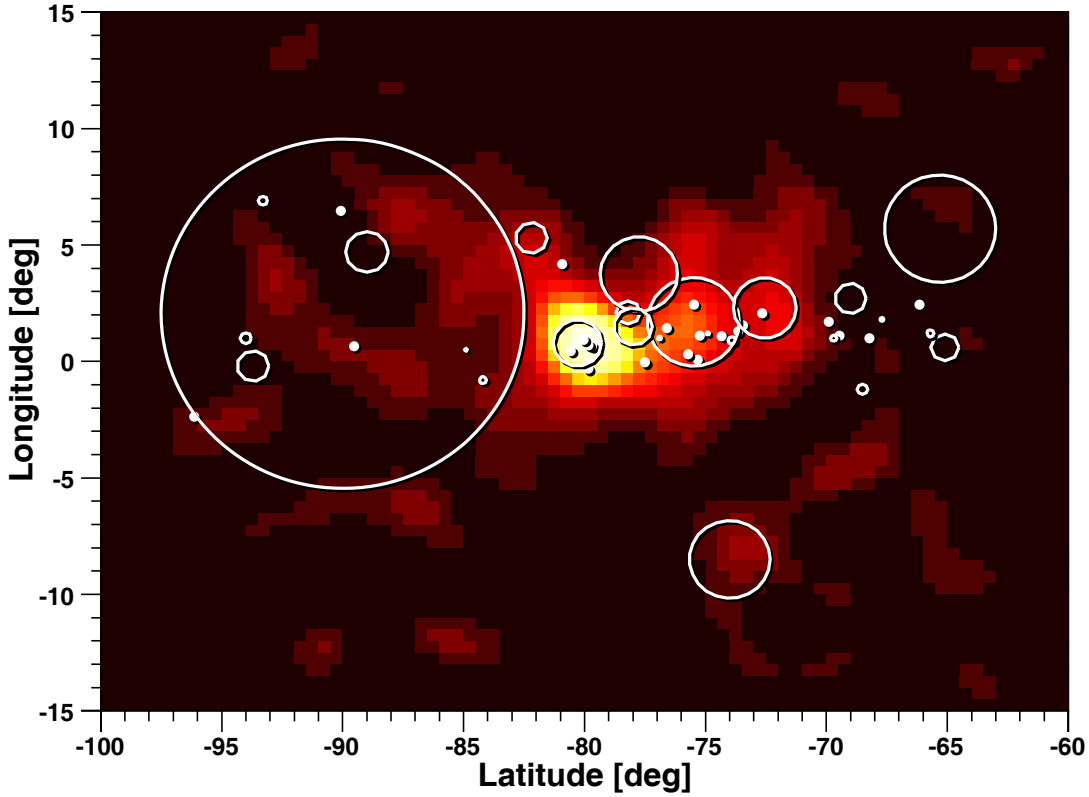

Figure 10.17: The Cygnus region in the light of radioactive ^{26}Al (1.809 MeV) as seen by MEGA after 3 years all-sky survey (LM-ML-EM-generated image obtained after 150 iterations). Name, position, extent, and strength of the individual sources can be found in the table below.

Point Sources				Extended Sources				
Name	Lat [°]	Long [°]	Flux [γ/cm^2/s]	Name	Lat [°]	Long [°]	Ext [°]	Flux [γ/cm^2/s]
WR129	-66.16	2.44	0.000 000 029	SNR1	-65.10	0.60	0.58	0.000 000 360
WR130	-68.22	0.98	0.000 000 166	SNR2	-65.30	5.70	2.30	0.000 000 360
WR132	-69.46	1.10	0.000 000 082	DA495	-65.70	1.20	0.15	0.000 000 024
WR131	-69.90	1.71	0.000 000 009	SNR4	-67.70	1.80	0.08	0.000 000 006
WR133	-72.65	2.06	0.000 000 260	SNR5	-68.50	-1.20	0.22	0.000 000 052
WR134	-73.45	1.55	0.000 000 400	CTB80	-69.00	2.70	0.65	0.000 000 127
WR135	-73.65	1.28	0.000 000 400	SNR7	-69.70	1.00	0.13	0.000 000 019
WR137	-74.33	1.09	0.000 000 211	SNR8	-73.90	0.90	0.17	0.000 000 127
WR138	-75.23	1.11	0.000 000 765	Cygnus Loop	-74.00	-8.50	1.67	0.000 001 675
WR141	-75.33	0.08	0.000 000 765	CTB87	-74.90	1.20	0.06	0.000 000 002
WR136	-75.48	2.43	0.000 000 765	SNR11	-76.90	1.00	0.08	0.000 000 008
WR142	-75.73	0.30	0.000 001 340	DR4	-78.20	2.10	0.50	0.000 000 080
WR139	-76.60	1.43	0.000 000 335	W63	-82.20	5.30	0.66	0.000 000 490
WR143	-77.50	-0.05	0.000 001 080	SNR14	-84.20	-0.80	0.15	0.000 000 018
WR145	-79.69	0.66	0.000 004 850	SNR15	-84.90	0.50	0.05	0.000 000 002
WR145a	-79.84	0.69	0.000 000 014	HB21	-89.00	4.70	0.88	0.000 000 455
WR147	-79.85	-0.32	0.000 002 700	DA530	-93.30	6.90	0.19	0.000 000 066
WR144	-80.04	0.93	0.000 000 195	DA551	-93.70	-0.20	0.66	0.000 000 475
WR146	-80.56	0.45	0.000 002 350	3C343.1	-94.00	1.00	0.23	0.000 000 056
WR140	-80.93	4.18	0.000 001 020	OB3	-72.55	2.30	1.3	0.000 005 450
WR149	-89.53	0.65	0.000 000 076	OB1	-75.5	1.70	1.9	0.000 003 650
WR148	-90.08	6.47	0.000 000 018	OB8	-77.75	3.75	1.6	0.000 000 450
WR150	-96.13	-2.38	0.000 000 046	OB9	-78.0	1.50	0.8	0.000 004 900
				OB2	-80.3	0.80	1.0	0.000 014 000
				OB7	-90.0	2.05	7.5	0.000 010 500

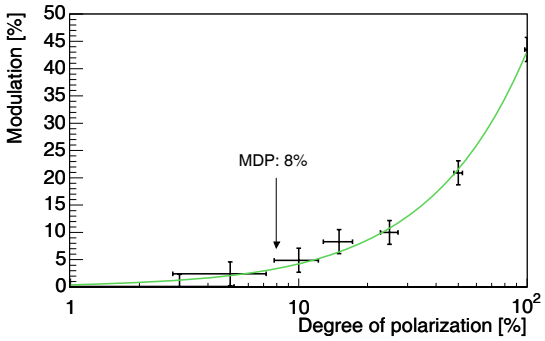

Figure 10.18: Modulation as a function of the degree of polarization of GRB910814: The minimum detectable polarization is 8% (90% confidence level)

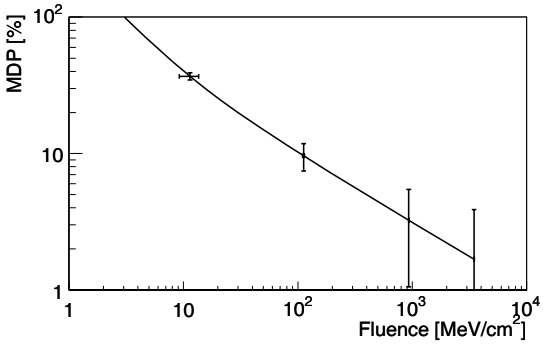

Figure 10.19: Minimum detectable polarization as a function of the fluence of the burst in the energy band between 50 keV and 10 MeV: The burst is assumed to have the same light curve and spectrum as GRB910814. The curve slightly flattens at higher fluence due to read-out limitations.

structed source position greatly reduces these events. The simulation has been performed with a slightly simplified geometry, which has almost the same amount of active and passive material, only the representation of the passive material outside the detector head is less detailed. Since the burst is source dominated, the slight differences do not play a significant role. Strong bursts might result in increased instrument dead time and/or telemetry or on-board data storage limitations may result in not all detectable photons from the burst actually being recorded. For the simulations, it is assumed that the telescope has a maximum possible read-out rate of 5000 coincident events per second.

Figure 10.18 shows the modulation of the azimuthal scatter angle distribution as a function of the degree of linear polarization of GRB910814. The minimum detectable polarization for this strong burst is roughly 8%. Since a significant amount of events has less than 511 keV and are not tracked, the final MDP will depend on the in-orbit thresholds of the detectors as well as on the trigger criteria used.

The minimum detectable polarization as a function of the fluence of a burst with the same spectral characteristics as GRB910814 is illustrated in Figure 10.19. Obviously, the higher the fluence and thus the number of detected photons, the easier it is to detect a polarization signal.

While the *first* incarnation of a MEGA satellite instrument discussed in this Chapter has not completely achieved all originally envisioned sensitivity improvements over its predecessors on the Compton Gamma-Ray Observatory, even this instrument would enable significant advances over existing observations: For the first time, sensitive measurements of gamma-ray polarization would be achievable. An all-sky survey in nuclear lines at ten times COMPTEL's sensitivity for equal mission time and with significantly better angular resolution would provide answers to many of the pressing questions in nuclear astrophysics being asked today, and wide field-of-view monitoring in the MeV continuum will provide insights into the behavior of a host of energetic sources, especially those exhibiting high variability.

Chapter 11

Closing remarks

The MEGA telescope is intended to operate in an energy regime astronomers have barely started to explore: COMPTEL provided the first all-sky survey in the MeV regime (0.75–30 MeV). SPI (20 keV–8 MeV) and IBIS (15 keV–10 MeV) on INTEGRAL followed, but especially IBIS performs best at tens to hundreds of keV. At several tens of MeV, neither MEGA's predecessor EGRET nor the future missions AGILE and GLAST provide a reasonable sensitivity. GLAST, however, will provide high sensitivity all-sky surveys above ∼100 MeV. The result is a sensitivity gap in the MeV regime which could best be filled by a future combined electron-tracking Compton and pair telescope such as MEGA. Moreover, in the particularly challenging energy regime around 1 MeV where Compton scattering dominates, MEGA — which could be developed into a satellite and be launch-ready in 4–5 years — will lay the groundwork for larger, more challenging missions that lie further in the future such as an Advanced Compton Telescope.

This work constitutes an important step towards such a new mission in medium-energy gamma-ray astronomy: All necessary tools to analyze the data of a future MEGA telescope have been developed and implemented, the performance of the prototype of such an instrument has been assessed, and one candidate satellite instrument concept has been fully characterized. It has been demonstrated that the pre-phase A geometry of the telescope in combination with the current version of data analysis tools already comes close to achieving the goal of a factor of 10 improvement in sensitivity with respect to past and current missions.

One core element of the data analysis is the reconstruction of the original interaction process — and thus the parameters of the incoming photon — from the measured hits. The largest achievement of the present work is the development of a completely novel approach to the reconstruction of the individual event; its performance significantly exceeds that of previous methods. The Bayesian approach used for electron tracking as well as Compton sequence reconstruction determines for each possible interaction sequence the probability that the event truly happened this way and is completely absorbed. It relies on a pre-calculated multidimensional instrument response. In contrast to previous approaches, Bayesian event reconstruction takes into account all relevant aspects of the interaction process. Moreover, the resulting measure of the quality of the event is a real probability — this allows to easily compare very different events such as tracked or not tracked, multiple or single Compton events. Mainly due to improved background rejection capabilities, this new approach outperforms the classic method on average by a factor of 1.5 in the critical measure of achieved sensitivity of the simulated MEGA satellite instrument.

Another vital aspect of a Compton or pair telescope are the associated image reconstruction techniques. Since Compton telescopes generally do not allow to unambiguously recover the origin of a single event, complex deconvolution techniques are necessary. The approach developed for MEGA is based on a list-mode maximum-likelihood expectation-maximization algorithm in combination with a realistic description of the different responses for the three main event types, not tracked events, tracked events, and pair events. It has been shown that the algorithm

accurately retrieves point sources at various energies and various incidence angles. Extended sources, multiple sources, and sources in the presence of high background are reconstructed well.

The accuracy of the simulations has been verified with measurements of the MEGA prototype. It was calibrated at the High Intensity Gamma Source of the Free Electron Laser facility at Duke University. Exposures to monoenergetic (range 710 keV to 49 MeV, $\Delta E/E < 2\%$), 100% linearly polarized pencil beams allowed the derivation of the spectral, imaging and polarization properties of the prototype.

The spectral performance of the prototype turned out to be modest. Only at 710 keV is the spectral resolution good enough to recover a photo peak with a 1σ energy resolution of $\sim$41 keV. At higher energies the modest energy resolution in the calorimeter (13% FWHM at 662 keV), in combination with high thresholds, large amounts of passive and too little active material, and non-linearities and time-variabilities in the detector response, made it impossible to fully absorb a significant amount of photons and to achieve an acceptable spectral resolution. However, integrating the above-mentioned effects into the simulation allowed to reproduce the measurements, demonstrating that the imperfections of the detector are sufficiently well understood.

The modest spectral properties above $\sim$1 MeV did not prevent the determination of the prototype's imaging properties. At 710 keV an angular resolution of $\sim 7^\circ$ for not tracked events is achieved, which improves to $\sim 4^\circ$ at 2 MeV. The angular resolution of tracked events improves from $\sim 9^\circ$ at 2 MeV to $\sim 3^\circ$ at 8 MeV, that for pair events from 12° at 12 MeV to 4.5° at 49 MeV. While for not tracked events at e.g. 2 MeV the energy resolution in tracker and calorimeter and the position resolution in the calorimeter contribute in equal parts to the angular resolution, for tracked events the energy resolution in the calorimeter dominates the angular uncertainty by a factor of three. For fully absorbed tracked events, the average size of the Compton arc decreases slightly from $\sim 32^\circ$ at 2 MeV to $\sim 27^\circ$ at 8 MeV, mainly due to event selection effects. The shapes and widths of the ARM and SPD profiles were accurately reproduced with simulations, and the underlying deficiencies of the detector are mostly understood.

A very promising aspect of the prototype performance is its capability to recover the polarization signal of the incident photons. At 710 keV the polarization modulation is most influenced by the limitations of the prototype detector; here a polarization modulation of 17% for a 100% linearly polarized incoming photon beam could be detected. Following expectations, the modulation decreases with higher energies to 13% at 2 MeV and 6% at 5 MeV. A tracking Compton telescope is especially well-suited for polarization studies because tracks and polarization share a common requirement: effectively recording Compton interactions with large scatter angles.

The developed software tools have also been applied to a MEGA satellite instrument based on the pre-phase A study. Extensive simulations of all expected background components have been performed. Event selections which optimize the continuum and narrow-line sensitivities have been determined. It was shown that a 5-year MEGA all-sky survey provides a factor of 2 to 17 improved continuum sensitivity compared to COMPTELs 9-year mission for any point on the sky. In the narrow-line regime, MEGA's sensitivity is roughly a factor of ten better than COMPTEL's, assuming equal mission time. After 5 years, a minimum polarization of 0.5% of a Crab-like source could be detected.

These sensitivities, achievable with an instrument that constitutes only a first reasonable guess at a good configuration, illustrate the large potential of a MEGA mission.

The analysis of the prototype data, as well as the simulation of both the satellite and the prototype, have revealed some **critical requirements for a future tracking Compton and pair telescope**. Following these guidelines should result in an even more promising MEGA instrument concept:

- Switching from a non-tracking to a tracking Compton telescope can provide a sensitiv-

ity advantage due to a less ambiguous detector response and correspondingly improved background suppression by transforming Compton event circles into arcs. However, those advantages can only be fully exploited, if the increased number of measurement points and the on average different scatter geometry of tracked events (larger Compton scatter angles) do not deteriorate the telescope's energy or position resolution or its overall efficiency.

- Additionally, a calorimeter with excellent energy resolution is crucial for any Compton telescope intending to measure gamma rays under large Compton scatter angles. At large angles, the uncertainty in the energy measurement of the scattered gamma ray has the most impact on the achieved angular resolution. This effect can clearly be seen both with the prototype and in the satellite simulations. Tracked events generally have a worse angular resolution than not tracked events, and the prototype as well as the pre-phase A instrument at least at lower energies are far away from the angular resolution limit given by the position resolution or by Doppler-broadening.

- A key requirement for any future MeV telescope is high efficiency. Even for the satellite instrument of the pre-phase A study, the total depth of the tracker represents only 17% of the radiation length of Silicon. Most photons pass through the tracker without interactions; many then interact first in the calorimeter. More Silicon would significantly improve the overall efficiency, especially at higher energies where the fraction of high energy electrons contained in the tracker would also increase. Since many photons escape from the prototype, the importance of a tightly-packed calorimeter completely surrounding the lower hemisphere of the tracker must be emphasized. This will also provide shielding against an important background component in low-earth orbit: photons originating from the Earth's atmosphere.

- The prototype's spectral performance also demonstrates the importance of minimizing passive material — above the tracker, in the tracker itself, and on the path of the scattered gamma ray into the calorimeter. The more passive material is present, the more likely at least one interaction does not occur in active material. If the resulting event structure is still compatible with a Compton interaction it becomes part of the background if it is not rejected by other background cuts. One important step in this direction would be to use $10{\times}10$ cm^2 instead of $6{\times}6$ cm^2 Silicon wafers. Minimizing the passive material has another crucial advantage: Passive as well as active material is activated in orbit; the subsequent decay results in secondary photons which contribute to the background.

- Low energy detection thresholds are particularly important in the tracker, especially for tracked events. Since the Compton interaction can occur at any depth in a Silicon layer, the deposit in the first layer might be very low. If it is below the threshold, the resulting non-negligible missing energy is hampering recovery of the photon's origin via the Compton equations. Another error is introduced by the wrongly reconstructed start position. Both effects decrease the angular resolution.

- To maximize the exposure of a scanning telescope, a wide field of view is necessary. The cubic shape of the investigated satellite geometry leads to a fairly modest field of view (HWHM $\sim$40° for tracked events); a flatter geometry could improve this. Since in the nuclear-line energy regime the length of the Compton arc is dominated by Molière scattering rather than the layer distance, moving the layers closer together has no negative impact. Only in the high-energy pair-production regime a resulting deterioration would be expected.

- The distribution of the azimuthal Compton scatter angle depends most on the photon's polarization at low photon energies and large scatter angles. Thus, Compton events should

be measured down to as low an energy as possible and the geometry must allow for large scatter angles. The latter should already be the case for any tracking Compton telescope because large electron energies — i.e. nice tracks — also correspond to large scatter angles.

For an actual satellite instrument, many trade-off studies will be necessary to finalize the concept. Parameters to be optimized include the thickness of the side and bottom calorimeters, the height of the instrument, the depth of the Silicon, and the size of the CsI crystals.

Improvements of the (prototype and) satellite detector design are definitely required for a space mission. Further **augmenting the data analysis tools**, especially the event and image reconstruction, could also contribute to optimizing a future mission's performance.

- The most significant improvements are expected in the pair regime. One important enhancement would be to reconstruct the total energy of the electron and positron tracks from a combination of their angular deviation, their energy deposits, and the opening angle of the pair events. This should help especially for events with uneven energy distribution: here, the momenta of electron and positron are needed to retrieve the original photon's direction. Moreover, most wrongly reconstructed pair events result from wrongly identified vertices caused by holes in the initial track signature. An improved vertex post-processing should help to eliminate wrongly reconstructed pair events. For example the vertex should be verified not only from top bottom, but also from bottom to top in order to determine whether the convergence point is really the vertex. In addition one could check if a Compton interaction might have preceeded the pair interaction.
- Enhancements in the Compton regime largely correspond to improvements of the data space used for the Bayesian event reconstruction. One important element which is still missing is the absorption probability towards the first interaction point. Because this requires a time-intensive integration over the Compton cone or arc for all possible event sequences, this has been postponed until more powerful computers become available.
- The current Bayesian data space requires the photon to be completely absorbed in order to be identified as a correct interaction. At higher energies very few interactions are completely absorbed. Constructing a new data space without this requirement could enable a reliable identifications of the first and second interaction point of incompletely absorbed events. Those could then be used together with completely absorbed events in a far more advanced imaging algorithm performing spectral and directional deconvolution in parallel. Unfortunately, such an approach will require more powerful computing resources, than the ones presently in use.
- The list-mode image reconstruction itself is still missing the normalizations required to recover a source's intensity. While simple spectral deconvolutions prove that it is possible to correctly recover a source's intensity from list-mode analysis even in the face of significant background, accomplishing this for image deconvolution requires additional response matrices and significant computing resources.

A MEGA space instrument incorporating at least a few of the recommended improvements should easily be able to provide at least a factor of ten in sensitivity improvement over previous missions in the whole medium-energy gamma-ray band from a few hundred keV to several tens of MeV for both continuum and line sources. Together with MEGA's unprecedented capability to measure gamma-ray polarization, this will enable the deepest view yet into the universe's most violent explosions and its most powerful and dynamic sources.

Part V

Appendix

Appendix A

Frequently used abbreviations and notations

Abbrevations

ARM	Angular resolution measure (see 2.2.5)
SPD	Scatter plane deviation (see 2.2.5)

Notations

E_i	Energy of initial gamma ray (Compton scattering/pair creation)
E_e	Energy of an electron (Compton scattering/pair creation)
E_p	Energy of an positron (Pair creation)
E_g	Energy of the scattered gamma ray (Compton scattering)
E_0	Rest energy of an electron (511 keV)
E_e^{rel}	Total relativistic energy of an electron
φ	"Compton scatter angle" of the gamma ray (Compton scattering)
ε	"Electron scatter angle" of the recoil electron (Compton scattering)
ϑ	Total scatter angle (Compton scattering)
χ	azimuthal (polar) Compton scatter angle of the gamma ray (Compton scattering)
$\vec{p}_i$, $\vec{e}_i$	Momentum/Direction of the initial gamma ray (Compton scattering/pair creation)
$\vec{p}_e$, $\vec{e}_e$	Momentum/Direction of an electron (Compton scattering/pair creation)
$\vec{p}_p$, $\vec{e}_p$	Momentum/Direction of a positron (pair creation)
$\vec{p}_n$, $\vec{e}_n$	Momentum/Direction of a nucleus (pair creation)
$\vec{p}_g$, $\vec{e}_g$	Momentum/Direction of a scattered gamma ray (Compton scattering)
Z	Atomic number
μ	quality factor (also called modulation) of a polarization response (Compton scattering/pair creation)
F_z e.g. F_3	3 sigma sensitivity limit
N_S	Number of source photons
N_B	Number of background photons
A_{eff}	Effective area of a telescope
T_{eff}	Effective observation time

Appendix B

Introduction to Bayes filters

Bayes filters are nowadays widely used in email spam detection. Inspired by their success in that field, their application for event reconstruction — filtering correctly reconstructed events from background — is investigated in Chapter 4 of this work. The following text is intended as a short and simple introduction of how Bayes filters can be used to differentiate between correct and false hit sequences.

The goal is to obtain a probability of whether a reconstruction is correct ("$\mathcal{C}$") based on a measured set of data $\vec{m}$: $p(\mathcal{C}|\vec{m})$. Applying Bayes' rule, this probabilty transforms to:

$$p(\mathcal{C}|\vec{m}) = \frac{p(\vec{m}|\mathcal{C})\, p(\mathcal{C})}{p(\vec{m})} \tag{B.1}$$

$p(\mathcal{C})$ is the probability that a correct sequence is given, $p(\vec{m})$ the probability that $\vec{m}$ is measured and $p(\vec{m}|\mathcal{C})$ is the probability that $\vec{m}$ is measured on the condition that the sequence is correct.

All variables on the right-hand side of the equation are accessible via simulation or calibration.

B.1 Example 1

In this very simple reconstruction example we want to determine if we have found the correct start point of a Compton electron track. For simplification, let us only look at the energies for the first Silicon layer of the track for a MEGA-like Compton telescope. Then our measured parameters are E_{tot} as the total energy of the electron and E_{dep} as the energy deposited in the first layer. Let's assume we have measured $E_i = 70$ keV of the $E_{tot} = 2000$ keV electron. From a large set of previous measurements, either by simulation or calibration, we got the following table for the distribution of correct and false start points for 2 MeV initial energy:

E_{dep} for $E_{tot} = 2$ MeV [keV]	0-50	50-100	100-150	150-200	> 200	Sum
Correct starts	243	265	143	132	217	1000
False starts	52	183	283	1354	1328	3000

From this table we can calculate all probabilities on the right-hand side of Equation B.1: The probability that we get our measured set of parameters given that the start-point is correct:

$$p(\vec{m}_1 = \{70|2000\}\,|\mathcal{C}) \approx \frac{265}{1000} = 0.265 \tag{B.2}$$

The probability to get the measurement:

$$p(\vec{m}_1 = \{70|2000\}) \approx \frac{265 + 183}{1000 + 3000} = 0.112 \tag{B.3}$$

The probability to find a correct start:

$$p\left(\mathcal{C}\right) \approx \frac{1000}{1000+3000} = 0.25 \tag{B.4}$$

Of course all these values are only approximations, since we would need infinite statistics and binning to get the real probabilities.

Thus the final probability that the start is correct based on the measurement is:

$$p\left(\mathcal{C}|\vec{m}_1 = \{70|2000\}\right) \approx 0.57 \tag{B.5}$$

B.2 Example 2

In this example we look two measurement points, e.g. the energies of the start layer and at the energies of the second layer the electron hits.

$$p\left(\mathcal{C}|\vec{m}_1 \cup \vec{m}_2\right) = \frac{p\left(\vec{m}_1 \cup \vec{m}_2|\mathcal{C}\right) p\left(\mathcal{C}\right)}{p\left(\vec{m}_1 \cup \vec{m}_2\right)} \tag{B.6}$$

Now we have to make the "naive" assumption that the probabilities $p\left(\vec{m}_1\right)$ and $p\left(\vec{m}_2\right)$ are independent:

$$p\left(\vec{m}_1 \cup \vec{m}_2|\mathcal{C}\right) = p\left(\vec{m}_1|\mathcal{C}\right) \cdot \left(\vec{m}_2|\mathcal{C}\right) \tag{B.7}$$

And we get:

$$p\left(\mathcal{C}|\vec{m}_1 \cup \vec{m}_2\right) = \frac{p\left(\vec{m}_1|\mathcal{C}\right) p\left(\vec{m}_2|\mathcal{C}\right) p\left(\mathcal{C}\right)}{p\left(\vec{m}_1 \cup \vec{m}_2\right)} \tag{B.8}$$

We get an analog equation for the "false" case:

$$p\left(\bar{\mathcal{C}}|\vec{m}_1 \cup \vec{m}_2\right) = \frac{p\left(\vec{m}_1|\bar{\mathcal{C}}\right) p\left(\vec{m}_2|\bar{\mathcal{C}}\right) p\left(\bar{\mathcal{C}}\right)}{p\left(\vec{m}_1 \cup \vec{m}_2\right)} \tag{B.9}$$

The denominator disappears if we calculate the ratio:

$$R = \frac{p\left(\mathcal{C}|\vec{m}_1 \cup \vec{m}_2\right)}{p\left(\bar{\mathcal{C}}|\vec{m}_1 \cup \vec{m}_2\right)} = \frac{p\left(\vec{m}_1|\mathcal{C}\right) p\left(\vec{m}_2|\mathcal{C}\right) p\left(\mathcal{C}\right)}{p\left(\vec{m}_1|\bar{\mathcal{C}}\right) p\left(\vec{m}_2|\bar{\mathcal{C}}\right) p\left(\bar{\mathcal{C}}\right)} \tag{B.10}$$

In addition we know that $p\left(\mathcal{C}|\vec{m}_1 \cup \vec{m}_2\right) + p\left(\bar{\mathcal{C}}|\vec{m}_1 \cup \vec{m}_2\right) = 1$. Thus the final solution is:

$$p\left(\mathcal{C}|\vec{m}_1 \cup \vec{m}_2\right) = \frac{p\left(\vec{m}_1|\mathcal{C}\right) p\left(\vec{m}_2|\mathcal{C}\right) p\left(\mathcal{C}\right)}{p\left(\vec{m}_1|\mathcal{C}\right) p\left(\vec{m}_2|\mathcal{C}\right) p\left(\mathcal{C}\right) + p\left(\vec{m}_1|\bar{\mathcal{C}}\right) p\left(\vec{m}_2|\bar{\mathcal{C}}\right) p\left(\bar{\mathcal{C}}\right)} \tag{B.11}$$

Bibliography

Agaronian, F. A. and Sunyaev, R. A. 'Gamma-ray line emission, nuclear destruction and neutron production in hot astrophysical plasmas - The deuterium boiler as a gamma-ray source.' *Monthly Notices of the Royal Astronomical Society*, **210**: 257–277, 1984.

Agostinelli, S. et al. 'Geant4 - A Simulation Toolkit.' *Nuclear Instruments and Methods A*, (506): 250–303, 2003.

Ahn, K. and Komatsu, E. 'Dark matter annihilation: The origin of cosmic gamma-ray background at 1-20 MeV.' *Physical Review D*, **72**(6): 061301, 2005.

Andritschke, R. 'Aufbau und Eichung der Kalorimeter fuer das Gammateleskop MEGA.' Diploma thesis, Technical University Munich, 2000. Available in German at the web-site: http://www.mpe.mpg.de/MEGA/mega-documents.html.

Andritschke, R. 'Calibration of the MEGA Prototype.' Ph.D. thesis, Technical University Munich, Germany, 2006. To be published.

Aprile, E. et al. 'Spectroscopy and Imaging Performance of the Liquid Xenon Gamma-Ray Imaging Telescope (LXeGRIT).' *Proc. SPIE*, **4140**, 2000.

Barrett, H. et al. 'List-Mode likelihood.' *J. Opt. Soc. Am. A*, **14**(10), 1997.

Berger, M. and Seltzer, S. 'Tables of Energy Losses and Ranges of Electrons and Positrons.' Technical Report NASA-SP-3012, NASA, 1964.

Bethe, H. A. 'Molières theory of multiple scattering.' *Physical Review*, **89**(6), 1953.

Bhattacharya, D. et al. 'Prototype TIGRE Compton γ-ray balloon-borne instrument.' *New Astronomy Reviews*, **48**: 287–292, 2004.

Bildsten, L. et al. 'Helium destruction and gamma-ray line emission in accreting neutron stars.' *The Astrophysical Journal*, **408**: 615–636, 1993.

Bloser, P. et al. 'Development of Silicon Strip Detectors For a Medium Energy Gamma-ray telescope.' *NIM A*, **512**: 220–228, 2003.

Boehm, C. et al. 'MeV Dark Matter: Has It Been Detected?' *Physical Review Letters*, **92**(10): 101301, 2004.

Boggs, S. et al. 'Overview of the nuclear Compton telescope.' *New Astronomy Reviews*, **48**: 251–256, 2004.

Boggs, S. et al. 'Report on the Advanced Compton Telescope vision mission study.' Technical report, NASA, 2005. In press.

Boggs, S. E. et al. 'Event reconstruction in high resolution Compton telescopes.' *Astron. Astrophys. Suppl. Series*, **145**: 311–321, 2000a.

Boggs, S. E. et al. 'Simulated Performance of a Germanium Compton Telescope.' In *Proceedings of the 4th INTEGRAL Workshop, Alicante, Spain*, 2000b.

Brun, R. and Rademakers, F. 'ROOT - An Object Oriented Data Analysis Framework.' *NIM A*, **389**: 81–86, 1997. See also http://root.cern.ch/.

Caroli, E. et al. 'Coded Aperture Imaging in X- and Gamma-Ray Astronomy.' *Space Science Reviews*, **45**: 349–403, 1987.

CERN: Application Software Group and Networks Division. 'Geant - Detector Description and Simulation Tool.' Technical report, CERN Geneva, 1993.

Coburn, W. and Boggs, S. 'Polarization of the prompt big gamma-ray emission from the big gamma-ray burst of 6 December 2002.' *Nature*, **423**: 415–417, 2003.

Compton, A. H. 'A quantum theory of the scattering of X-ray by light elements.' *Physical Review*, **21**(5), 1923.

de Gouveia dal Pino, E. M. 'Astrophysical jets and outflows.' *Advances in Space Research*, **35**: 908–924, 2005.

Diehl, R. et al. 'Astrophysical constraints from gamma-ray spectroscopy.' *Nuclear physics A*, 2005. In press.

DuMond, J. W. M. 'Compton Modified Line Structure and its Relation to the Electron Theory of Solid Bodies.' *Phys. Rev.*, **33**: 643–658, 1929.

Dyks, J. et al. 'Relativistic Effects and Polarization in Three High-Energy Pulsar Models.' *The Astrophysical Journal*, **606**: 1125–1142, 2004.

Evans, R. *The atomic nucleus*. McGraw-Hill Book Company Inc., 1958.

Fichtel, C. et al. 'High-Energy Gamma-ray Results from the Second Small Astronomy Satellite.' *The Astrophysical Journal*, **198**: 163–182, 1975.

Forrest, D. J. et al. 'The gamma ray spectrometer for the Solar Maximum Mission.' *Solar Physics*, **65**: 15–23, 1980.

Gehrels, N. and other. 'GLAST: the next-generation high energy gamma-ray astronomy mission.' *Astroparticle Physics*, **11**(1): 277–282, 1999.

Gehrels, N. et al. 'The SWIFT Gamma-Ray Burst Mission.' *The Astrophysical Journal*, **611**: 1005–1020, 2004.

Georgii, R. et al. 'COMPTEL upper limits for the ^{56}Co γ-ray emission from SN1998bu.' *Astronomy and Astrophysics*, **394**: 517–523, 2002.

Grindlay, J. et al. 'EXIST: mission design concept and technology program.' In Truemper, J. and Tananbaum, H., editors, *X-Ray and Gamma-Ray Telescopes and Instruments for Astronomy*, volume 4851, pages 331–334. SPIE, 2003.

Halloin, H. 'CLAIRE: Premières Lumières d'une Lentille Gamma.' Ph.D. thesis, Université Paul Sabatier de Toulouse, 2003.

Harris, M. J. et al. 'Detection of γ-ray lines from interstellar ^{60}Fe by the high resolution spectrometer SPI.' *Astronomy and Astrophysics*, **433**: L49–L52, 2005.

Hernanz, M. 'Classical nova explosions.' In Hameury, J. and Lasota, J., editors, *The Astrophysics of Cataclysmic Variables and Related Objects*. ASP Conference Series, 2004.

Hjorth, J. et al. 'The optical afterglow of the short γ-ray burst GRB 050709.' *Nature*, **437**: 859–861, 2005.

Hurford, G. et al. 'The RHESSI Imaging Concept.' *Solar Physics*, **210**(1-2): 61 – 86, 2002.

Hurley, K. et al. 'An exceptionally bright flare from SGR 1806-20 and the origins of short-duration big gamma-ray bursts.' *Nature*, **434**: 1098–1103, 2005.

Inoue, H. et al. 'Astro-E2: the third X-ray observatory in the 21st Century.' In Truemper, J. and Tananbaum, H., editors, *X-Ray and Gamma-Ray Telescopes and Instruments for Astronomy*, volume 4851, pages 289–292. SPIE, 2003.

Iyudin, A. et al. 'COMPTEL observations of Ti-44 gamma-ray line emission from CAS A.' *Astronomy and Astrophysics*, **284**(1): L1–L4, 1994.

Iyudin, A. et al. 'Resonant absorption troughs in gamma-ray spectra of QSO.' *Astronomy and Astrophysics*, **436**: 763–784, 2005.

Kanbach, G. et al. 'The project EGRET (Energetic Gamma-Ray Experiment Telescope) on NASA's Gamma-Ray Observatory (GRO).' *Space Science Reviews*, **49**: 69–84, 1988.

Kanbach, G. et al. 'Development and calibration of the tracking Compton/Pair telescope MEGA.' *Nuclear Instruments and Methods in Physics Research A*, **541**: 310–322, 2005.

Kippen, R. 'The GEANT low energy Compton scattering (GLECS) package for use in simulating advanced Compton telescopes.' *New Astronomy Reviews*, **48**: 221–226, 2004.

Klein, O. and Nishina, T. 'Über die Streuung von Strahlung durch freie Elektronen nach der neuen relativistischen Quantendynamik von Dirac.' *The European Physical Journal A - Hadrons and Nuclei (Historical Archive)*, **52**(11-12): 853–868, 1929.

Knödelseder, J. 'Prospects in space-based gamma-ray astronomy.' In Favata, F. and Gimenez, A., editors, *Proc. 39th ESLAB Symposium*, 2005.

Knödelseder, J. et al. 'The all-sky distribution of 511 keV electron-positron annihilation emission.' *Astronomy and Astrophysics*, **441**: 513–532, 2005.

Kurfess, J. et al. 'An advanced Compton telescope based on thick, position-sensitive solid-state detectors.' *New Astronomy Reviews*, **48**: 293–298, 2004.

Lange, K. and Carson, R. 'EM reconstruction algorithms for emission and transmission tomography.' *Journal of Computer Assisted Tomography*, **8**(2): 306–316, 1984.

Lebrun, F. et al. 'Compact sources as the origin of the soft γ-ray emission of the Milky Way.' *Nature*, **428**: 293–296, 2004.

Lei, F. et al. 'Compton scatter polarimetry in gamma-ray astronomy.' *Space Sci. Rev.*, **82**: 309–388, 1997.

Leibundgut, B. 'Type Ia Supernovae.' *The Astron Astrophys Rev*, **10**: 179–209, 2000.

Lin, R. et al. 'The Reuven-Ramaty High-Energy Solar Spectroscopic Imager (RHESSI).' *Solar Physics*, **219**: 3–32, 2002.

Litvinenko, V. et al. 'High power inverse Compton gamma-ray source at Duke storage ring.' *SPIE*, **2521**: 55–77, 1995.

Litvinenko, V. et al. 'Gamma-Ray production in a storage Ring Free-Electron Laser.' *Physical Review Letters*, **78**(24): 4569–4572, 1997.

Lucy, L. B. 'An iterative technique for the rectification of observed distributions.' *The Astronomical Journal*, **79**: 745–754, 1974.

Massaglia, S. 'Constraining the parameters of AGN jets.' *Astrophysics and Space Science*, **287**: 223–233, 2003.

McConnell, M. et al. 'COMPTEL All-Sky Imaging at 2.2 MeV.' In *AIP Conf. Proc. 410: Proceedings of the Fourth Compton Symposium*, page 1099, 1997.

Milne, P. et al. 'Advanced Compton Telescope designs and SN science.' *New Astronomy Reviews*, **48**: 617–623, 2002.

Modesitt, G. and Koch, H. 'Nuclear Impulse in Electron Pair Creation.' *Physical Review*, **77**(2): 175–179, 1950.

Morris, D. J. et al. 'Evidence for ^{56}Co Line Emission from the Type Ia Supernova 1991 T Using COMPTEL.' In *Seventeenth Texas Symposium on Relativistic Astrophysics and Cosmology*, pages 397–400, 1995.

Mowlavi, N. et al. 'Search for ^{26}Al in Gamma Velorum.' In Schöenfelder, V., Lichti, G., and Winkler, C., editors, *ESA SP-552: 5th INTEGRAL Workshop on the INTEGRAL Universe*, 2004.

Nefzger, C. 'Entwicklung von Methoden zur Auswertung von Einzel-Ereignissen des neuartigen Gamma-Teleskops MEGA.' Diploma thesis, Technical University Munich, 2000. Available in German at the web-site: http://www.mpe.mpg.de/MEGA/mega-documents.html.

Oberlack, U. et al. 'COMPTEL limits on ^{26}Al 1.809 MeV line emission from gamma^2 Velorum.' *Astronomy and Astrophysics*, **353**: 715–721, 2000a.

Oberlack, U. et al. 'A Compton scattering sequence reconstruction algorithm for the liquid xenon gamma-ray imaging telescope (LXeGRIT).' In R.B. James, R. S., editor, *Hard X-Ray, Gamma-Ray, and Neutron Detector Physics II*, volume 4141, pages 168–177. SPIE, 2000b.

O'Neill, T. J. 'Tracking, Imaging, and Polarimeter Properties of the TIGRE Instrument.' *Astronomy and Astrophysics Supplement Series*, **120**, 1996.

Owens, A. et al. 'The Transient Gamma-Ray Spectrometer.' *IEEE Transactions on Nuclear Science*, **39**(2): 559–567, 1991.

Palacios, A. et al. 'New estimates of the contribution of Wolf-Rayet stellar winds to the Galactic ^{26}Al.' *Astronomy and Astrophysics*, **429**: 613–624, 2005.

Park, S. H. et al. 'Spatial distribution and polarization of γ-rays generated via Compton backscattering in the Duke/OK-4 storage ring FEL.' *Nuclear Instruments and Methods in Physics Research A*, **475**: 425–431, 2001.

Particle Data Group. 'Review of Particle Physics.' *Physics Letters B*, **592**(1-4), 2004.

Plüschke, S. '^{26}Al Ursprung und OB-Assoziationen.' Ph.D. thesis, Technische Universität München, 2001.

Prantzos, N. 'Radioactive ^{26}Al and ^{60}Fe in the Milky Way: implications of the RHESSI detection of ^{60}Fe.' *Astronomy and Astrophysics*, **420**: 1033–1037, 2004.

Press, W. *Numerical recipes in C: the art of science computing.* Cambridge, 1992.

Ramaty, R., Kozlovsky, B., and Lingenfelter, R. 'Nuclear Gamma-Ray From Energetic Particle Interactions.' *The Astrophysical Journal Supplement Series*, **40**: 487–526, 1979.

Renaud, M. et al. 'An INTEGRAL/IBIS view of Young Galactic SNRs through the ^{44}Ti gamma-ray lines.' *New Astronomy Reviews*, 2005. In preparation.

Ribberfors, R. 'Relationship of the relativistic Compton cross section to the momentum distribution of bound electron states. II. Effects of anisotropy and polarization.' *Physical Review B*, **12**: 3136–3141, 1975.

Ribberfors, R. and Berggren, K.-F. 'Incoherent-X-ray-scattering functions and cross sections by means of a pocket calculator.' *Physical Review A*, **26**: 3325–3333, 1982.

Richardson, W. H. 'Bayesian-based iterative method of image restoration.' *Optical Society of America Journal A*, 1972.

Riess, A. et al. 'Observational Evidence from Supernovae for an Accelerating Universe and a Cosmological Constant.' *The Astronomical Journal*, **116**: 1009–1038, 1998.

Schaefer, B. E. et al. 'High-energy spectral breaks in gamma-ray bursts.' *The Astrophysical Journal*, **393**: L51–L54, 1992.

Schmid, G. J. et al. 'A γ-ray tracking algorithm for the GRETA spectronometer.' *NIM A*, **430**: 69–83, 1999.

Schönfelder, V. et al. 'Instrument description and performance of the imaging gamma-ray telescope COMPTEL aboard the Compton Gamma-Ray Observatory.' *The Astrophysical Journal Supplement Series*, **86**: 657–692, 1993.

Schönfelder, V. et al. 'The first COMPTEL source catalogue.' *Astronomy and Astrophysics Supplement*, **143**: 145–179, 2000.

Schönfelder, V. et al. 'Ti-44 Gamma-Ray Line Emission from Cas A and RXJ0852-4622/GROJ0852-4642.' In McConnell, M. and Ryan, J., editors, *The Fifth Compton Symposium*, volume 510. AIP Conference Proceedings, 2000.

Schopper, F. 'Entwicklung eines Teleskops zur Abbildung von Gammastrahlung mittels Comptonstoß und Paarerzeugung.' Ph.D. thesis, Technical University Munich, Germany, 2001.

Sizun, P. et al. 'The INTEGRAL/SPI Response and the Crab Observations.' In *ESA SP-552: 5th INTEGRAL Workshop on the INTEGRAL Universe*, pages 815–818, 2004.

Skinner, G. 'Diffractive/refractive optics for high energy astronomy: I. Gamma-ray phase Fresnel lenses.' *Astronomy & Astrophysics*, **375**: 691–700, 2001.

Smith, D. M. 'Gamma-Ray Line Observations with RHESSI.' In *ESA SP-552: 5th INTEGRAL Workshop on the INTEGRAL Universe*, pages 45–48, 2004.

Stanek, K. et al. 'Spectroscopic discovery of the supernova 2003dh associated with GRB 030329.' *The Astrophysical Journal*, **591**: L17–L20, 2003.

Stecker, F. and Salamon, M. 'The Extragalactic Gamma-Ray Background.' In Ritz, S., Gehrels, N., and Shrader, C., editors, *Gamma-ray Astrophysics*, pages 432–441. AIP, New York, 2001.

Strigari, L. et al. 'The concordance cosmic star formation rate: implications from and for the supernova neutrino and gamma ray backgrounds.' *Journal of Cosmology and Astroparticle Physics*, 2005.

Strong, A. W. et al. 'A New Determination Of The Diffuse Galactic and Extragalactic Gamma-Ray Emission.' In *AIP Conf. Proc. 745: High Energy Gamma-Ray Astronomy*, pages 585–590, 2005.

Tavani, M. et al. 'The AGILE instrument.' In Truemper, J. and Tananbaum, H., editors, *X-Ray and Gamma-Ray Telescopes and Instruments for Astronomy*, volume 4851, pages 1151–1162. SPIE, 2003.

Thompson, D. J. et al. 'Calibration of the Energetic Gamma-Ray Experiment Telescope (EGRET) for the Compton Gamma-Ray Observatory.' *The Astrophysical Journal Supplement Series*, **86**: 629–656, 1993.

van der Marel, J. and Cederwall, B. 'Backtracking as a way to reconstruct Compton scattered γ-rays.' *NIM A*, **437**: 538–551, 1999.

von Ballmoos, P. et al. 'The MAX Mission: Focusing on High-Sensitivity Gamma-Ray Spectroscopy.' In *ESA SP-552: 5th INTEGRAL Workshop on the INTEGRAL Universe*, pages 747–750, 2004.

Watanabe, K. and Hartmann, D. 'Contributions of GRBs and Cen A-like Radio Galaxies to the Cosmic Gamma-ray Background.' In Ritz, S., Gehrels, N., and Shrader, C., editors, *Gamma-ray Astrophysics*, pages 442–445. AIP, New York, 2001.

Weidenspointner, G. et al. 'MGGPOD: a Monte Carlo Suite for Modeling Instrumental Line and Continuum Backgrounds in Gamma-Ray Astronomy.' *The Astrophysical Journal Supplement Series*, **156**: 69–91, 2005.

Wigger, C. et al. 'Can RHESSI be used as GRB Polarimeter?' In Schöenfelder, V., Lichti, G., and Winkler, C., editors, *ESA SP-552: 5th INTEGRAL Workshop on the INTEGRAL Universe*, 2004.

Wilderman, S. et al. 'List-mode Maximum Likelihood Reconstruction of Compton Scatter Camera Images in Nuclear Medicine.' *IEEE Trans. Nucl. Sci.*, **45**: 957, 1998.

Winkler, C. et al. 'The INTEGRAL mission.' *Astronomy and Astrophysics*, **411**: L1–L6, 2003.

Wolter, D. et al. 'MEGA Pre-Phase A Study.' Technical report, DaimlerCrysler Aerospace, Jena-Optronik GmbH, 2000.

Wunderer, C. et al. 'The ACT Vision Mission Study Simulation Effort.' *New Astronomy Reviews*, 2006. In press.

Zoglauer, A. 'Methoden der Bildrekonstruktion fuer das Comptonteleskop MEGA.' Diploma thesis, Technical University Munich, 2000. Available in German at the web-site: http://www.mpe.mpg.de/MEGA/mega-documents.html.

Acknowledgments

This work would not have been possible without the support and contributions of numerous others, and I would like to express my sincere gratitude to all of them:

- Prof. Volker Schönfelder for providing me the opportunity to work on such an interesting but sometimes really challenging topic, and for his continued interest in the completion of this work.
- Gottfried Kanbach, my advisor, for all his guidance, his support and all the fruitful discussions, for proof-reading many manuscripts, for his readiness to accept telephone calls on weekends and late at night, for giving me the opportunity to present my work at international meetings, and of course for his unbreakable enthusiasm for MEGA even when the detector didn't want to run at all.
- Robert Andritschke for getting the MEGA job done, for providing the excellent calibration of the prototype, which took him a year of 36-hour days, for his patience with MEGA (and not making good on his threats to throw the prototype out of the window), for his excellent skills in electronics, without which MEGA probably would have measured only random noise, for his friendship since the first day when we both started studying physics, for ... ok if I would list everything he has done for MEGA, then this text would go on for a while ... he was the real MEGA-man during the last five years!
- Trixi Wunderer for cheering me up during the darkest moments of the MEGA data analysis, for seeing the MEGA performance in much more positive light than I would ever be able to, for her excellent and elaborate proofreading of this work, for taking care of my well-being especially at the end phase of this work, and finally for hiding all the Easter eggs — which MEGA all found!
- Florian Schopper for laying the ground for the MEGA prototype, inspiring me to use list-mode as the image reconstruction algorithm of choice for MEGA, and introducing me to MEGA with one of the shortest job interviews ever ("Kannst du programmieren?").
- Fritz Schrey for taking care of numerous smaller and larger problems of the MEGA mechanics and electronics and organizing the logistics of the Duke campaign, for making sure that we all got our daily lunch at noon sharp ("Geh'ma jetzt endlich essen!?") — and of course for the propeller, which enabled the "supernova remnant" measurement!
- Peter Bloser for numerous helpful discussions on polarization and pair production and his support during all the calibrations of the MEGA prototype.
- Werner Collmar for introducing me to COMPASS, for providing me with COMPTEL data, and of course for an apartment in Garching really close to MPE.
- Karsten Kretschmer, Alexander Stefanescu and Christian Clemens for all the fruitful discussions about Linux, Bash, physics, astronomy, etc.

- Vladimir Litvineko and his crew at HIGS, for providing the excellent calibration beam; thanks also to all others who helped during the Duke campaign.
- Georg Weidenspointer and Steve Sturner for implementing the ACT/MEGAlib extension into MGeant/MGGPOD, which enabled the orbital background simulations for MEGA.
- Steve Boggs for giving me the opportunity to finish this thesis at the Space Science Laboratory in Berkeley, California — long after MPE stopped its financial support, and to Jason Bowen and Mark Bandstra for some helpful discussions.

And of course a big thank you to all who helped to get MEGA up and running at MPE and to all the other gamma-ray astronomers at MPE and SSL for their support during this work and for providing the excellent work atmosphere at both places.

Above all my very special thanks goes to my parents and grandparents — without their continuing support this work would have never been possible!

Thank you — Dankeschön!